Acta Pharmacologica Sinica (2012) 33: 717–727
 1671-4083/12 $32.00
www.nature.com/aps

Original Article

Classical eyeblink conditioning using electrical stimulation of caudal mPFC as conditioned stimulus is dependent on cerebellar interpositus nucleus in guinea pigs

Guang-yan WU[1, 2, #], Juan YAO[2, #], Zheng-li FAN[2], Lang-qian ZHANG[2], Xuan LI[2], Chuang-dong ZHAO[3], Zhen-hua ZHOU[4], Jian-feng SUI[1, 2, *]

[1]Department of Physiology, College of Basic Medical Sciences, Third Military Medical University, Chongqing 400038, China; [2]Experimental Center of Basic Medicine, College of Basic Medical Sciences, Third Military Medical University, Chongqing 400038, China; [3]Department of Neurosurgery, General Hospital of Ji-nan Command, Ji-nan 250003, China; [4]Department of Neurology, Southwest Hospital, Third Military Medical University, Chongqing 400038, China

Aim: To determine whether electrical stimulation of caudal medial prefrontal cortex (mPFC) as conditioned stimulus (CS) paired with airpuff unconditioned stimulus (US) was sufficient for establishing eyeblink conditioning in guinea pigs, and whether it was dependent on cerebellar interpositus nucleus.
Methods: Thirty adult guinea pigs were divided into 3 conditioned groups, and trained on the delay eyeblink conditioning, short-trace eyeblink conditioning, and long-trace eyeblink conditioning paradigms, respectively, in which electrical stimulation of the right caudal mPFC was used as CS and paired with corneal airpuff US. A pseudo conditioned group of another 10 adult guinea pigs was given unpaired caudal mPFC electrical stimulation and the US. Muscimol (1 μg in 1 μL saline) and saline (1 μL) were infused into the cerebellar interpositus nucleus of the animals through the infusion cannula on d 11 and 12, respectively.
Results: The 3 eyeblink conditioning paradigms have been successfully established in guinea pigs. The animals acquired the delay and short-trace conditioned responses more rapidly than long-trace conditioned responses. Muscimol infusion into the cerebellar interpositus nucleus markedly impaired the expression of the 3 eyeblink conditioned responses.
Conclusion: Electrical stimulation of caudal mPFC is effective CS for establishing eyeblink conditioning in guinea pigs, and it is dependent on the cerebellar interpositus nucleus.

Keywords: associative learning; memory; eyeblink conditioning; medial prefrontal cortex; cerebellar interpositus nucleus; muscimol; guinea pig

Acta Pharmacologica Sinica (2012) 33: 717–727; doi: 10.1038/aps.2012.32; published online 7 May 2012

Introduction

Classical eyeblink conditioning is one of the most widely used model systems for studying the behavioral and neurobiological mechanisms of associative learning and memory[1–3]. All variant of eyeblink conditioning involve paired presentations of a behaviorally neutral conditioned stimulus (CS; *eg*, a tone or light) and an unconditioned stimulus (US; *eg*, a corneal airpuff or periorbital shock). Initially, the organisms could produce only a reflexive eyeblink unconditioned response (UR) to the US. After hundreds of paired presentations of the CS and the US, the organisms could learn to close the eyes in response to the CS before the onset of the US (called the conditioned response, CR). According to the temporal relationship between the CS and the US, there are two commonly used procedures in eyeblink conditioning: trace and delay paradigms. In the trace eyeblink conditioning (TEC), a temporal gap occurs between the offset of the CS and the onset of the US, which is in contrast to the delay eyeblink conditioning (DEC), in which the CS overlaps the US and the two stimuli are terminated at the same time. It is well established that the brainstem-cerebellar circuit is the essential circuitry for the DEC[1, 3–6]. In addition, components of the auditory CS pathway (*eg*, the inferior colliculus or auditory thalamus) have

# The two authors contributed equally to this work.
* To whom correspondence should be addressed.
E-mail jfsui2003@yahoo.com.cn
Received 2012-02-19 Accepted 2012-03-14

recently been added to the DEC circuit[7–14]. In contrast, several forebrain structures, such as the medial prefrontal cortex (mPFC)[15–21] and the hippocampus[22–26], are required for TEC in addition to a brainstem-cerebellar circuit[27–31].

It has been reported that electrical stimulations of the several key components in the auditory or visual CS pathway, including the cochlear nucleus[32], medial auditory thalamic[11], auditory cortex[33], lateral geniculate, superior colliculus, visual cortex[34,], pontine nuclei[6, 35–37], cerebellar mossy fiber[38, 39], parallel fibers[40, 41], interpositus nucleus[42, 43], *etc*, can serve as effective CSs for establishing eyeblink conditioning. Moreover, eyeblink conditioning has also been successfully achieved by using stimulation of other brain areas outside of CS pathway, like the primary somatosensory cortex, the coronal-precruciate cortex[44–46], *etc*. However, less work has been done to examine whether stimulation of the highest level in the hierarchical organization of the mammalian cortex (*ie*, PFC) is a sufficient CS to support associative eyeblink conditioning.

Cumulative evidence has demonstrated that PFC is implicated in many critical cognitive functions[47–49] and that mPFC is closely involved in associative learning[50] such as eyeblink conditioning[15–18, 51]. Electrical stimulation of the right rostal PFC of a cat was an effective CS for eyeblink conditioning[52]. Given that the caudal mPFC input to the pontine nuclei is necessary for eyeblink conditioning[6], it can be hypothesized that electrical stimulation of the caudal mPFC as a CS paired with an airpuff US is sufficient for establishing eyeblink conditioning, and that it is dependent on the cerebellar interpositus nucleus. The present study was designed to determine whether electrical stimulation of caudal mPFC is a sufficient CS for establishing eyeblink conditioning, and whether it is dependent on the cerebellar interpositus nucleus. Furthermore, the caudal mPFC play an important role in long TEC (*eg*, TEC with a 500-ms trace interval, the interval between CS offset and US onset)[6, 17, 18, 53, 54], but not in short TEC (*eg* TEC with a 150-ms trace interval) or DEC[6, 17–19, 21, 55–59]. Thus, the current study was also designed to examine the differences in CRs among the three eyeblink conditioning paradigms when the caudal mPFC was selected as the site at which CS stimulation was applied.

Materials and methods

Subjects

A total of 40 adult female albino Dunkin-Hartley guinea pigs were included in the study. The guinea pigs weighed 500–550 g and were approximately 4–5 months old at the time of surgery. Before the experiments and between the conditioning sessions, these animals were individually housed in standard plastic cages that operated on a 12:12 light/dark cycle. The animals were granted free access to food and water *ad libitum*. The room temperature was maintained at 25±1 °C. All experiments were performed between 8:00 AM and 6:00 PM during the light portion of the cycle. The experimental procedures were approved by the Animal Care Committee of the Third Military Medical University and were performed in accordance with the principles outlined in the NIH Guide for the Care and Use of Laboratory Animals. All efforts were made to optimize comfort and to minimize the use of the animals.

Surgery

The animals were allowed to remain undisturbed in their cages for 1 week prior to surgery. The guinea pigs were anesthetized with a mixture of ketamine (80 mg/kg, ip; Hengrui, Lianyungang, China) and xylazine (5 mg/kg, ip; Sigma-Aldrich, St Louis, MO, USA). The anesthetized animal's head was secured to a stereotaxic apparatus (SR-6N, Narishige, Tokyo, Japan) with lambda positioned 1.0 mm ventral to bregma. A longitudinal incision was subsequently made to reveal the skull onto which a Plexiglas headstage (1.0 cm× 1.0 cm×0.5 cm), designed to secure the animal's head, was cemented with dental cement using four stainless steel anchoring screws. One small hole (diameter: 1.0 mm) was drilled on the right side of the skull centered on the right caudal mPFC at the following stereotaxic coordinates: anteroposterior (AP) +13.0 mm, mediolateral (ML) 1.0 mm relative to the frontal zero plane, and the midline sinus, respectively. Then, a stainless steel stimulating electrode (No 792500, A-M Systems, Sequim, WA, USA; coated diameter: 33.20 μm, bare diameter: 254.00 μm) was implanted into the right caudal mPFC through the hole according to an atlas of the guinea pig brain[60], and the electrode's tip was directed to the following stereotaxic coordinates: AP+13.0 mm, ML 1.0 mm, dorsoventral (DV)-2.5 mm to the skull surface (Figure 1A, 1B). Moreover, another small hole (diameter: 1.0 mm) was drilled on the left side of the skull centered on the left cerebellar interpositus nucleus at the following stereotaxic coordinates: AP-3.0 mm, ML 2.5 mm relative to the frontal zero plane, and the midline sinus, respectively. Then, a stainless steel guiding cannula (No 62001, RWD, Shenzhen, China; external diameter: 0.67 mm, internal diameter: 0.30 mm) was implanted into the left cerebellar interpositus nucleus through the hole according to an atlas of the guinea pig brain[60], and its tip was directed to the following stereotaxic coordinates: (AP-3.0 mm, ML 2.5 mm, DV-5.5 mm) (Figure 1A, 1B). The infusion cannula (No 62201, RWD, Shenzhen, China; external diameter: 0.20 mm, internal diameter: 0.10 mm) extended 0.5 mm beyond the tip of the guiding cannula to the final infusion position at the following stereotaxic coordinates: (AP-3.0 mm, ML 2.5 mm, DV-6.0 mm). The reference electrode was a copper wire (0.5 mm in diameter) attached to the four stainless steel anchoring screws implanted into the skull. This wire was not in direct contact with the skull or brain tissue. To prevent occlusion, a removable stainless steel stylet (No 62101, RWD, Shenzhen, China) was inserted into the guiding cannula. The stylet provided up to 0.5 mm of extension beyond the tip of the guiding cannula. The stimulating electrode, reference electrode, and guiding cannula were fixed to the skull with dental cement. Finally, a small nylon loop was sutured into but not through the edge of the upper left eyelid. In the present study, this loop was utilized to attach the upper left eyelid to a movement-measuring device. After the surgery, the animals were allowed 1 week of

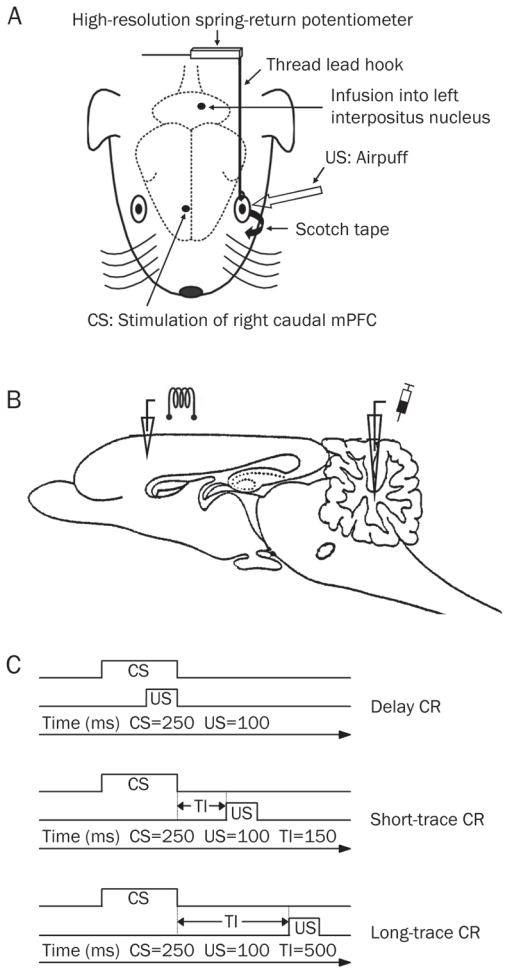

Figure 1. Experimental design. (A) The upper left eyelid movements were measured by a high-resolution spring-return potentiometer that was attached via a thread lead that was hooked through a nylon loop, which was sutured into the left upper eyelid, and the left lower eyelid was taped open. One electrode was implanted in the right caudal medial prefrontal cortex (mPFC) and one infusion guiding cannula was implanted in left cerebellar interpositus nucleus. Electrical stimulation of right caudal mPFC was used as a conditioned stimulus (CS), and airpuff was presented to the left cornea as an unconditioned stimulus (US). (B) Diagram of the sagittal section of guinea pig brain, showing the stimulating and infusion sites. (C) Schematic diagram showing the delay, short-trace, and long-trace eyeblink conditioned response (CR) paradigms used in the present study. Note that the CS, US, and total trial lengths were equal in each conditioning. Short and long-trace CR were different in trace interval (TI) length.

recovery.

Apparatus

Eyelid movements were measured by a high-resolution spring-return potentiometer (JZ101, XH, Beijing, China) that was attached via a thread lead hooked through the nylon loop sutured into the upper left eyelid. A stimulator (YC-2, Cheng Yi, Chengdu, China) was used to deliver a stimulation CS, while a plastic pipe placed 1.0 cm from the animal's left eyeball was used to deliver a corneal airpuff US (Figure 1A). A custom computerized monitoring system controlled presentations of the CS and US. Eyelid-movement mechanograms and applied-stimuli markers were digitized by a data-acquisition system (RM6280C, Cheng Yi, Chengdu, China) at a sample rate of 10 kHz and were acquired using the system's built-in software (v 4.7). A Windows PC was used to store and analyze the behavioral data.

Behavioral procedures

The 40 guinea pigs were divided into four groups: delay conditioned (n=10), short-trace conditioned (n=10), long-trace conditioned (n=10), and pseudo-conditioned (n=10). Each group represented one training paradigm. Following postoperative recovery, the animals were adapted to the experimental environment for two sessions at 60 min per session. These two sessions were followed by 10 consecutive daily sessions of acquisition training. Immediately following acquisition training, the three conditioned groups underwent 2 consecutive daily sessions of drug infusion. During the acquisition sessions and the drug infusion sessions, the animals were restrained in a Plexiglas container (25 cm×15 cm×15 cm) located in a sound- and light-attenuated chamber, and their heads were secured with blunt ear bars that pressed on the headstages. The left eye of the animal was held open in a confirmable position, with the nylon loop sutured into the left upper eyelid, which was linked to the high-resolution spring-return potentiometer. The voltage level represented the eyeblink baseline position, which was manually calibrated to a constant value. Moreover, the animal's left lower eyelid was taped open. These two measures ensured continual exposure of the left cornea.

During behavioral training, electrical stimulation of the caudal mPFC functioned as the CS, which was a 200-Hz, 250-ms train of monophasic pulses (cathodal, square, current level of 50–200 μA, a pulse duration of 0.1 ms). The electrical stimulation parameters were chosen based on the recent studies[8, 11, 14, 58]. The stimulation intensity for each guinea pig was set carefully before training by increasing the test current until a behavioral response was observed to avoid biasing the experimental results through an electrical startle response and a spreading of the electrical stimulation current to remote brain areas, such as hippocampus, premotor cortex, and somatosensory cortex. The current was then turned down in 5-μA increments until there was no observable behavioral response. Typical behavioral responses observed from the test stimulation included movements of the eyelid, eye, ear and/or head[8, 11, 14, 58]. In most of the cases (28/37) in the present experiment, the threshold stimulation was between 50–120 μA. An additional evoked field potentials recording test showed that the caudal mPFC stimulation with 200 μA or below did not evoke any field potential in the motor cortex, somatosensory cortex, or the cerebellar cortex (date not shown). The US was a 100-ms, 3.0-psi airpuff. A daily acquisition training session consisted of five 10-trial blocks. However, a daily infusion session (d 11 and d 12) consisted of three 10-trial blocks before the infusion and five 10-trial blocks after the infusion.

Moreover, each block comprised nine CS-US paired trials and one CS alone trial. The trials were separated by a variable intertrial interval of 20–40 s with a mean intertribal interval of 30 s. For the delay-conditioning paradigm, the US terminated simultaneously with the offset of the CS (the interstimulus interval was 150 ms). For the short-trace and long-trace conditioning paradigms, a stimulus-free trace interval of 150 ms or 500 ms was interposed between the CS termination and the US onset, respectively (Figure 1C). For the pseudo-conditioning paradigm, the US was presented at a random interval between 1 and 10 s after the CS onset. All experiments were performed during the light phase of the light/dark cycle.

Drug infusions

Two drug infusion sessions were conducted during d 11 and d 12. Each infusion session began with three blocks of training to establish a baseline of response prior to each drug infusion. Drug infusions were performed 20 min before the subsequent beginning of conditioning training. Muscimol (Sigma-Aldrich, St Louis, MO, USA), which produces inactivation only to the soma of neurons but not to the fibers of passage, was dissolved in saline (phosphate buffer, pH 7.4), which served as the vehicle prior to use. During the first infusion session (d 11), 1.0 μg muscimol in 1.0 μL saline was infused into the guinea pigs' left cerebellar interpositus nucleus. Infusion procedures for each animal included removal of the internal stylet from the guiding cannula, insertion of a stainless steel infusion cannula that extended 0.5 mm below the tip of the guiding cannula, infusion of the drug at 0.5 μL/min via polyethylene tubing connected to a microsyringe, removal of the needle 5 min after the cessation of infusion, and finally, reinsertion of the internal stylet. During the second infusion session (d 12), 1.0 μL saline was infused into the guinea pigs' left cerebellar interpositus nucleus. The drug infusion procedures used in the second infusion session were the same as those used in the first infusion session. All of the animals were allowed 24 h to recover between the infusion sessions. Several prior studies that used similar infusion procedures have reported that muscimol spread maximally within the 10–20 min following infusion, that the effective inactivation radius was 1.5–2.0 mm, and that the blocking effect persisted for a period of up to 2.0 h in both cortical and subcortical tissues[61–63]. However, in present study, the exact drug diffusion into each animal is unknown because the spread of the three drugs was not measured directly.

Histology

After the completion of behavioral experiments, all of the animals were given a lethal dose of pentobarbital sodium (150 mg/kg, ip; SCRC, Shanghai, China) and were perfused transcardially with physiological saline followed by 4% paraformaldehyde, which was prepared in phosphate-bufferer (0.1 mol/L, pH 7.4). The brains were removed from the skulls and stored in 4% paraformaldehyde for several days. Four days prior to sectioning, the brains were transferred to a 30% sucrose/4% paraformaldehyde solution. Frozen coronal sections measuring 30 μm in thickness were taken from the sites of the electrode and infusion cannula implantation. The slices were stained with cresyl violet. The locations of the electrode and infusion cannula tips within the brains were carefully determined using a light microscope (SMZ1500, Nikon, Tokyo, Japan) with a digital camera (DXM1200F, Nikon, Tokyo, Japan) and were drawn onto plates using a stereotaxic atlas of the guinea pig brain[60].

Behavioral data analysis

For each training trial, 2000-ms time periods were recorded during the conditioning trials and 12-s time periods were recorded during the pseudo-conditioning trials beginning 800 ms before the onset of the CS. Drug infusions were not recorded. All data presented in this paper are measurements of the left upper eyelid movements. The parameters of eyeblink responses were analyzed using custom software.

Each CS-US paired trial presented during the conditioning training was subdivided into three discontinuous analysis periods: (1) a "baseline" period, which occurred at 0–800 ms before the CS onset; (2) a "CR" period, which occurred at 140 ms before the US onset; and (3) a "UR" period, which occurred at 0–250 ms after the US onset. The "baseline" period and "CR" period of each CS-alone trial were divided in the same manner as the baseline and CR periods from the CS-US paired trials for the same training paradigm. A significant eyelid movement was defined as an increase in mechanogram amplitude that was greater than the mean baseline amplitude and had four times the standard deviation of the baseline activity. In addition, the significant eyelid movement required a minimal duration of 15 ms. Any significant eyelid movement during the latter two periods defined above was counted as a CR or a UR, respectively. The percentage of CR (CR%) was defined as the ratio of the number of trials containing the CR to the total number of valid trials. The CR peak amplitude was defined as the maximum amplitude change from baseline during the CR period. The trials containing CR were selected for analysis of CR peak amplitude. The CR relative peak latency was defined as the time interval from the CR peak to the US onset.

Only the CR% was analyzed for the animals that received pseudo-conditioning training. For each trial, a significant eyelid movement that occurred within the time period 140 ms before the US onset was defined as a CR-like eyeblink response.

Statistical analysis

All data were expressed as means±SEM. Statistical significance was determined by a least significant difference (LSD) *post-hoc* test following a two-way repeated measures analyses of variance (ANOVA), a separate one-way repeated measures ANOVA, or a separate one-way ANOVA using the SPSS software for Windows package (v 18.0). A value of $P<0.05$ was considered statistically significant.

Results

Electrode and infusion cannula tips placements

Placement of the electrode cannula and infusion tips was carefully checked before the behavioral analysis commenced. An animal's data were excluded from the analysis if the electrode tip was not in the right caudal mPFC or the infusion cannula tip was not in the left cerebellar interpositus nucleus. Electrode tip placements in the right caudal mPFC were verified by examining a series of coronal sections. All electrode tips were placed in the right caudal mPFC (n=37). The infusion cannula tip placements in the left cerebellar interpositus nucleus were also verified by examining a series of coronal sections (Figure 2A). Most of the infusion cannula tip placements were in or near the left cerebellar interpositus nucleus (n=35) with one exception each in the delay and short-trace conditioned group (Figure 2B).

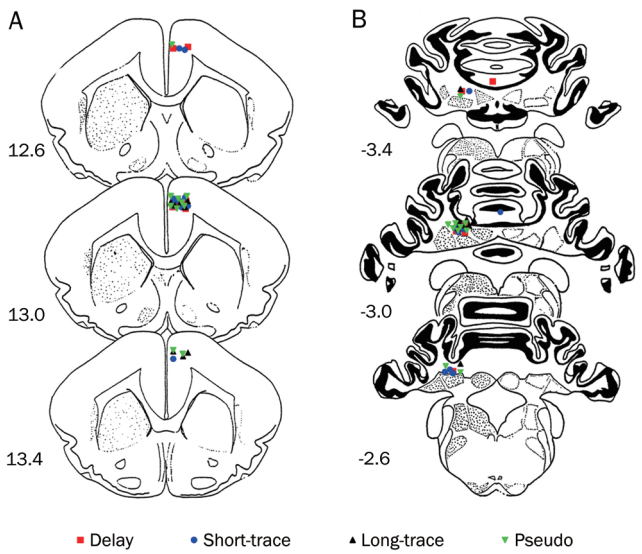

Figure 2. Histological reconstructions of the electrode and infusion cannula tips. Schematic illustration of the locations of all electrode tips (A) and all infusion cannula tips (B) for the delay (■; n=9), short-trace (●; n=10), long-trace (▲; n=8), and pseudo conditioned (▼; n=10) groups, respectively. Note that one infusion cannula tip of the delay conditioned group and one infusion cannula tip of the short-trace conditioned group were not in or near the left cerebellar interpositus nucleus. Numbers to the left represent distance (mm) from the frontal zero plane. The coronal brain plates are adapted from the atlas of Rapisarda and Bacchelli (1977).

Acquisition of eyeblink conditioning by the guinea pigs

The data from two animals in the delay-conditioned group, from one animal in the short-trace conditioned group and from two animals in long-trace conditioned group were removed from the analysis, because either the infusion cannula tips placements were not in or near the left cerebellar interpositus nucleus (n=2) or the animal had died before the end of the experiment (n=3). The CR% increased as a function of sessions for the delay, short-trace and long-trace conditioned groups (Figure 3A). This increase was confirmed by a two-way repeated measures ANOVA, there was a significant interaction between groups and sessions [$F_{(27,279)}$=7.289, P<0.001], and significant main effects of group [$F_{(3,31)}$=39.295, P<0.001] and session [$F_{(9,279)}$=38.940, P<0.001]. Furthermore, LSD *post-hoc* tests revealed that the CR% of the delay, short-trace, and long-trace conditioned groups was significantly higher than the CR% of the pseudo-conditioned group (P<0.001, P<0.001, and P=0.026, respectively; Figure 3A). The simple main effects of session for CR% during acquisition training were further analyzed using separate one-way repeated measures ANOVA.

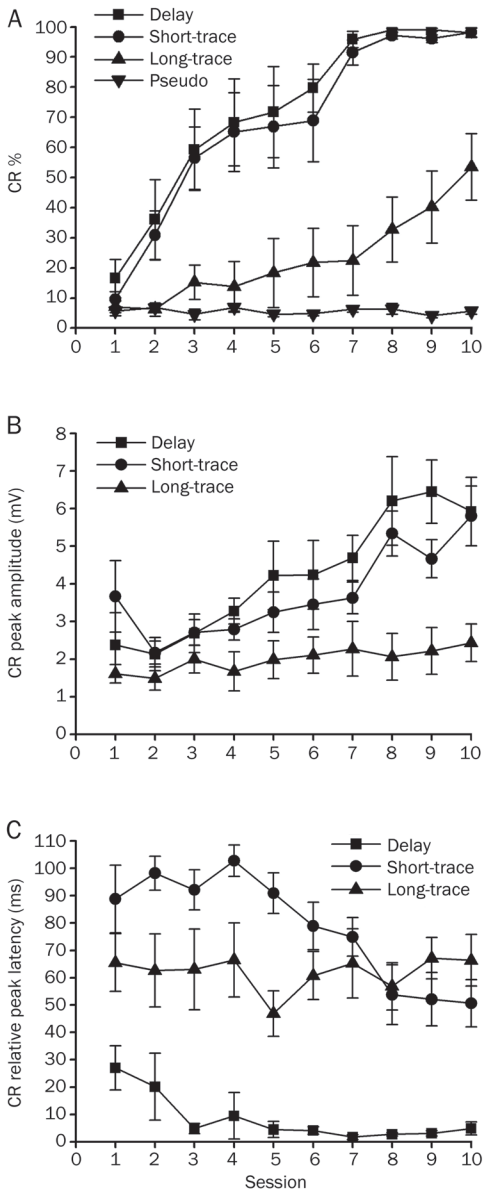

Figure 3. Acquisition of the eyeblink conditioned responses (CR) for delay (n=8), short-trace (n=9), long-trace (n=8), and pseudo (n=10) conditioned groups given training with a right caudal mPFC conditioned stimulus (CS) across 10 acquisition training sessions. (A) CR percentage, (B) CR peak amplitude, and (C) CR relative peak latency are given as mean±standard error (SEM). Error bars represent the SEM.

This analysis revealed that the simple main effects of session on CR% were significant for the delay [$F_{(9,63)}$=14.517, P<0.001], short-trace [$F_{(9,72)}$=2.332, P<0.001], and long-trace [$F_{(9,63)}$=5.543, P<0.001] conditioned groups, but not for the pseudo-conditioned group [$F_{(9,81)}$=0.626, P=0.772; Figure 3A].

To investigate the effects of the different conditioning training paradigms on the CR pattern, CR peak amplitude and relative peak latency was analyzed for all of the animals. LSD *post-hoc* tests confirmed that the CR peak amplitude in the long-trace conditioned group was significantly lower than that in the delay (P<0.001) and short-trace (P=0.002) conditioned groups. The latter two groups did not differ significantly from each other (P=0.356; Figure 3B). In addition, a separate one-way repeated measures ANOVA revealed that the simple main effects of session on the CR peak amplitude were significant for both the delay [$F_{(9,63)}$=5.143, P<0.001] and short-trace [$F_{(9,72)}$=4.529, P<0.001] conditioned groups, but not for the long-trace conditioned group [$F_{(9,81)}$=0.873, P=0.554; Figure 3B].

Furthermore, LSD *post-hoc* tests revealed that the CR relative peak latency in the delay conditioned group was significantly lower than that in either the short-trace (P<0.001) or the long-trace (P<0.001) conditioned groups. The latter two groups differed significantly from each other (P=0.019; Figure 3C). Moreover, the LSD *post-hoc* tests confirmed that the CR relative peak latency during session 1 was significantly higher than during session 10 for the delay (P=0.041) and short-trace (P=0.043) conditioned groups, but not for the long-trace conditioned group (P=0.994; Figure 3C).

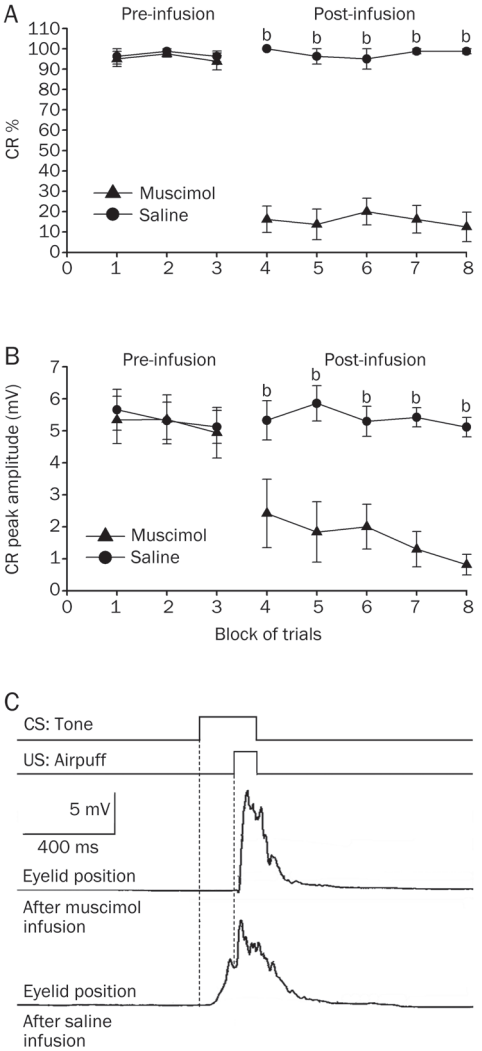

Figure 4. Delay conditioned group data for the effects of muscimol (▲) and saline (●) infused into the left cerebellar interpositus nucleus. (A) Infusion of muscimol abolished the responses almost completely as illustrated by its effects on the percentage of trials in which the delay CRs were seen, whereas infusion of saline had no significant effect on the delay CRs. (B) Muscimol infusion significantly decreased the peak amplitude of the delay CRs. (C) Eyelid position of an animal after muscimol and saline infusion in the sixth trial. Upper panel: the conditioning paradigm illustrating the timing of the CS and the US. Middle panel: eyelid position after muscimol infusion. Lower panel: eyelid postion after saline infusion. All data are from the same animals. Mean±SEM. n=8. ^bP<0.05 *vs* control.

Effects of muscimol infusion into the left cerebellar interpositus nucleus on DEC expression

Infusion of muscimol into the left cerebellar interpositus nucleus significantly decreased the CR% (Figure 4A, right panel) and the CR peak amplitude for the group that received delay conditioning (Figure 4B, right panel). A two-way repeated measures ANOVA performed on CR% (Figure 4A, left panel) and CR peak amplitude (Figure 4B, left panel) revealed there was no significant effect of trial block [$F_{(1,14)}$=0.299, P=0.593 and $F_{(1,14)}$=0.028, P=0.870, respectively] during the pre-infusion block (trial blocks 1–3). However, the two-way repeated measures ANOVA confirmed that the CR% (Figure 4A, right panel) and the CR peak amplitude (Figure 4B, right panel) for the animals that received the muscimol infusion were significantly lower than those observed for the animals that received the saline infusion [$F_{(1,14)}$=25.599, P<0.001 and $F_{(1,14)}$=36.147, P<0.001, respectively] during the post-infusion block (trial blocks 4–8).

Effects of muscimol infusion into the left cerebellar interpositus nucleus on short TEC expression

Infusion of muscimol into the left cerebellar interpositus nucleus significantly decreased the CR% (Figure 5A, right panel) and the CR peak amplitude for the group that received short-trace conditioning (Figure 5B, right panel). A two-way repeated measures ANOVA performed on CR% (Figure 5A, left panel) and CR peak amplitude (Figure 5B, left panel) revealed that there was no significant effect of trial block [$F_{(1,16)}$=0.250, P=0.624 and $F_{(1,16)}$=0.516, P=0.483, respectively] during the pre-infusion block (trial blocks 1–3). However, the two-way repeated measures ANOVA confirmed that the CR% (Figure 5A, right panel) and the CR peak amplitude (Figure 5B, right panel) for the animals that received the muscimol infusion were significantly lower than for the animals that received the saline infusion [$F_{(1,16)}$=72.147, P<0.001 and $F_{(1,16)}$=33.558, P<0.001, respectively] during the post-infusion

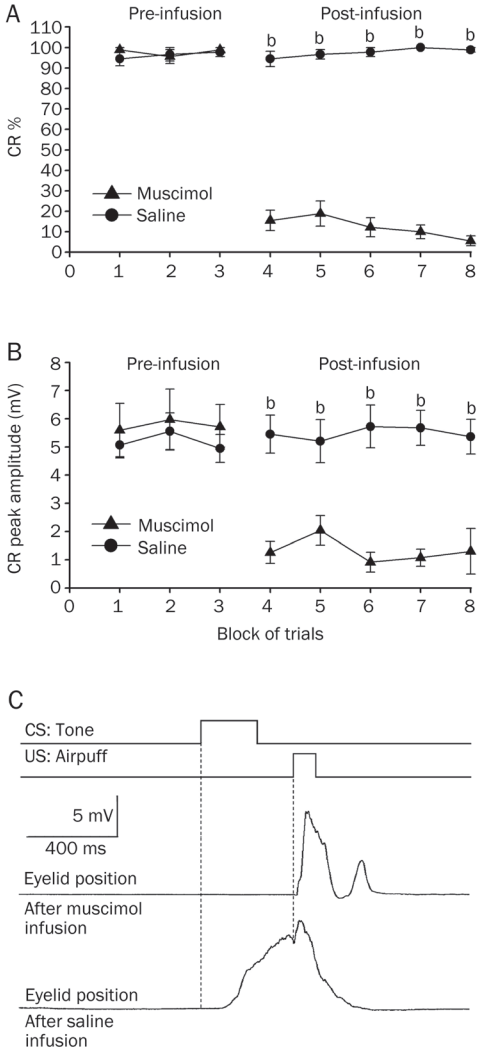

Figure 5. Short-trace conditioned group data for the effects of muscimol (▲), and saline (●) infused into the left cerebellar interpositus nucleus. (A) Infusion of muscimol abolished the responses almost completely as illustrated by its effects on the percentage of trials in which the short-trace CRs are seen, whereas infusion of saline had no significant effect on the short-trace CRs. (B) Muscimol infusion significantly decreased the peak amplitude of the short-trace CRs. (C) Eyelid position of an animal after muscimol and saline infusion in the sixth trial. Upper panel: the conditioning paradigm illustrating the timing of the CS and the US. Middle panel: eyelid position after muscimol infusion. Lower panel: eyelid postion after saline infusion. All data are from the same animals. Mean±SEM. n=9. ^{b}P<0.05 *vs* control.

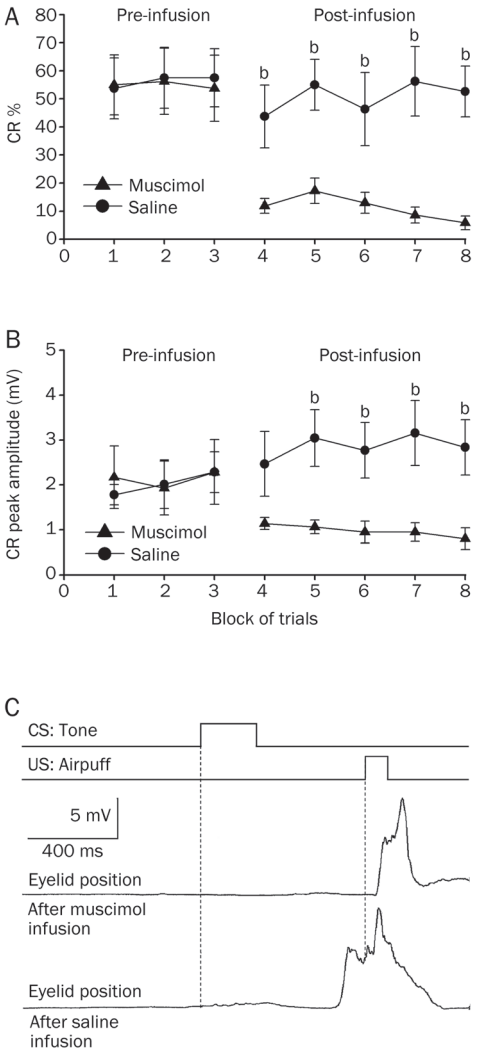

Figure 6. Long-trace conditioned group data for the effects of muscimol (▲) and saline (●) infused into the left cerebellar interpositus nucleus. (A) Infusion of muscimol abolished the responses almost completely as illustrated by its effects on the percentage of trials in which the long-trace CRs are seen, whereas infusion of saline had no significant effect on the long-trace CRs. (B) Muscimol infusion had significant effect on peak amplitude of the long-trace CRs. (C) Eyelid position of an animal after muscimol and saline infusion in the sixth trial. Upper panel: the conditioning paradigm illustrating the timing of the CS and the US. Middle panel: eyelid position after muscimol infusion. Lower panel: eyelid postion after saline infusion. All data are from the same animals. Mean±SEM. n=8. ^{b}P<0.05 *vs* control.

block (trial blocks 4–8).

Effects of muscimol infusion into the left cerebellar interpositus nucleus on long TEC expression

Infusion of muscimol into the left cerebellar interpositus nucleus significantly decreased the CR% (Figure 6A, right panel) and the CR peak amplitude (Figure 6B, right panel) for the group that received long-trace conditioning. A two-way repeated measures ANOVA performed on CR% (Figure 6A, left panel) and CR peak amplitude (Figure 6B, left panel) revealed that there was no significant effect of trial block [$F_{(1,14)}$=0.007, P=0.933 and $F_{(1,14)}$=0.089, P=0.770, respectively] during the pre-infusion block (trial blocks 1–3). In contrast, the two-way repeated measures ANOVA confirmed that the CR% (Figure 6A, right panel) and the CR peak amplitude (Figure 6B, right panel) for the animals that received the muscimol infusion were significantly lower than for the animals that received the saline infusion [$F_{(1,14)}$=25.801, P<0.001 and

$F_{(1,14)}$=8.313, P<0.001, respectively] during the post-infusion block (trial blocks 4–8).

Discussion

In the initial portion of this study, it was demonstrated that electrical stimulation of the caudal mPFC as a CS paired with an airpuff US was sufficient for establishing eyeblink conditioning in guinea pigs. In contrast, unpaired presentations of the stimulation CS and airpuff US did not obtain CR across 10 d of training, suggesting that CRs observed in the conditioned groups were due to associative learning. Against our expectations, the guinea pigs acquired long TEC slower than both DEC and short TEC, in agreement with the previous studies using peripheral CS (*eg*, a tone or a light CS) in eyeblink conditioning[64, 65]. There is a possibility that the longer trace interval between the CS and the US makes it difficult for them to timely converge inside brain, and that additional brain regions such as the hippocampus, mPFC and amygdala are required for establishment of long TEC[6, 13, 17, 18, 22–24, 53, 54, 66–69]. There were significant increases in CR amplitudes and decreases in CR relative peak latency in both delay and short-trace, but not in long-trace conditioned groups, attributing to that long TEC had not been well learned during successive 10 sessions. Moreover, an additional evoked field potentials recording test showed that the caudal mPFC stimulation with 200 μA or below did not evoke any field potential in the motor cortex, somatosensory cortex, or the cerebellar cortex. Thus, the current results provide direct support for our hypothesis that electrical stimulation of mPFC as a CS paired with an airpuff US is sufficient for establishing eyeblink conditioning.

In the second portion of this study, infusion of muscimol into the left interpositus nucleus impaired CRs expression in the three conditioned groups, suggesting that the interpositus nucleus is critical for expression of this special CR. It is consistent with the findings of the previous studies using peripheral CS in eyeblink conditioning that cerebellar interpositus nucleus plays an essential role in CR expression[4, 27, 29, 31, 66, 70, 71]. Steinmetz[72] speculated that the cerebellum may only be involved in simple, discrete, aversive, and somatic associative learning that occurs with a relatively short interstimulus interval. The current results support his speculation, and show that the expression of this special CR, which is also a simple, discrete, somatic, aversive, and defensive behavior induced by stimulation of caudal mPFC as a CS, is still dependent on the cerebellum. The results from the present study further imply that it is the features of the CR rather than the CS that decide whether the cerebellum is necessary for CR operation.

Given that mPFC is necessary for long TEC[6, 17, 18, 53, 54], but not for DEC and short TEC[6, 17–19, 21, 55–59], it is expected that long TEC would be acquired more rapidly than DEC and short TEC at least in some manner when stimulation of the caudal mPFC, part of the long TEC circuit, was used as a CS. However, the present results show that the guinea pigs acquired DEC and short TEC more rapidly than long TEC. The current findings combined with the results of previous studies may indicate that one brain area at which an effective and sufficient stimulation CS for establishing CR was applied can not be interpreted as an essential area for classical eyeblink conditioning. For instance, lesions of the visual cortex did not prevent acquisition of CRs with a light CS[73], suggesting that the visual cortex is not involved in the process of CR acquisition, whereas stimulation of the visual cortex can be successfully used as a CS to establish CR[34]. Moreover, although lesions of the pretectal nuclei[73] and hippocampus[22–24, 68] retarded acquisition of eyeblink conditioning, stimulation of the anterior pretectal nucleus[11] and of the CA1 layer of hippocampus[74] can not be served as effective CSs for establishing eyeblink conditioning. Therefore, the present results only suggest that electrical stimulation of mPFC is a very effective and sufficient CS for establishing eyeblink conditioning, and that it is dependent on the cerebellar interpositus nucleus, but can not be interpreted as providing evidence that mPFC is critically involved in DEC, short TEC, or long TEC.

It is worth noting that long TEC with a tone CS acquisition requires mPFC that persists mossy fiber activity through the stimulus-free trace interval to overlap in time with the US[6, 75, 76]. In the present study, however, the guinea pigs could develop long TEC to mPFC stimulation CS even when it did not co-terminate with the US. There is a possibility that the mPFC activity which begins during the stimulation CS and persists beyond the stimulation CS offset to overlap with the US may induce long TEC successful establishment. Indeed, it is reported that the activity in the neurons of mPFC began during the tone CS and persisted to overlap with the US during TEC[77].

Despite careful and detailed analysis of the CRs acquisition to electrical CSs by previous studies, it is difficult to establish a minimum range of current for the electrical CS which is required for obtaining CR. The threshold stimulation of CS required to establish the CR in the present study was lower than that in most previously studies (50–200 μA in current study vs 180–250 μA for visual cortex stimulation[34]). This difference may in part due to differences in current spread at different sites of stimulation, but may also relate to differences in the numbers of cells which must be excited for the CS to be effective[45].

One of our primary purposes here was to test the effects of stimulation of the caudal mPFC on CR establishment. Whether or not stimulation of other areas of PFC can obtain the CR is an important issue, and should be investigated in future studies. While the distributed pattern of activation induced by electrical stimulation in awake animals is currently unknown[78], an additional evoked field potentials recording test showed that the caudal mPFC stimulation with 200 μA or below did not evoke any field potential in the motor cortex, somatosensory cortex, or the cerebellar cortex. Thus, the present experiment could rule out the possibility that stimulation of the caudal mPFC significantly activates other areas of cortex. In addition, the lesion and field potential data suggest that the lateral pontine nuclei conveys necessary CS signals to the cerebellum in eyeblink conditioning[79, 80]. Recent studies suggest that mossy fiber activity driven by input from mPFC

to lateral pontine nuclei which persists through the stimulus-free trace interval to overlap in time with the US supports the auditory TEC [6, 75, 76]. Therefore, the lateral pontine nuclei may also convey the electrical CS signals to the cerebellum in the three types of eyeblink conditioning induced by the electrical stimulation of caudal mPFC. However, this hypothesis needs further testing.

In conclusion, the results from this study show that electrical stimulation of caudal mPFC was a very effective CS for establishing eyeblink conditioning, and that the CR is dependent on the cerebellar interpositus nucleus. Moreover, the guinea pigs acquired delay and short-trace CRs more rapidly than long-trace CR. However, the current results should not be interpreted as providing evidence that mPFC is involved in DEC, short TEC, or long TEC.

Acknowledgements

This work was supported by Grants from the National Natural Science Foundation of China (No 30771769). We thank the assistance of De-ying CHEN in preparing the photomicrographs.

Author contribution

Jian-feng SUI and Guang-yan WU designed research; Guang-yan WU, Juan YAO, Zheng-li FAN, and Lang-qian ZHANG performed research; Juan YAO, Xuan LI, Chuang-dong ZHAO, and Zhen-hua ZHOU analyzed data; Jian-feng SUI and Guang-yan WU wrote the paper.

References

1 Christian KM, Thompson RF. Neural substrates of eyeblink conditioning: acquisition and retention. Learn Mem 2003; 10: 427–55.
2 Christian KM, Thompson RF. Long-term storage of an associative memory trace in the cerebellum. Behav Neurosci 2005; 119: 526–37.
3 Thompson RF. In search of memory traces. Annu Rev Psychol 2005; 56: 1–23.
4 Weeks AC, Connor S, Hinchcliff R, LeBoutillier JC, Thompson RF, Petit TL. Eye-blink conditioning is associated with changes in synaptic ultrastructure in the rabbit interpositus nuclei. Learn Mem 2007; 14: 385–9.
5 Green JT, Arenos JD. Hippocampal and cerebellar single-unit activity during delay and trace eyeblink conditioning in the rat. Neurobiol Learn Mem 2007; 87: 269–84.
6 Kalmbach BE, Ohyama T, Kreider JC, Riusech F, Mauk MD. Interactions between prefrontal cortex and cerebellum revealed by trace eyelid conditioning. Learn Mem 2009; 16: 86–95.
7 Halverson HE, Lee I, Freeman JH. Associative plasticity in the medial auditory thalamus and cerebellar interpositus nucleus during eyeblink conditioning. J Neurosci 2010; 30: 8787–96.
8 Halverson HE, Freeman JH. Medial auditory thalamic input to the lateral pontine nuclei is necessary for auditory eyeblink conditioning. Neurobiol Learn Mem 2010; 93: 92–8.
9 Halverson HE, Poremba A, Freeman JH. Medial auditory thalamus inactivation prevents acquisition and retention of eyeblink conditioning. Learn Mem 2008; 15: 532–8.
10 Freeman JH, Halverson HE, Hubbard EM. Inferior colliculus lesions impair eyeblink conditioning in rats. Learn Mem 2007; 14: 842–6.
11 Campolattaro MM, Halverson HE, Freeman JH. Medial auditory thalamic stimulation as a conditioned stimulus for eyeblink conditioning in rats. Learn Mem 2007; 14: 152–9.
12 Halverson HE, Freeman JH. Medial auditory thalamic nuclei are necessary for eyeblink conditioning. Behav Neurosci 2006; 120: 880–7.
13 Oswald BB, Knuckley B, Maddox SA, Powell DA. Ibotenic acid lesions to ventrolateral thalamic nuclei disrupts trace and delay eyeblink conditioning in rabbits. Behav Brain Res 2007; 179: 111–7.
14 Halverson HE, Freeman JH. Ventral lateral geniculate input to the medial pons is necessary for visual eyeblink conditioning in rats. Learn Mem 2010; 17: 80–5.
15 Simon B, Knuckley B, Churchwell J, Powell DA. Post–training lesions of the medial prefrontal cortex interfere with subsequent performance of trace eyeblink conditioning. J Neurosci 2005; 25: 10740–6.
16 Oswald BB, Maddox SA, Powell DA. Prefrontal control of trace eyeblink conditioning in rabbits: role in retrieval of the CR? Behav Neurosci 2008; 122: 841–8.
17 Oswald BB, Maddox SA, Tisdale N, Powell DA. Encoding and retrieval are differentially processed by the anterior cingulate and prelimbic cortices: a study based on trace eyeblink conditioning in the rabbit. Neurobiol Learn Mem 2010; 93: 37–45.
18 Powell DA, Churchwell J, Burriss L. Medial prefrontal lesions and Pavlovian eyeblink and heart rate conditioning: effects of partial reinforcement on delay and trace conditioning in rabbits (Oryctolagus cuniculus). Behav Neurosci 2005; 119: 180–9.
19 Weible AP, McEchron MD, Disterhoft JF. Cortical involvement in acquisition and extinction of trace eyeblink conditioning. Behav Neurosci 2000; 114: 1058–67.
20 Weible AP, Weiss C, Disterhoft JF. Activity profiles of single neurons in caudal anterior cingulate cortex during trace eyeblink conditioning in the rabbit. J Neurophysiol 2003; 90: 599–612.
21 Takehara-Nishiuchi K, Kawahara S, Kirino Y. NMDA receptor-dependent processes in the medial prefrontal cortex are important for acquisition and the early stage of consolidation during trace, but not delay eyeblink conditioning. Learn Mem 2005; 12: 606–14.
22 Weiss C, Bouwmeester H, Power JM, Disterhoft JF. Hippocampal lesions prevent trace eyeblink conditioning in the freely moving rat. Behav Brain Res 1999; 99: 123–32.
23 Beylin AV, Gandhi CC, Wood GE, Talk AC, Matzel LD, Shors TJ. The role of the hippocampus in trace conditioning: temporal discontinuity or task difficulty? Neurobiol Learn Mem 2001; 76: 447–61.
24 Tseng W, Guan R, Disterhoft JF, Weiss C. Trace eyeblink conditioning is hippocampally dependent in mice. Hippocampus 2004; 14: 58–65.
25 Solomon PR, Vander Schaaf ER, Thompson RF, Weisz DJ. Hippocampus and trace conditioning of the rabbit's classically conditioned nictitating membrane response. Behav Neurosci 1986; 100: 729–44.
26 Moyer JR Jr, Deyo RA, Disterhoft JF. Hippocampectomy disrupts trace eye-blink conditioning in rabbits. Behav Neurosci 1990; 104: 243–52.
27 Hu B, Yang L, Huang LS, Chen H, Zeng Y, Feng H, *et al*. Effect of cerebellar reversible inactivations on the acquisition of trace conditioned eyeblink responses in guinea pigs: comparison of short and long trace intervals. Neurosci Lett 2009; 459: 41–5.
28 Hu B, Lin X, Huang LS, Yang L, Feng H, Sui JF. Involvement of the ipsilateral and contralateral cerebellum in the acquisition of unilateral classical eyeblink conditioning in guinea pigs. Acta Pharmacol Sin 2009; 30: 141–52.
29 Pakaprot N, Kim S, Thompson RF. The role of the cerebellar inter-

positus nucleus in short and long term memory for trace eyeblink conditioning. Behav Neurosci 2009; 123: 54–61.
30 Takehara K, Kawahara S, Kirino Y. Time-dependent reorganization of the brain components underlying memory retention in trace eyeblink conditioning. J Neurosci 2003; 23: 9897–905.
31 Woodruff-Pak DS, Lavond DG, Thompson RF. Trace conditioning: abolished by cerebellar nuclear lesions but not lateral cerebellar cortex aspirations. Brain Res 1985; 348: 249–60.
32 Freeman JH, Duffel JW. Eyeblink conditioning using cochlear nucleus stimulation as a conditioned stimulus in developing rats. Dev Psychobiol 2008; 50: 640–6.
33 Knowlton BJ, Thompson RF. Conditioning using a cerebral cortical conditioned stimulus is dependent on the cerebellum and brain stem circuitry. Behav Neurosci 1992; 106: 509–17.
34 Halverson HE, Hubbard EM, Freeman JH. Stimulation of the lateral geniculate, superior colliculus, or visual cortex is sufficient for eyeblink conditioning in rats. Learn Mem 2009; 16: 300–7.
35 Freeman JH Jr, Rabinak CA. Eyeblink conditioning in rats using pontine stimulation as a conditioned stimulus. Integr Physiol Behav Sci 2004; 39: 180–91.
36 Rosen DJ, Steinmetz JE, Thompson RF. Classical discrimination conditioning of the rabbit's eyelid response using pontine stimulation as a conditioned stimulus. Behav Neural Biol 1989; 52: 51–62.
37 Steinmetz JE, Lavond DG, Thompson RF. Classical conditioning in rabbits using pontine nucleus stimulation as a conditioned stimulus and inferior olive stimulation as an unconditioned stimulus. Synapse 1989; 3: 225–33.
38 Steinmetz JE, Rosen DJ, Chapman PF, Lavond DG, Thompson RF. Classical conditioning of the rabbit eyelid response with a mossy-fiber stimulation CS: I. Pontine nuclei and middle cerebellar peduncle stimulation. Behav Neurosci 1986; 100: 878–87.
39 Steinmetz JE, Rosen DJ, Woodruff-Pak DS, Lavond DG, Thompson RF. Rapid transfer of training occurs when direct mossy fiber stimulation is used as a conditioned stimulus for classical eyelid conditioning. Neurosci Res 1986; 3: 606–16.
40 Shinkman PG, Swain RA, Thompson RF. Classical conditioning with electrical stimulation of cerebellum as both conditioned and unconditioned stimulus. Behav Neurosci 1996; 110: 914–21.
41 Jirenhed DA, Hesslow G. Time course of classically conditioned Purkinje cell response is determined by initial part of conditioned stimulus. J Neurosci 2011; 31: 9070–4.
42 Poulos AM, Thompson RF. Timing of conditioned responses utilizing electrical stimulation in the region of the interpositus nucleus as a CS. Integr Physiol Behav Sci 2004; 39: 83–94.
43 Jimenez-Diaz L, Navarro-Lopez Jde D, Gruart A, Delgado-Garcia JM. Role of cerebellar interpositus nucleus in the genesis and control of reflex and conditioned eyelid responses. J Neurosci 2004; 24: 9138–45.
44 Leal-Campanario R, Delgado-Garcia JM, Gruart A. Microstimulation of the somatosensory cortex can substitute for vibrissa stimulation during Pavlovian conditioning. Proc Natl Acad Sci U S A 2006; 103: 10052–7.
45 Woody CD, Yarowsky PJ. Conditioned eye blink using electrical stimulation of coronal-precruciate cortex as conditional stimulus. J Neurophysiol 1972; 35: 242–52.
46 Troncoso J, Munera A, Delgado-Garcia JM. Classical conditioning of eyelid and mystacial vibrissae responses in conscious mice. Learn Mem 2004; 11: 724–6.
47 Goldman-Rakic PS. Cellular and circuit basis of working memory in prefrontal cortex of nonhuman primates. Prog Brain Res 1990; 85: 325–35; discussion 35–6.
48 Goldman-Rakic PS. Cellular basis of working memory. Neuron 1995; 14: 477–85.
49 Fuster JM. The prefrontal cortex — an update: time is of the essence. Neuron 2001; 30: 319–33.
50 Corbit LH, Balleine BW. The role of prelimbic cortex in instrumental conditioning. Behav Brain Res 2003; 146: 145–57.
51 Powell DA, Skaggs H, Churchwell J, McLaughlin J. Posttraining lesions of the medial prefrontal cortex impair performance of Pavlovian eyeblink conditioning but have no effect on concomitant heart rate changes in rabbits (Oryctolagus cuniculus). Behav Neurosci 2001; 115: 1029–38.
52 Doty RW, Larsen RM, Ruthledge LT Jr. Conditioned reflexes established to electrical stimulation of cat cerebral cortex. J Neurophysiol 1956; 19: 401–15.
53 Simon B, Knuckley B, Churchwell J, Powell DA. Post-training lesions of the medial prefrontal cortex interfere with subsequent performance of trace eyeblink conditioning. J Neurosci 2005; 25: 10740–6.
54 Oswald BB, Maddox SA, Powell DA. Prefrontal control of trace eyeblink conditioning in rabbits: role in retrieval of the CR? Behav Neurosci 2008; 122: 841–8.
55 Kronforst-Collins MA, Disterhoft JF. Lesions of the caudal area of rabbit medial prefrontal cortex impair trace eyeblink conditioning. Neurobiol Learn Mem 1998; 69: 147–62.
56 Chachich M, Powell DA. Both medial prefrontal and amygdala central nucleus lesions abolish heart rate classical conditioning, but only prefrontal lesions impair reversal of eyeblink differential conditioning. Neurosci Lett 1998; 257: 151–4.
57 Powell DA, Skaggs H, Churchwell J, McLaughlin J. Posttraining lesions of the medial prefrontal cortex impair performance of Pavlovian eyeblink conditioning but have no effect on concomitant heart rate changes in rabbits (Oryctolagus cuniculus). Behav Neurosci 2001; 115: 1029–38.
58 Leal–Campanario R, Fairen A, Delgado-Garcia JM, Gruart A. Electrical stimulation of the rostral medial prefrontal cortex in rabbits inhibits the expression of conditioned eyelid responses but not their acquisition. Proc Natl Acad Sci U S A 2007; 104: 11459–64.
59 McLaughlin J, Skaggs H, Churchwell J, Powell DA. Medial prefrontal cortex and pavlovian conditioning: trace versus delay conditioning. Behav Neurosci 2002; 116: 37–47.
60 Rapisarda C, Bacchelli B. The brain of the guinea pig in stereotaxic coordinates. Arch Sci Biol (Bologna) 1977; 61: 1–37.
61 Martin JH. Autoradiographic estimation of the extent of reversible inactivation produced by microinjection of lidocaine and muscimol in the rat. Neurosci Lett 1991; 127: 160–4.
62 Martin JH, Ghez C. Pharmacological inactivation in the analysis of the central control of movement. J Neurosci Methods 1999; 86: 145–59.
63 Sarihi A, Motamedi F, Naghdi N, Rashidy-Pour A. Lidocaine reversible inactivation of the median raphe nucleus has no effect on reference memory but enhances working memory versions of the Morris water maze task. Behav Brain Res 2000; 114: 1–9.
64 Hu B, Chen H, Yang L, Tao ZF, Yan J, Zhang YH, *et al*. Changes of synaptic ultrastructure in the guinea pig interpositus nuclei associate with response magnitude and timing after trace eyeblink conditioning. Behav Brain Res 2012; 226: 529–37.
65 Kotani S, Kawahara S, Kirino Y. Trace eyeblink conditioning in decerebrate guinea pigs. Eur J Neurosci 2003; 17: 1445–54.
66 Green JT, Arenos JD. Hippocampal and cerebellar single-unit activity during delay and trace eyeblink conditioning in the rat. Neurobiol Learn Mem 2007; 87: 269–84.
67 Vogt LJ, Vogt BA, Sikes RW. Limbic thalamus in rabbit: architecture, projections to cingulate cortex and distribution of muscarinic acetyl-

choline, GABAA, and opioid receptors. J Comp Neurol 1992; 319: 205–17.
68 Debiec J, LeDoux JE, Nader K. Cellular and systems reconsolidation in the hippocampus. Neuron 2002; 36: 527–38.
69 Powell DA, Churchwell J. Mediodorsal thalamic lesions impair trace eyeblink conditioning in the rabbit. Learn Mem 2002; 9: 10–7.
70 Hu B, Chen H, Feng H, Zeng Y, Yang L, Fan ZL, *et al*. Disrupted topography of the acquired trace-conditioned eyeblink responses in guinea pigs after suppression of cerebellar cortical inhibition to the interpositus nucleus. Brain Res 2010; 1337: 41–55.
71 Garcia KS, Mauk MD. Pharmacological analysis of cerebellar contributions to the timing and expression of conditioned eyelid responses. Neuropharmacology 1998; 37: 471–80.
72 Steinmetz JE. Brain substrates of classical eyeblink conditioning: a highly localized but also distributed system. Behav Brain Res 2000; 110: 13–24.
73 Koutalidis O, Foster A, Weisz DJ. Parallel pathways can conduct visual CS information during classical conditioning of the NM response. J Neurosci 1988; 8: 417–27.
74 Prokasy WF, Kesner RP, Calder LD. Posttrial electrical stimulation of the dorsal hippocampus facilitates acquisition of the nictitating membrane response. Behav Neurosci 1983; 97: 890–6.
75 Kalmbach BE, Ohyama T, Mauk MD. Temporal patterns of inputs to cerebellum necessary and sufficient for trace eyelid conditioning. J Neurophysiol 2010; 104: 627–40.
76 Wada N, Kishimoto Y, Watanabe D, Kano M, Hirano T, Funabiki K, *et al*. Conditioned eyeblink learning is formed and stored without cerebellar granule cell transmission. Proc Natl Acad Sci U S A 2007; 104: 16690–5.
77 Siegel JJ, Kalmbach B, Chitwood RA, Mauk MD. Persistent activity in a cortical-to-subcortical circuit: bridging the temporal gap in trace eyelid conditioning. J Neurophysiol 2012; 107: 50–64.
78 Okuda Y, Shikata H, Song WJ. A train of electrical pulses applied to the primary auditory cortex evokes a conditioned response in guinea pigs. Neurosci Res 2011; 71: 103–6.
79 Bao S, Chen L, Thompson RF. Learning- and cerebellum-dependent neuronal activity in the lateral pontine nucleus. Behav Neurosci 2000; 114: 254–61.
80 Steinmetz JE, Logan CG, Rosen DJ, Thompson JK, Lavond DG, Thompson RF. Initial localization of the acoustic conditioned stimulus projection system to the cerebellum essential for classical eyelid conditioning. Proc Natl Acad Sci U S A 1987; 84: 3531–5.

Acta Pharmacologica Sinica (2012) 33: 728–736
 1671-4083/12 $32.00
www.nature.com/aps

Original Article

Comparison of the effects of DC031050, a class III antiarrhythmic agent, on hERG channel and three neuronal potassium channels

Ping LI[1], Hai-feng SUN[1], Ping-zheng ZHOU[1], Chao-ying MA[2], Guo-yuan HU[1], Hua-liang JIANG[1], Min LI[1], Hong LIU[1, *], Zhao-bing GAO[1, *]

[1]*State Key Laboratory of Drug Research, Shanghai Institute of Materia Medica, Chinese Academy of Sciences, Shanghai 201203, China;* [2]*Life Science and Engineering College of Southwest Jiaotong University, Chengdu 610031, China*

Aim: This study was conducted to test the selectivity of DC031050 on cardiac and neuronal potassium channels.
Methods: Human ether-à-go-go related gene (hERG), KCNQ and Kv1.2 channels were expressed in CHO cells. The delayed rectifier potassium current (I_K) was recorded from dissociated hippocampal pyramidal neurons of neonatal rats. Whole-cell voltage patch clamp was used to record the voltage-activated potassium currents. Drug-containing solution was delivered using a RSC-100 Rapid Solution Changer.
Results: Both DC031050 and dofetilide potently inhibited hERG currents with IC_{50} values of 2.3±1.0 and 17.9±1.2 nmol/L, respectively. DC031050 inhibited the I_K current with an IC_{50} value of 2.7±1.5 μmol/L, which was >1000 times the concentration required to inhibit hERG current. DC031050 at 3 μmol/L did not significantly affect the voltage-dependence of the steady activation, steady inactivation of I_K, or the rate of I_K from inactivation. Intracellular application of DC031050 (5 μmol/L) was insufficient to inhibit I_K. DC031050 up to 10 μmol/L had no effects on KCNQ2 and Kv1.2 channel currents.
Conclusion: DC031050 is a highly selective hERG potassium channel blocker with a substantial safety margin of activity over neuronal potassium channels, thus holds significant potential for therapeutic application as a class III antiarrhythmic agent.

Keywords: dofetilide; DC031050; class III antiarrhythmic agent; hERG; KCNQ; Kv1.2; delayed rectifier potassium current

Acta Pharmacologica Sinica (2012) 33: 728–736; doi: 10.1038/aps.2012.41; published online 21 May 2012

Introduction

Potassium channel blockers are categorised as class III antiarrhythmic agents due to their ability to prolong the duration of the cardiac action potential[1–4]. These drugs include ibutilide, somatilide, sotalol, azimilide, droneradone and amiodarone, which elicit their actions by blocking one or more cardiac potassium channels, such as I_{Kr}, I_{Ks} and I_{Kur}, among others. The class III antiarrhythmic drugs have been subject to extensive clinical investigation as safer and more effective alternatives to class I drugs, which exhibit recognised risks in selected populations[5–7]. However, numerous noncardiac side effects, such as nausea, drizzles and headaches, also frequently occur with the use of class III antiarrhythmic drugs. Some adverse effects outside of cardiac tissues are consistent with the observation that the class III agents have been found to act on noncardiac ion channels. For example, tedisamil, a class III agent that is currently under evaluation in clinical trials, inhibits a calcium-dependent potassium (BK) channel of rat hippocampal CA1 neurons and guinea-pig portal vein smooth muscle cells. The inhibition of neuronal BK channels was thought to be related to nervous system toxicity associated with tedisamil[8, 9]. E4031, a potent I_{Kr} blocker, exhibits inhibitory effects on all transient, sustained and inwardly rectifying potassium currents of rat taste cells[10]. Therefore, the assessment of the effects elicited by class III agents on noncardiac channels is important for evaluating the safety and clinical side effects of these drugs at an early stage of the drug discovery process.

Dofetilide is a relatively new class III antiarrhythmic drug that has been approved for the conversion of atrial fibrillation and flutter and the maintenance of normal sinus rhythm. It selectively blocks the rapid delayed rectifier potassium channel (I_{Kr}), but does not slow the delayed rectifier potassium channel (I_{Ks}) I_{K1}, sodium channels or calcium channels[11, 12]. To discover more effective class III antiarrhythmic agents, we

* To whom correspondence should be addressed.
E-mail zb.gao@mail.shcnc.ac.cn (Zhao-bing GAO);
hliu@mail.shcnc.ac.cn (Hong LIU).
Received 2012-02-10 Accepted 2012-03-28

have designed and synthesised a series of new methylsulfonamido phenylethylamine analogues based on the structure and pharmacophore of dofetilide[13, 14]. Biological assays using guinea pig atria indicated that all of the analogues exert significant class III activities, including the prolongation of action potential duration and of effective refractory duration. Of all of the analogues, DC031050 (*N*-Benzyl-*N*-[2-(*p*-methanesulfonamindo phenoxy)ethyl]-*p*-methanesulfonamido Phenethylamine) was identified as one of the most effective compounds. At the very low concentration of 16 nmol/L, DC031050 prolonged the effective refractory period for 10 ms. Furthermore, at a concentration of 10 μmol/L, DC031050 improved the force of constriction significantly more (24%) than dofetilide (17%)[14]. A comparison of the chemical structures of DC031050 and dofetilide revealed that the substitution of the methyl group with a benzyl group in DC0310590 improves its biological activity (Figure 1)[14], representing a modification strategy of dofetilide to obtain more effective class III agents. Prior to further modification, we sought to further understand the durability of these dofetilide-like class III analogues by assessing whether they acted on noncardiac channels. Thus, we evaluated DC031050 for its effects on three types of voltage-gated neuronal potassium channels: KCNQ2, Kv1.2 and a delayed rectifier in hippocampal neurons. Our results showed that only the delayed rectifier channel was inhibited by DC031050, but at ~1000 times the concentration needed to block hERG.

Materials and methods

Compound synthesis

DC031050 was prepared according to previously reported procedures[13, 14]. The chemical structure of DC031050 is shown in Figure 1.

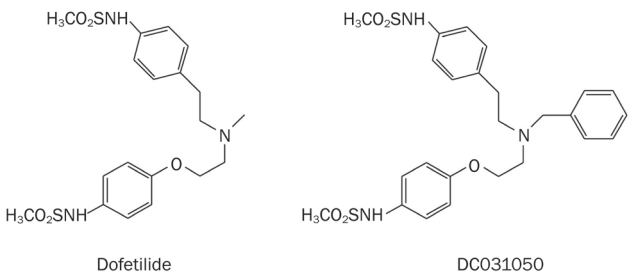

Figure 1. The chemical structure of compound DC031050 and dofetilide.

Preparation of dissociated hippocampal pyramidal neurons

Hippocampal neurons were dissociated from 5- to 9-day-old Sprague-Dawley rats as described previously. Briefly, mini-slices (500 μm) of the hippocampal CA1 region were cut in an ice-cold, oxygenated dissociation solution containing the following components (in mmol/L): Na_2SO_4 82, K_2SO_4 30, $MgCl_2$ 5, HEPES 10 and glucose 10 (pH 7.3). The slices were incubated in a dissociation solution containing protease XXIII (3 mg/mL) at 32°C for 8 min. The solution was then replaced with dissociation solution containing trypsin inhibitor type II-S (1 mg/mL) and bovine serum albumin (1 mg/mL). The slices were allowed to cool to room temperature in an oxygenated solution. Before recording, the slices were triturated using a series of fire-polished Pasteur pipettes with progressively decreasing tip diameters. The dissociated neurons were placed into a recording dish and perfused with an external solution containing the following components (in mmol/L): NaCl 135, KCl 5, $MgCl_2$ 2, HEPES 10, glucose 10 and tetrodotoxin 0.001 (pH 7.3).

Cell culture and transfection

Chinese hamster ovary (CHO) cells were grown in 50/50 DMEM/F12 (Cellgro, Manassas, VA) supplemented with 10% fetal bovine serum (FBS) and 2 mmol/L *L*-glutamine (Gibco, Carlsbad, CA, USA). To overexpress the KCNQ and hERG channel proteins, the cells were split 24 h before transfection, plated into 60-mm dishes, and transfected with the appropriate plasmids using the Lipofectamine 2000™ reagent (Invitrogen, Carlsbad, CA, USA), according to the manufacturer's protocols. Twenty-four hours after transfection, the cells were split and re-plated onto coverslips coated with poly-*L*-lysine (Sigma-Aldrich, St Louis, MO, USA). A green fluorescent protein (GFP) expression plasmid (Amaxa, Gaithersburg, MD, USA) was cotransfected to allow for the identification of transfected cells by fluorescence microscopy.

Whole-cell voltage-clamp recording of hippocampal neurons and cultured CHO cells

The recordings were made at 21–23°C using an Axopatch 200B amplifier (Molecular Devices, Sunnyvale, CA, USA). Electrodes with a tip resistance of 3–5 MΩ were pulled from borosilicate glass pipettes (World Precision Instruments, Sarasota, Fl) and filled with a pipette solution containing the following components (in mmol/L): KCl 140, $MgCl_2$ 1, $CaCl_2$ 1, HEPES 10 and EGTA 10 (pH 7.3). Voltage protocols were provided by pClamp 9.2 software via a DigiData-1322A interface (Molecular Devices, Sunnyvale, CA, USA). Series resistance was compensated by 75%–85%. For hippocampal neurons, the bath solution contained the following components (in mmol/L): NaCl 135, KCl 5, $MgCl_2$ 2, HEPES 10, glucose 10 and tetrodotoxin 0.001 (pH 7.3). The cells were maintained at -50 mV. The delayed rectifier current (I_K) in hippocampal neurons was elicited by a series of 400-ms depolarising steps from -70 mV to +70 mV in 10 mV incremental steps following a 600-ms hyperpolarising pre-pulse to -110 mV and a 50-ms interval at -50 mV immediately after the pre-pulse to inactivate the transient component of the current. The resulting signals were sampled at frequencies of 10–40 kHz and filtered at 2–10 kHz. Linear leak and residual capacitance currents were subtracted on-line using a P/4 protocol. Unless otherwise stated, all I_K amplitudes were obtained at 300 ms after the initiation of the stimulating pulse. The effect of DC031050 was assessed after the neurons were exposed to the drug for 40 s, and a minimum of 5-s interval was used between stimulations.

For cultured CHO cells, the pipette solution contained the following components (in mmol/L): KCl 145, $MgCl_2$ 1, EGTA 5, HEPES 10, and Mg-ATP 5 (pH=7.3 with KOH). The extracellular solution contained the following components (in mmol/L): NaCl 140, KCl 3, $CaCl_2$ 2, $MgCl_2$ 1.5, HEPES 10, and glucose 10 (pH=7.4 with NaOH).

Drug application

DC031050 was dissolved in dimethylsulfoxide (DMSO) to prepare a 10 mmol/L stock solution, from which the appropriate volumes were added to the external or pipette solutions to produce the desired concentrations. DMSO (less than 0.1% in the final dilution) elicited no observable effect on the K^+ currents. For the electrophysiological recordings in neurons, the external solution containing DC031050 was delivered using a RSC-100 Rapid Solution Changer (BioLogic Co, France) that could change the external solution over the recorded neuron during a 10-ms period. For recordings in cultured CHO cells, a constant perfusion of extracellular solution was maintained using a BPS perfusion system (ALA scientific Instruments, Westburg, NY, USA). The DC031050 in the pipette solution was diffused into the neuron, and changes were recorded immediately after the rupture of the membrane patch. Unless otherwise stated, all chemicals were purchased from Sigma-Aldrich China Inc.

Data analysis

The concentration of DC031050 required to inhibit 50% of the K^+ currents (IC_{50}) was determined by fitting normalised data to the equation $I/I_0=1/\{1+([C]/IC_{50})^n\}$, where I_0 and I are the current amplitudes measured in the absence and presence of the drug, respectively. [C] is the concentration of the drug in the external solution, and n is the Hill coefficient. For analysing the voltage-dependence of the steady-state activation or inactivation of the K^+ currents, normalised conductance or current was plotted against the membrane potential and fitted to the Boltzmann equations as follows: $Y=1/\{1+\exp[(V-V_{1/2})/k]\}$, where Y is the normalised conductance or current, V is the test potential, $V_{1/2}$ is the voltage at half-maximal activation or inactivation, and k is the slope factor. The time course of recovery of the K^+ currents from inactivation was fitted with a mono-exponential function as follows: $I/I_{max}=A*\{1(\exp[(\Delta t/\tau]\}$, where I_{max} is the maximal current amplitude, I is the current after a recovery period of Δt, τ the time constant, and A is the amplitude coefficient. Data are presented as mean±SEM. Statistical significance was assessed using Student's *t*-test, where $P<0.05$ was considered significant.

Results

Inhibition of hERG channel by DC031050

In our previous study, DC031050 exhibited typical class III agent activity in biological assays using guinea pig atria[14]. Given its structural similarity with dofetilide, we hypothesised that the biological activity of DC031050 was elicited by its inhibition of hERG channels. To test our hypothesis, hERG channel proteins were transiently expressed in CHO cells, and the resulting currents elicited by depolarisation step pulses followed by repolarisation to -50 mV were recorded. As shown in Figure 2A & B, hERG currents were completely inhibited by 10 μmol/L DC031050[15]. At 20 min after washout, the inhibitory effects were not reversed. Analysis of the concentration-response relationships revealed an IC_{50} value of 2.3±1.0 nmol/L. In contrast, the IC_{50} of dofetilide on hERG channels is 17.9±1.2 nmol/L (Figure 2D). The more potent inhibition of hERG channels by DC031050 compared to dofetilide is consistent with the potent biological activity of DC031050 observed *in vivo*[13, 14].

Lack of effect of DC031050 on neuronal KCNQ2 and Kv1.2 channels expressed in CHO cells

KCNQ channels, also called Kv7 channels, include five members. KCNQ2 and KCNQ3 form heterotetramers in the neurons and mediate the M current, a potassium current could be inhibited by activation of muscarinic receptor. Inhibition of the M current by a mutation of KCNQ2 or KCNQ3 can result in various pathologies including benign familial neonatal convulsion, a form of neuronal hyperexcitibility[16–18]. The importance of Kv1.2 channels in controlling neuronal excitability has been demonstrated by the observation that Kv1.x (Kv1.1 and Kv1.2) channel-inhibiting venom toxins induce seizures in rodents[19]. To evaluate the effect of DC0310050 on the neuronal potassium channels KCNQ2 and Kv1.2, two neuronal potassium channels that are important in the control of neuronal excitability, were expressed in CHO cells, and the voltage-dependent channel activation was measured in the presence and absence of this drug. As shown in Figure 3, 10 μmol/L DC031050 did not significantly affect the current amplitude of either KCNQ2 or Kv1.2, suggesting that DC031050 might exhibit specificity for cardiac I_{Kr} channels.

Concentration-dependent inhibition of I_K by DC031050 in rat hippocampal neurons

The delayed rectifier outward potassium channel in neuronal tissues is a major potassium channel that is responsible for spike repolarisation, and it plays a similar role as I_{Kr} in the cardiac tissues[20]. The delayed rectifier potassium currents (I_K) were elicited in dissociated rat hippocampal pyramidal neurons by applying a 400-ms depolarising step to +40 mV, following a 600-ms hyperpolarising pre-pulse to -110 mV and a 50-ms interval at -50 mV immediately after the pre-pulse. Figure 4A shows representative superimposed traces before and after the application of increasing concentrations of DC031050 from 0.1 μmol/L to 10 μmol/L. DC031050 exhibited clear inhibition of I_K in a concentration-dependent manner, and the inhibition was more pronounced at the later or steady state phase of the current development. Using 10 μmol/L DC031050, the peak current was reduced by approximately 50%, whereas the steady-state current at 300 ms was almost completely blocked. Unless stated otherwise, we used the amplitude of I_K at the steady state (300 ms) for all subsequent analyses. The concentration-response curve revealed an IC_{50} value of 2.7±1.5 μmol/L, and a Hill coefficient of 1.1±0.2

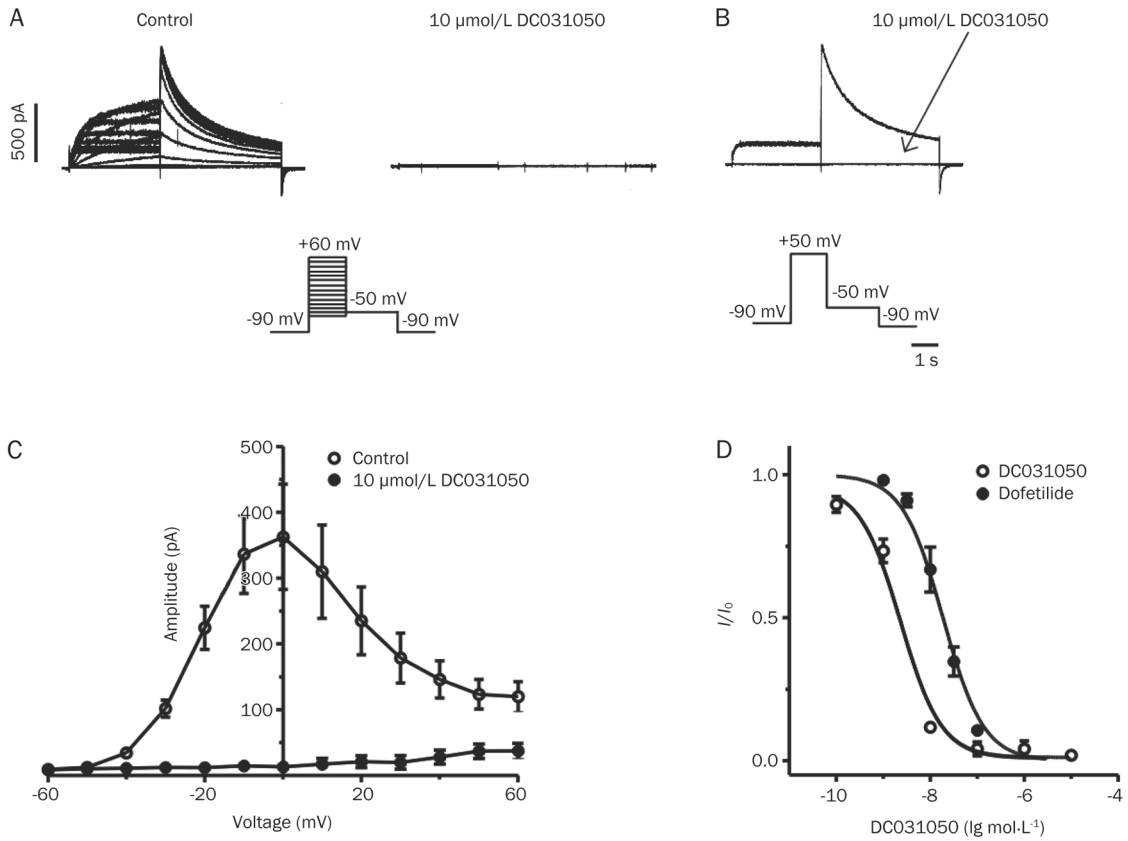

Figure 2. Concentration-dependent inhibition on hERG channel by DC031050. (A) Representative traces of hERG response to a series of depolarizing steps from -60 to +60 mV with 10 mV increment, delivered every 10 s, in the absence (control, left) and presence of 10 μmol/L DC031050 (right). (B) Overlap of representative traces of hERG responses to a depolarization step to +50 mV in the absence and presence of 10 μmol/L DC031050 . (C) The *I–V* plot of hERG (the tail after returning to -50 mV) in the absence (control, open circle) and presence of 10 μmol/L DC031050 (filled circle) (n=4). (D) Dose dependence of hERG channel inhibition on DC031050 and dofetilide (n=6).

for the DC031050-induced inhibition of I_K (Figure 4B, n=6). The inhibitory effect was reversible, as the current returned to near-control levels upon washout for 40 s (Figure 4C).

In addition to inducing a concentration-dependent reduction of I_K amplitude, DC031050 markedly accelerated the decay of the current, which appeared as a more pronounced inhibition of the steady-state current than of the peak current (Figure 4A & 4C). To quantify this effect, the decay time course of I_K was fitted with a mono-exponential function. As shown in Figure 4D, the acceleration of the current decay was also concentration-dependent. The decay time constant (τ) decreased gradually (208.4, 163.3, 155.5, 112.7, 75.8, and 54.4 ms) with increasing concentrations of DC031050 (0, 0.1, 0.3, 1, 3, and 10 μmol/L, respectively). Similar results were observed in 4 individual neurons. Plotting the time constant against the concentration revealed an IC_{50} value of 1.2±0.7 μmol/L (n=4), which is essentially identical to the IC_{50} value obtained using steady-state current amplitude.

Effect of DC031050 on the kinetic properties of neuronal I_K

The inhibition of neuronal I_K by DC031050 was voltage-independent. Figures 5A & 5B show the representative traces and current-voltage (I/V) relationships of I_K in the absence and presence of 3 μmol/L DC031050. The current was activated at 50 mV, and the control I/V relationship was almost linear at depolarising potentials. After treatment with 3 μmol/L DC031050, the I/V curve of I_K exhibited an apparent proportional downward shift, where the I/I_0 values (I_0 represents the original current without the drug) were nearly constant at all depolarising step pulses (Figure 5B). The I/I_0 values at 0 mV, 20 mV, 40 mV, and 60 mV were 50.8%±4.9%, 46.9%±4.4%, 49.2%±4.2%, and 49.0%±2.4%, respectively (n=6, P>0.05).

In addition, treatment with 3 μmol/L DC031050 did not significantly change the voltage-dependence of the activation of steady-state currents (Figure 5C), the voltage-dependence of inactivation (Figure 5D), or the rate of channel recovery from inactivation (Figure 5E). In the presence of 3 μmol/L DC031050, the voltage for half-maximal activation was -8.4±1.6 mV compared to -6.9±1.0 mV for the control (n=6, P>0.05); the voltage for half-maximal inactivation was -78.7±1.1 mV compared to -81.9±1.3 mV for the control treatment (n=6, P>0.05); and the time constant of recovery from inactivation was 261.4±39.1 ms compared to 223.7±16.4 ms for the control treatment (n=6, P>0.05).

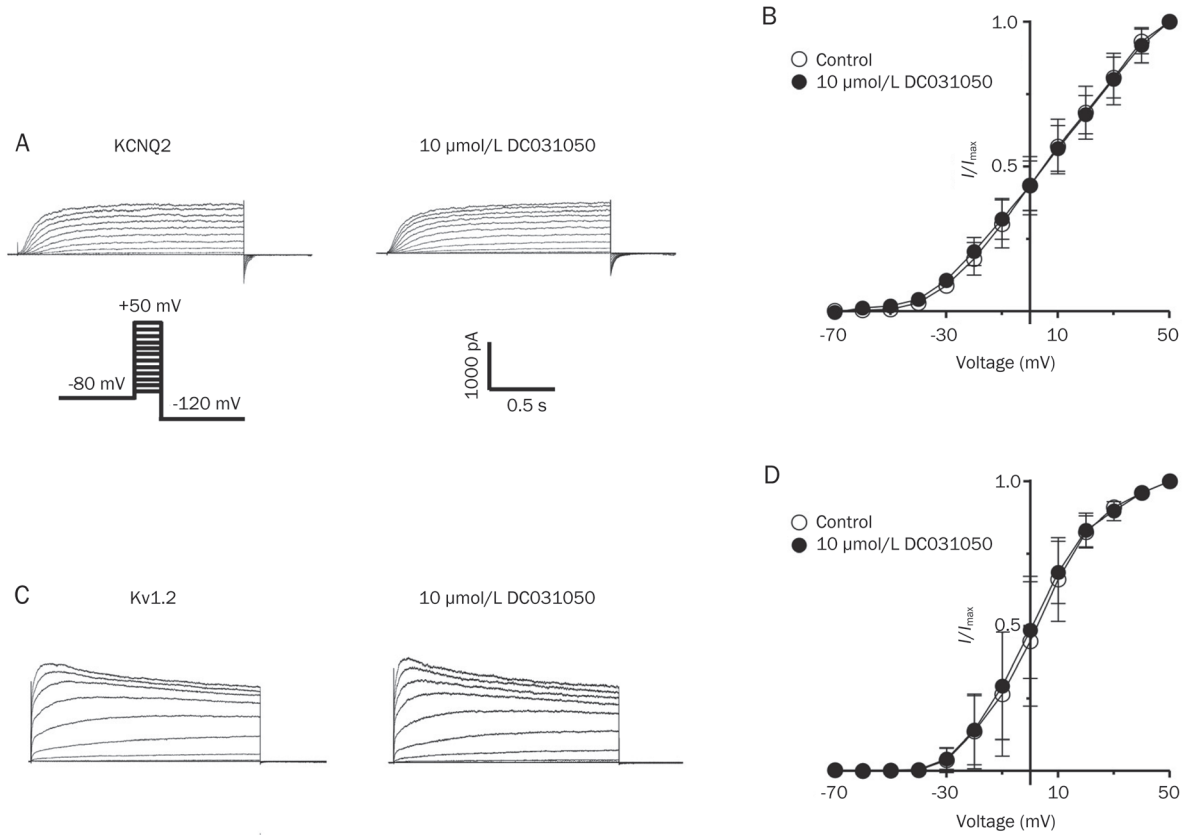

Figure 3. Effects of DC031050 on KCNQ2 and Kv1.2 channels expressed in CHO cells. (A) Representative KCNQ2 traces elicited by a series of depolarizing steps from -70 mV to +50 mV with 10 mV increment, delivered every 3 s, in the absence (left) and presence of 10 μmol/L DC031050 (right). (B) Summary data showing the relative activity of KCNQ2 in the presence of 10 μmol/L DC031050 normalized to that of control (n=7). (C) Representative Kv1.2 traces elicited by a series of depolarizing steps from -90 mV to +50 mV with 10 mV increment, delivered every 3.5 s, in the absence (left) and presence of 10 μmol/L DC031050 (right). (D) Summary of normalized data for 10 μmol/L DC031050 effect on Kv1.2 channel (n=4).

DC031050 acts at the extracellular face of the neuronal I_K channel

To determine the inhibitory mechanism of DC031050, we took two different approaches. First, we assessed the effects of the intracellular application of the compound. In control neurons dialysed with the normal pipette solution (see Methods), I_K exhibited a slight decrease (less than 10%) within 10 min after membrane rupture. We applied 5 μmol/L DC031050 for the intracellular application because the external application of the same concentration inhibited the K^+ currents by approximately 70%–90% (Figure 4A). However, as shown in Figures 6A & 6B, the time course of I_K in neurons dialysed with the pipette solution containing 5 μmol/L DC031050 exhibited results that were almost identical to that of the control-treated group (n=5 for each), indicating that the intracellular application of 5 μmol/L DC031050 was insufficient to inhibit I_K.

The above findings support the idea that the DC031050 might act at extracellular site(s). The binding site of TEA, a well-known potassium channel blocker, has been found to localise to the outer mouth of the KcsA channel[21, 22]. To determine if the action sites of DC031050 includes the outer mouth of the delayed rectifier K^+ channel, the inhibitory effects of DC031050 were tested in the presence or absence of 15 mmol/L TEA in the external solution. Interestingly, co-treatment with 15 mmol/L TEA significantly reduced the inhibitory effect of DC031050. For example, treatment with 3 μmol/L DC031050 resulted in an I/I_0 value of 75.2%±9.2% in the presence of 15 mmol/L TEA compared to 47.8%±8.4% induced by the control treatment (n=5, P<0.05). In the presence of 15 mmol/L TEA, the concentration response curve of DC031050 was significantly right-shifted compared to the control treatment, with the IC_{50} increasing to 7.4±1.2 μmol/L from 2.7±1.5 μmol/L in the control (n=5, P<0.05).

Discussion

Class III antiarrhythmic agents and their inhibitory effects on noncardiac potassium channels

On the basis of their dominant electrophysiological activities, antiarrhythmic drugs are categorised into four broad classes: I, II, III, and IV. Class I agents are sodium channels blockers that inhibit the impulse conduction and contractility in myocardial tissues; class II agents are beta-blockers; class III agents delay the repolarisation of cardiac myocytes; and class IV agents are calcium channel blockers[23]. Atrial fibrillation (AF) represents

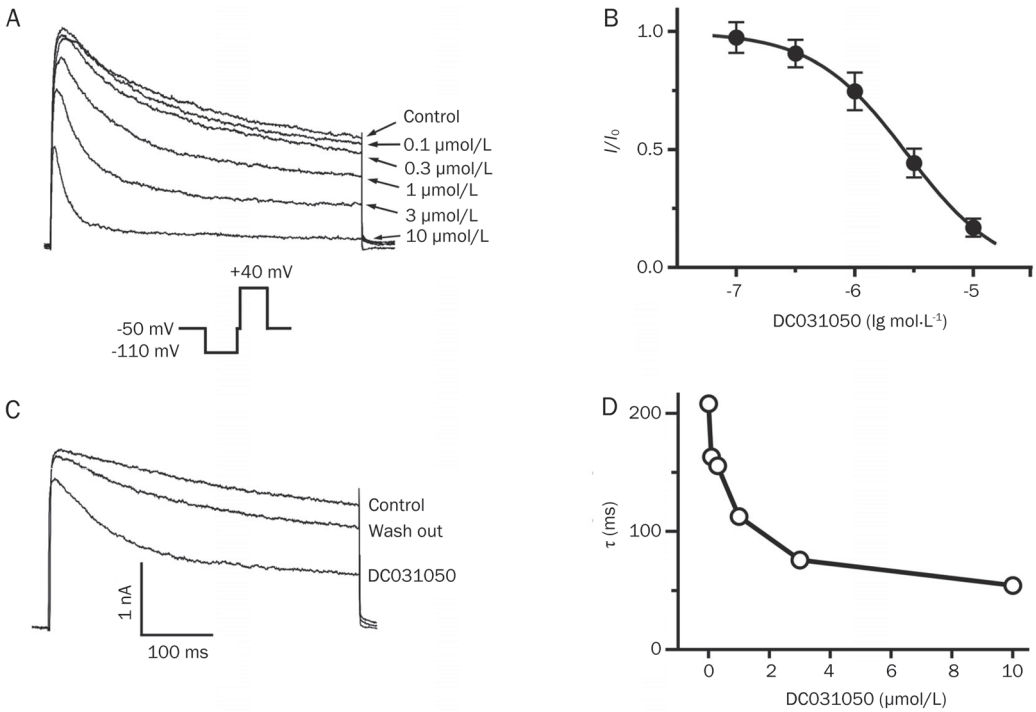

Figure 4. Concentration-dependent inhibition on I_K by DC031050. (A) Representative traces of delayed rectifier K^+ currents (I_K) in the presence of increasing concentrations of DC031050 (0, 0.1, 0.3, 1, 3, and 10 μmol/L) recorded from one hippocampal neuron. Currents were elicited with steps to +40 mV and measured at 300 ms latency of the test pulses. (B) Concentration-inhibition curve of DC031050 on I_K. Each symbol represents the mean±SEM. n=6. (C) The superimposed traces before, during and 40 s after washout of 3 μmol/L DC031050. (D) DC031050 accelerated decay of I_K. The plot was the decay time constant of the current traces in control (A) and against the concentrations of DC031050. Similar results were obtained from 4 neurons.

a major type of arrhythmia for which antiarrhythmic drugs have a predominant clinical application. Since the 1990s, class IA agents, such as quinidine, have not been the first choice for the treatment of atrial fibrillation because of increased mortality[24]. Such agents have since been displaced by an increasing interest in class III agents that primarily prolong cardiac action potential repolarisation[4, 25]. However, the application of class III agents for the conversion and prevention of atrial fibrillation in high-risk patients has not yielded the successful results expected. For example, long-term treatment with the class III agent *D*-sotalol is associated with an increased risk of mortality compared with treatment with placebo[1, 26]. In addition to the severe risk to cardiac tissues, the tolerance of certain class III agents has yielded disappointing results. For example, the class III agent amiodarone is associated with a 41% discontinuation rate that is attributed to its side effects and toxicity in liver, thyroid and pulmonary tissues[27].

Dofetilide (Tikosyn™) is a relatively recent class III antiarrhythmic drug that has been approved for the conversion of AF and the maintenance of normal sinus rhythm. Dofetilide has a higher safety profile than most other class III agents. In 10 randomised trials for treatment of supraventricular arrhythmias, the hazard ratio for death of dofetilide was 1.1 (95% confidence interval 0.3–4.3), indicating no evidence of a side effect for dofetilide on mortality rates[28, 29]. Two separate Danish Investigations of Arrhythmia and Mortality on Dofetilide (DIAMOND) studies performed in high-risk patients also demonstrated the safety of dofetilide[29]. Why dofetilide exhibited a low mortality ratio, whereas other class III agents (*eg*, *D*-sotalol) increased mortality, remains elusive. Because of the high safety profile of dofetilide, we designed and synthesised a series of structural analogues with the goal of developing novel class III antiarrhythmic agents. The biological activities of these analogues were assessed in biological assays using guinea pig atrial tissues. DC031050 was identified as one of the most potent compounds that demonstrated typical class III antiarrhythmic agent activity[13, 14].

However, similar to other class III antiarrhythmic agents, dofetilide exhibits general noncardiac side effects, including headache, dizziness, rash and some nervous system effects, such as paralysis, migraine and syncope[30, 31]. Although there is no direct evidence linking these side effects to the dysfunction of noncardiac ion channels, the functional disorders of noncardiac ion channels are known to cause these syndromes. For example, mutations of brain-specific P/Q type calcium channels were linked to familial hemiplegic migraines[32], whereas the functional down-regulation of Kir2.6, an inwardly rectifying potassium channel, was linked to thyrotoxic hypokalemic periodic paralysis[33]. Consistent with its adverse effects in the nervous system, a low concentration (100 μmol/L) of

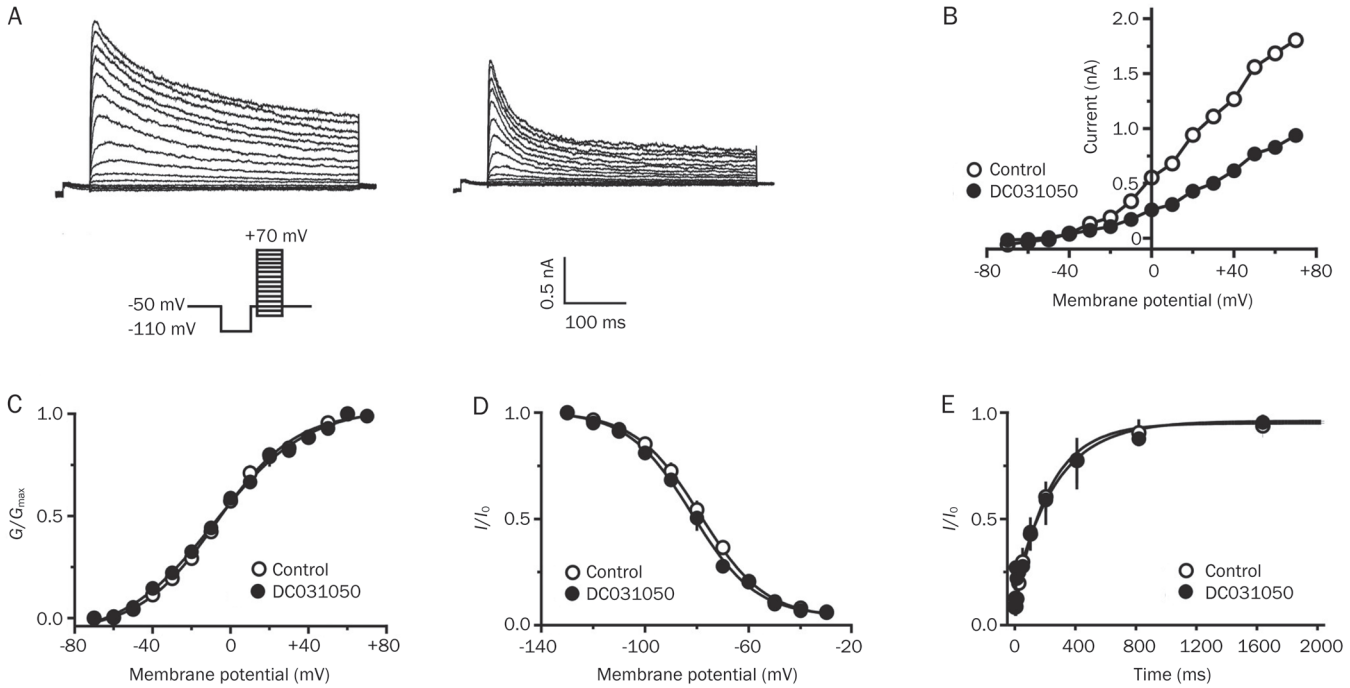

Figure 5. Effects of DC031050 on kinetic properties of I_K. (A) Responses of a representative neuron to a series of depolarizing steps from -70 to +70 mV with 10 mV increment, delivered every 10 s, in the absence and (control, left) and presence of 3 μmol/L DC031050 (right). (B) Current-Voltage (*I*/*V*) curves of I_K before and during application of 3 μmol/L DC031050. (C, D, and E) show the voltage-dependence of activation (C), inactivation (D) and the time course of recovery from inactivation (E), in the absence and presence of 3 μmol/L DC031050. Three different protocols were used. The protocol to study voltage-dependent activation is shown in inset. For studying the steady-state inactivation, neurons were held at 0 mV, and currents were elicited with a series of 600-ms prepulses at different hyperpolarizing potentials followed by a 400-ms step to +40 mV, then back to 0 mV, delivered every 10 s. For studying the time course of recovery from inactivation, neurons were held at 0 mV, and currents were elicited on return from hyperpolarizing prepulse of varying durations at -110 mV to +40 mV, delivered every 10 s. Current of peak were used for plotting.

dofetilide acted on ion channels in hippocampal neurons (*eg*, the voltage-independent block of a calcium-dependent potassium channel (BK))[34]. Notably, the plasma concentration of dofetilide exceeds 100 nmol/L when administered at 1 mg twice daily continuously for 24 h[35].

DC031050 is a dofetilide analogue that more potently blocks hERG channels, with an excellent safety margin on neuronal potassium channels

In the current study, we confirmed that DC031050 is a potent and complete blocker of hERG, with an IC_{50} value of 2.3 nmol/L, which is significantly less than the IC_{50} of dofetilide on hERG channels (17.9 nmol/L). hERG channels are cardiac potassium channels that are known to significantly influence the duration of cardiac action potentials. Thus, the electrophysiological data on heterologously expressed hERG channels is consistent with the results obtained from biological assays using guinea pig atria[13, 14]. Surveying a number of noncardiac potassium channels revealed that DC031050 (at 10 μmol/L concentration) elicited negligible effects on KCNQ2 and Kv1.2 channels that were expressed in CHO cells, but was sufficient to block I_K in rat hippocampal neurons. The IC_{50} of DC031050 on I_K was 2.7 μmol/L, which is more than 1000-fold higher than that on hERG. Thus, DC031050 should provide a broad concentration range for the selective therapeutic blockade of hERG channels without affecting other noncardiac potassium channels. The high selectivity of DC031050 on hERG channels strongly supports its potential for therapeutic application as a class III antiarrhythmic agent. The inhibitory effects on neuronal I_K at the micromolar concentrations argue for further early drug discovery stage evaluation of the effects of this compound on noncardiac channels to obtain safer class III antiarrythymia drugs. This is particularly important given that, in addition to I_K, KCNQ2 and Kv1.2, there are many other types of potassium channels that are expressed in neuronal tissues. To fully discern the safety of DC031050, the effects of the drug on other noncardiac potassium channels should be further studied.

Inhibition of neuronal delayed rectifier potassium channel by DC031050

The inhibition of DC031050 on the delayed rectified potassium channels in rat hippocampal neurons is dose dependent and exhibits the following principal properties. (1) DC031050 markedly accelerated the decay of I_K in a concentration-dependent manner, which is consistent with more potent inhibition of the steady state current than of the peak current. These data suggest that DC031050 might be an open-channel blocker,

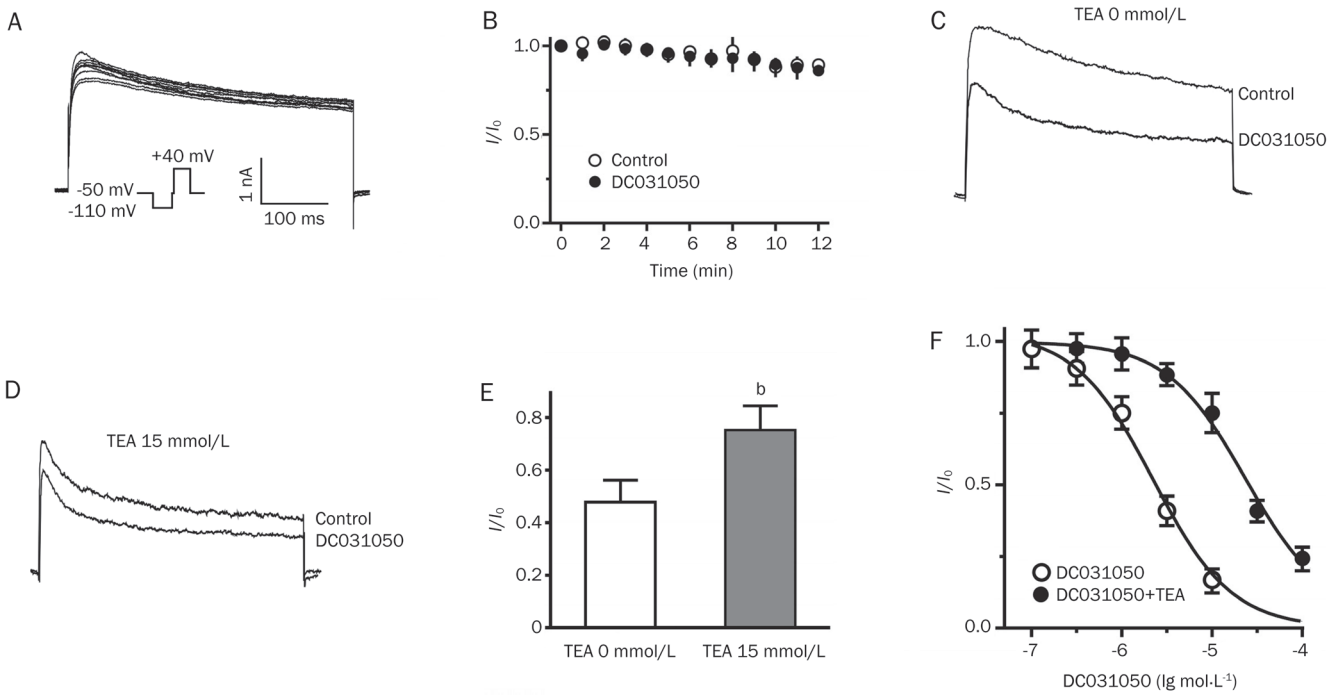

Figure 6. DC031050 acts on extracellular side of I_K channel. (A) A family of representative traces of I_k elicited by steps to +40 mV every 1 min during intracellular dialysis of 5 μmol/L DC031050. (B) The relative current (I/I_0) against recording time shows the lack of effect of intracellular application of DC031050. Zero in the abscissa indicates the time when patch membrane was ruptured. (C, D) Superimposed traces show DC031050 inhibition in the presence and absence of 15 mmol/L TEA in the external solution, respectively. (E) Normalized current in the presence of 5 μmol/L DC031050 as compared to control without or with 15 mmol/L TEA in the external solution. Each column is mean±SEM. (n=5, P<0.05). (F) Concentration response curve of inhibition by DC031050 in the presence and absence of 15 mmol/L TEA in the external solution. Currents were normalized to that in the absence of DC031050 in the same experiment (n=6).

indicating that opening of the channel is a prerequisite to blocking. Alternatively, DC031050 might accelerate the inactivation of I_K. (2) DC031050 does not alter the kinetic properties of I_K. DC031050 elicited no significant effects on either the voltage-dependence of inactivation or the time course of recovery from inactivation, which precludes the notion that this drug might act through acceleration of channel inactivation.

Two experiments supported the notion that DC031050 might act at the extracellular face of I_K channels. In contrast to the marked inhibition of I_K elicited by the external perfusion of 5 μmol/L DC031050, the intracellular application of the same concentration of this drug elicited a negligible effect. Furthermore, the inhibition of DC031050 was diminished by co-treatment with 15 mmol/L TEA, which is known to block potassium channels from the extracellular face. This indicates that when a TEA molecule occupies the external TEA binding site, a steric hindrance effect might prevent DC031050 from interacting with the channel. Combined with the observed acceleration of decay and the lack of effects on kinetics, DC031050 appears to be an open channel blocker, which acts at an external binding site(s) on the outer mouth of the neuronal delayed rectifier potassium channel.

In summary, we have identified DC031050, an analogue of dofetilide, as a highly selective hERG potassium channel blocker with an excellent safety margin over neuronal potassium channels. DC031050 exhibits therapeutic potential as a class III antiarrhythmic agent. Our study strongly supports the evaluation of effects elicited by class III agents on noncardiac channels at early stages of the drug discovery process.

Acknowledgements

We gratefully acknowledge Michael Xi ZHU for his comments on this manuscript and the financial support from the National Natural Science Foundation of China (81072579, 20872153, and 81025017).

Author contribution

Zhao-bing GAO, Hong LIU, and Hua-liang JIANG designed research; Ping LI, Hai-feng SUN and Ping-zheng ZHOU performed research; all authors analyzed data; Ping LI, Hai-feng SUN, Hong LIU, Zhao-bing GAO, and Guo-yuan HU wrote the paper.

References

1 Lazzara R. From first class to third class: recent upheaval in antiarrhythmic therapy — lessons from clinical trials. Am J Cardiol 1996; 78: 28–33.

2 Phillips GB, Morgan TK Jr, Nickisch K, Lind JM, Gomez RP, Wohl RA, *et al*. Synthesis and cardiac electrophysiological activity of aryl-substituted derivatives of the class III antiarrhythmic agent sematilide.

Potential class I/III agents. J Med Chem 1990; 33: 627–33.
3 Selnick HG, Liverton NJ, Baldwin JJ, Butcher JW, Claremon DA, Elliott JM, *et al*. Class III antiarrhythmic activity *in vivo* by selective blockade of the slowly activating cardiac delayed rectifier potassium current I_{Ks} by (*R*)-2-(2,4-trifluoromethyl)-*N*-[2-oxo-5-phenyl-1-(2,2,2-trifluoroethyl)-2,3-dihydro-1*H*-benzo[e][1,4]diazepin-3-yl]acetamide. J Med Chem 1997; 40: 3865–8.
4 Sahar DI, Reiffel JA, Bigger JT Jr, Squatrito A, Kidwell GA. Efficacy, safety, and tolerance of *d*-sotalol in patients with refractory supraventricular tachyarrhythmias. Am Heart J 1989; 117: 562–8.
5 Vaughan Williams EM. A classification of antiarrhythmic actions reassessed after a decade of new drugs. J Clin Pharmacol 1984; 24: 129–47.
6 Colastsky TJ. Ahtiarrhythmic drugs: where are we going? Technical review. Pharm News 1995; 2: 17–23.
7 MacNeil DJ. The side effect profile of class III antiarrhythmic drugs: focus on *d,l*-sotalol. Am J Cardiol 1997; 80: 90G–98G.
8 Pfrunder D, Kreye VA. Tedisamil blocks single large-conductance Ca^{2+}-activated K^+ channels in membrane patches from smooth muscle cells of the guinea-pig portal vein. Pflugers Arch 1991; 418: 308–12.
9 Church J, McLarnon JG. Tedisamil blocks BK-type Ca^{2+}-dependent K^+ channels and modulates action potentials in rat hippocampal neurons. Neurosci Lett 2002; 319: 79–82.
10 Sun XD, Herness MS. Inhibition of potassium currents by the antiarrhythmic drug E4031 in rat taste receptor cells. Neurosci Lett 1996; 204: 149–52.
11 Lenz TL, Hilleman DE. Dofetilide, a new class III antiarrhythmic agent. Pharmacotherapy 2000; 20: 776–86.
12 Lenz TL, Hilleman DE. Dofetilide: a new antiarrhythmic agent approved for conversion and/or maintenance of atrial fibrillation/atrial flutter. Drugs Today (Barc) 2000; 36: 759–71.
13 Liu H, Ji M, Jiang H, Liu L, Hua W, Chen K, *et al*. Computer-aided design, synthesis and biological assay of *p*-methylsulfonamido phenylethylamine analogues. Bioorg Med Chem Lett 2000; 10: 2153–7.
14 Liu H, Ji M, Luo X, Shen J, Huang X, Hua W, *et al*. New *p*-methylsulfonamido phenylethylamine analogues as class III antiarrhythmic agents: design, synthesis, biological assay, and 3D-QSAR analysis. J Med Chem 2002; 45: 2953–69.
15 Kiehn J, Lacerda AE, Wible B, Brown AM. Molecular physiology and pharmacology of HERG. Single-channel currents and block by dofetilide. Circulation 1996; 94: 2572–9.
16 Xiong Q, Gao Z, Wang W, Li M. Activation of Kv7 (KCNQ) voltage-gated potassium channels by synthetic compounds. Trends Pharmacol Sci 2008; 29: 99–107.
17 Shapiro MS, Roche JP, Kaftan EJ, Cruzblanca H, Mackie K, Hille B. Reconstitution of muscarinic modulation of the KCNQ2/KCNQ3 K^+ channels that underlie the neuronal M current. J Neurosci 2000; 20: 1710–21.
18 Wang HS, Pan Z, Shi W, Brown BS, Wymore RS, Cohen IS, *et al*. KCNQ2 and KCNQ3 potassium channel subunits: molecular correlates of the M-channel. Science 1998; 282: 1890–3.
19 Bagetta G, Nistico G, Dolly JO. Production of seizures and brain damage in rats by alpha-dendrotoxin, a selective K^+ channel blocker. Neurosci Lett 1992; 139: 34–40.
20 Storm JF. Action potential repolarization and a fast after-hyperpolarization in rat hippocampal pyramidal cells. J Physiol 1987; 385: 733–59.
21 Guidoni L, Carloni P. Tetraethylammonium binding to the outer mouth of the KcsA potassium channel: implications for ion permeation. J Recept Signal Transduct Res 2002; 22: 315–31.
22 Heginbotham L, MacKinnon R. The aromatic binding site for tetraethylammonium ion on potassium channels. Neuron 1992; 8: 483–91.
23 Singh BN, Hauswirth O. Comparative mechanisms of action of antiarrhythmic drugs. Am Heart J 1974; 87: 367–82.
24 Effect of the antiarrhythmic agent moricizine on survival after myocardial infarction. The Cardiac Arrhythmia Suppression Trial II Investigators. N Engl J Med 1992; 327: 227–33.
25 Singh BN. The coming of age of the class III antiarrhythmic principle: retrospective and future trends. Am J Cardiol 1996; 78: 17–27.
26 Julian DG, Prescott RJ, Jackson FS, Szekely P. Controlled trial of sotalol for one year after myocardial infarction. Lancet 1982; 1: 1142–7.
27 Grimm W, Maisch B. Sudden cardiac death in dilated cardiomyopathy — therapeutic options. Herz 2002; 27: 750–9.
28 Frost L, Mortensen PE, Tingleff J, Platou ES, Christiansen EH, Christiansen N. Efficacy and safety of dofetilide, a new class III antiarrhythmic agent, in acute termination of atrial fibrillation or flutter after coronary artery bypass surgery. Dofetilide Post-CABG Study Group. Int J Cardiol 1997; 58: 135–40.
29 Pedersen OD, Bagger H, Keller N, Marchant B, Køber L, Torp-Pedersen C, *et al*. Efficacy of dofetilide in the treatment of atrial fibrillation-flutter in patients with reduced left ventricular function: a Danish investigations of arrhythmia and mortality on dofetilide (diamond) substudy. Circulation 2001; 104: 292–6.
30 Rasmussen HS, Allen MJ, Blackburn KJ, Butrous GS, Dalrymple HW. Dofetilide, a novel class III antiarrhythmic agent. J Cardiovasc Pharmacol 1992; 20 Suppl 2: S96–105.
31 Falk RH, Pollak A, Singh SN, Friedrich T. Intravenous dofetilide, a class III antiarrhythmic agent, for the termination of sustained atrial fibrillation or flutter. Intravenous Dofetilide Investigators. J Am Coll Cardiol 1997; 29: 385–90.
32 Terwindt GM, Ophoff RA, Haan J, Vergouwe MN, van Eijk R, Frants RR, *et al*. Variable clinical expression of mutations in the P/Q-type calcium channel gene in familial hemiplegic migraine. Dutch Migraine Genetics Research Group. Neurology 1998; 50: 1105–10.
33 Ryan DP, da Silva MR, Soong TW, Fontaine B, Donaldson MR, Kung AW, *et al*. Mutations in potassium channel Kir2.6 cause susceptibility to thyrotoxic hypokalemic periodic paralysis. Cell 2010; 140: 88–98.
34 McLarnon JG, Wang XP. Actions of cardiac drugs on a calcium-dependent potassium channel in hippocampal neurons. Mol Pharmacol 1991; 39: 540–6.
35 Walker DK, Alabaster CT, Congrave GS, Hargreaves MB, Hyland R, Jones BC, *et al*. Significance of metabolism in the disposition and action of the antidysrhythmic drug, dofetilide. *In vitro* studies and correlation with *in vivo* data. Drug Metab Dispos 1996; 24: 447–55.

Acta Pharmacologica Sinica (2012) 33: 737–742
 1671-4083/12 $32.00
www.nature.com/aps

Original Article

β-Asarone protects PC12 cells against OGD/R-induced injury via attenuating Beclin-1-dependent autophagy

Zhen-tao MO, Yong-qi FANG*, Yu-ping HE, Sheng ZHANG

The First Affiliated Hospital of Guangzhou University of Chinese Medicine, Guangzhou 510405, China

Aim: To explore the effects of β-asarone from *Acorus Tatarinowii* Schott on autophagy in an ischemic stroke model of PC12 cells.
Methods: The ischemic stroke model of PC12 cells was made by OGD/R (2 h oxygen-glucose deprivation followed by 24 h reperfusion). Drug administration was started 1 h before OGD and last for 3 h. Then the cells were incubated in the drug-free and full culture medium under normoxic conditions for 24 h. After the treatments, Beclin-1, intracellular free calcium concentration ($[Ca^{2+}]_i$) and mitochondrial membrane potential (MMP) were analyzed using flow cytometry. Cell viability was measured using MTT assay. Cell morphology was studied under inverted phase contrast microscope, and autophagosomes were observed under transmission electron microscope.
Results: Pretreatment with β-asarone (20, 30, or 45 μg/mL) or the calcium channel antagonist nimodipine (10 μmol/L) significantly increased the cell viability and MMP, and decreased Beclin-1 expression and $[Ca^{2+}]_i$ in OGD/R-treated PC12 cells. Under inverted phase contrast microscope, pretreatment with β-asarone or nimodipine dramatically increase the number of cells and improved the cellular morphology. Autophagosomes were found in OGD/R-treated PC12 cells as well as in drug plus OGD/R-treated PC12 cells.
Conclusion: β-Asarone protects PC12 cells against OGD/R-induced injury partly due to attenuating Beclin-1-dependent autophagy caused by decreasing $[Ca^{2+}]_i$ and increasing MMP.

Keywords: β-asarone; PC12 cells; oxygen-glucose deprivation/reperfusion; autophagy; Beclin-1; $[Ca^{2+}]_i$; MMP; nimodipine

Acta Pharmacologica Sinica (2012) 33: 737–742; doi: 10.1038/aps.2012.35; published online 30 Apr 2012

Introduction

Oxygen-glucose deprivation and reperfusion (OGD/R) leads to neuronal insult. Autophagy, a process of self-eating, is usually induced by starvation, ischemia and hypoxia, growth factor deficiency, *etc.* It helps to maintain cell homeostasis[1–3], but excessive autophagy may also leads to autophagic neuron death and apoptosis[4–6]. β-asarone, one of chief constituents from *Acorus Tatarinowii* Schott, can easily pass through the blood brain barrier[7], and shows various neuroprotective effects such as protecting neuron against apoptosis[8–11]. However, the effect of β-asarone on autophagy in a model of ischemic stroke *in vitro* is rarely reported. PC12 cell line is derived from a pheochromocytoma of the rat adrenal medulla. It can acquire neuron-like properties when exposed to nerve growth factor (NGF)[12]. Therefore, it is widely used as an *in vitro* model of cerebral ischemia/reperfusion[13, 14]. Intracellular free calcium concentration ($[Ca^{2+}]_i$) and mitochondrial membrane potential (MMP) are important indicators to reflect cell injury. It is reported that autophagy can be induced by increased $[Ca^{2+}]_i$ and decreased MMP[15, 16]. Beclin-1, an autophagy related gene, is an essential indicator of autophagy. Flow cytometry is adopted as an important quantitative analysis, but Beclin-1 analysis by flow cytometry was merely reported until we established a method of quantitative analysis of Beclin-1[17]. In this research, we studied the protective mechanism of β-asarone in OGD/R treated PC12 cells by evaluation of Beclin-1, $[Ca^{2+}]_i$, MMP and cell viability and observation of autophagosomes and cellular morphology. Control group treated with nimodipine (a calcium antagonist) was established to explore whether β-asarone has effects on $[Ca^{2+}]_i$ and MMP so as to reduce autophagy.

Materials and methods

β-asarone preparation

β-asarone (cis forms of 2,4,5-trimethoxy-1-propenylbenzene) is a fat-soluble substance with a small molecular weight. It was extracted from *Acorus Tatarinowii* Schott according to the procedure that we have reported[18]. β-asarone, the purity of

* To whom correspondence should be addressed.
E-mail fangyq2@163.com
Received 2012-02-10 Accepted 2012-03-19

which was up to 99.55%, was confirmed by gas chromatography-mass (GC-MS), infrared spectrum (IR), and nuclear magnetic resonance (NMR) detection.

Cell cultures

PC12 cells (Culture Collection of Chinese Academy of Science, Shanghai, China) were seeded in 25-cm^2 polystyrene flasks (Corning Costar Corp, USA) with 4.5 g/mL glucose in Dulbecco's modifed Eagle's medium (DMEM) (Gibco, USA), containing 5% heat-inactivated foetal bovine serum(Gibco, USA) and 5% horse serum (Gibco, USA). The cells were incubated under an atmosphere of 95% air and 5% CO_2. Culture medium was replaced every 48 h.

Glucose deprivation and hypoxia/reperfusion

PC12 cells were washed with phosphate buffer solution (PBS) for one time and incubated in Earle's balanced salt solution (116 mmol/L NaCl, 5.4 mmol/L KCl, 0.8 mmol/L $MgSO_4$, l mmol/L NaH_2PO_4, 0.9 mmol/L $CaCl_2$, and 10 mg/L phenol red). And then the cells were incubated in a hypoxia chamber (Themo scientific, USA) with a compact gas oxygen controller to maintain oxygen concentration at 1% by injecting a gas mixture of 94% N_2 and 5% CO_2 for 2 h. After hypoxia, the cells were transferred back to full culture medium with oxygen for 24 h. Normal control cells were incubated in a regular cell culture incubator under normoxic conditions.

Drugs

PC12 cells were incubated with full culture medium containing β-asarone (20, 30, or 45 μg/mL) or nimodipine (10 μmol/L) under normoxic conditions for 1 h before hypoxia. The full culture medium containing drug was discarded. The cells were rinsed once with PBS, and incubated with Earle's balanced salt solution containing β-asarone (20, 30, or 45 μg/mL) or nimodipine (10 μmol/L) for 2 h of hypoxia. The Earle's balanced salt solution was discarded, and then PC12 cells were incubated with full culture medium free of drug under normoxic conditions for 24 h.

3-(4,5-dimethylthiazol-2-yl)-2,5-diphenyltetrazolium bromide (MTT) for cell viability

PC12 cells were seeded into 96-well plastic plates with 0.1 mL at the density of 3×10^4 cells/mL. Then after growth for 48 h, the cells were treated with OGD/R as described above. After 24 h reperfusion, the MTT colorimetric assay was performed. It contained 10 samples in normal control group, OGD/R treated group and OGD/R+drug treated groups respectively. 110 μL of MTT (10 mg/mL) dissolved in full culture medium was added to each well. Plates were incubated at 37 °C in normoxia for 4 h. 150 μL of Dimethyl sulfoxide (DMSO) was added to each well for 10 min to dissolve the dark blue crystals and the absorbance was read at 570 nm on a microplate reader (Themo scientific, USA).

Flow cytometric analysis of Beclin-1 expression

PC12 cells were seeded into 24-well plastic plates with 1 mL at the density of 1×10^5 cells/mL. It contained 10 samples in normal control group, OGD/R treated group and OGD/R+drug treated groups, respectively. PC12 cells were harvested by trypsinization [0.25% trypsin/2.6 mmol/L ethylenediaminetetraacetic acid (EDTA), Gibico, USA] and incubated in 2 mL 2% (*v/v*) bovine serum albumin (BSA)/PBS for 30 min. Permeabilization of the cells was done using fixation and permeabilization (Invitrogen, Beijing, China), according to the manufacturer instructions. Then the cells were incubated with mouse anti-human Beclin-1 monoclonal antibody (100 μL, 2: 100 dilution, Santa Cruz Biotechnology, catalog No sc-48381, USA) at room temperature for 30 min. After washing with 2% BSA/PBS once, cells were incubated with PE-conjugated goat anti-mouse IgG1 antibody (0.005 μg/μL, Mutiscience, catalog No gam0041, China) in the darkness at room temperature for 30 min. The control cells were incubated with the secondary antibody alone. After washing once with 2% BSA/PBS, the fluorescence of 10 000 cells was analyzed by flow cytometer (Beckman Coulter, Florida, American, 488 nm) using the EXPO32 data analysis system (Beckman Coulter, Florida, USA).

Flow cytometric analysis of MMP and $[Ca^{2+}]_i$

PC12 cells were seeded in 24-well plastic plates with 1 mL at the density of 1×10^5 cells/mL. Then after growth for 48 h, the cells were treated with OGD/R as described above. Normal control group, OGD/R treated group and OGD/R+drug groups contained 10 samples, respectively. After 24 h reperfusion, cells were harvested, washed with 2 mL PBS once, centrifuged for 5 min at 1000 r/min (TDL-5-A Low Speed Centrifuge, Shanghai, China) and pelleted. The cells were resuspended in 0.5 mL PBS. For MMP detection, cell suspensions were incubated with Rhodamine123 (Rho123) (final concentration 10 μg/mL, ALEXIS, USA, catalog No alx-610-018-m005) in the darkness at 37 °C for 30 min. For $[Ca^{2+}]_i$ detection, cell suspensions were incubated with Fura 3-acetoxymethyl ester (Fluo-3am) (final concentration 5 μmol/L, BIOTIUM, USA, catalog No 50013) in the darkness at 37 °C for 40 min. Then cell suspensions were centrifuged at 1000 r/min for 5min. After washing once in 2 mL PBS, the cells were resuspended in 0.5 mL PBS. The fluorescence of 10 000 cells was analyzed by flow cytometry (488 nm). The mean fluorescence intensity of Rho123 represented the state of depolarization of MMP. The mean fluorescence intensity of Fluo-3 was used as the indication of $[Ca^{2+}]_i$ quantity.

Inverted phase contrast microscope for observation of cellular morphology

After normoxic, hypoxic or hypoxic+drug treatment (OGD 2 h+R 24 h), cellular morphology were observed under inverted phase contrast microscope (×200, Olympus, Japan).

Transmission electron microscope for observation of autophagy

After normoxic, hypoxic or hypoxic+drug treatment (OGD 2 h+R 24 h), the cells were trypsinized and pelleted. The cells were suspended and fixed with 2% glutaraldehyde in 0.1 mol/L PBS (pH 7.4) at 4 °C for 2 h and postfixed with 1%

osmium tetroxide in 0.1 mol/L PBS (pH 7.4) at 4 °C for 2 h. After washing twice with PBS, cells were subsequently washed with 50% acetone for 10 min, with 70% acetone for 10 min, twice with 80% acetone for 10 min, twice with 90% acetone for 10 min, twice with 100% acetone for 10 min and embedded in Epon 812 resin. The blocks were cut into ultrathin sections by a ultramicrotome and stained with uranyl acetate and lead citrate. The ultrastructure of the cells was then observed under a transmission electron microscope (H-600, HITACHI, Japan).

Statistical analysis

Measurement data were expressed as mean±standard deviation (Mean±SD). Statistical significance was determined by independent-samples *t*-test. A value of $P<0.05$ was considered significant. All statistical analyses were performed with version SPSS 13.0 statistical software.

Results

Effect of β-asarone on cell viability and MMP in OGD/R treated PC12 cells

Cell viability [optical density value (OD value)] and MMP were 0.79±0.04, 542.5±26.6 in normal control cells. They were significantly decreased in OGD/R treated cells (0.46±0.02 in OD value, 335.2±19.3 in MMP, $P<0.001$). After treatment with β-asarone (20, 30, or 45 μg/mL,) or nimodipine (10 μmol/L), respectively, cell viability and MMP were dramatically increased. Cell viability was restored to near normal levels (0.79±0.04 in OD value) at the dose of 30 μg/mL of β-asarone or 10 μmol/L of nimodipine (0.75±0.09, 0.74±0.04 in OD value, respectively, $P>0.05$) (Table 1, Figure 1).

Effect of β-asarone on Beclin-1 and $[Ca^{2+}]_i$ in OGD/R treated PC12 cells

Beclin-1 expression and $[Ca^{2+}]_i$ were 6.3%±0.8%, 124.7±14.9 in normal cultured cells respectively. They were dramatically increased after OGD/R treatment (28.5%±2.3% in Beclin-1, 294.9±42.7 in $[Ca^{2+}]_i$, respectively, $P<0.001$). After incubation with β-asarone (20, 30, or 45 μg/mL) or nimodipine (10 μmol/L) respectively, Beclin-1 expression and $[Ca^{2+}]_i$ were both significantly reduced ($P<0.001$). As for β-asarone (30 μg/mL) group and nimodipine (10 μmol/L) group, Beclin-1 expression was reduced to 17.6%±2.6% and 15.6%±2.5%, respectively, and $[Ca^{2+}]_i$ was decreased to 132.4±25.5 and 139.0±19.0, respectively. For $[Ca^{2+}]_i$, there was no significant difference between β-asarone (30 μg/mL) group and normal control group or between nimodipine (10 μmol/L) group and normal control group ($P>0.05$) (Figure 2, 3).

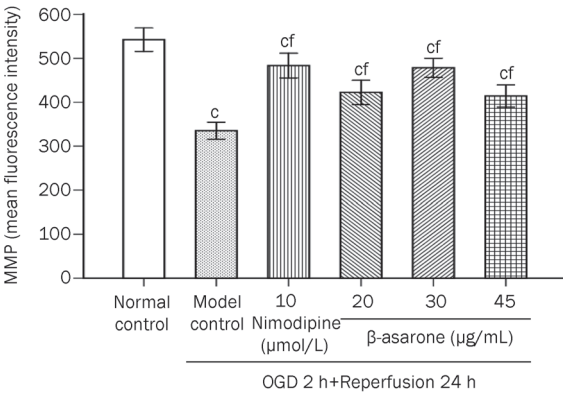

Figure 1. Effect of β-asarone on MMP in OGD/R treated PC12 cells. Model control cells were treated with 2 h OGD followed by 24 h reperfusion. The treated cells were incubated with nimodipine (10 μmol/L) or β-asarone (20, 30, or 45 μg/mL) 1 h before OGD and 2 h throughout OGD, followed by their transfer to full and drug-free culture medium under normoxic conditions for 24 h. Normal control cells were incubated in a regular cell culture incubator under normoxic conditions. After these treatments, MMP was analyzed using flow cytometry. The mean fluorescence intensity of Rho123 represented the state of depolarization of MMP. Mean±SD for 10 samples. $^cP<0.01$ *vs* normal control group. $^fP<0.01$ *vs* model control group.

Table 1. Effect of β-asarone on cell viability and MMP in OGD/R treated PC12 cells.

Groups	*n*	Cell viability (OD value)
Normal control	10	0.79±0.04
Model control	10	0.46±0.02^c
Nimodipine (10 μmol/L)	10	0.74±0.04^f
β-asarone (20 μg/mL)	10	0.64±0.07^{cf}
β-asarone (30 μg/mL)	10	0.75±0.09^f
β-asarone (45 μg/mL)	10	0.56±0.08^{cf}

Normal control cells were grown in full culture medium under normoxic conditions. Model control cells were treated with OGD/R (2 h OGD+24 h R). Therapeutic cells were incubated with nimodipine (10 μmol/L) or beta-asarone (20, 30, or 45 μg/mL) respectively for 3 h (1 h before OGD and 2 h OGD). They were incubated with full and drug-free culture medium for 24 h. β-asarone (20, 30, or 45 μg/mL) and nimodipine (10 μmol/L) both significantly increased cell viability and MMP in OGD/R treated cells. Mean±SD for 10 samples. $^cP<0.01$ *vs* normal control. $^fP<0.01$ *vs* OGD/R treated group.

Observation of cellular morphology

Cellular morphology was observed under inverted phase contrast microscope. The number of neurons showed a significant reduction. The PC12 cells exhibited round, slender and degenerated morphology after OGD/R treatment. However, the number of cells showed a dramatic increase. The cells exhibited improved cellular morphology after treatment with β-asarone (20, 30, or 45 μg/mL) or nimodipine (10 μmol/L), respectively. These observations were in accordance with the results of MTT assay (Figure 4).

Observation of ultrastructural morphology of autophagosome

Representative ultrastructural morphology of autophagy was observed under transmission electron microscopy. Normal morphology was observed in cells cultured under normal conditions (Figure 5A), autophagic morphology could be observed in cells treated with OGD/R, OGD/R+nimodipine

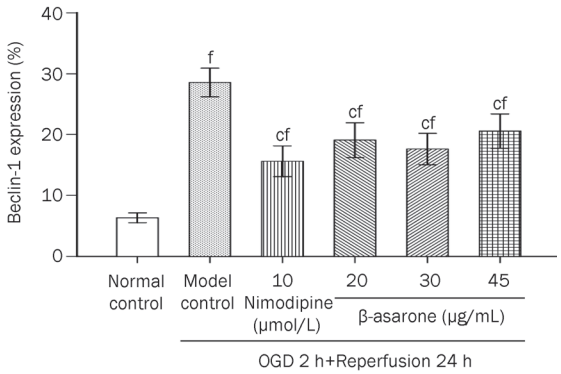

Figure 2. Effect of β-asarone on Beclin-1 expression in OGD/R treated PC12 cells. Model control cells were treated with 2 h OGD followed by 24 h reperfusion. The treated cells were incubated with nimodipine (10 μmol/L) or β-asarone (20, 30, or 45 μg/mL) 1 h before OGD and 2 h throughout OGD, followed by their transfer to full and drug-free culture medium under normoxic conditions for 24 h. Normal control cells were incubated in a regular cell culture incubator under normoxic conditions. After these treatments, Beclin-1 expression was analyzed using flow cytometry. Beclin-1 was represented as a percentage of positive expression. Mean±SD for 10 samples. $^{c}P<0.01$ *vs* normal control group. $^{f}P<0.01$ *vs* model control group.

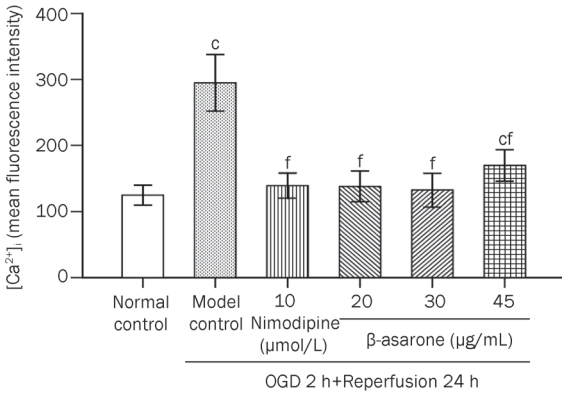

Figure 3. Effect of β-asarone on $[Ca^{2+}]_i$ in OGD/R treated PC12 cells. Model control cells were treated with 2 h OGD followed by 24 h reperfusion. The treated cells were incubated with nimodipine (10 μmol/L) or β-asarone (20, 30, or 45 μg/mL) 1 h before OGD and 2 h throughout OGD, followed by their transfer to full and drug-free culture medium under normoxic conditions for 24 h. Normal control cells were incubated in a regular cell culture incubator under normoxic conditions. After these treatments, $[Ca^{2+}]_i$ was analyzed using flow cytometry. The mean fluorescent intensity of Fluo-3 was used as the indication of $[Ca^{2+}]_i$ quantity. Mean±SD for 10 samples. $^{c}P<0.01$ *vs* normal control group. $^{f}P<0.01$ *vs* model control group.

(10 μmol/L) and OGD/R+β-asarone (20, 30, and 45 μg/mL) (Figure 5B–5F). The results indicated that OGD/R can generate autophagy, and β-asarone can attenuate OGD/R-induced autophagy in PC12 cells.

Discussion

β-asarone (cis forms of 2,4,5-trimethoxy-1-propenylbenzene) is a fat-soluble substance with a small molecular weight. It is extracted from *Acorus Tatarinowii* Schott. The absorption and elimination of β-asarone are rapid *in vivo*. β-asarone is easy to pass through blood brain barrier. Brain is an important organ of distribution of β-asarone. In the rat serum, elimination half-life and peak time are 54 and 12 min, respectively[7]. The half lives of β-asarone in blood, hippocampus, cortex, brain stem, thalamus, and cerebellum of rabbits are 1.3801, 1.300, 1.937, 7.142, 2.832, and 8.149 h, respectively[19]. β-asarone is excreted in urine, feces and bile, and the excretion efficiency is about 62% in urine, 22% in feces, and 16% in bile of rabbits. About 22% β-asarone is converted into α-asarone. Most β-asarone is excreted in 12 h[20].

β-asarone has significant pharmacological effects on central nervous system. It has effects on multi-target genes in mouse brain[8]. It can obviously increase the expression of c-fos in epilepsy rat brain[9], and attenuate neuronal apoptosis induced by β-amyloid in rat hippocampus and in PC12 cells[10, 11]. But it may also have side effects. It is reported that β-asarone could cause acute respiratory disturbance by inhibition of neurotransmission in the medullary respiratory neuronal network[21]. In this study, we observed that β-asarone could aggravate OGD/R induced injury of the cells when they had been incubated with β-asarone for too long, such as 24 h.

β-asarone can reduce neuronal apoptosis and protect neurons. However, its effect on autophagy in an ischemic stroke model of PC12 cells is rarely reported. Since PC12 cells possess the neuron-like properties, the protective effect of β-asarone on OGD/R induced injury in PC12 cells can demonstrate the possible protective mechanism of β-asarone on neurons following cerebral ischemia/reperfusion in a certain extent. Therefore, PC12 cells were established to an *in vitro* model of ischemia/reperfusion in this study. Autophagy is cellular process of degrading long-lived protein and organelles through the lysosomal pathway. It plays an important role in providing energy and turning over useless, superfluous and damaged organelles to maintain intracellular homeostasis. Activity of autophagy increases when cell injury, nutritional deficiencies, growth factors deficit or high energy demand occurs. However, excessive autophagy also leads to autophagic neuron death and apoptosis[4–6]. Beclin-1, a key regulatory gene of autophagy, is first discovered in mammalian. It regulates localization of other autophagy-related proteins to autophagosome[22, 23].

It is widely accepted that mitochondria are factories for energy production. And they are also the targets for autophagy. MMP is a sensitive indicator for evaluation of mitochondrial function. When mitochondrial membrane is damaged due to hypoxia, MMP decreases, which leads to ATP deficit and engulfment of damaged mitochondrial by the autophagosomes[16, 24]. ATP deficit during ischemia and reperfusion leads to damage of energy-dependent ion pump on cellular membrane, concentration disorder of intracellular and extracellular ion, depolarization, and overload of intracellular Ca^{2+} which in turn leads to a decrease of MMP[25]. Ca^{2+} partici-

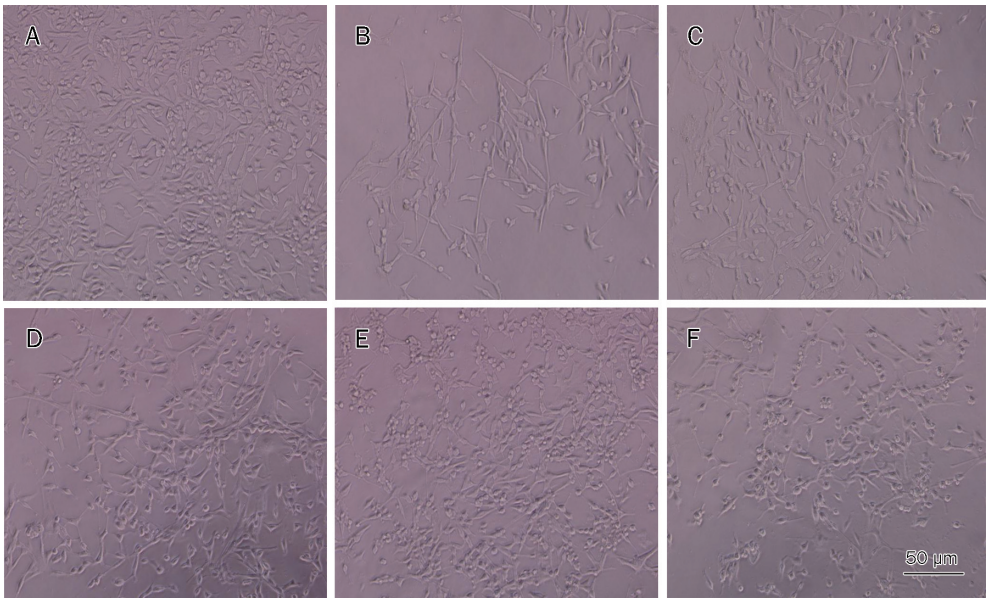

Figure 4. Cellular morphology was observed under inverted phase contrast microscope. Normal neuronal morphology was seen in the bright field images (A, ×200). The number of cells showed a significant reduction. The cells exhibited round, slender and degenerated morphology after OGD/R (B, ×200). The number of cells showed a dramatic increase. The cells exhibited improved cellular morphology after treatment with β-asarone (20, 30, or 45 μg/mL) (D, E, F, ×200) or nimodipine (10 μmol/L) (C, ×200).

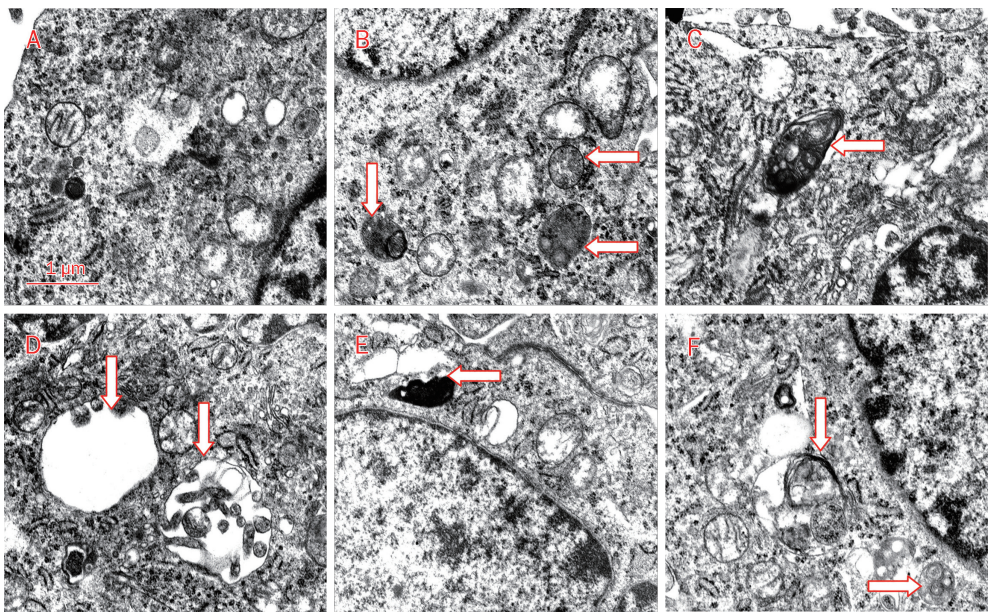

Figure 5. Representative ultrastructural morphology of autophagy. Normal morphology of cytoplasm, cell organelles in normal control group (A, ×20 000), characteristic ultrastructural morphology of autophagy in OGD/R treated group (B, ×17 000), β-asarone (20, 30, or 45 μg/mL, respectively) group (D, E, F, ×20 000), and nimodipine (10 μmol/L) group (C, ×20 000). Arrows indicate autophagosomes.

pates in formation of autophagosome as an important regulatory factor. It modulates localization of atg18 to autophagosomal membranes[15]. Removal of intracellular calcium can inhibit autophagy. For example, thapsigargin inhibits release of sarcoplasmic reticulum calcium, which also reduces autophagic flux by 50%[26]. Ca^{2+} leads to endoplasmic reticulum misfolded proteins and mitochondria depolarization, which induces autophagy of general and specific organelles so as to reestablish cellular homeostasis[27]. Taken together, MMP and Ca^{2+} are both closely related with autophagy.

In this study, we showed that β-asarone and nimodipine both significantly increased cell viability and MMP, and

improved cellular morphology in OGD/R treated PC12 cells but decreased Beclin-1 and $[Ca^{2+}]_i$. These results suggested that increased $[Ca^{2+}]_i$ and decreased MMP may induced Beclin-1 dependent autophagy, which is accordance with above listed studies. β-asarone can protect PC12 cells against OGD/R induced injury. It may attenuate Beclin-1 expression partly by decreasing $[Ca^{2+}]_i$ and increasing MMP as nimodipine does.

Acknowledgements

This work was supported by the Guangdong Natural Science Foundation of China (No 2003C34403).

Author contribution

Zhen-tao MO and Yong-qi FANG designed the research; Zhen-tao MO, Yu-ping HE, and Sheng ZHANG performed the research; Zhen-tao MO analyzed the data and wrote the paper.

References

1 Ginet V, Puyal J, Clarke PG, Truttmann AC. Enhancement of autophagic flux after neonatal cerebral hypoxia-ischemia and its region-specific relationship to apoptotic mechanisms. Am J Pathol 2009; 175: 1962–74.
2 Alirezaei M, Kemball CC, Flynn CT, Wood MR, Whitton JL, Kiosses WB. Short-term fasting induces profound neuronal autophagy. Autophagy 2010; 6: 702–10.
3 Ecker N, Mor A, Journo D, Abeliovich H. Induction of autophagic flux by amino acid deprivation is distinct from nitrogen starvation-induced macroautophagy. Autophagy 2010; 6: 879–90.
4 Chu CT. Autophagic stress in neuronal injury and disease. J Neuropathol Exp Neurol 2006; 65: 423–32.
5 Qin AP, Zhang HL, Qin ZH. Mechanisms of lysosomal proteases perticipating in cerebral ischemia-induced neuronal death. Neurosci Bull 2008; 24: 117–23.
6 Uchiyama Y, Koike M, Shibata M. Autophagic neuron death in neonatal brain isehemia/hypoxia. Autophagy 2008; 4: 404–8.
7 Wu HB, Fang YQ. Pharmacokinetics of β-asarone in rats. Yao Xue Xue Bao 2004; 39: 836–8. Chinese.
8 Fang Y, Li L, Wu Q. Effects of beta-asaron on gene expression in mouse brain. Zhong Yao Cai 2003; 26: 650–2. Chinese.
9 Fang YQ, Fang RM, Fang GL, Jiang Y, Fu SY. Effects of beta-asarone on expression of c-fos in kindling epilepsy rat brain. Zhongguo Zhong Yao Za Zhi 2008; 33: 534–6. Chinese.
10 Li C, Xing G, Dong M, Zhou L, Li J, Wang G, *et al*. Beta-asarone protection against beta-amyloid-induced neurotoxicity in PC12 cells via JNK signaling and modulation of Bcl-2 family proteins. Eur J Pharmacol 2010; 635: 96–102.
11 Liu J, Li C, Xing G, Zhou L, Dong M, Geng Y, *et al*. Beta-asarone attenuates neuronal apoptosis induced by Beta amyloid in rat hippocampus. Yakugaku Zasshi 2010; 130: 737–46.
12 Greene LA, Tischler AS. Establishment of a noradrenergic clonal line of rat adrenal pheochromocytoma cells which respond to nerve growth factor. Proc Natl Acad Sci U S A 1976; 73: 2424–8.
13 Li CT, Zhang WP, Fang SH, Lu YB, Zhang LH, Qi LL, *et al*. Baicalin attenuates oxygen-glucose deprivation-induced injury by inhibiting oxidative stress-mediated 5-lipoxygenase activation in PC12 cells. Acta Pharmacol Sin 2010; 31: 137–44.
14 Zhu JR, Tao YF, Lou S, Wu ZM. Protective effects of ginsenoside Rb(3) on oxygen and glucose deprivation-induced ischemic injury in PC12 cells. Acta Pharmacol Sin 2010; 31: 273–180.
15 Grotemeier A, Alers S, Pfisterer SG, Paasch F, Daubrawa M, Dieterle A, *et al*. AMPK-independent induction of autophagy by cytosolic Ca^{2+} increase. Cell Signal 2010; 22: 914–925.
16 Loor G, Kondapalli J, Iwase H, Chandel NS, Waypa GB, Guzy RD, *et al*. Mitochondrial oxidant stress triggers cell death in simulated ischemia-reperfusion. Biochim Biophys Acta 2011; 1813: 1382–94.
17 Liu L, Fang YQ, Xue ZF, He YP, Fang RM, Li L. Beta-asarone attenuates ischemia-reperfusion-induced autophagy in rat brains via modulating JNK, p-JNK, Bcl-2 and Beclin 1. Eur J Pharmacol 2012; 680: 34–40.
18 Liu, L, Fang, YQ. Analysis of the distribution of β-asarone in rat hippocampus, brainstem, cortex and cerebellum with GC-MS. J Med Plants Res 2011; 5: 1728–34.
19 Fang YQ, Shi C, Liu L, Fang RM. Pharmacokinetics of β-asarone in rabbit blood, hippocampus, cortex, brain stem, thalamus and cerebellum. Pharmazie 2012; 67: 120–3.
20 Fang YQ, Shi C, Liu L, Fang RM. Analysis of transformation and excretion of β-asarone in rabbits with GC-MS. Eur J Drug Metab Pharmacokinet 2012. Doi: 10.1007/S13318-012-0083-Z.
21 Qiu D, Hou L, Chen Y, Zhou X, Yuan W, Rong W, *et al*. Beta-asarone inhibits synaptic inputs to airway preganglionic parasympathetic motoneurons. Respir Physiol Neurobiol 2011; 177: 313–9.
22 Liang XH, Jackson S, Seaman M, Brown K, Kempkes B, Hibshoosh H, *et al*. Induction of autophagy and inhibition of tumorigenesis by beclin 1. Nature 1999; 402: 672–6.
23 Backer JM. The regulation and function of Class III PI3Ks: novel roles for Vps34. Biochem J 2008; 410: 1–17.
24 Matsuda N, Sato S, Shiba K, Okatsu K, Saisho K, Gautier CA, *et al*. PINK1 stabilized by mitochondrial depolarization recruits Parkin to damaged mitochondria and activates latent Parkin for mitophagy. J Cell Biol 2010; 189: 211–21.
25 Krieger C, Duchen MR. Mitochondria Ca^{2+} and neurodegenerative disease. Eur J Pharmacol 2002; 447: 177–88.
26 Brady NR, Hamacher-Brady A, Yuan H, Gotdieb RA. The autophagic response to nutrient deprivation in the hl-1 cardiac myocyte is modulated by Bcl-2 and sarco/endoplasmic retieulum calcium stores. FEBS J 2007; 274: 3184–97.
27 Vicencio JM, Lavandero S, Szabadkai G. Ca^{2+}, autophagy and protein degradation: Thrown off balance in neurodegenerative disease. Cell Calcium 2010; 47: 112–21.

Acta Pharmacologica Sinica (2012) 33: 743–751
 1671-4083/12 $32.00
www.nature.com/aps

Original Article

The regulation of N-terminal Huntingtin (Htt552) accumulation by Beclin1

Jun-chao WU[1], Lin QI[1], Yan WANG[1], Kimberly B KEGEL[2], Jennifer YODER[2], Marian DIFIGLIA[2], Zheng-hong QIN[1], Fang LIN[1, *]

[1]Department of Pharmacology, Laboratory of Aging and Nervous Diseases, Soochow University School of Pharmaceutical Science, Suzhou 215123, China; [2]Department of Neurology, Laboratory of Cellular Neurobiology, Massachusetts General Hospital and Harvard Medical School, Charlestown, MA 02129, USA

Aim: Huntingtin protein (Htt) was a neuropathological hallmark in human Huntington's Disease. The study aimed to investigate whether the macroautophagy regulator, Beclin1, was involved in the degradation of Htt.
Methods: PC12 cells and primary cultured brain neurons of rats were examined. pDC316 adenovirus shuttle plasmid was used to mediate the expression of wild-type Htt-18Q-552 or mutant Htt-100Q-552 in PC12 cells. The expression of the autophagy-related proteins LC3 II and Beclin1, as well as the lysosome-associated enzymes Cathepsin B and L was evaluated using Western blotting. The locations of Beclin1 and Htt were observed with immunofluorescence and confocal microscope.
Results: Htt552 expression increased the expression of LC3 II, Beclin1, cathepsin B and L in autophagy/lysosomal degradation pathway. Treatment with the autophagy inhibitor 3-MA or the proteasome inhibitors lactacystin and MG-132 increased Htt552 levels in PC12 cells infected with Ad-Htt-18Q-552 or Ad-Htt-100Q-552. The proteasome inhibitor caused a higher accumulation of Htt552-18Q than Htt552-100Q, and the autophagy inhibitor resulted in a higher accumulation of Htt552-100Q than Htt552-18Q. Similar results were observed in primary cultured neurons infected with adenovirus. In Htt552-expressing cells, Beclin1 was redistributed from the nucleus to the cytoplasm. Htt siRNA prevented Beclin1 redistribution in starvation conditions. Blockade of Beclin1 nuclear export by leptomycin B or Beclin1 deficiency caused by RNA interference induced the formation of mHtt552 aggregates.
Conclusion: Beclin1 regulates the accumulation of Htt via macroautophagy.

Keywords: Huntingtin (Htt); Beclin1; protein degradation; autophagy; RNA interference; ubiquitin-proteasome system; autophagy/lysosome pathway

Acta Pharmacologica Sinica (2012) 33: 743–751; doi: 10.1038/aps.2012.14; published online 30 April 2012

Introduction

Huntington's disease (HD) is a neurodegenerative disorder caused by the expansion of a trinucleotide (CAG) repeat encoding polyglutamine (polyQ) in the N-terminal region of the Huntingtin (Htt) protein. A neuropathological hallmark in human HD and mouse models is the intracellular accumulation of N-terminal Htt fragments[1], suggesting that aberrant Htt proteolysis and/or dysfunctional clearance of Htt fragments may underlie the neuropathology in HD. Several proteases, including caspases, calpains and aspartyl endopeptidases, cleave Htt within the N-terminal region, and *in vitro* studies have demonstrated that N-terminal Htt fragments with expanded polyglutamine have enhanced cytotoxicity[2]. Although some evidence shows that wild-type Htt has an essential role in developmental and cellular processes[3–7], the physiological role of Htt still needs further investigation. DiFiglia's lab was the first to find that cytoplasmic mHtt aggregates had a distribution similar to that of autophagosomes-lysosomes in postmortem HD brains[8] and suggested a possible role for autophagy in HD. Later, with *in vitro* and invertebrate model systems, other work also indicated that autophagy is an important component of the cellular response to mHtt[9–13]. Recently, Heng *et al* employed a novel knock-in HD mouse model and reported an association of mHtt immunoreactive cytoplasmic aggregates with autophagosomes and the early and sustained induction of autophagy-associated proteins, suggesting that autophagy is indeed an important component of the neuronal response to mHtt expression *in vivo*[14].

Htt is the first neuronal protein shown to be a caspase substrate with defined sites for caspase-3 at amino acids 513 and 552, for caspase-2 at amino acid 552, and for caspase-6 at amino acid 586. Using an antibody that only detects caspase-

* To whom correspondence should be addressed.
E-mail bluestonelin@hotmail.com
Received 2011-11-13 Accepted 2012-02-01

cleaved Htt, Wellington *et al* demonstrated that Htt was cleaved *in vivo* specifically at the caspase consensus site at amino acid 552. This form of Htt was also detected in control human brains and in HD brains with early phase neuropathology, as well as in wild-type and HD transgenic mouse brains before the onset of neurodegeneration. These data suggest that caspase cleavage of Htt would be a normal physiological event[15]. However, in HD, the N-terminal fragments resulting from the cleavage of mutant Htt have the potential to increase cytotoxicity and accumulation because of the presence of the expanded polyglutamine tract. In previous research, various fragments (N-terminal 171 aa or 5′–3 kb) were used[13, 16], but all of these fragments do not exist in physiological conditions. In this study, the 552 aa fragment was used to produce results which would approach the HD pathophysiological conditions closely.

In HD, mHtt forms aggregates (Htt body) both in the nucleus and the cytoplasm, including in the neuronal synapse[17, 18]. Numerous studies verified that an expanded polyQ tract provoked a dominant gain-of-function neurotoxicity. Treatment with Congo Red or trehalose reduced the accumulation of overexpressed expanded polyQ-positive proteins, increased the rate of their degradation and alleviated neurological symptoms in HD transgenic mouse models[12, 19, 20]. Eukaryotic cells have two major protein degradation pathways. One is the ubiquitin-proteasome pathway that is responsible for the selective degradation of most short-lived proteins[21, 22]. Neuronal N-terminal-Htt inclusions are highly ubiquitinated. However, it was reported that mutant Htt impaired synaptic ubiquitin-proteasome system activity in cultured neurons and in HD mouse brains expressing either N-terminal or full-length mutant Htt[17]. The other protein degradation pathway is the autophagy/lysosomal pathway that consists of the delivery of intracellular and endocytosed proteins to the lysosomes. Autophagosomes sequester the cytoplasmic portions, intracellular organelles fuse with lysosomes and the sequestered materials are then degraded by cathepsins found in the lysosomes[23, 24]. The addition of 3-methyladenine (3-MA), an inhibitor of class III phosphatidylinositol 3-kinase and autophagy, increased Htt aggregate formation in x57 cells, while rapamycin, an inducer of autophagy, reduced them[11]. The transgenic mice with N-terminal fragment had improved performance in behavioral tests when the Htt aggregates were decreased. These results support a potential role of both the proteasome and autophagy in regulating the turnover of expanded polyQ proteins.

Class III PI 3-kinase and its product, phosphatidylinositol 3-phosphate (PI 3-P), are involved in the autophagy signaling pathway. The PI 3-kinase inhibitors, wortmannin and 3-MA, can inhibit the formation of autophagosomes. This indicates that PI 3-kinase activity is important in the early phase of autophagic vesicle formation[25]. Beclin1 is the ortholog of Atg6, a part of the PI 3-kinase complex, and it plays a role in autophagic vesicle formation in yeast. The PI3-kinase complex may also be functional in the mammalian system[26]. The expression of Beclin1 in MCF7 cells activated the formation of autophagic vesicles and the degradation of long-lived proteins upon amino-acid starvation. In addition, 3-MA is able to restrain autophagy induced by Beclin1 in MCF-7 cells[27]. The accumulated mutant Htt can recruit Beclin1 and impair the Beclin1-mediated long-lived protein turnover. Thus, sequestration of Beclin1 in the vulnerable neuronal population of HD patients might reduce Beclin1 function and the autophagic degradation of mutant Htt in these neurons[28].

In this study, we verified that the autophagy/lysosome pathway is involved in the degradation of both wild-type and mutant Htt552 in PC12 cells and primary neurons. Htt stimulates the nuclear export of Beclin1, thereby facilitating the autophagic process. Additionally, we found that Beclin1 was an important protein involved in Htt552 degradation, particularly degradation of the mutant form of the protein.

Materials and methods

Materials and drugs

The Htt expression plasmids, pcDNA3-Htt-18Q-969aa-552stop and pcDNA3-Htt-100Q-969aa-552stop, were provided by Dr Marian DiFIGLIA (Massachusetts General Hospital and Harvard Medical School, USA). Both of the two constructs encode an N-terminal Htt fragment of 969 aa with a stop codon after 552 aa. The 18Q is a wild-type Htt with 18 repeats of CAG, while 100Q is a mutant Htt with 100 CAG repeats. Rat PC12 cells were purchased from the Shanghai Institute of Cell Biology (Shanghai, China). Leptomycin B was purchased from Merck Chemicals (Germany). The 3-methyladenine (3-MA) was obtained from Sigma-Aldrich Co (St Louis, MO, USA). The MG-132 and lactacystin were from Enzo Life Sciences, Inc (Farmingdale, NY, USA). Concentrations of 10 nmol/L leptomycin B, 10 mmol/L 3-MA, 10 nmol/L MG-132, and 200 nmol/L lactacystin were used in experiments.

Cell culture

The PC12 cells were cultured in 60-mm dishes in DMEM supplemented with 10% FBS, 4.5% glucose, 100 mg/L streptomycin, 100 units/L penicillin, and incubated in a humidified atmosphere of 5% CO_2 at 37 °C.

Pregnant rats at embryonic day 16 were used to create primary neuronal cultures. This procedure included the anesthetization of the rat, sterilization of the incision site and removal of the embryos into a dish containing pre-cooled sterile PBS. The brains of the pups were collected, and then the cortical hemispheres were dissected and placed in a new tube with 10 mL PBS on ice. The tissue was rinsed with pre-cooled PBS 2–3 times, incubated with 10 mL of 2.5% trypsin: DMEM medium (1:1) at 37 °C for 15–20 min, centrifuged at 1200 r/min at 4 °C for 3 min and rinsed 2–3 times with DMEM/F12 medium containing 10% FBS. The tissue pellets were resuspended and incubated in 0.125 mg DNase I in 10 mL of DMEM/F12 containing 10% FBS at 37 °C for 5 min. Samples were then centrifuged at 1400 r/min at 4°C for 3 min. Cells were resuspended to the desired concentration with neurobasal medium (NBM) supplemented with B27, 1% pen/strep and 25 μmol/L glutamine. Single cell suspensions were obtained by pass-

ing the cell suspension through a 40-μm cell strainer. Cells were plated on poly-*D*-lysine-coated dishes or plates with a density of 1×10^5 cells/cm^2 and then incubated in a humidified atmosphere of 5% CO_2 at 37 °C. After 3–4 d, half of the medium was replaced with fresh DMEM with 10% FBS/Pen-strep and 10 μmol/L AraC. After another 24 h, the medium was replaced with NBM supplemented with B27, pen/strep, and 2 mmol/L *L*-glutamine. Lastly, half of the medium was replaced every 3–4 d. The neurons matured after 7 d in culture.

Adenovirus mediated Htt expression system

The N-terminus of wild-type (18Q) and mutant (100Q) Htt, with 3 kb cDNAs and a stop codon at 552 aa, were cloned into the pDC316 adenovirus shuttle plasmid. Wild-type and mutant Htt cDNAs were excised from their parental vectors using *Bam*HI and *Xba*I and then ligated to *Bam*HI/*Xba*I-digested pUC18, an intermediate vector. Next, these cDNAs were ligated to *Bgl*II/*Sal*I-digested pDC316. Two independent adenovirus shuttle plasmids, pDC316-Htt-18Q-552stop and pDC316-Htt-100Q-552stop, were obtained.

Three independent adenoviruses, including Ad-null, Ad-Htt-18Q-552stop, and Ad-Htt-100Q-552stop, were obtained by co-transfection of 293 cells with the backbone plasmid pBHG10 and the shuttle plasmids, pDC316, pDC316-Htt-18-Q-552stop, or pDC316-Htt-100Q-552stop. Cytopathic effects happened at 7th day after transfection and both the cells and the supernatant were collected at 10th day. This was the first generation adenovirus. The later proliferation of adenovirus was also manuplated in 293 cells. The fourth generation adenovirus was used in the later experiments.

Protein preparation and Western blot analysis

Cells were harvested and rinsed with ice-cold PBS twice. Each volume of the cell pellet was lysed by five volumes of the Western blot lysing buffer. After being centrifuged at 10 600×*g* at 4 °C for 10 min, the supernatant was preserved at -70 °C for later use. The protein concentration was determined with a BCA kit (Pierce, USA). The protein samples were denatured by boiling for 5 min in loading buffer, subjected to 10% SDS-PAGE, and then electroblotted onto nitrocellulose membranes (Amersham Biosciences, Piscataway, USA). The membranes were then blocked with 5% non-fat milk for 1 h and first probed with the mouse monoclonal Htt antibody (Chemicon, Temecula, CA) at a dilution of 1:2000 overnight at 4 °C. Next, the membranes were incubated with a horseradish peroxidase-conjugated secondary antibody for 1 h. Lastly, they were visualized by an enhanced chemiluminescence (ECL) kit (Pierce, Rockford, IL, USA).

Immunofluorescence

PC12 cells were plated in 24-well plates containing poly-*D*-lysine-coated coverslips, and the transfection was performed when cells reached 80% confluence, approximately 24 h after plating. According to the MOI 20, mixed adenovirus in 0.25 mL medium with 5% FBS was transferred to planted cells. After a 2-h incubation, the medium was removed and the cells were cultured in 0.5 mL of fresh, antibiotic-free DMEM. Every 24 h, the medium was changed with fresh, antibiotic-free complete medium. After 24, 48, or 72 h, cells were washed with PBS and fixed in pre-cooled ethanol for 15 min at room temperature. After another wash with PBS, they were incubated in PBS with 0.1% Triton X-100 for 10 min. The cells were then incubated for 1 h in a blocking solution of PBS supplemented with 2% non-fat milk (Guangming Milk, Shanghai, China) at room temperature. Next, the cells were incubated overnight at 4 °C in a blocking solution containing the primary antibody. The cells were then incubated for 2 h at room temperature with secondary antibodies coupled with fluorophores. The expression of Htt was detected with the mouse monoclonal Htt antibody at a dilution of 1:2000 as the first antibody and the FITC-conjugated donkey anti-mouse antibody with a dilution of 1:800 as the second antibody. The expression of Beclin1 was detected with the rabbit polyclonal BECN antibody (Santa Cruz Biotechnologies, Santa Cruz, CA, USA) with a dilution of 1:400 as the first antibody and cy3-conjugated donkey anti-rabbit antibody with a dilution of 1:800 as the second antibody. Lastly, cells were incubated with 300 nmol/L 4′,6-diamidino-2-phenylindole (DAPI) for 15 min. The immunostained cells were examined with laser confocal microscopy (C1Sl, Nikon, Tokyo, Japan).

Quantitative analysis of cells

To quantify the location of Htt and Beclin1, PC12 cells were examined with a 60×objective. Confocal images were obtained from ten fields each for the control and treatment conditions. Each field contained 15–20 cells for analysis. Images were coded before evaluation. Up to 100 cells per coverslip were selected at random for the analysis of the signal intensity using Sigma Scan Pro 5. The boundaries of the cell membrane and the nucleus were outlined, and the average intensity was recorded. The immunoreactivity of Htt and Beclin1 was determined with Sigma Scan Pro 5 using a calculation of the ratio of the stain intensity in the nucleus and in the whole cell. At least 50 cells were used for the quantitative analysis. All data are presented as the mean±SEM. Statistical analysis was carried out using Dunnett's test, considering $P<0.05$ as significant.

RNA interference

The double-stranded Beclin1 and Htt siRNA sequences were designed according to the cDNAs sequences of rat Beclin1 and human Htt. We chose the most effective pair among three pairs tested for their efficiency in the knockdown of target genes. The sequences used for the experiments included 5′-UGAGGAUGACAGUGAACAGTT-3′ and 5′-CUGUU-CACUGUCAUCCUCATT-3′ for Beclin1 and 5′-GCUUCG-GAGUGACAAGGAATT-3′ and 5′-UUCCUUGUCACUC-CGAAGCTG-3′ for Htt. The siRNA was synthesized by the Genepharma company in China.

PC12 cells were plated in 24-well plates and incubated in complete medium without antibiotics for 24 h. The knockdown experiment was then performed. First, 1 μL Lipo-

fectamine 2000 was diluted with 50 μL Opti-MEMI reduced serum medium and then incubated at room temperature for 5 min. A volume of 2 μL siRNA was also diluted with 50 μL Opti-MEMI reduced serum medium. The two solutions were gently mixed and incubated for another 20 min at room temperature. The mixture solution was added to cells containing approximately 400 μL normal medium. The cells were then incubated in a humidified atmosphere of 5% CO_2 at 37 °C. After the cells were transfected for 24 h, the efficiency of the siRNAs was determined by Western blot.

Results

The high efficiency expression of Htt552 in PC12 cells

The expression of Htt552 was achieved by insertion of a stop codon after amino acid residue 552 in the 3-kb Htt cDNA. As expected, the expressed wild-type Htt with 1–552 aa (Htt552-18Q) migrated at 89 kDa, while mutant Htt (Htt552-100Q) migrated at 115 kDa (Figure 1A). Our immunofluorescent results showed that the transfection efficiency was approximately 60%–70% at an MOI 30 (Figure 1B) and approximately 90% at an MOI 100 (data not shown). Both wild-type and mutant Htt552 were primarily distributed in the cytoplasm with little or no aggregation.

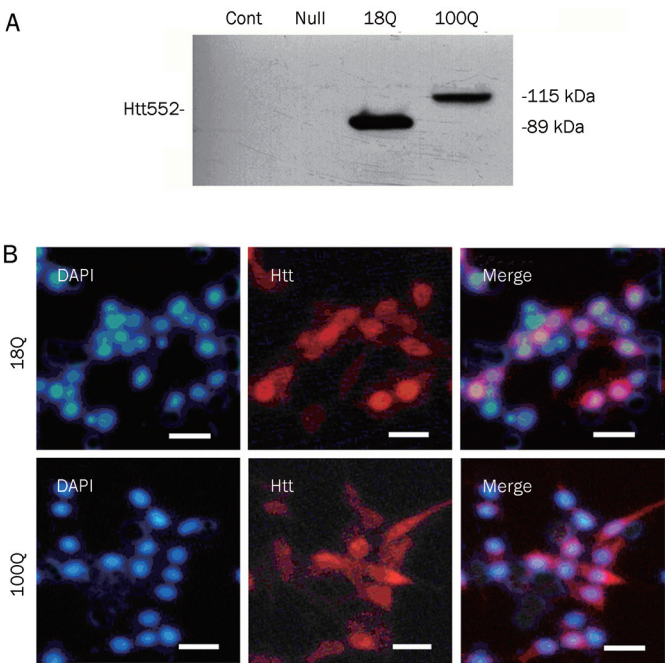

Figure 1. The expression of Htt552 in PC12 cells. PC12 cells were infected with Ad-Htt-18Q-552, Ad-Htt-100Q-552, or Ad-null at MOI 30 and harvested 24 h later for Western blot analysis. Both wild-type and mutant Htt552 were expressed at the expected molecular mass (A). PC12 cells were infected with Ad-Htt-18Q-552, Ad-Htt-100Q-552 at MOI 30 for 24 h and then processed for double immunofluorescence of Htt (red) and the nuclear marker DAPI (blue). Cells were examined with fluorescent microscopy (400×, scale bar=10 μm). Both wild-type and mutant Htt552 had a high expression of Htt552, and the rate of transfection reached approximately 60%–70%.

Htt552 expression increased autophagy activity

LC3 II is an important protein involved in the formation of autophagosomes. Western blot analysis showed that the level of LC3 II was lower in both normal cells and adenovirus-null infected cells, but it was significantly higher in the cells expressing wild-type or mutant Htt552. Beclin1 is essential for the formation of autophagosomes and cytosol-to-vacuole vesicles[29]. Beclin1 was also prominently increased after Htt552 expression. In addition, the levels of cathepsin B and L were increased in Htt-expressing cells. Both the expression of autophagy-related proteins and the enzymes found in lysosomes increased, suggesting that autophagy was activated in Htt-expressing cells (Figure 2).

Both autophagy and proteasome prevent the accumulation of Htt552

The ubiquitin-proteasome system and autophagy/lysosome pathway are two primary protein degradation pathways that can be activated by different substrates. Treatment with the autophagy inhibitor 3-MA or the proteasome inhibitors lactacystin and MG-132 increased Htt552 levels in PC12 cells infected with Ad-Htt-18Q-552 or Ad-Htt-100Q-552 (Figure 3A). The proteasome inhibitor caused a higher accumulation of Htt552-18Q than Htt552-100Q, and the autophagy inhibitor resulted in a higher accumulation of Htt552-100Q than Htt552-18Q. This suggests that the proteasome plays a key role in the metabolism of Htt552-18Q, whereas autophagy plays a major role in the metabolism of Htt552-100Q. Similar results were observed for our primary cultured neurons infected with adenovirus (Figure 3B). These results support that both the ubiquitin-proteasome system and autophage-lysosomal pathway play a role in the clearance of Htt552.

Beclin1 redistributed from the nucleus in Htt552-expressing cells

The export of Beclin1 from the nucleus is the first step in the process of autophagy[30]. Beclin1 deficiency leads to impaired autophagy function in mammalian cells[26, 31]. Our immunofluorescence results showed that the basal level of Beclin1 was low and distributed mainly in the nucleus of control cells. After expression of Htt552, the levels of Beclin1 greatly increased in the cytosol. Furthermore, the expression of Beclin1 in the cytosol increased as the expression of Htt552 increased (Figure 4).

Htt siRNA prevented the redistribution of Beclin1 in starvation conditions

It is known that starvation or amino acid deprivation stimulates the nuclear export of Beclin1 and activates autophagy. Thus, we evaluated the role of Htt in the redistribution of Beclin1 during starvation conditions. The knockdown of endogenous Htt was achieved with the transfection of PC12 cells with Htt siRNA. The Htt siRNA was selected from three siRNAs that were designed based on Htt cDNA. The endogenous Htt in PC12 cells was difficult to detect by normal Western blot; therefore, PC12 cells were transfected with Htt siRNAs 6 h before they were infected with Ad-Htt-18Q-552.

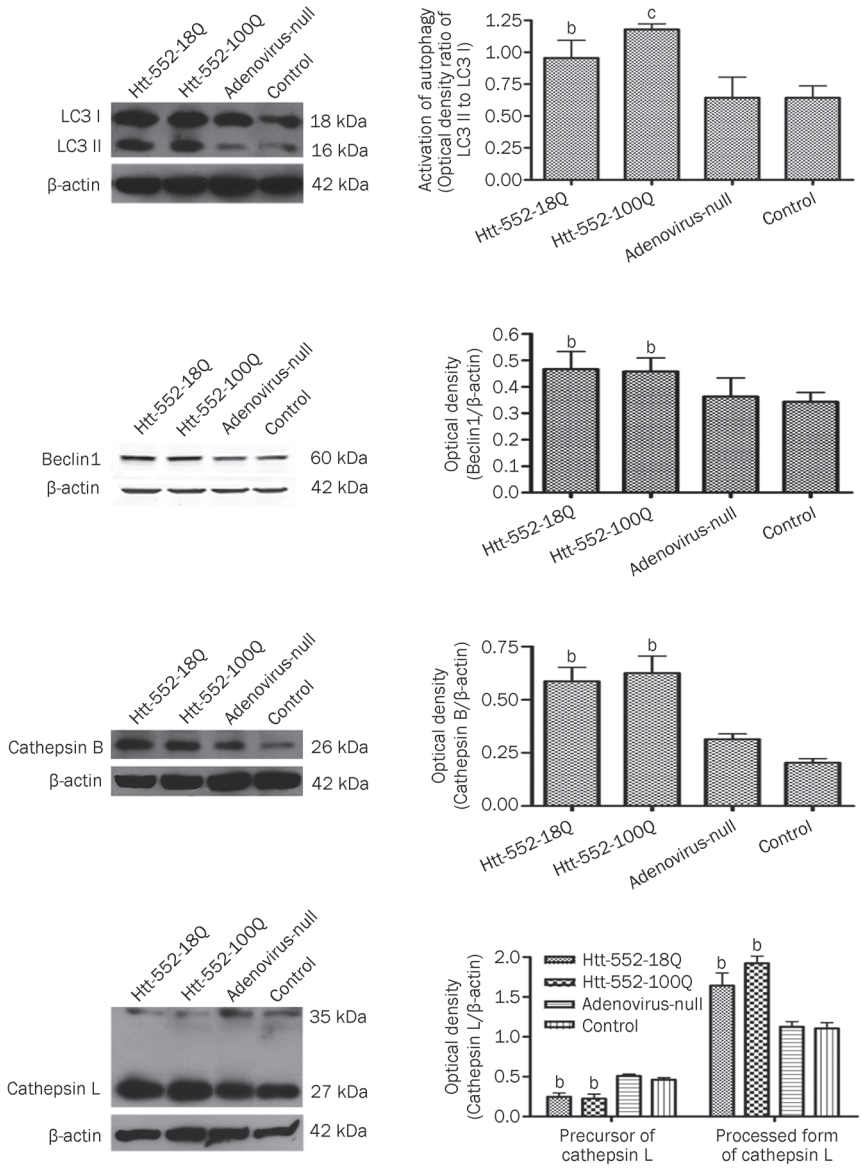

Figure 2. Autophagy was activated by Htt552 expression. PC12 cells were infected with Ad-Htt-18Q-552, Ad-Htt-100Q-552, or Ad-null at MOI 30 and harvested 24 h later for Western blot analysis. The protein levels of LC3 I and LC3 II increased after Htt552 expression. The data are expressed as a ratio of LC3 II/LC3 I. Beclin1, cathepsin B and the processed form of cathepsin L (bottom panel) were also upregulated after Htt552 expression. The densities of protein bands were analyzed with an image analyzer (Sigma Scan Pro 5) and normalized to the loading control (β-actin). The data are represented as the mean±SEM. Statistical comparisons were carried out with an ANOVA followed by a Dunnett's test. $^{b}P<0.05$, $^{c}P<0.01$ *vs* control.

After 24 h, Western blot analysis was used to detect the levels of Htt552. siRNA3 was the most efficient in reducing Htt552 expression and was used for the subsequent studies. PC12 cells were transfected with Htt siRNAs for 24 h in normal culture medium with 10% FBS and then in fresh medium without FBS for another 24 h. The cells were harvested for immunofluorescence procedure. The results showed that the redistribution of Beclin1 during starvation was inhibited by the knockdown of Htt552, suggesting that Htt may be involved in Beclin1 activation through the enhancement of Beclin1 export from the nucleus to the cytoplasm (Figure 5).

Blockade of Beclin1 nuclear export or Beclin1 deficiency induced the formation of mHtt552 aggregates

The Rev-type NES forms a complex with the nuclear export receptor, CRM1, and Ran GTP. Leptomycin B can bind to CRM1 and block the formation of this complex, thereby blocking the nuclear exportation of the Rev-type nuclear export signal (NES)-containing proteins. Beclin1 contains a leptomycin B-sensitive leucine-rich nuclear export signal that is responsible for its efficient nuclear export. This export is required for autophagy and tumor suppressor function[30]. Therefore, 10 nmol/L leptomycin B was added to PC12 cells after Htt552 expression. Leptomycin B was added 18 h after adenovirus infection to prevent its influence on the viral infection capacity. After 24 h of treatment with leptomycin B, the cells were fixed and immunofluorescence was performed. The results showed that leptomycin B restrained Beclin1 in the nucleus, and mHtt formed aggregates in the cytosol in some Htt-expressing cells (Figure 6B). In addition, Western blot analysis showed that the expression of Htt552 increased after the treatment with leptomycin B (Figure 6A).

To verify the important role of Beclin1 in Htt degradation, two Beclin1 siRNAs were designed and tested for their effi-

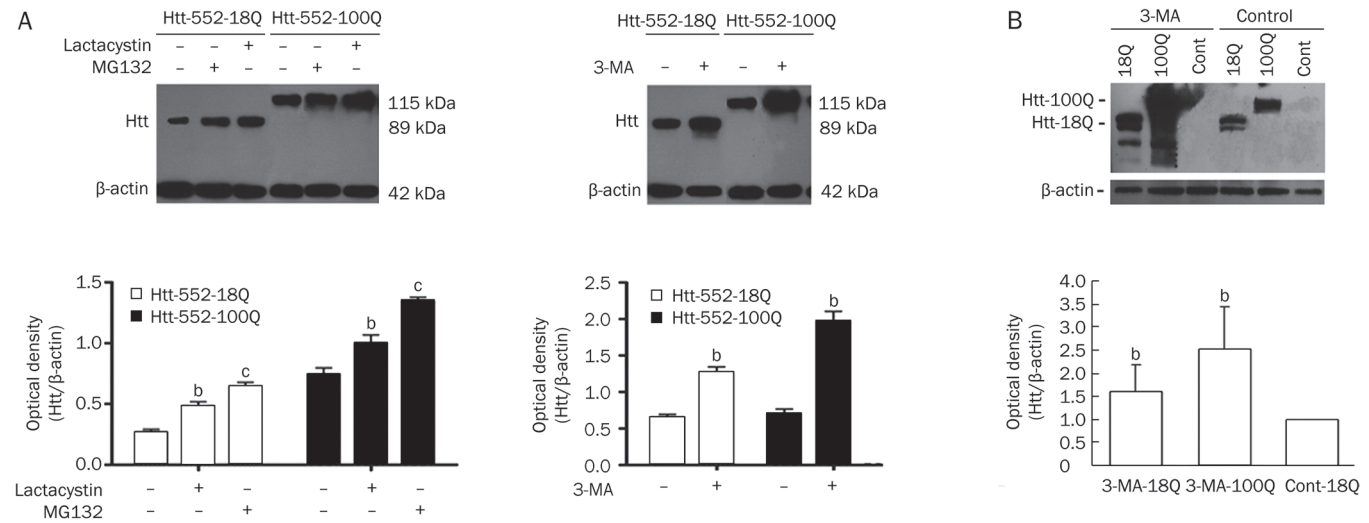

Figure 3. Both the UPS and ALP play a role in the clearance of Htt552. PC12 cells were infected with Ad-Htt-18Q-552, Ad-Htt-100Q-552, or Ad-null at MOI 30, and primary neurons were infected at MOI 100. After 24 h, cells were treated with the proteasome inhibitors, MG132 and lactacystin, or the autophagy inhibitor, 3-MA, for 18 h. Cells were then lysed for Western blot analysis. Treatment with MG-132, lactacystin (left panel in A) and 3-MA (right panel in A) increased the levels of Htt552. Treatment with 3-MA also increased the levels of Htt552 in rat primary cultured neurons (B). The densities of protein bands were analyzed with an image analyzer (Sigma Scan Pro 5) and normalized to the loading control (β-actin). The data are represented as the mean±SEM. Statistical comparisons were carried out with an ANOVA followed by a Dunnett's test. $^{b}P<0.05$, $^{c}P<0.01$ *vs* control.

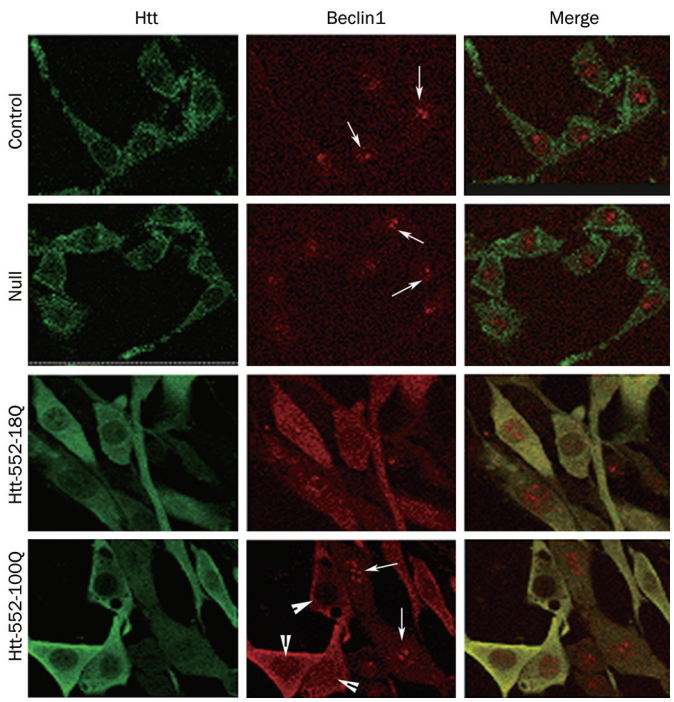

Figure 4. Beclin1 levels increased after Htt552 expression in PC12 cells. PC12 cells expressing Htt552 were fixed with pre-cooled EtOH and processed for double immunofluorescence of Htt552 (green) and Beclin1 (red). Cells were analyzed with a confocal microscope (600×). After Htt552 expression, Beclin1 was upregulated in the cytoplasm but reduced in the nucleus, indicating the activation of Beclin1 and the presence of autophagy. The thin arrow refers to Beclin1 in the nucleus, and the arrowhead refers to the export of Beclin1 to the cytoplasm.

ciency in reducing Beclin1 levels. siRNA1 was more efficient at reducing the levels of Beclin1 and was used in subsequent experiments. The RNA interference of Beclin1 resulted in the formation of mutant Htt552 aggregates (Figure 7), suggesting that Beclin1 is involved in the clearance of Htt552.

Discussion

The accumulation of misfolded proteins in the affected neurons is a common characteristic of several neurological disorders. Macroautophagy (commonly referred to as autophagy) is a crucial cellular process for the bulk degradation of organelles and long-lived proteins. Cytoplasmic substrates are delivered via autophagosomes to lysosomes and degraded. Several studies have suggested an altered autophagy function in HD. Our present results show that both proteasome and autophagy participate in the degradation of wild-type and mutant Htt552. Previous data suggest that proteasome inhibition causes a greater accumulation of mutant Htt than inhibition of autophagy[32]. According to our experiments, we believe that the different model systems and different concentrations of lactacystin or 3-MA can produce conflicting results. To verify the roles of these pathways, additional work should be done to determine the concentration and the specificity of stimulators or inhibitors of autophagy or the proteasome and utilize the knockdown of specific proteins. However, our results are consistent with previous work which shows that both the proteasome and autophagy affect the degradation of Htt. Far less is known about the molecular events controlling Htt degradation by autophagy in mammalian cells.

Beclin1 is a mammalian ortholog of Atg6/Vps30, a component of the Class III phosphatidylinositol 3-kinase complex in

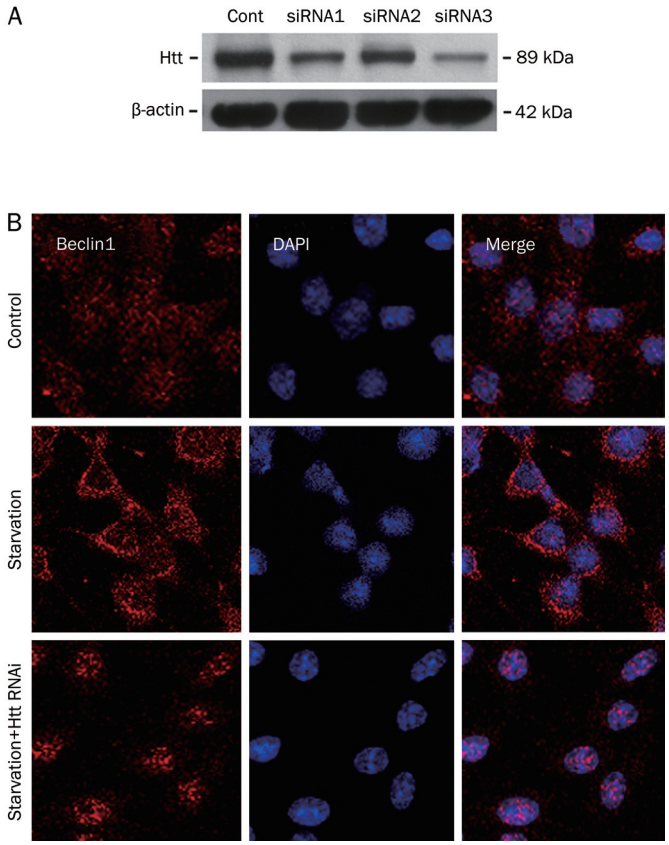

Figure 5. The effect of Htt on the activation of Beclin1. PC12 cells were transfected with Htt siRNAs for 6 h. They were then infected with Ad-Htt-18Q-552 at MOI 30 and harvested 24 h later for Western blot analysis. siRNA3 was the most efficient of the samples tested (A). Next, PC12 cells were transfected with Htt siRNA in normal culture medium with 10% FBS for 24 h and then changed to fresh medium without FBS and cultured for another 24 h. Lastly, cells were harvested for immunofluorescence. Knockdown of Htt retained Beclin1 in the nucleus during starvation conditions (B). This result suggests that the activation of Beclin1 was inhibited.

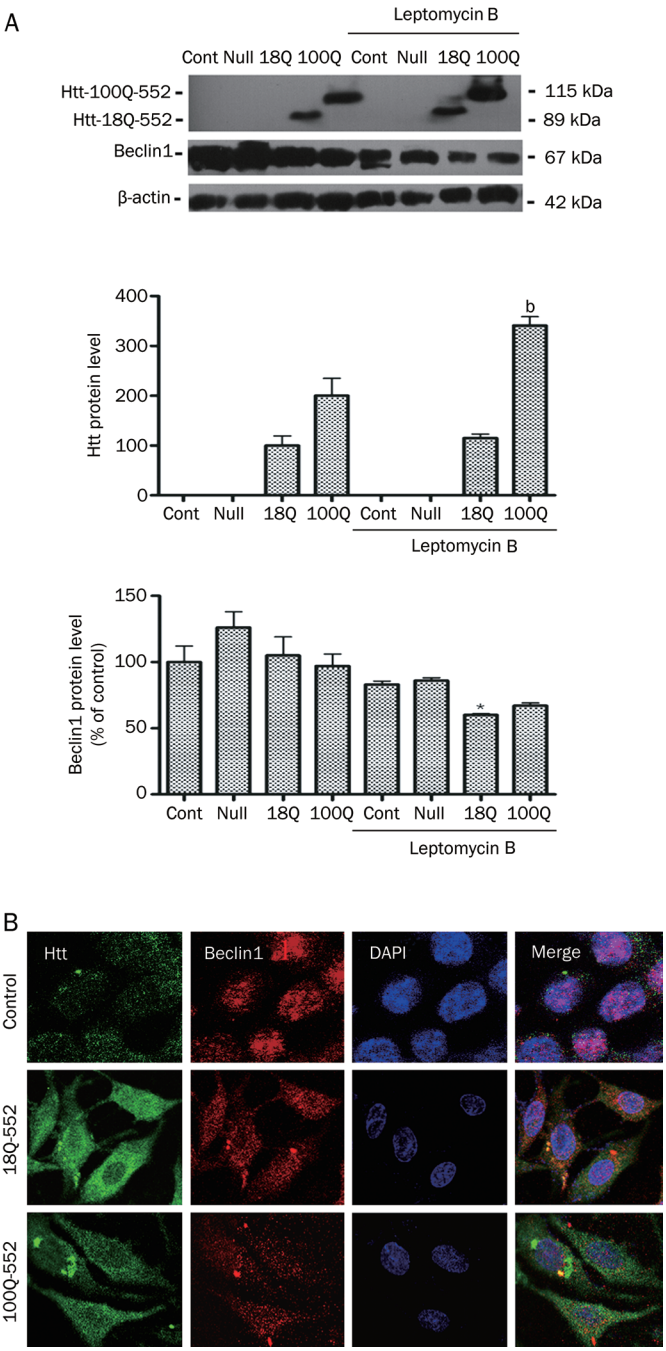

Figure 6. Leptomycin B induced the formation of Htt552 aggregates. PC12 cells were infected with Ad-Htt-18Q-552, Ad-Htt-100Q-552, or Ad-null at MOI 30 and were then treated with leptomycin B for 18 h. Western blot results showed that leptomycin B inhibited the increase of Beclin1 after Htt552 expression (A). The densities of protein bands were analyzed with an image analyzer (Sigma Scan Pro 5) and normalized to the loading control (β-actin). The data are represented as the mean±SEM. Statistical comparisons were carried out using an ANOVA followed by Dunnett's test. $^{b}P<0.05$ *vs* cells without leptomycin B treatment. Immunofluorescence results showed that leptomycin B restrained Beclin1 (red) in the nucleus (B). Protein aggregates of mutant Htt552 (green) were observed in some cells. Cells were detected with a confocal microscope (×600).

yeast[33]. The Class III PI 3-kinase and its product, PI 3-P, are involved in the autophagy signaling pathway. It has been verified that Beclin1 contains a core of closely spaced leucine residues that conform to the consensus motif of the NES[27, 30]. Subcellular redistribution and compartmental sequestration of proteins have emerged as important mechanisms in the regulation of cellular responses. Beclin1 plays an important role in macroautophagy by stimulating the formation of autophagosomes. In our study, the levels of Beclin1 increased in the cytoplasm. We also observed that the high expression of mHtt552 resulted in a greater effect on reducing the nuclear level of Beclin1 when compared to lower levels of mHtt552. Moreover, the downregulation of Beclin1 by siRNA and the inhibition of Beclin1 nuclear export by leptomycin B led to the accumulation of Htt552 and the formation of mHtt552 oligomers, even aggregates. These results indicate that Beclin1 is a

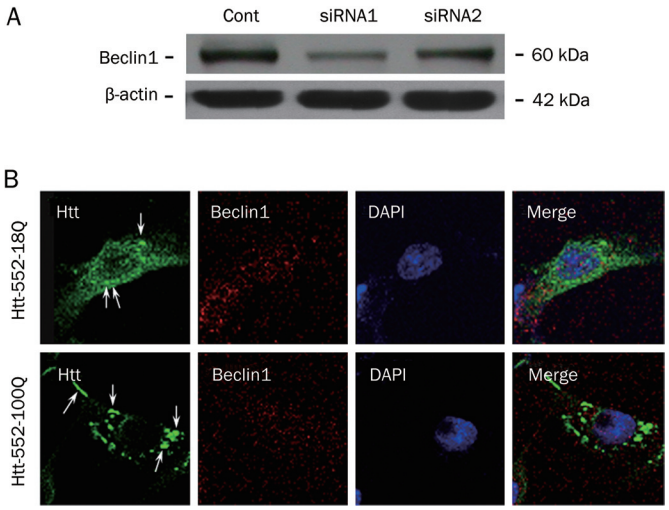

Figure 7. Beclin1 RNAi induced the formation of Htt552 aggregates. To detect the efficiency of Beclin1 RNAi, PC12 cells were transfected with Beclin1 siRNAs and harvested 24 h later for Western blot analysis. siRNA1 was the most efficient of the samples tested (A). PC12 cells were transfected with Beclin1 siRNA1 for 6 h and were then infected with Ad-Htts. After 48 h, cells were fixed and processed for double immunofluorescence of Htt (green) and the nuclear marker DAPI (blue). Cells were analyzed with a confocal microscope (×600). Mutant Htt552 clearly formed aggregates after Beclin1 levels were reduced (B).

necessary protein in the autophagic degradation of Htt552.

Our study suggests a possible role of Beclin1 in the autophagic degradation of mutant Htt552. Thus, Beclin1 may be a useful target for the treatment of HD.

Acknowledgements

This work was supported by grants from the National Natural Science Foundation of China (No 30600197) and the Natural Science Foundation of Jiangsu Province for College (No 09KJB310014).

Author contribution

Fang LIN and Zheng-hong QIN designed the study. Jun-chao WU, Fang LIN, Lin QI, and Yan WANG performed the research. Kimberly B KEGEL and Jennifer YODER contributed the plasmids. Jun-chao WU and Fang LIN analyzed the data and wrote the manuscript. Zheng-hong QIN and Marian DIFIGILA revised the paper.

Abbreviations

HD, Huntington's disease; Htt, Huntingtin; polyQ, polyglutamine; siRNA, small interference RNA; WT, wild type; LC3, light chain 3.

References

1 Kim YJ, Yi Y, Sapp E, Wang Y, Cuiffo B, Kegel KB, *et al*. Caspase 3-cleaved N-terminal fragments of wild-type and mutant Htt are present in normal and Huntington's disease brains, associate with membranes, and undergo calpain-dependent proteolysis. Proc Natl Acad Sci USA 2001; 98: 12784–9.
2 Qin ZH, Gu ZL, Lin F. The advancement of molecular pathology of Huntington's disease. Chin Pham Bull 2004; 20: 378–82.
3 Gauthier LR, Charrin BC, Borrell-Pages M, Dompierre JP, Rangone H, Cordelieres FP, *et al*. Huntingtin controls neurotrophic support and survival of neurons by enhancing BDNF vesicular transport along microtubules. Cell 2004; 118: 127–38
4 Rigamonti D, Bauer JH, De-Fraja C, Conti L, Sipione S, Sciorati C, *et al*. Wild-type huntingtin protects from apoptosis upstream of caspase-3. J Neurosci 2000; 20: 3705–13.
5 Nasir J, Floresco SB, O'Kusky JR, Diewert VM, Richman JM, Zeisler J, *et al*. Targeted disruption of the Huntington's disease gene results in embryonic lethality and behavioral and morphological changes in heterozygotes. Cell 1995; 81: 811–23.
6 Duyao MP, Auerbach AB, Ryan A, Persichetti F, Barnes GT, McNeil SM, *et al*. Inactivation of the mouse Huntington's disease gene homolog Hdh. Science 1995; 269: 407–10.
7 Zeitlin S, Liu JP, Chapman DL, Papaioannou VE, Efstratiadis A. Increased apoptosis and early embryonic lethality in mice nullizygous for the Huntington's disease gene homologue. Nat Genet 1995; 11: 155–63.
8 Sapp E, Schwarz C, Chase K, Bhide PG, Young AB, Penney J, *et al*. Huntingtin localization in brains of normal and Huntington's disease patients. Ann Neurol 1997; 42: 604–12.
9 Kegel KB, Kim M, Sapp E, McIntyre C, Castano JG, Aronin N, DiFiglia M. Huntingtin expression stimulates endosomal-lysosomal activity, endosome tubulation, and autophagy. J Neurosci 2000; 20: 7268–78.
10 Ravikumar B, Duden R, Rubinsztein DC. Aggregate-proneproteins with polyglutamine and polyalanine expansions are degraded by autophagy. Hum Mol Genet 2002; 11: 1107–17.
11 Ravikumar B, Vacher C, Berger Z, Davies JE, Luo S, Oroz LG, *et al*. Inhibition of mTOR induces autophagy and reduces toxicity of polyglutamine expansions in fly and mouse models of Huntington disease. Nat Genet 2004; 36: 585–95.
12 Sarkar S, Davies JE, Huang Z, Tunnacliffe A, Rubinsztein DC. Trehalose, a novel mTOR-independent autophagy enhancer, accelerates the clearance of mutant huntingtin and alpha-synuclein. J Biol Chem 2007; 282: 5641–52.
13 Qin ZH, Wang Y, Kegel KB, Kazantsev A, Apostol BL, Thompson LM, *et al*. Autophagy regulates the processing of amino terminal huntingtin fragments. Hum Mol Genet 2003; 12: 3231–44.
14 Heng MY, Duong DK, Albin RL, Tallaksen-Greene SJ, Hunter JM, Lesort MJ, *et al*. Early autophagic response in a novel knock-in model of Huntington disease. Hum Mol Genet 2010; 19: 3702–20.
15 Wellington CL, Ellerby LM, Gutekunst CA, Rogers D, Warby S, Graham RK, *et al*. Caspase cleavage of mutant Htt precedes neurodegeneration in Huntington's disease. J Neurosci 2002; 22: 7862–72.
16 Zhai W, Jeong H, Cui LB, Krainc D, Tjian R. *In vitro* analysis of Htt-mediated transcriptional repression reveals multiple transcription factor targets. Cell 2005; 123: 1241–53.
17 Wang J, Wang CE, Orr A, Tydlacka S, Li SH, Li XJ. Impaired ubiquitin-proteasome system activity in the synapses of Huntington's disease mice. J Cell Biol 2008; 180: 1177–89.
18 Bergamini E, Cavallini G, Donati A, Gori Z. The role of macroautophagy in the ageing process, anti-ageing intervention and age-associated diseases. Int J Biochem Cell B 2004; 36: 2392–404.
19 Heiser V, Scherzinger E, Boeddrich A, Nordhoff E, Lurz R, Schugardt N, *et al*. Inhibition of huntingtin fibrillogenesis by specific antibodies and small molecules: implications for Huntington's disease therapy. Proc

Natl Acad Sci U S A 2000; 97: 6739–44.
20 Sarkar S, Rubinsztein DC. Huntington's disease: degradation of mutant huntingtin by autophagy. FEBS J 2008; 275: 4263–70.
21 Chen JJ, Lin F, Qin ZH. The roles of the proteasome pathway in signal transduction and neurodegenerative diseases. Neurosci Bull 2008; 24: 183–94.
22 Miller RJ, Wilson SM. Neurological disease: UPS stops delivering! Trends Pharmacol Sci 2003; 24:18–23.
23 Klionsky DJ, Emr SD. Autophagy as a regulated pathway of cellular degradation. Science 2000; 290: 1717–21.
24 Levine B, Klionsky DJ. Development by self-digestion: molecular mechanisms and biological functions of autophagy. Dev Cell 2004; 6: 463–77.
25 Shintani T, Klionsky DJ. Autophagy in health and disease: a double-edged sword. Science 2004; 306: 990–5.
26 Tassa A, Roux MP, Attaix D, Bechet DM. Class III phosphoinositide 3-kinase-Beclin1 complex mediates the amino acid-dependent regulation of autophagy in C2C12 myotubes. Biochem J 2003; 376: 577–86.
27 Liang XH, Jackson S, Seaman M, Brown K, Kempkes B, Hibshoosh H, *et al*. Induction of autophagy and inhibition of tumorigenesis by Beclin 1. Nature (London) 1999; 402: 672–6.
28 Shibata M, Lu T, Furuya T, Degterev A, Mizushima N, Yoshimori T, *et al*. Regulation of intracellular accumulation of mutant Huntingtin by Beclin 1. J Biol Chem 2006; 281: 14474–85.
29 Saeki K, Yuo A, Okuma E, Yazaki Y, Susin SA, Kroemer G, *et al*. Bcl-2 down-regulation causes autophagy in a caspase-independent manner in human leukemic HL-60 cells. Cell Death Differ 2000; 7: 1263–9.
30 Liang XH, Yu J, Brown K, Levine B. Beclin 1 contains a leucine-rich nuclear export signal that is required for its autophagy and tumor suppressor function. Cancer Res 2001; 61: 3443–9.
31 Yamamoto A, Cremona ML, Rothman JE. Autophagy-mediated clearance of Htt aggregates triggered by the insulin-signaling pathway. J Cell Biol 2006; 172: 719–31.
32 Li X, Wang CE, Huang S, Xu X, Li XJ, Li H, *et al*. Inhibiting the ubiquitin-proteasome system leads to preferential accumulation of toxic N-terminal mutant huntingtin fragments. Hum Mol Genet 2010; 19: 2445–55.
33 Kihara A, Kabeya Y, Ohsumi Y, Yoshimori T. Beclin-phosphatidylinositol 3-kinase complex functions at the trans-Golgi network. EMBO Rep 2001; 2: 330–5.

Acta Pharmacologica Sinica (2012) 33: 752–760
 1671-4083/12 $32.00
www.nature.com/aps

Original Article

18β-Glycyrrhetinic acid preferentially blocks late Na current generated by ΔKPQ Nav1.5 channels

Yi-mei DU[1, #], Cheng-kun XIA[2, #], Ning ZHAO[1], Qian DONG[1], Ming LEI[1, 3], Jia-hong XIA[2, *]

[1]Ion Channelopathy Research Center, Institute of Cardiology and [2]Department of Cardiovascular Surgery, Union Hospital, Tongji Medical College, Huazhong University of Science and Technology, Wuhan 430022, China, [3]Cardiovascular Research Group, School of Clinical and Laboratory Sciences, University of Manchester, Manchester, M13 9NT, UK

Aim: To compare the effects of two stereoisomeric forms of glycyrrhetinic acid on different components of Na^+ current, HERG and Kv1.5 channel currents.
Methods: Wild-type (WT) and long QT syndrome type 3 (LQT-3) mutant ΔKPQ Nav1.5 channels, as well as HERG and Kv1.5 channels were expressed in *Xenopus* oocytes. In addition, isolated human atrial myocytes were used. Two-microelectrode voltage-clamp technique was used to record the voltage-activated currents.
Results: Superfusion of 18β-glycyrrhetinic acid (18β-GA, 1–100 μmol/L) blocked both the peak current ($I_{Na,P}$) and late current ($I_{Na,L}$) generated by WT and ΔKPQ Nav1.5 channels in a concentration-dependent manner, while 18α-glycyrrhetinic acid (18α-GA) at the same concentrations had no effects. 18β-GA preferentially blocked $I_{Na,L}$ (IC_{50}=37.2±14.4 μmol/L) to $I_{Na,P}$ (IC_{50}=100.4±11.2 μmol/L) generated by ΔKPQ Nav1.5 channels. In human atrial myocytes, 18β-GA (30 μmol/L) inhibited 47% of $I_{Na,P}$ and 87% of $I_{Na,L}$ induced by *Anemonia sulcata* toxin (ATX-II, 30 nmol/L). Superfusion of 18β-GA (100 μmol/L) had no effects on HERG and Kv1.5 channel currents.
Conclusion: 18β-GA preferentially blocked the late Na current without affecting HERG and Kv1.5 channels.

Keywords: anti-arrhythmia agent; 18β-glycyrrhetinic acid; Nav1.5 channel; HERG channel; Kv1.5 channel; human atrial myocyte; *Anemonia sulcata* toxin; long QT syndrome

Acta Pharmacologica Sinica (2012) 33: 752–760; doi: 10.1038/aps.2012.22; published online 21 May 2012

Introduction

Activation of the cardiac voltage-gated sodium channel (Nav1.5) generates two types of inward currents, a large peak transient current (<3 ms) ($I_{Na,P}$) and another current of weak intensity that spans the action potential (>300 ms). The transient current initiates the rapid upstroke of the action potential, whereas the late persistent sodium current ($I_{Na,L}$) does not have a well-defined function, although it has been shown to affect the duration of the action potential. Recently, the role of $I_{Na,L}$ in controlling cardiac action potential repolarization and its importance in arrhythmogenesis has received increased attention[1].

An abnormal increase in $I_{Na,L}$ current, produced by the delayed opening of Na^+ channels, prolongs action potential repolarization and can lead to failed repolarization (early after-depolarizations) and Na^+-induced Ca^{2+} overloading that triggers delayed after-depolarizations, calcium oscillations, and rapid tachyarrhythmia such as ventricular tachycardia (VT) or fibrillation[1]. The reduction of $I_{Na,L}$ would therefore be expected to have therapeutic potential[2–4]. For example, ranolazine, a relatively selective inhibitor of $I_{Na,L}$, has been shown to be effective in reducing angina and the incidence of non-sustained VT in patients with ischemic heart disease[5–7].

Pronounced $I_{Na,L}$ was also observed in the congenital long QT syndrome (LQTS) caused by the mutation of Nav1.5. The most severe defect observed to date has been associated with the ΔKPQ mutation. The loss of three amino acids in the intercellular linker between domains 3 and 4 has been associated with LQTS. In the clinic, LQTS can most commonly be produced as an adverse effect to the drug due to blockade of the rapid component of the delayed rectifier potassium current, I_{Kr}[8]. HERG expresses a rapid delayed rectifier current (I_{Kr}), and the testing of potential drugs for their ability to block HERG is required for drug approval[8]. Kv1.5 conducts ultra-rapid delayed rectifier current (I_{Kur}) in the human atria[9, 10], and the loss-of-function mutation might also result in LQTS and cardiac arrest[11].

# These authors contributed equally to the paper.
* To whom correspondence should be addressed.
E-mail xiajiahong@hotmail.com
Received 2011-12-24 Accepted 2012-02-28

Recently, we reported that glycyrrhetinic acid (GA), an active ingredient of licorice[12], blocks both I_{NaP} and $I_{Na,L}$[13]. However, GA exists in two different stereoisomeric forms, the *trans* form and the *cis* form. The two forms have different physical and chemical properties and pharmacological effects[14]. Therefore, the purpose of the present study was to determine the action of 18β-GA and 18α-GA on $I_{Na,P}$ and $I_{Na,L}$ using wild-type (WT) and mutant ΔKPQ Nav1.5 channels expressed in *Xenopus* oocytes. Our results indicate that 18β-GA blocked WT and ΔKPQ Nav1.5 channels; however, 18α-GA had no significant effect on either channel. We further characterized the inhibition of WT and ΔKPQ Nav1.5 channels by 18β-GA and have demonstrated that 18β-GA preferentially blocks the $I_{Na,L}$ produced by ΔKPQ Nav1.5 channels in a concentration-dependent tonic manner. Moreover, we investigated the effects of 18β-GA on HERG and Kv1.5 channels and found that 18β-GA had no obvious effects on either channel. Finally, we evaluated the blockage effects of 18β-GA on $I_{Na,P}$ and $I_{Na,L}$ induced by ATX-II in human atrial myocytes, to further determine the prospects of this drug for treatment in human cardiovascular disease.

Materials and methods

Drugs

18α-GA and 18β-GA were purchased from Sigma (USA) and prepared initially as a 100 mmol/L stock solution by dissolving in 100% DMSO. Before use in an experiment, the stock solution was diluted with ND96 solution to reach the desired final concentration. The percentage of DMSO in the final solution was ≤0.1%, which alone showed no detectable effect on the sodium current. ATX-II was purchased from Sigma (USA) and dissolved in distilled water.

In vitro transcription of cRNA and functional expression in *Xenopus* oocytes

In vitro transcription of cRNAs and the isolation of oocytes were performed as previously described[13, 15, 16]. The plasmid pTracer-SV40 containing WT or ΔKPQ human Nav1.5 genes was a kind gift from Dr Thomas ZIMMER of Friedrich Schiller University Jena. HERG was subcloned into the pSP64 plasmid, which was a kind gift from Prof Michael C SANGUINETTI (University of Utah, USA). The human Kv1.5 gene (a gift from Dr Maria L GARCIA, Merck & Co, Inc, USA) was subcloned into a pCI-neo vector. Stage IV and V oocytes were injected with cRNA and then incubated in ND96 solution supplemented with 100 U/mL penicillin, 100 U/mL streptomycin and 2.5 mmol/L sodium pyruvate at 18 °C for 3 to 7 d before use in voltage-clamp experiments. ND96 solution contains (in mmol/L) 96 NaCl, 2 KCl, 1.8 $CaCl_2$, 2 $MgCl_2$, and 5 HEPES; the pH was adjusted to 7.5 with NaOH. The amount of cRNA injected was varied according to the purpose of the experiment. For $I_{Na,P}$, the amount of cRNA was adjusted to yield peak currents in the range of 4–8 μA to minimize space clamp heterogeneities and series resistance errors; $I_{Na,L}$ measurements required peak current amplitudes of greater than 10 μA to maximize the signal.

Two-microelectrode voltage clamp

Standard two-microelectrode voltage clamp techniques and a TEV-200A amplifier (Dagan Corporation) were used to record currents at room temperature (22–24 °C). Glass microelectrodes were filled with 3 mol/L KCl, and their tips were broken to obtain resistances of 0.5 to 1.5 MΩ. pCLAMP software (version 9.0; Molecular Devices, Union City, CA, USA) and a 1322A analog/digital interface (Molecular Devices) were used to generate voltage commands.

The voltage protocols used to obtain currents are described in the results. The data for activation and steady-state inactivation were fitted with a simple Boltzmann function: $I/I_{max}=\{1+\exp[V_m-V_{1/2})/k]\}$, where I/I_{max} is the relative current, $V_{1/2}$ is the half-maximum voltage of activation or inactivation, and k is the slope factor. The recovery time course was fitted with the biexponential function: $I/I_{max}=A_o+A_f(1-\exp[-t/\tau_f])+A_s(1-\exp[-t/\tau_s])$, where τ and A are the time constants and the corresponding relative amplitude, respectively.

The amplitudes of $I_{Na,P}$ were measured as maximal amplitudes during the first 5 ms of the depolarizing pulse and the $I_{Na,L}$ as the mean current amplitude of the last 10 ms of the pulse. The concentration required for a 50% block of current (IC_{50}) was determined by fitting the data to a Hill equation using five concentrations of drug (6–27 oocytes/point).

Human atrial myocyte isolation and whole-cell patch clamp

Human atrial myocytes were enzymatically dissociated as described previously[17]. Right atrial appendage tissues were obtained during atriotomy in patients undergoing coronary artery bypass grafting. All patients were free of supraventricular tachyarrhythmia and symptomatic congestive heart failure, and all atrial tissues were grossly normal at the time of cardiac surgery. Using a patch-clamp amplifier (Axon-200 B, Molecular Devices), the whole-cell patch clamp technique was used to record the I_{Na}. The series resistance averaged 1.6±0.4 MΩ after compensating for approximately 80% of the initial value. The pipette solution contained (in mmol/L) 120 CsCl, 1 $CaCl_2$, 5 $MgCl_2$, 5 Na_2ATP, 10 TEACl, 11 EGTA and 10 HEPES (pH 7.3 with CsOH). The bath solution for $I_{Na,P}$ recording contained (in mmol/L) 25 NaCl, 105 CsCl, 1.8 $CaCl_2$, 1 $MgCl_2$, 0.05 $CdCl_2$, 10 HEPES and 10 glucose (pH 7.4 with CsOH). The bath solution used to measure the $I_{Na,L}$ induced by ATX-II recording contained (in mmol/L) 135 NaCl, 1.8 $CaCl_2$, 1 $MgCl_2$, 0.05 $CdCl_2$, 10 HEPES and 10 glucose (pH 7.4 with NaOH).

Data analysis

pCLAMP 9.0 and Origin 7.5 (Microcal Software, Northampton, MA, USA) software were used for data acquisition and analysis. Values are expressed as the mean±SD. Analyses of variance (ANOVA) for repeated measures and the Holm-Sidak multiple comparison post-test or Student's *t*-test (InStat 2.04; GraphPad Software) were employed to determine statis-

tical significance (P<0.05).

Results

Effects of 18α-GA and 18β-GA on WT and ΔKPQ Nav1.5 channels

We first compared the effects of 18α-GA and 18β-GA on I_{Na} produced by WT (Figure 1) and ΔKPQ (Figure 2) Nav1.5 channels expressed in *Xenopus* oocytes. Currents were elicited by a series of 500-ms depolarizing steps from a hold potential of -120 mV with an interpulse interval of 10 s. Original $I_{Na,P}$ traces of WT Nav1.5 channel-mediated current before and after superfusion with 100 μmol/L 18α-GA or 30 μmol/L 18β-GA are shown in Figures 1A and 1C, respectively. Figures 2A and 2C show one typical current trace of ΔKPQ Nav1.5 channel current elicited by a depolarizing pulse to -20 mV, which demonstrates the incomplete inactivation of $I_{Na,L}$ and the effects of 100 μmol/L 18α-GA and 100 μmol/L 18β-GA, respectively. Application of 18β-GA significantly inhibited the I_{Na} produced by both WT and ΔKPQ Nav1.5 channels (Figures 1D and 2D), while 18α-GA had no obvious effects on WT and ΔKPQ Nav1.5 channels (Figures 1B and 2B).

Concentration-dependent tonic block of WT and ΔKPQ Nav1.5 channels by 18β-GA

We then examined the dose-dependent and tonic blockage effects of 18β-GA on WT and ΔKPQ Nav1.5 channels. Oocytes were held at -120 mV, and currents were evoked by depolarization to -20 mV every 10 s. This infrequent pulsing protocol should minimize the effects of a frequency-dependent block, therefore providing a reasonable estimate of the extent to which 18β-GA induces a tonic block of I_{Na}. The upper panel of Figure 3A shows the experimental recordings of $I_{Na,P}$ from WT Nav1.5 channels before and after the successive application of 1, 30, and 100 μmol/L 18β-GA. The upper panels of Figures 3B and 3C show the superimposed $I_{Na,P}$ and $I_{Na,L}$ traces of ΔKPQ Nav1.5 channels and the blocking effects of 18β-GA at 1, 30 and 100 μmol/L, respectively.

Because there was no detectable $I_{Na,L}$ in WT Nav1.5 channels, only the suppression of $I_{Na,P}$ was analyzed. The lower panels of Figure 3 show the concentration-response curves for 18β-GA after application to the WT and ΔKPQ Nav1.5 channels. The smooth lines represent the best fits of the data using the Hill equation, with the parameters of the fits shown in Figure 3. The Hill coefficients of 18β-GA binding to WT and ΔKPQ Nav1.5 channels were not significantly different from 1, suggesting that only one drug molecule is necessary to block the channel. The 18β-GA block of $I_{Na,P}$ and $I_{Na,L}$ in ΔKPQ Nav1.5 channels exhibited IC_{50} values of 100.4±11.2 μmol/L and 37.2±14.4 μmol/L, respectively. These results demonstrated

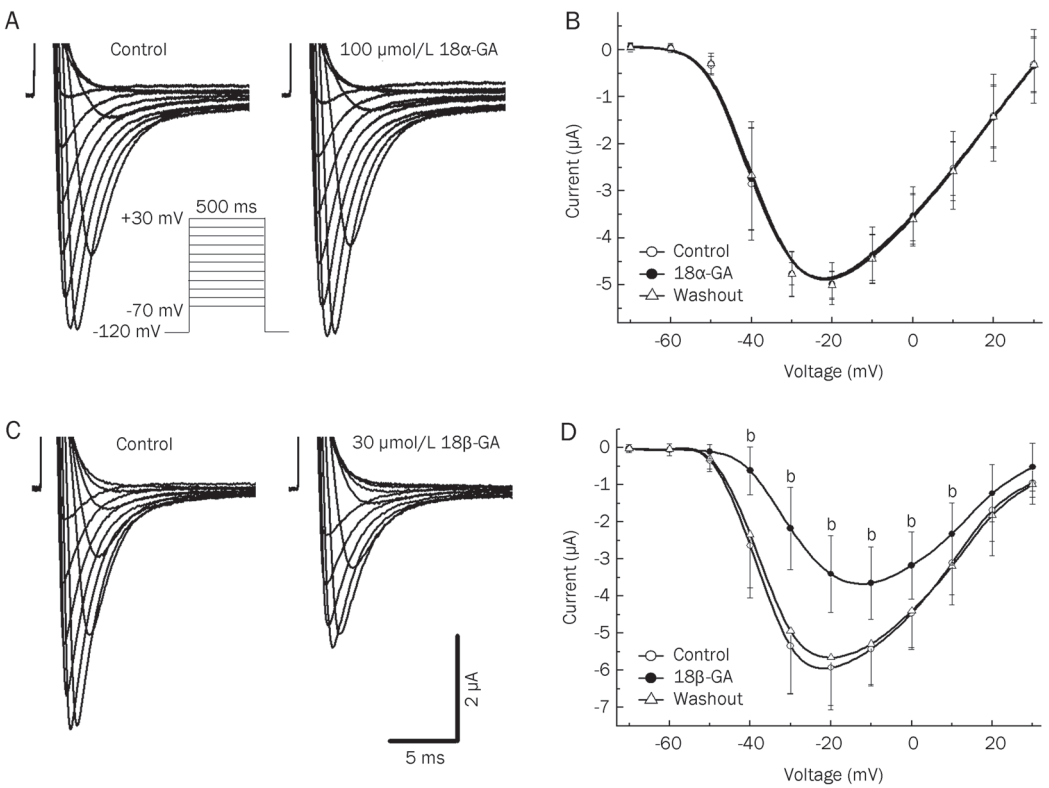

Figure 1. Effects of 18α-GA and 18β-GA on $I_{Na,P}$ mediated by the WT Nav1.5 channel. (A) and (C) Representative current traces elicited by 500-ms test pulses from -70 mV to 30 mV with 10 mV increments at 0.1 Hz in typical oocytes perfused before and after in 100 μmol/L 18α-GA (A) or 30 μmol/L 18β-GA (C). The membrane potential was held at -120 mV. (B) and (D) Averaged current-voltage relationships of $I_{Na,P}$ before and after perfusion with 100 μmol/L 18α-GA (B) or 30 μmol/L 18β-GA (D); n=6 per group; ^bP<0.05.

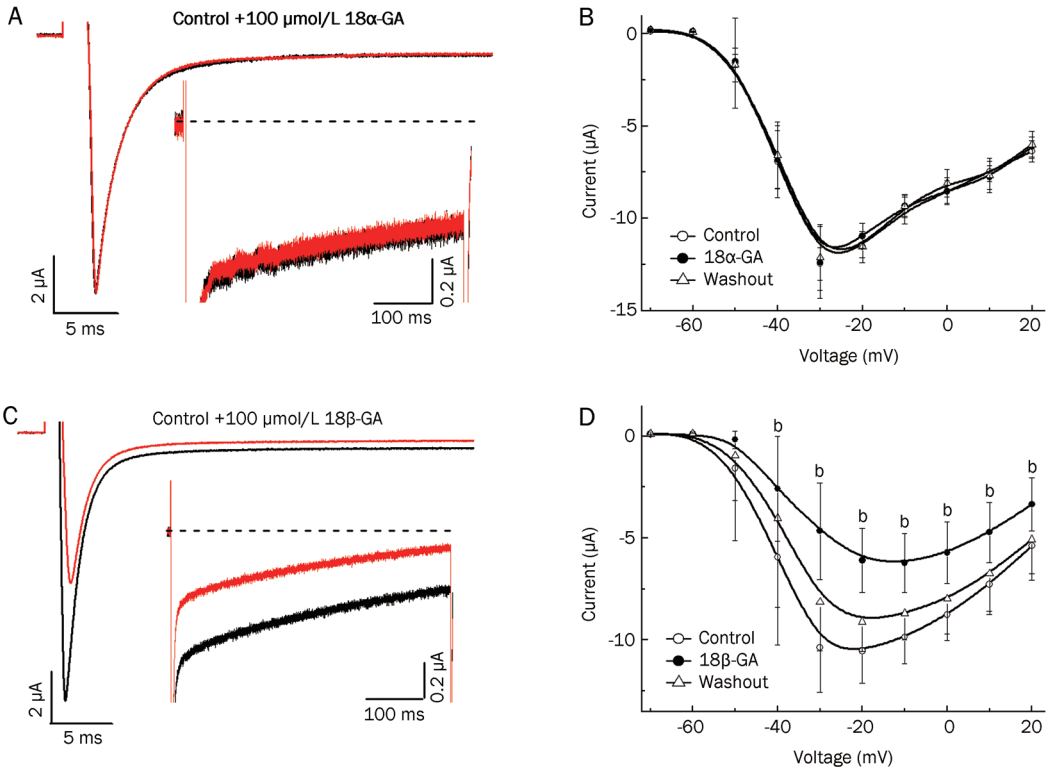

Figure 2. Effects of 18α-GA and 18β-GA on ΔKPQ Nav1.5 channels. (A) and (C) Original current recordings in the absence and presence of 100 μmol/L 18α-GA (A) or 18β-GA (C). Current was elicited by a depolarizing pulse from a holding potential of -120 mV to -30 mV for 500 ms. Insets show magnified current traces for comparison of the late component. (B) and (D) Averaged current-voltage relationships of $I_{Na,P}$ before and after perfusion with 100 μmol/L 18α-GA (B) or 18β-GA (D); n=6 per group; ^bP<0.05.

that 18β-GA exhibited greater degrees of tonic inhibition of $I_{Na,L}$ compared with $I_{Na,P}$ when applied to ΔKPQ Nav1.5 channels.

Rate-dependent block of WT andΔKPQ Nav1.5 channels by 18β-GA

To study the rate-dependent block (phasic block), a series of 30 repetitive impulses to -20 mV from a holding potential of -120 mV were applied at 1, 2, and 4 Hz, according to the method proposed by Rajamani *et al*[18]. The amplitude of currents was normalized to the current during the first impulse and plotted as a function of the pulse number. Lidocaine is a clinically used class I anti-arrhythmic agent, and its action on Nav1.5 channels has been studied extensively (reviewed by Sheets *et al*[19]). In the presence of 18β-GA (30 μmol/L), $I_{Na,P}$ of WT Nav1.5 channels did not change after 30 repetitive depolarizing events at 4 Hz (approximately 0.93 at the 30th pulse, n=6 in each group, Figure 4A). On the contrary, lidocaine (100 μmol/L) caused a significant rate-dependent reduction in the current conducted by the WT Nav1.5 channel (P<0.05 at 1 Hz and 2 Hz, P<0.01 at 4 Hz, n=5, Figure 4B), which is similar to other reports[20, 21]. The $I_{Na,P}$ mediated by the WT Nav1.5 channel (Figure 4A) shows that the administration of 18β-GA at 100 μmol/L caused an additional phasic block of $I_{Na,P}$ and $I_{Na,L}$ at ΔKPQ Nav1.5 channels (P<0.05, n=6, Figures 4C and 4D).

Voltage dependence of the activation and inactivation of WT and ΔKPQ Nav1.5 channels in the absence and presence of 18β-GA

Voltage-dependent activation and steady-state inactivation of WT and ΔKPQ Nav1.5 channels were measured and fitted with Boltzmann equations. The former was evaluated as normalized conductance-voltage relationships, and the latter was determined using a double-pulse as indicated in the protocol diagram in Figure 1S. The parameters are summarized in Table 1. Treatment with 18β-GA significantly shifted the $V_{1/2}$ of activation curves in the positive direction and $V_{1/2}$ of the steady-state inactivation curves in the negative direction; these shifts were completely recovered after washout. These results confirmed and extended our previous study on GA[13] and suggested that 18β-GA alters the gating function of both WT and ΔKPQ Nav1.5 channels.

The recovery time course of WT and ΔKPQ Nav1.5 channels from inactivation had fast (τ_f) and slow components (τ_s) (Figure 1S and Table 2). The application of 18β-GA significantly slowed the recovery of WT (30 μmol/L) and ΔKPQ (100 μmol/L) Nav1.5 channels. Table 2 summarizes the above parameters of WT and ΔKPQ Nav1.5 channels. These results suggest that 18β-GA could act on both fast and slow inactiva-

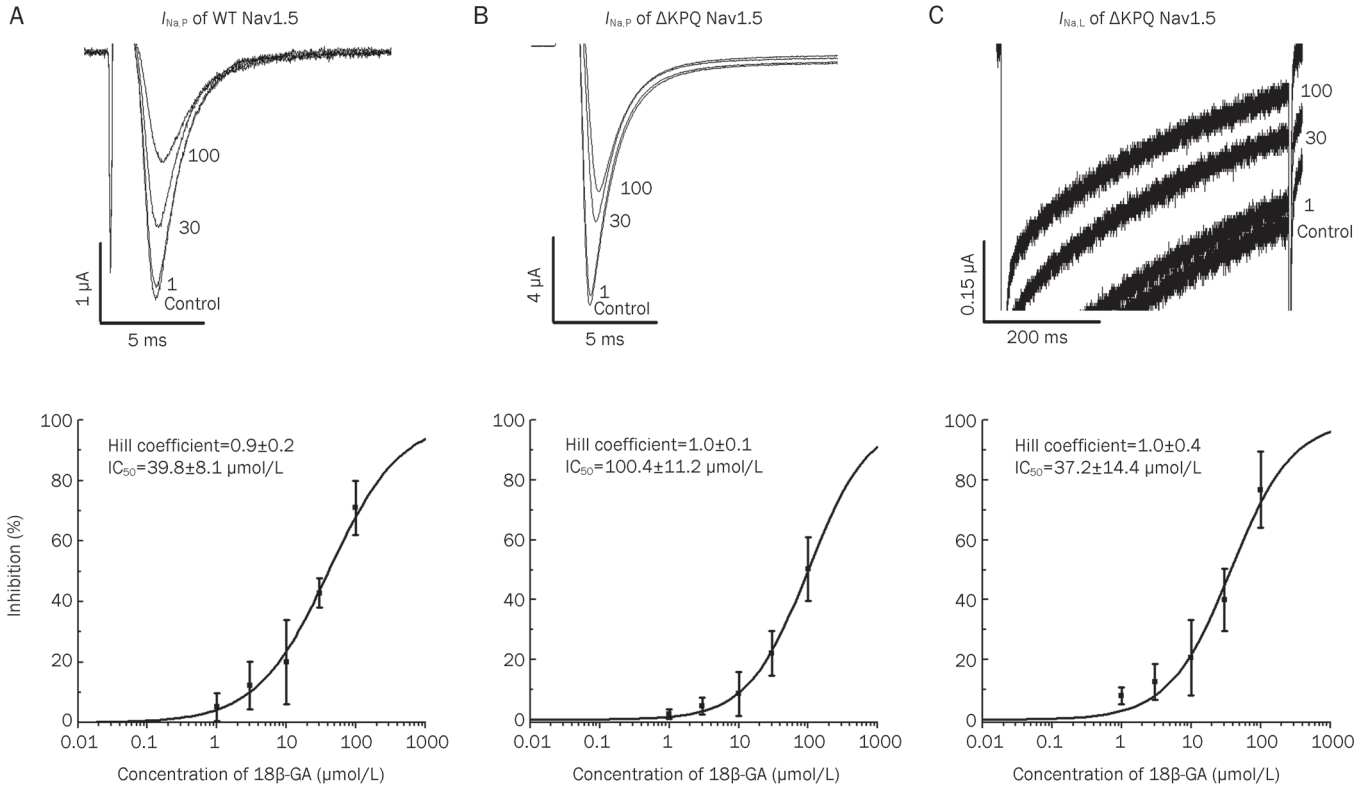

Figure 3. Concentration-dependent block by 18β-GA of WT $I_{Na,P}$ (A), ΔKPQ $I_{Na,P}$ (B), and $I_{Na,L}$ (C). I_{Na} was elicited by a depolarizing pulse from a holding potential of -120 mV to -30 mV for 500 ms at 0.1 Hz. Representative traces (upper panels) were superimposed before (control) and during perfusion of 18β-GA (1–100 μmol/L). (B, C) are traces from the same oocyte on an expanded scale. Summarized dose-response data (lower panels) fitted with the Hill equation. IC_{50} values and the Hill coefficient are provided in the figure. n=6–27 oocytes/point.

Table 1. Comparative activation and inactivation parameters of WT (at 30 μmol/L) and ΔKPQ (at 100 μmol/L) $I_{Na,P}$ in the absence (control) and presence of 18β-GA. Mean±SD. n=6 per group. [b]P<0.05 *vs* control.

	WT				ΔKPQ			
	Activation		Inactivation		Activation		Inactivation	
	$V_{1/2}$	K	$V_{1/2}$	K	$V_{1/2}$	K	$V_{1/2}$	K
Control	-33.8±1.8	6.7±1.6	-81.8±0.4	7.2±0.3	-36.2±1.8	7.0±1.5	-75.1±0.4	4.8±0.4
18β-GA	-25.1±1.9[b]	7.7±1.7	-88.1±0.3[b]	6.9±0.2[b]	-28.6±1.6[b]	7.8±1.3[b]	-80.5±0.5[b]	5.1±0.4
Washout	-31.6±1.7	7.6±1.5	-83.0±0.4	7.2±0.4	-33.2±1.8	7.0±1.5	-75.4±0.4	4.7±0.4

tion components of WT and ΔKPQ Nav1.5 channels.

Table 2. Recovery inactivation parameters of WT (at 30 μmol/L) and ΔKPQ (at 100 μmol/L) $I_{Na,P}$ in the absence (control) and presence of 18β-GA. Mean±SD. n=6 per group. [b]P<0.05 *vs* control.

	Control		18β-GA	
	τ_f	τ_s	τ_f	τ_s
WT	11.8±2.4	261.7±26.0	22.1±7.4[b]	342.7±36.1[b]
ΔKPQ	5.8±1.1	201.2±40.5	7.3±2.0[b]	272.0±34.0[b]

Effects of 18β-GA on HERG and Kv1.5 channels

Our previous study demonstrated that GA had no significant effect on L-type calcium current ($I_{Ca,L}$) or hyperpolarization-activated inward current (I_f) in rabbit sinoatrial node pacemaker cells[13]. In this study, we extended our previous study to investigate the effects of 18β-GA on HERG and Kv1.5 channels. Figures 5A and 5B show the experimental current recordings obtained from HERG and Kv1.5 channels before and after the application of 100 μmol/L 18β-GA. The voltage protocols are presented in the inset of Figure 5. 18β-GA at 100 μmol/L had no inhibitory effects on either HERG (n=6) or Kv1.5 channels (n=7). No significant effect of 18α-GA (100

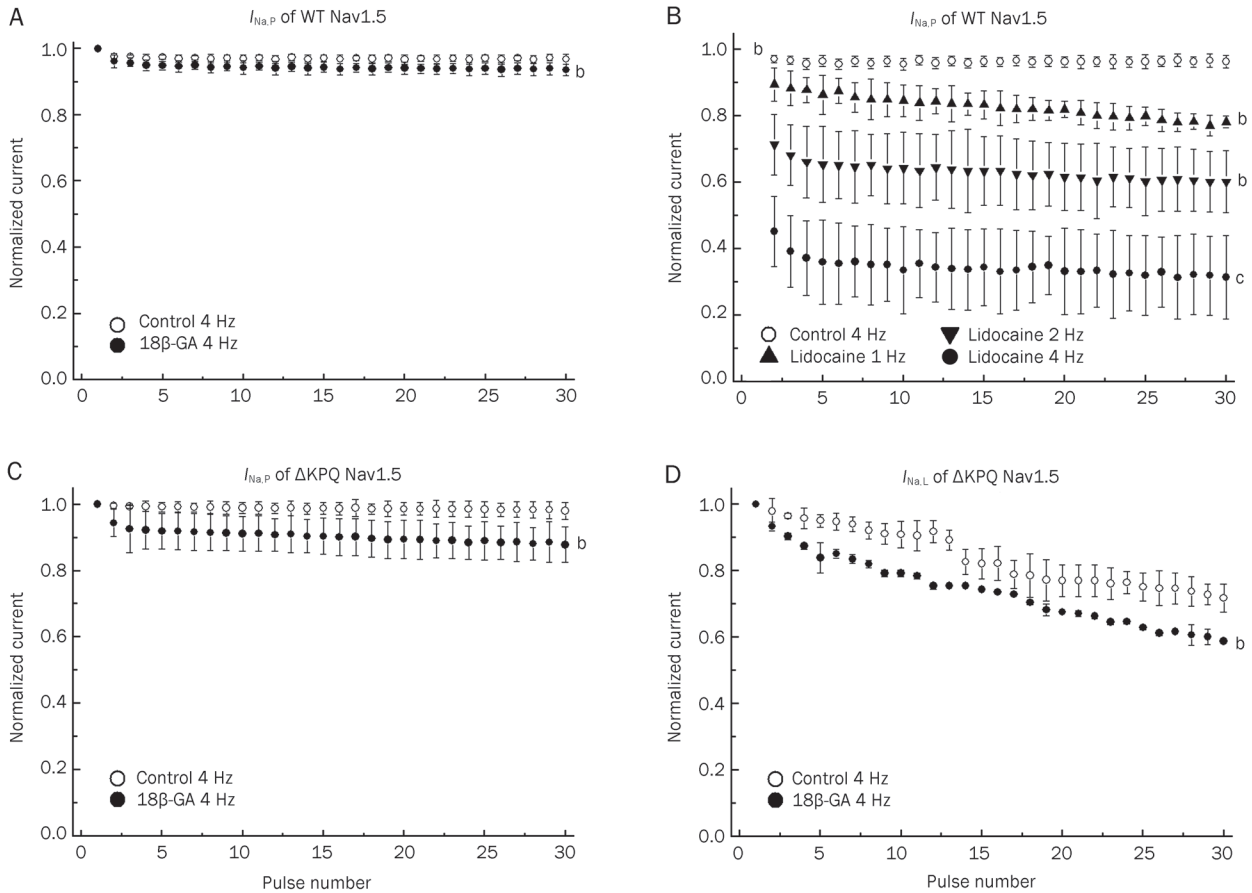

Figure 4. Rate-dependent blockade of WT and ΔKPQ Nav1.5 channels. I_{Na} was elicited by a series of 30 depolarizing pulses of -120 mV to -20 mV at different stimulation frequencies. The relative current amplitude elicited by each pulse was normalized to the respective amplitudes the currents elicited by the first pulse and plotted against each pulse number: for WT $I_{Na,P}$, 30 μmol/L 18β-GA at 4 Hz (A) (n=6) and 100 μmol/L lidocaine at 1, 2, and 4 Hz (B) (n=5); for ΔKPQ, 100 μmol/L 18β-GA of $I_{Na,P}$ (C) and $I_{Na,L}$ (D) at 4 Hz (n=6). ^bP<0.05, ^cP<0.01.

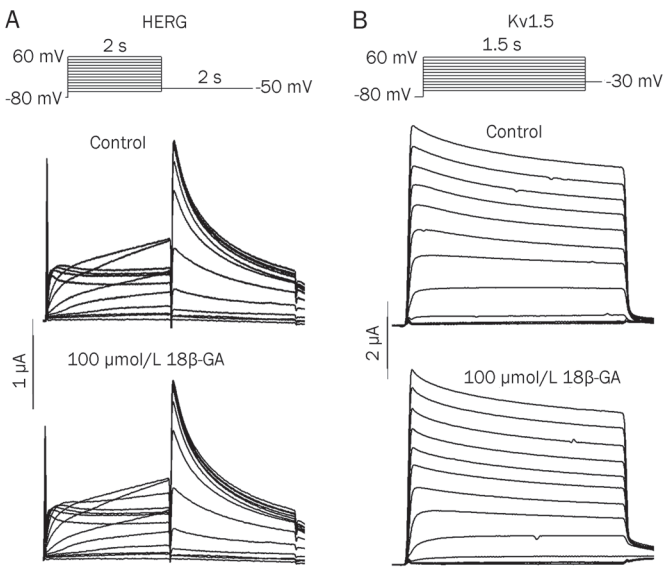

Figure 5. Effects of 18β-GA on HERG (A) and Kv1.5 potassium channels expressed in *Xenopus* oocytes. The voltage protocols are shown in the upper panels. 18β-GA at 100 μmol/L had no significant effects on HERG (n=6) or Kv1.5 channels (n=7).

μmol/L) on HERG was observed (data not shown).

Inhibition of $I_{Na,P}$ and $I_{Na,L}$ induced by ATX-II in human atrial myocytes after exposure to 18β-GA

Figure 6A shows superimposed typical recordings of $I_{Na,P}$ in the absence and presence of 30 μmol/L 18β-GA in freshly isolated human atrial myocytes. Figure 6B shows typical traces of $I_{Na,L}$ induced by ATX-II (30 nmol/L) and the effect of 18β-GA at 30 μmol/L. Currents were obtained with a depolarizing step to -20 mV from a holding potential of -80 mV. 18β-GA at 30 μmol/L blocked the $I_{Na,P}$ and $I_{Na,L}$ induced by ATX-II by approximately 47% and 87%, respectively (P<0.05, Figure 6C). These results confirmed the preferential blockage effects of 18β-GA on $I_{Na,L}$ produced by ΔKPQ Nav1.5 channels expressed in *Xenopus* oocytes.

Discussion

In the present study, we compared the electrophysiological effects of two stereoisomeric forms of glycyrretinic acid, 18α- and 18β-GA, on WT and ΔKPQ Nav1.5 channels expressed in *Xenopus* oocytes. The key findings were that 18β-GA inhibited both channels, while 18α-GA had no significant effects on

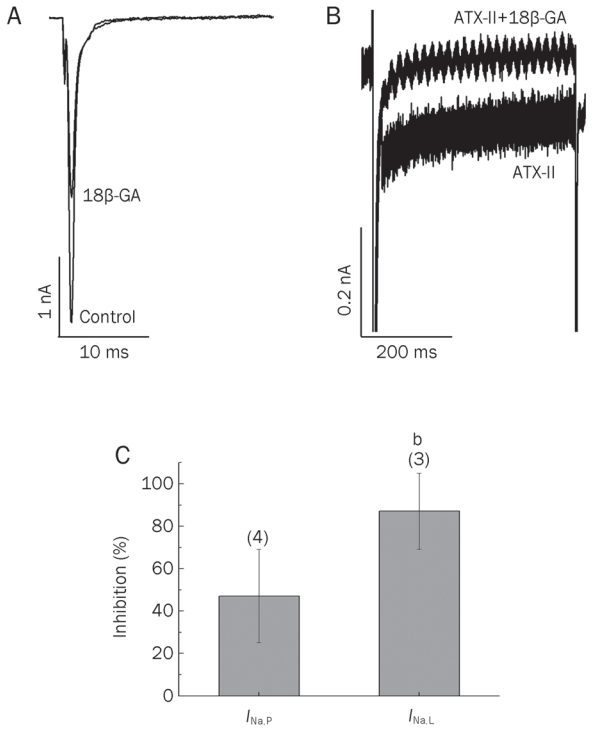

Figure 6. Effects of 18β-GA on $I_{Na,P}$ and $I_{Na,L}$ induced by ATX-II in isolated human atrial myocytes. (A) Original $I_{Na,P}$ recoding in control oocytes and in the presence of 30 μmol/L 18β-GA. Current was elicited by a depolarizing pulse from a holding potential of -80 mV to -30 mV for 100 ms. (B) Representative $I_{Na,L}$ induced by ATX-II (30 nmol/L) in the absence and in the presence of 30 μmol/L 18β-GA. Current was elicited by a depolarizing pulse from a holding potential of -80 mV to -30 mV for 500 ms. (C) The bar graph shows the percentage of inhibition of $I_{Na,P}$ and $I_{Na,L}$ induced by ATX-II mediated by 30 μmol/L 18β-GA. The numbers of cells are indicated in parentheses. $^bP<0.05$.

either WT or ΔKPQ channels. This is the first study to examine the effects of 18β-GA on WT and ΔKPQ Nav1.5 channels as well as HERG and Kv1.5 potassium channels. Our results suggest that 18β-GA preferentially blocks the $I_{Na,L}$ generated by ΔKPQ Nav1.5 channels in a concentration-dependent tonic manner without significant effects on either HERG or Kv1.5 potassium channels. The greater inhibition of 18β-GA on $I_{Na,L}$ induced by ATX-II was also observed in human atrial myocytes.

In this study, we compared the pharmacological effects of two stereoisomeric forms of GA (18α- and 18β-) on WT and ΔKPQ Nav1.5 channels. We observed that 18α-GA had no significant effects on either WT or ΔKPQ Nav1.5 channels, even at a very high concentration (100 μmol/L). 18β-GA, however, significantly inhibited both WT and ΔKPQ Nav1.5 channels. Our results demonstrated that 18β-GA but not 18α-GA blocked WT and ΔKPQ Nav1.5 channels. One possible explanation regarding the difference in blocking effects between the two stereoisomers is the stereochemical structure. Conformational analysis showed that in 18α-GA, the hydrogen atom of C18 is not in the same plane with the carboxyl chain of C30. In contrast, in 18β-GA, the hydrogen atom and the carboxyl chain are in the same plane. Consistent with our results, different potencies of 18α-GA and 18β-GA have been observed in other pharmacological contexts[22, 23]. For example, 18α-GA blocks voltage-gated potassium channels in vascular smooth muscle cells, while 18β-GA does not[24].

Our previous study showed that GA blocked the $I_{Na,P}$ mediated by the WT Nav1.5 channel (approximately 33% at 90 μmol/L) and the $I_{Na,L}$ mediated by the ΔKPQ Nav1.5 channel (IC_{50}=67±7.08 μmol/L)[13]. In this study, 18β-GA inhibited the $I_{Na,P}$ mediated by the WT Nav1.5 channel with an IC_{50} of 40 μmol/L and blocked $I_{Na,P}$ and $I_{Na,L}$ currents mediated by the ΔKPQ Nav1.5 channel at IC_{50} values of 100 μmol/L and 37 μmol/L, respectively. Therefore, 18β-GA was a more potent $I_{Na,P}$ and $I_{Na,L}$ blocker than GA; its potency to block $I_{Na,L}$ was approximately three-fold greater than its potency in blocking the $I_{Na,P}$ mediated by the ΔKPQ Nav1.5 channel.

Following tonic block, 30 depolarizing pulses were delivered to determine the extent of phasic block, the rate-dependent block, at different frequencies (1, 2, and 4 Hz). For the WT Nav1.5 channel, at 4 Hz, the $I_{Na,P}$ remaining at the 30th pulse was 94% of the 1st pulse in the presence of 30 μmol/L 18β-GA. In contrast to 18β-GA, lidocaine caused a much greater reduction at the 30th pulse *vs* the 1st pulse (~21%). This result implies that 18β-GA caused much less phasic block than lidocaine. Similar results were also found for the $I_{Na,P}$ and $I_{Na,L}$ currents of the ΔKPQ Nav1.5 channel. Our results suggest that 18β-GA caused a potent tonic block with little additional phasic block at WT and ΔKPQ Nav1.5 channels, which was different from the effect of lidocaine as well as the reported effects of mexiletine[25] and ranolazine[18].

Phasic block is a characteristic of most class I anti-arrythmic drugs[19], but it also accounts for the unfavorable lethal proarrythymias induced by these drugs[26]. 18β-GA, which exhibits less potent phasic block, may prevent excessive blockage of I_{Na} in the treatment of tachyarrhythmia and may reduce the frequency of bradycardia. We found that $I_{Na,L}$ exhibited a significant rate-dependent reduction similar to the observation reported by Guo *et al*[27], who suggested that the $I_{Na,L}$ mediated by the ΔKPQ Nav1.5 channel was more pronounced at low heart rates. This may explain the clinical findings that ventricular tachyarrythmias and sudden cardiac death in patients with LQT3 tend to occur during sleep or at rest, when the heart rate is slow[28]. Ranolazine has recently been used to treat LQT-3 patents expressing the ΔKPQ channel[29]. Ranolazine exhibits strong rate-dependent inhibition, as ranolazine produced less inhibition when $I_{Na,L}$ was more pronounced at a slower heart rate[18]. Unlike ranolazine[18], 18β-GA produced a potent tonic block of $I_{Na,L}$, which resulted in stronger anti-arrythmic effects. Recently, a more selective potent $I_{Na,L}$ blocker, F15845, also characterized by tonic blockade, has been demonstrated to be effective in preventing ischemia-induced arrhythmia[30].

HERG expresses I_{Kr}, and blockage of HERG is believed to cause LQT, which can induce EAD and a Torsades de-Pointes-type of ventricular arrhythmia, as observed after treatment

with class I or class III anti-arrhythmic drugs including ranolazine[9, 31, 32]. Kv1.5 conducts I_{Kur} in the human atria[9, 10]. This channel is also found in the ventricle, but its role remains unknown. 18β-GA at 100 μmol/L demonstrated no inhibition of HERG or Kv1.5 channels, which suggested that 18β-GA might not increase QT. However, further study is required to investigate the effects of 18β-GA on QT because other potassium currents, such as transient outward current (I_{to}), slow delayed rectifier current (I_{Ks}) and inward rectifier current (I_{K1}), also determine QT duration.

Up-regulated $I_{Na,L}$ has been demonstrated to be a major contributor to intracellular Na^+ accumulation during many pathological conditions, such as ischemia or hypoxia, leading to elevated levels of intracellular Ca^{2+} that have entered the cell through the reverse-mode Na^+–Ca^{2+} exchanger, which is followed by arrhythmogenesis and ultimately cell death. The inhibition of $I_{Na,L}$ and prevention of Na^+ overload may therefore be cardioprotective[3, 33–36]. 18β-GA preferentially blocks the $I_{Na,L}$ induced by ATX-II (mimicking $I_{Na,L}$ activation evoked by ischemia[36]) in isolated human atrial myocytes. Experiments on isolated human atrial myocytes confirmed the potency of 18β-GA to reduce $I_{Na,L}$ in a more physiological environment. Through blockade of $I_{Na,L}$, 18β-GA can alleviate $I_{Na,L}$-associated arrhythmias[37] and cardiac injury after myocardial ischemia[38].

In conclusion, our results show that 18β-GA but not 18α-GA preferentially blocks $I_{Na,L}$. 18β-GA had no significant effects on HERG or Kv1.5 channels. Our results suggest that 18β-GA has significant potential for development as a novel anti-arrhythmic agent, particularly in $I_{Na,L}$-associated arrhythmias and myocardial ischemia. Care should be taken in applying the results from heterologous expression studies to the clinical management of patients. Temperature, lipid environment, subunit composition and additional post-translational modifications of Na^+ channels in cardiomyocytes may also affect the degree of blockade by 18β-GA. Nonetheless, further evaluation of the therapeutic potential of 18β-GA is warranted.

Acknowledgements

This work was supported by the National Natural Science Foundation of China (No 30971243, 81170164 to Dr Yi-mei DU, No 30872542 to Dr Jia-hong XIA) and the Open Foundation of Hubei Key Laboratory of Biological Targeted Therapy No 2010-79 to Dr Cheng-kun XIA.

We thank Drs Thomas ZIMMER (Friedrich Schiller University, Germany), Michael C SANGUINETTI (University of Utah, USA) and Maria L GARCIA (Merck & Co, Inc, USA) for generously providing the cDNA plasmid vector.

Author contribution

Jia-hong XIA, Ming LEI, and Yi-mei DU designed the research program; Yi-mei DU, Cheng-kun XIA, Ning ZHAO, and Qian DONG performed the research; Yi-mei DU, Cheng-kun XIA, Ming LEI, and Jia-hong XIA analyzed the data and drafted the article.

Supplementary information

Supplementary figure is available at the Acta Pharmacologica Sinica website.

References

1 Noble D, Noble PJ. Late sodium current in the pathophysiology of cardiovascular disease: consequences of sodium-calcium overload. Heart 2006; 92: v1–v5.
2 Hale SL, Shryock JC, Belardinelli L, Sweeney M, Kloner RA. Late sodium current inhibition as a new cardioprotective approach. J Mol Cell Cardiol 2008; 44: 954–67.
3 Morita N, Lee JH, Xie Y, Sovari A, Qu Z, Weiss J N, *et al*. Suppression of re-entrant and multifocal ventricular fibrillation by the late sodium current blocker ranolazine. J Am Coll Cardiol 2011; 57: 366–75.
4 Shryock JC, Belardinelli L. Inhibition of late sodium current to reduce electrical and mechanical dysfunction of ischaemic myocardium. Br J Pharmacol 2008; 153: 1128–32.
5 Antzelevitch C, Burashnikov A, Sicouri S, Belardinelli L. Electrophysiologic basis for the antiarrhythmic actions of ranolazine. Heart Rhythm 2011; 8: 1281–90.
6 Jacobshagen C, Belardinelli L, Hasenfuss G, Maier LS. Ranolazine for the treatment of heart failure with preserved ejection fraction: background, aims, and design of the RALI-DHF study. Clin Cardiol 2011; 34: 426–32.
7 Conti CR. Ion channel therapy of ischemic heart disease: from calcium channel blockers to late sodium current inhibition. Clin Cardiol 2011; 34: 66–7.
8 Witchel HJ. Drug-induced hERG block and long QT syndrome. Cardiovasc Ther 2011; 29: 251–9.
9 Nerbonne JM. Molecular basis of functional voltage-gated K^+ channel diversity in the mammalian myocardium. J Physiol 2000; 525: 285–98.
10 Fedida D, Wible B, Wang Z, Fermini B, Faust F, Nattel S, *et al*. Identity of a novel delayed rectifier current from human heart with a cloned K^+ channel current. Circ Res 1993; 73: 210–6.
11 Nielsen NH, Winkel BG, Kanters JK, Schmitt N, Hofman-Bang J, Jensen HS, *et al*. Mutations in the Kv1.5 channel gene KCNA5 in cardiac arrest patients. Biochem Biophys Res Commun 2007; 354: 776–82.
12 Fiore C, Eisenhut M, Ragazzi E, Zanchin G, Armanini D. A history of the therapeutic use of liquorice in Europe. J Ethnopharmacol 2005; 99: 317–24.
13 Du Y, Zhang S, Wu H, Zou A, Lei M, Cheng L, *et al*. Glycyrretinic acid blocks cardiac sodium channels expressed in *Xenopus* oocytes. J Ethnopharmacol 2009; 125: 318–23.
14 Wang ZY, Agarwal R, Zhou ZC, Bickers DR, Mukhtar H. Inhibition of mutagenicity in *Salmonella typhimurium* and skin tumor initiating and tumor promoting activities in SENCAR mice by glycyrrhetinic acid: comparison of 18 alpha- and 18 beta-stereoisomers. Carcinogenesis 1991; 12: 187–92.
15 Du YM, Zhang XX, Tu DN, Zhao N, Liu YJ, Xiao H, *et al*. Molecular determinants of Kv1.5 channel block by diphenyl phosphine oxide-1. J Mol Cell Cardiol 2010; 48: 1111–20.
16 Tu DN, Liao YH, Zou AR, Du YM, Run Q, Wang XP, *et al*. Electropharmacological properties of telmisartan in blocking hKv1.5 and HERG potassium channels expressed on *Xenopus* laevis oocytes. Acta Pharmacol Sin 2008; 29: 913–22.
17 Xiao H, Wang M, Du Y, Yuan J, Zhao G, Tu D, *et al*. Agonist-like autoantibodies against calcium channel in patients with dilated cardiomyopathy. Heart Vessels 2011. doi: 10.1007/s00380-011-0176-7.
18 Rajamani S, El-Bizri N, Shryock JC, Makielski JC, Belardinelli L. Use-

dependent block of cardiac late Na^+ current by ranolazine. Heart Rhythm 2009; 6: 1625–31.
19 Sheets MF, Fozzard HA, Lipkind GM, Hanck DA. Sodium channel molecular conformations and antiarrhythmic drug affinity. Trends Cardiovasc Med 2010; 20: 16–21.
20 Gintant GA, Hoffman BF. Use-dependent block of cardiac sodium channels by quaternary derivatives of lidocaine. Pflugers Arch 1984; 400: 121–9.
21 Fan XR, Ma JH, Zhang PH, Xing JL. Blocking effect of methylflavonolamine on human $Na_V1.5$ channels expressed in *Xenopus* laevis oocytes and on sodium currents in rabbit ventricular myocytes. Acta Pharmacol Sin 2010; 31: 297–306.
22 Chintharlapalli S, Papineni S, Jutooru I, Mcalees A, Safe S. Structure-dependent activity of glycyrrhetinic acid derivatives as peroxisome proliferator-activated receptor {gamma} agonists in colon cancer cells. Mol Cancer Ther 2007; 6: 1588–98.
23 Zani F, Cuzzoni MT, Daglia M, Benvenuti S, Vampa G, Mazza P. Inhibition of mutagenicity in *Salmonella typhimurium* by *Glycyrrhiza glabra* extract, glycyrrhizinic acid, 18 alpha- and 18 beta-glycyrrhetinic acids. Planta Med 1993; 59: 502–7.
24 Guan BC, Si JQ, Jiang ZG. Blockade of gap junction coupling by glycyrrhetinic acids in guinea pig cochlear artery: a whole-cell voltage- and current-clamp study. Br J Pharmacol 2007; 151: 1049–60.
25 Wang DW, Yazawa K, Makita N Jr, George AL, Bennett PB. Pharmacological targeting of long QT mutant sodium channels. J Clin Invest 1997; 99: 1714–20.
26 Mestre M, Djellas Y, Carriot T, Cavero I. Frequency-independent blockade of cardiac Na^+ channels by riluzole: comparison with established anticonvulsants and class I anti-arrhythmics. Fundam Clin Pharmacol 2000; 14: 107–17.
27 Guo D, Lian J, Liu T, Cox R, Margulies KB, Kowey PR, *et al*. Contribution of late sodium current (I_{Na-L}) to rate adaptation of ventricular repolarization and reverse use-dependence of QT-prolonging agents. Heart Rhythm 2011; 8: 762–9.
28 Schwartz PJ, Priori SG, Spazzolini C, Moss AJ, Vincent GM, Napolitano C, *et al*. Genotype-phenotype correlation in the long-QT syndrome: gene-specific triggers for life-threatening arrhythmias. Circulation 2001; 103: 89–95.
29 Moss AJ, Zareba W, Schwarz KQ, Rosero S, Mcnitt S, Robinson JL. Ranolazine shortens repolarization in patients with sustained inward sodium current due to type-3 long-QT syndrome. J Cardiovasc Electrophysiol 2008; 19: 1289–93.
30 Pignier C, Rougier JS, Vie B, Culie C, Verscheure Y, Vacher B, *et al*. Selective inhibition of persistent sodium current by F 15845 prevents ischaemia-induced arrhythmias. Br J Pharmacol 2010; 161: 79–91.
31 Sanguinetti MC, Jiang C, Curran ME, Keating MT. A mechanistic link between an inherited and an acquired cardiac arrhythmia: HERG encodes the I_{Kr} potassium channel. Cell 1995; 81: 299–307.
32 Rajamani S, Shryock JC, Belardinelli L. Rapid kinetic interactions of ranolazine with HERG K^+ current. J Cardiovasc Pharmacol 2008; 51: 581–9.
33 Lindegger N, Hagen BM, Marks AR, Lederer WJ, Kass RS. Diastolic transient inward current in long QT syndrome type 3 is caused by Ca^{2+} overload and inhibited by ranolazine. J Mol Cell Cardiol 2009; 47: 326–34.
34 Vacher B, Pignier C, Letienne R, Verscheure Y, Le Grand B. F 15845 inhibits persistent sodium current in the heart and prevents angina in animal models. Br J Pharmacol 2009; 156: 214–25.
35 Wu L, Ma J, Li H, Wang C, Grandi E, Zhang P, *et al*. Late sodium current contributes to the reverse rate-dependent effect of I_{Kr} inhibition on ventricular repolarization. Circulation 2011; 123: 1713–20.
36 Belardinelli L, Shryock J C, Fraser H. Inhibition of the late sodium current as a potential cardioprotective principle: effects of the late sodium current inhibitor ranolazine. Heart 2006; 92: v6–v14.
37 Chen R, Yuan C. Experimental anti-arrhythmic effects of zhigancao (prepared licorice) injection. Zhongguo Zhong Yao Za Zhi 1991; 16: 617–9. Chinese.
38 Miura T, Ohnuma Y, Kuno A, Tanno M, Ichikawa Y, Nakamura Y, *et al*. Protective role of gap junctions in preconditioning against myocardial infarction. Am J Physiol Heart Circ Physiol 2004; 286: H214–21.

Acta Pharmacologica Sinica (2012) 33: 761–766

www.nature.com/aps

Original Article

Combined administration of anisodamine and neostigmine produces anti-shock effects: involvement of α7 nicotinic acetylcholine receptors

Li SUN[#], Gu-fang ZHANG[#], Xin ZHANG, Qing LIU, Jian-guo LIU, Ding-feng SU[*], Chong LIU[*]

Department of Pharmacology, Second Military Medical University, Shanghai 200433, China

Aim: To evaluate the anti-effects of anisodamine and neostigmine in animal models of endotoxic and hemorrhagic shock.
Methods: Kunming mice were injected with lipopolysaccharide (LPS 30 mg/kg, ip) to induce endotoxic shock. Anisodamine (12.5, 25, and 50 mg/kg, ip) and neostigmine (12.5, 25, and 50 μg/kg, ip) were administered immediately after LPS injection. Survival rate was monitored, and the serum levels of TNF-α and IL-1β were analyzed using ELISA assays. The effects of anisodamine and neostigmine were also examined in α7 nicotinic acetylcholine receptor (α7 nAChR) knockout mice with endotoxic shock and in Beagle dogs with hemorrhagic shock.
Results: In mice with experimental endotoxemia, combined administration of anisodamine and neostigmine significantly increased the survival rate and decreased the serum levels of inflammatory cytokines, as compared to those produced by either drug alone. The anti-shock effect of combined anisodamine and neostigmine was abolished in α7 nAChR knockout mice. On the other hand, intravenous injection of the combined anisodamine and neostigmine, or the selective α7 nAChR agonist PNU282987 exerted similar anti-shock effects in dogs with hemorrhagic shock.
Conclusion: The results demonstrate that combined administration of anisodamine and neostigmine produces significant anti-shock effects, which involves activation of α7 nAChRs.

Keywords: anisodamine; neostigmine; PNU282987; α7 nicotinic acetylcholine receptor; endotoxic shock; hemorrhagic shock

Acta Pharmacologica Sinica (2012) 33: 761–766; doi: 10.1038/aps.2012.26; published online 14 May 2012

Introduction

Anisodamine (6-[s]hydroxyhyoscyamine) is a naturally occurring tropane alkaloid found in some plants within the Solanaceae family[1]. It is an anticholinergic drug that does not cross into the central nervous system and is widely used clinically in China for various types of shock, especially septic shock[2, 3]. The mechanisms of anisodamine's beneficial effects on septic shock are mainly attributed to its amelioration of blood flow in the microcirculation. However, the molecular mechanisms of these effects remain unclear[4, 5]. Recently, a study conducted in this laboratory demonstrated that the anti-shock effects of anisodamine occur mainly via activation of the α7 nicotinic acetylcholine receptor (α7nAChR)[6].

The central nervous system regulates the production of proinflammatory cytokines through the efferent vagus nerve, termed the "cholinergic anti-inflammatory pathway"[7, 8]. Acetylcholine, the principal neurotransmitter of the vagus nerve, inhibits the production of proinflammatory cytokines from endotoxin-stimulated macrophages through the α7nAChR[9–11]. Studies have shown that activation of the α7nAChR-dependent cholinergic anti-inflammatory pathway can control the production of proinflammatory cytokines in experimental models of endotoxic shock and hemorrhagic shock[12, 13]. Our previous studies have shown that anisodamine blocks muscarinic receptors and promotes increased endogenous acetylcholine binding to the α7nAChR[6].

To produce therapeutic effects, a very large dose of anisodamine must be administered. Neostigmine is a cholinesterase inhibitor that increases endogenous acetylcholine. It is reasonable to speculate that combining anisodamine and neostigmine could augment anti-shock efficacy through activation of the α7nAChR-dependent cholinergic anti-inflammatory pathway. In addition, the side effects of neostigmine may be antagonized by blocking muscarinic receptors. To test this

# These two authors contributed equally to this work.
* To whom correspondence should be addressed.
E-mail wanlc2004@yahoo.com.cn (Chong LIU);
dfsu2008@gmail.com (Ding-feng SU)
Received 2011-12-19 Accepted 2012-02-29

hypothesis, we carried out a series of experiments in a murine endotoxic shock model and a dog hemorrhagic shock model.

Materials and methods

Animals and agents

Kunming mice (22–28 g) and Beagle dogs (8–10 kg) were purchased from Sino-British SIPPR/BK Laboratory Animal Ltd (Shanghai, China). Mice deficient in the α7nAChR were purchased from Jackson Laboratory (B6.129S7-Chrna7tm1Bay, Stock Number: 003232, Bar Harbor, MA, USA). All animals were maintained at 22 °C under a 12/12-h light/dark cycle and had free access to water and a standard diet. All experimental procedures were approved by the local ethics committee.

Anisodamine hydrochloride was obtained from Fu-Ma Chemical and Engineering Company (Hangzhou, China). Neostigmine methylsulphate was obtained from San-Wei Pharmaceutical Company (Shanghai, China). LPS was purchased from Sigma (*Escherichia coli*, 0111:B4, St Louis, MO, USA).

Hemorrhagic shock model

Hemorrhagic shock was induced according to a protocol by Bruegger and colleagues[14]. Briefly, animals were anesthetized with sodium pentobarbital (30 mg/kg, iv), and an endotracheal tube was inserted to maintain normocapnia. A 16-gauge Teflon arterial catheter was inserted into the femoral artery for bloodletting to induce hemorrhagic shock and to measure mean arterial blood (MAP). A polyethylene tube was placed into the femoral vein for drug delivery. After completing the surgical preparation, a 30-min stabilization period began. Subsequently, hemorrhagic shock was initiated by stepwise withdrawal of blood from the femoral artery. MAP was reduced to 45 mmHg within 15 min. This blood pressure was maintained for 30 min by re-infusing heparinized blood with an automated device. Sham hemorrhagic-shock dogs underwent all surgical procedures without bleeding.

Effects of combining anisodamine/neostigmine on survival rate in LPS-induced shock mice

Mice received 30 mg/kg LPS (ip), followed by saline, anisodamine (12.5–50 mg/kg, ip, n=20 per group), neostigmine (12.5–50 μg/kg, ip, n=20 per group) or a combination of anisodamine and neostigmine (n=20 per group). In another set of experiments, the mice were challenged with LPS (30 mg/kg, ip), followed by saline or anisodamine/neostigmine combined (25 mg/kg and 25 μg/kg, ip, n=20 per group) at 0, 3, and 6 h. Survival rate was monitored for 72 h. During the observation period, the animals were maintained at 22 °C on a 12-h light/dark cycle and had free access to water and a standard diet.

Effects of combining anisodamine/neostigmine on serum cytokines in LPS-induced shock mice

Blood was collected 90 min after the LPS challenge for the TNF-α assay and at 4 h after LPS for the IL-1β assay. Serum TNF-α/IL-1β levels were determined using standard ELISA assays (R&D Systems, Minneapolis, MN, USA).

Effects of combining anisodamine/neostigmine on survival rate in α7nAChR knockout mice challenged with LPS

The genotypes of the animals were confirmed by polymerase chain reaction (PCR) according to a protocol by Jackson Laboratory (Figure 1). α7nAChR knockout mice or wild-type controls (10 weeks of age) received LPS (20 mg/kg, ip), followed by saline or anisodamine/neostigmine combined (25 mg/kg and 25 μg/kg, ip, n=15). Survival rate was monitored for 72 h.

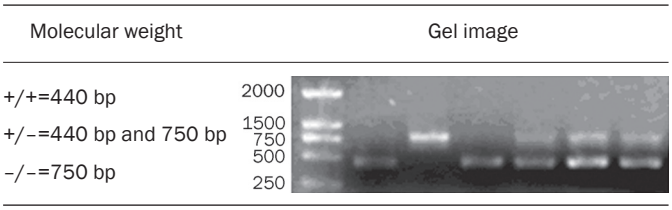

Figure 1. PCR results of the α7nAChR knockout mice and wild-type mice.

Effects of combining anisodamine/neostigmine on serum TNF-α in hemorrhagic shock dogs

Beagle dogs were subjected to hemorrhagic shock and then received saline, anisodamine (2.63 mg/kg, iv) plus neostigmine (5.25 μg/kg, iv), or PNU282987 (a selective α7nAChR agonist, 3.37 mg/kg, iv) (n=6). A separate group of dogs (n=6) receiving sham operations were also included for comparison. Blood was collected 20 min after the drug treatment for the TNF-α assay.

Effects of combining anisodamine/neostigmine on hepatic injury in hemorrhagic shock dogs

Liver tissue specimens were collected at the end of Experiment 4, rinsed with saline, fixed in 4% paraformaldehyde for 24 h, and embedded in paraffin. Tissue sections (2 μm) were stained with hematoxylin and eosin (H&E) using a routine protocol, and examined under a light microscope[15].

Effects of combining anisodamine/neostigmine on hemodynamics and survival rate in hemorrhagic shock dogs

Beagle dogs were subjected to hemorrhagic shock and then received saline, anisodamine (2.63 mg/kg, iv) plus neostigmine (5.25 μg/kg, iv), or PNU282987 (3.37 mg/kg, iv) (n=6). A separate group of dogs (n=6) receiving sham operations were also included for comparison. Blood pressure was monitored for 60 min following drug treatment in hemorrhagic dogs. Survival rate was monitored for 2 h. MAP was only calculated over the first 60 min since death started to occur at 60 min.

Statistical analysis

Data involving two groups were analyzed with Student's t-tests. For experiments involving more than two groups, the

data were analyzed with a one-way ANOVA, followed by the Dunnett's *t*-test for multiple comparisons. Serial data of MAP were analyzed with a repeated measures ANOVA. Survival rate was examined using the Kaplan-Meier analysis followed by a Cox regression test. All of the data are expressed as the mean±SD. Statistical significance was set at $P<0.05$.

Results

Effects of combining anisodamine/neostigmine on survival rate in LPS-induced shock mice

In response to a lethal dose of LPS, all mice displayed decreased activity, piloerection, periocular discharge, and diarrhea. The survival rate at 72 h was 23%. Anisodamine (12.5, 25, and 50 mg/kg) increased the survival rate to 56%, 64%, 56%, respectively. Neostigmine (12.5, 25, and 50 μg/kg) increased the survival rate to 52%, 64%, and 72%, respectively. Combining anisodamine/neostigmine (12.5 mg/kg and 25 μg/kg) increased the survival rate to 83%. An increased dose of the combined treatment (25 mg/kg and 25 μg/kg) increased the survival rate to 92% (Table 1 and Figure 2). When given 3 and 6 h after LPS exposure, the combined treatment (25 mg/kg and 25 μg/kg) increased the survival rate to 78% and 82% (Figure 3). When treatment was delayed for 12 h, no significant reduction in mortality was achieved (data not shown).

Table 1. Effects of anisodamine and neostigmine on survival rate in LPS-induced endotoxic shock mice. Mice were injected with LPS (30 mg/kg, ip), followed by saline, anisodamine (12.5, 25, and 50 mg/kg, ip), neostigmine (12.5, 25, and 50 μg/kg, ip), or a combination of anisodamine and neostigmine. Survival rate was monitored for the ensuing 72 h. *n*=20 per group.

Neo (μg/kg)	Ani (mg/kg)			
	0	12.5	25	50
0	23%	56%	64%	56%
12.5	52%	56%	76%	52%
25	64%	83%	92%	56%
50	72%	67%	72%	68%

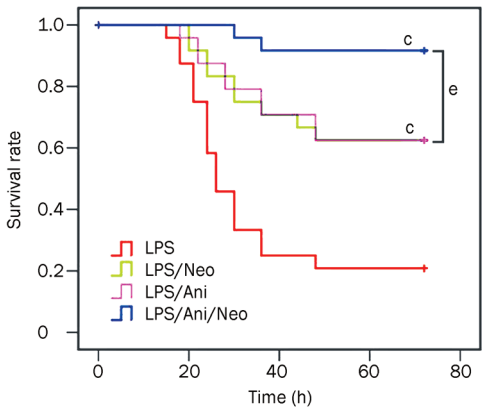

Figure 2. Effects of combining anisodamine and neostigmine on survival rate in LPS-induced endotoxic shock mice. Mice received LPS (30 mg/kg, ip), followed by vehicle, anisodamine (25 mg/kg, ip), neostigmine (25 μg/kg, ip), or a combination of anisodamine (25 mg/kg, ip) and neostigmine (25 μg/kg, ip). *n*=20 per group. $^{c}P<0.01$ *vs* LPS; $^{e}P<0.05$ *vs* Ani or Neo.

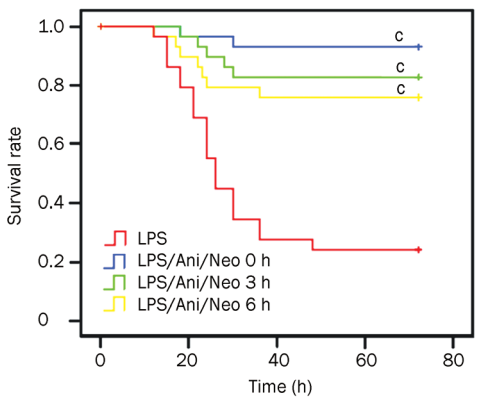

Figure 3. Therapeutic window for combining anisodamine and neostigmine in LPS-induced shock mice. Mice were injected with LPS (30 mg/kg, ip), followed by saline or a combination of anisodamine (25 mg/kg, ip) and neostigmine (25 μg/kg, ip) at 0, 3, and 6 h after LPS. Survival rate was monitored for the ensuing 72 h. *n*=20 per group. $^{c}P<0.01$ *vs* LPS.

Effects of combining anisodamine/neostigmine on serum cytokine in LPS-induced shock mice

Both anisodamine and neostigmine significantly decreased serum TNF-α and IL-1β in LPS-induced shock mice ($P<0.05$ *vs* saline control; Figure 4). A combination of anisodamine and neostigmine (25 mg/kg and 25 μg/kg) further decreased serum TNF-α and IL-1β ($P<0.05$ *vs* anisodamine or neostigmine alone; Figure 4).

Effects of combining anisodamine/neostigmine on survival rate in α7nAChR knockout mice challenged with LPS

In wild-type mice, anisodamine/neostigmine combination (25 mg/kg and 25 μg/kg) significantly increased the survival rate (90% *vs* 42%, $P<0.01$, Figure 5A). In α7nAChR knockout mice, the combined treatment (25 mg/kg and 25 μg/kg) did not improve survival rate (38.5% *vs* 15.4%, $P>0.05$, Figure 5B).

Effects of combining anisodamine/neostigmine on serum TNF-α in hemorrhagic shock dogs

Hemorrhagic shock induced a significant increase of serum TNF-α ($P<0.01$ *vs* sham control). Anisodamine/neostigmine combination significantly decreased serum TNF-α in hemorrhagic shock dogs ($P<0.01$ *vs* saline control). PNU282987, a selective α7nAChR agonist, also decreased serum TNF-α (Figure 6).

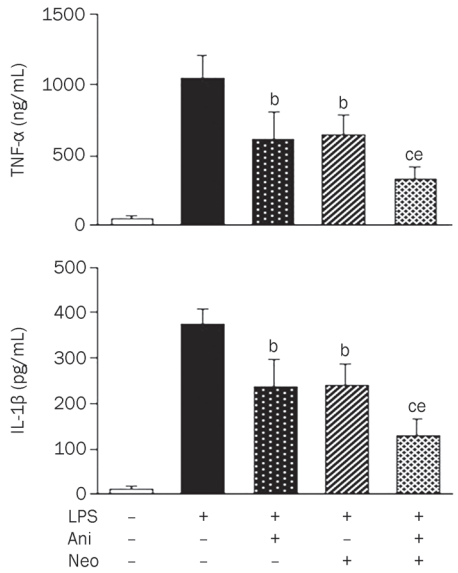

Figure 4. Effects of combining anisodamine and neostigmine on inflammatory cytokines in serum in LPS-induced shock mice. Mice received LPS (30 mg/kg, ip), followed by saline, anisodamine (25 mg/kg, ip), neostigmine (25 μg/kg, ip), or a combination of anisodamine (25 mg/kg, ip) and neostigmine (25 μg/kg, ip). Blood samples were obtained 90 min later for the TNF-α assay, and 4 h later for the IL-1β assay. n=8 per group. ^{b}P<0.05, ^{c}P<0.01 *vs* LPS; ^{e}P<0.05 *vs* Ani or Neo.

Effects of combining anisodamine/neostigmine on hepatic injury in hemorrhagic shock dogs

Hemorrhagic shock induced significant hepatic damage, *eg*, widened portal areas, thin fibrous septa, and inflammatory cell infiltration (Figure 7B *vs* Figure 7A in sham control). It induced bridging or septal fibrosis, connecting portal areas and central veins in a portal-to-portal, portal-to-central, and/or central-to-central pattern. Collagen fibers were clearly visible in the septa. Anisodamine/neostigmine combined ameliorated the damage induced by hemorrhagic shock, decreasing infiltration by inflammatory cells, and putrescence of hepatic cells (Figure 7C). PNU282987 also attenuated the hepatic injury induced by hemorrhagic shock (Figure 7D).

Effects of combining anisodamine/neostigmine on hemodynamics and survival rate in hemorrhagic shock dogs

The combination of anisodamine and neostigmine significantly increased MAP and prolonged survival rate induced by hemorrhagic shock. PNU282987 also increased MAP and survival rate (Figure 8).

Discussion

The results from the current study demonstrate that the combined use of anisodamine and neostigmine is more effective than either drug alone on controlling inflammation and increased survival rate in LPS-induced shock mice. Remarkably, such treatment was effective even when given 3–6 h after LPS exposure. The combined treatment also alleviated hemorrhagic shock.

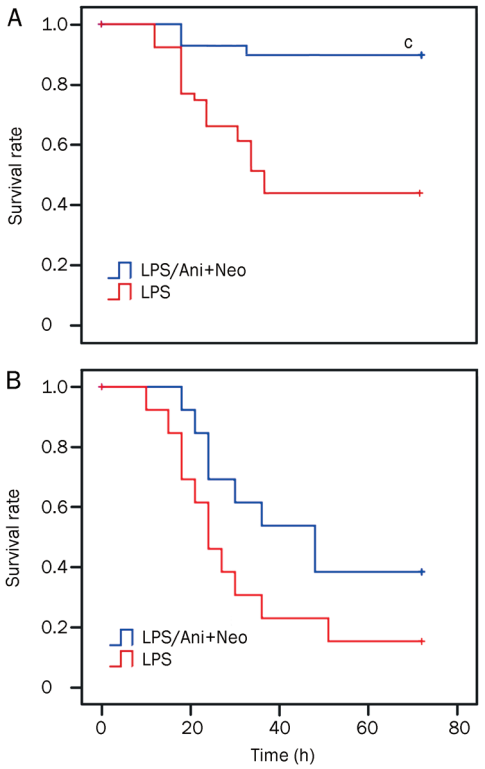

Figure 5. Effects of combining anisodamine and neostigmine on survival rate in α7nAChR knockout mice challenged with LPS. α7nAChR knockout mice (B) or wild-type mice (A) received LPS (20 mg/kg, ip), followed by saline or a combination of anisodamine (25 mg/kg, ip) and neostigmine (25 μg/kg, ip). Survival rate was monitored for the ensuing 72 h. n=15 per group. ^{c}P<0.01 *vs* LPS.

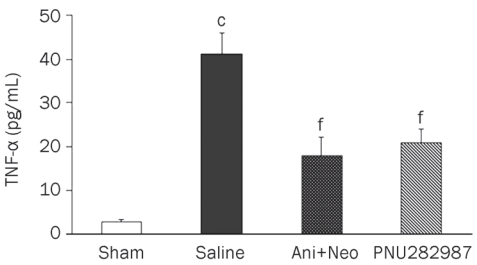

Figure 6. Effects of combining anisodamine and neostigmine on serum TNF-α in hemorrhagic shock dogs. Hemorrhagic shock was induced by gradient bloodletting until the mean arterial pressure was stabilized at 45 mmHg, followed by saline or a combination of anisodamine (2.63 mg/kg, iv) and neostigmine (5.25 μg/kg, iv) or PNU282987 (3.37 mg/kg, iv). Blood samples were collected 20 min after treatment. n=6 per group. ^{c}P<0.01 *vs* Sham; ^{f}P<0.01 vs Saline.

The cholinergic anti-inflammatory pathway has been increasingly implicated in inflammatory diseases, including endotoxic shock. Activation of this anti-inflammatory pathway can be achieved by the following: 1) direct stimulation of the vagus nerve[16, 17], 2) the use of nicotine or nicotinic agonists

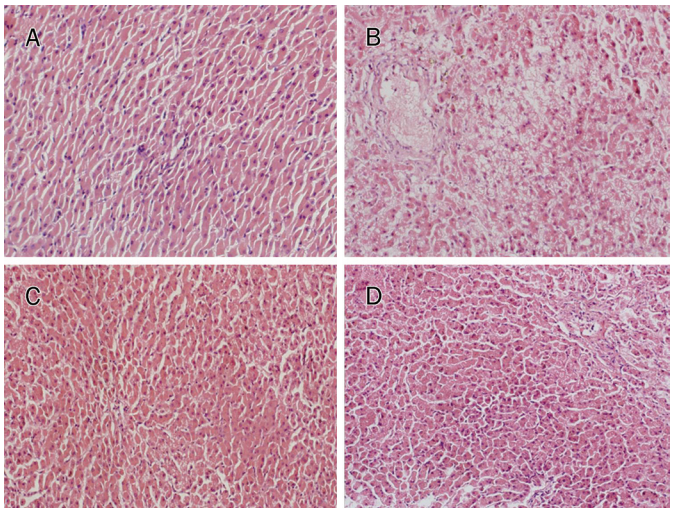

Figure 7. Effects of combining anisodamine and neostigmine on hepatic injury in hemorrhagic shock dogs. (A) Sham control. Light micrographs showing hepatic tissue appeared normal; (B) Hemorrhagic shock. The hemorrhagic shock operation resulted in widened portal areas, thin fibrous septa throughout the hepatic parenchyma, and inflammatory cell infiltration; (C) Anisodamine (2.63 mg/kg, iv) and neostigmine (5.25 μg/kg, iv) and (D) PNU282987 (3.37 mg/kg, iv). Both anisodamine/neostigmine combined and PNU282987 treatment produced less infiltration by inflammatory cells, and less putrescence of hepatic cells. *n*=6 per group. Magnification: 200× .

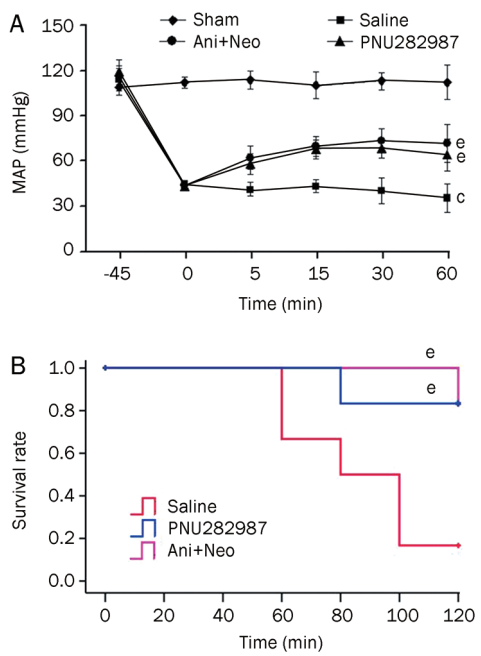

Figure 8. Effects of combined anisodamine and neostigmine on MAP and survival rate in hemorrhagic shock dogs. Hemorrhagic shock was induced by gradient bloodletting until the mean arterial pressure was stabilized at 45 mmHg, followed by saline or a combination of anisodamine (2.63 mg/kg, iv) and neostigmine (5.25 μg/kg, iv) or PNU282987 (3.37 mg/kg, iv). *n*=6 per group. (A) MAP was calculated over the first 60 min. $^{c}P<0.01$ *vs* Sham; $^{e}P<0.05$, $^{f}P<0.01$ *vs* Saline. (B) Survival rate was monitored for the ensuing 2 h. $^{e}P<0.05$ *vs* Saline.

(GTS-21, CAP55) to activate the α7nAChR[18–20], and 3) the use of cholinesterase inhibitors (physostigmine, galantamine)[21–23]. Our previous studies demonstrated that anisodamine could produce anti-inflammatory actions through indirectly activating the α7nAChR. Here, we examined the anti-shock effects of combining anisodamine/neostigmine and found that the combination of anisodamine and neostigmine could produce robust anti-shock effects even at small doses. Combining anisodamine/neostigmine significantly decreased serum TNF-α and IL-1β and improved the survival rate in LPS-induced shock mice. In α7nAChR knockout mice, the combined treatment did not improve the survival rate, suggesting that the beneficial effects of combining anisodamine/neostigmine on endotoxic shock is mediated primarily by the α7nAChR.

The initial presentation of endotoxic shock is often nonspecific, and its severity is concealed[24, 25]. Patients who arrive at the ICU with a seemingly benign infection can progress within hours to a devastating condition[26, 27]. A delay in the diagnosis and management of critically ill patients during the first six hours of ICU admission has been associated with higher mortality rates and increased utilization of hospital resources[28, 29]. Based on this finding, the concept of 'golden hours' is widely acknowledged[30, 31]. In the present study, we found that the combined treatment of anisodamine and neostigmine could significantly improve survival rate in animals, even 3–6 h after LPS exposure. This finding extends the window of treatment following LPS administration and may have clinical relevance. Inflammatory cytokines plays an important role in acute hypovolemic hemorrhagic shock because anti-TNF-α monoclonal antibodies could increase survival, improve hypotension, and attenuate impairment in vascular reactivity[32]. Recent studies have demonstrated that electrical stimulation of efferent vagal fibers could rapidly reverse hypotension, counteract hepatic NF-κB activation, reduce TNF-α plasma levels and improve survival rate in experimental hemorrhagic shock rats[13, 33]. Systemic administration of an acetylcholinesterase inhibitor also improves outcomes after hemorrhagic shock[22]. In our study, combining anisodamine and neostigmine markedly decreased serum TNF-α and prevented organ damage (as exemplified by the liver results presented here) induced by hemorrhagic shock. The combined treatment also improved hypotension and prolonged the survival rate in hemorrhagic shock dogs. PNU282987, a selective α7nAChR agonist, had similar effects, suggesting the involvement of the α7nAChR.

Several methods can be used to activate the cholinergic anti-inflammatory pathway. However, much work needs to be performed to successfully apply these methods in clinical practice. Anisodamine and neostigmine are both used in clinical practice. We believe that, if titrated properly and carefully, an anisodamine/neostigmine cocktail may be clinically useful.

In summary, this study demonstrated that combining anisodamine and neostigmine could increase the survival rate in a murine endotoxic shock model and a dog hemorrhagic shock model through activation of the cholinergic anti-inflammatory pathway. Our findings may have important implications toward the development of new treatment strategies for endo-

toxic shock, hemorrhagic shock and other inflammatory diseases.

Acknowledgements

This study was supported by the National Natural Science Foundation of China (30900529).

Author contribution

Li SUN, Gu-fang ZHANG, and Xin ZHANG performed the mouse experiments; Qing LIU and Jian-guo LIU performed the dog experiments; Ding-feng SU designed the research; Qing LIU and Chong LIU designed the research, analyzed the data and wrote the paper.

References

1 Poupko JM, Baskin SI, Moore E. The pharmacological properties of anisodamine. J Appl Toxicol 2007; 27: 116–21.
2 Wang ST, Kuo NL. Experience in emergency treatment of shock due to infection. Chin Med J 1978; 6: 497–500.
3 Xiu RJ. Studies on microcirculation in the Institute of Basic Medical Sciences, Chinese Academy of Medical Sciences. Microvasc Res 1980; 20: 371–3.
4 Varma DR, Yue TL. Adrenoceptor blocking properties of atropine-like agents anisodamine and anisodine on brain and cardiovascular tissues of rats. Br J Pharmacol 1986; 87: 587–94.
5 Zhang WW, Song MK, Cui YY, Wang H, Zhu L, Niu YY, *et al*. Differential neuropsychopharmacological influences of naturally occurring tropane alkaloids anisodamine versus scopolamine. Neurosci Lett 2008; 443: 241–5.
6 Liu C, Shen FM, Le YY, Kong Y, Liu X, Cai GJ, *et al*. Antishock effect of anisodamine involves a novel pathway for activating alpha7 nicotinic acetylcholine receptor. Crit Care Med 2009; 37: 634–41.
7 Borovikova LV, Ivanova S, Zhang M, Yang H, Botchkina GI, Watkins LR, *et al*. Vagus nerve stimulation attenuates the systemic inflammatory response to endotoxin. Nature 2000; 405: 458–62.
8 Wang H, Yu M, Ochani M, Amella CA, Tanovic M, Susarla S, *et al*. Nicotinic acetylcholine receptor alpha7 subunit is an essential regulator of inflammation. Nature 2003; 421: 384–8.
9 Tattevin P, Monnier D, Tribut O, Dulong J, Bescher N, Mourcin F, *et al*. Enhanced indoleamine 2,3-dioxygenase activity in patients with severe sepsis and septic shock. J Infect Dis 2010; 201: 956–66.
10 Lavoie PM, Huang Q, Jolette E, Whalen M, Nuyt AM, Audibert F, *et al*. Profound lack of interleukin (IL)-12/IL-23p40 in neonates born early in gestation is associated with an increased risk of sepsis. J Infect Dis 2010; 202: 1754–63.
11 Zhang XH, Lei H, Liu AJ, Zou YX, Shen FM, Su DF. Increased oxidative stress is responsible for severer cerebral infarction in stroke-prone spontaneously hypertensive rats. CNS Neurosci Ther 2011; 17: 590–8.
12 Wang H, Liao H, Ochani M, Justiniani M, Lin X, Yang L,*et al*. Cholinergic agonists inhibit HMGB1 release and improve survival in experimental sepsis. Nat Med 2004; 10: 1216–21.
13 Guarini S, Altavilla D, Cainazzo MM, Giuliani D, Bigiani A, Marini H, *et al*. Efferent vagal fiber stimulation blunts nuclear factor-kappa B activation and protects against hypovolemic hemorrhagic shock. Circulation 2003; 107: 1189– 94.
14 Bruegger D, Kemming GI, Jacob M, Meisner FG, Wojtczyk CJ, Packert KB, *et al*. Causes of metabolic acidosis in canine hemorrhagic shock: role of unmeasured ions. Crit Care 2007; 11: R130.
15 Liu C, Zhang GF, Song SW, Cai GJ, Liu WH, Miao CY, *et al*. Effects of ketanserin on endotoxic shock and baroreflex function in rodents. J Infect Dis 2011; 204: 1605–12.
16 Bernik TR, Friedman SG, Ochani M, DiRaimo R, Ulloa L, Yang H, *et al*. Pharmacological stimulation of the cholinergic antiinflammatory pathway. J Exp Med 2002; 195: 781–8.
17 Li M, Zheng C, Sato T, Kawada T, Sugimachi M, Sunagawa K. Vagal nerve stimulation markedly improves long-term survival after chronic heart failure in rats. Circulation 2004; 109: 120–4.
18 Pavlov VA, Ochani M, Yang LH, Gallowitsch-Puerta M, Ochani K, Lin X, *et al*. Selective alpha7-nicotinic acetylcholine receptor agonist GTS-21 improves survival in murine endotoxemia and severe sepsis. Crit Care Med 2007; 35: 1139–44.
19 Van Westerloo DJ, Giebelen IA, Florquin S, Bruno MJ, Larosa GJ, Ulloa L, *et al*. The vagus nerve and nicotinic receptors modulate experimental pancreatitis severity in mice. Gastroenterology 2006; 130: 1822–30.
20 Martin LF, Kem WR, Freedman R. Alpha-7 nicotinic receptor agonists: potential new candidates for the treatment of schizophrenia. Psychopharmacology 2004; 174: 54–64.
21 Hofer S, Eisenbach C, Lukic IK, Schneider L, Bode K, Brueckmann M, *et al*. Pharmacologic cholinesterase inhibition improves survival in experimental sepsis. Crit Care Med 2008; 36: 404–8.
22 Mathis KW, Sulzer J, Molina PE. Systemic administration of a centrally acting acetylcholinesterase inhibitor improves outcome from hemorrhagic shock during acute alcohol intoxication. Shock 2010; 34: 162–8.
23 Pavlov VA, Parrish WR, Rosas-Ballina M, Ochani M, Puerta M, Ochani K, *et al*. Brain acetylcholinesterase activity controls systemic cytokine levels through the cholinergic anti-inflammatory pathway. Brain Behav Immun 2009; 23: 41–5.
24 Dellinger RP, Carlet JM, Masur H, Gerlach H, Calandra T, Cohen J, *et al*. Surviving Sepsis Campaign guidelines for management of severe sepsis and septic shock. Crit Care Med 2004; 32: 858–72.
25 American college of chest physicians/society of critical care medicine consensus conference: definitions for sepsis and organ failure and guidelines for the use of innovative therapies in sepsis. Crit Care Med 1992; 20: 864–74.
26 Rivers EP, McIntyre L, Morro DC, Rivers KK. Early and innovative interventions for severe sepsis and septic shock: taking advantage of a window of opportunity. CMAJ 2005; 173: 1054–65.
27 Rivers E, Nguyen B, Havstad S, Ressler J, Muzzin A, Knoblich B, *et al*. Early goal-directed therapy in the treatment of severe sepsis and septic shock. N Engl J Med 2001; 345: 1368–77.
28 Lundberg JS, Perl TM, Wiblin T, Costigan MD, Dawson J, Nettleman MD, *et al*. Septic shock: an analysis of outcomes for patients with onset on hospital wards versus intensive care units. Crit Care Med 1998; 26: 1020–4.
29 Engoren M. The effect of prompt physician visits on intensive care unit mortality and cost. Crit Care Med 2005; 33: 727–32.
30 Blow O, Magliore L, Claridge JA, Butler K, Young JS. The golden hour and the silver day: detection and correction of occult hypoperfusion within 24 hours improves outcome from major trauma. J Trauma 1999; 47: 964–9.
31 Bledsoe BE. The Golden Hour: fact or fiction? Emerg Med Serv 2002; 31: 105.
32 Squadrito F, Altavilla D, Ioculano M, Calapai G, Zingarelli B, Saitta A, *et al*. Passive immunization with antibodies against tumor necrosis factor (TNF-α) protects from the lethality of splanchnic artery occlusion shock. Circ Shock 1992; 37: 236–44.
33 Guarini S, Cainazzo MM, Giuliani D, Mioni C, Altavilla D, Marini H, *et al*. Adrenocorticotropin reverses hemorrhagic shock in anesthetized rats through the rapid activation of a vagal anti-inflammatory pathway. Cardiovasc Res 2004; 63: 357–65.

Acta Pharmacologica Sinica (2012) 33: 767–774
 1671-4083/12 $32.00
www.nature.com/aps

Original Article

Biphasic regulation of P-glycoprotein function and expression by NO donors in Caco-2 cells

Ru DUAN, Nan HU, Hai-yan LIU, Jia LI, Hai-fang GUO, Can LIU, Li LIU*, Xiao-dong LIU*

Key Laboratory of Drug Metabolism and Pharmacokinetics, China Pharmaceutical University, Nanjing 210009, China

Aim: To investigate the effects of nitric oxide (NO) donors on the function and expression of P-glycoprotein (P-gp) in Caco-2 cells.
Methods: Caco-2 cells were exposed to NO donors for designated times. P-gp function and expression were assessed using Rhodamine123 uptake assay and Western blotting, respectively. Intracellular reactive oxygen species (iROS) and intracellular reactive nitrogen species (iRNS) levels were measured using ROS and RNS assay kits, respectively.
Results: Exposure of Caco-2 cells to 0.1 or 2 mmol/L of sodium nitroprusside (SNP) affected the function and expression of P-gp in concentration- and time-dependent manners. A short-term (4 h) exposure reduced P-gp function and expression accompanied with significantly increased levels of iROS and iRNS. In contrast, a long-term (24 h) exposure stimulated the P-gp function and expression. The stimulatory effects of 2 mmol/L SNP was less profound as compared to those caused by 0.1 mmol/L SNP. The other NO donors SIN-1 and SNAP showed similar effects. Neither the NO scavenger PTIO (2 mmol/L) nor soluble guanylate cyclase inhibitor ODQ (50 μmol/L) reversed the SNP-induced alteration of P-gp function. On the other hand, free radical scavengers ascorbate, glutathione and uric acid (2 mmol/L for each), PKC inhibitor chelerythrine (5 μmol/L), PI3K/Akt inhibitor wortmannin (1 μmol/L) and p38 MAPK inhibitor SB203580 (10 μmol/L) reversed the upregulation of P-gp function by the long-term exposure to SNP, but these agents had no effect on the impaired P-gp function following the short-term exposure to SNP.
Conclusion: NO donors time-dependently regulate P-gp function and expression in Caco-2 cells: short-term exposure impairs P-gp function and expression, whereas long-term exposure stimulates P-gp function and expression. The regulation occurs via a NO-independent mechanism.

Keywords: Caco-2 cells; P-glycoprotein; Rhodamine123 uptake; NO donors; NO; PKC; PI3K/Akt; p38 MAPK

Acta Pharmacologica Sinica (2012) 33: 767–774; doi: 10.1038/aps.2012.25; published online 30 Apr 2012

Introduction

P-glycoprotein (P-gp), an ATP-binding cassette (ABC) drug efflux transporter, is widely expressed in various tissues including brain, lungs, liver, kidney, gastrointestinal tract, skin and muscle tissue[1]. P-gp has a wide range of substrates, including anticancer agents, calcium channel blockers, antibiotics, cardiac glycosides and immunosuppressants[2]. Clinical reports have underlined the effect of changes in the functional activity of P-gp on the bioavailability and disposition of therapeutic agents[3].

Previous reports have indicated that the expression and function of P-gp are dysregulated under pathophysiological situations such as diabetes mellitus[4, 5], chronic renal failure[6] and inflammation[7]. It is becoming increasingly clear that nitric oxide and its related nitrogen species (NOx)[8] are crucial regulatory mediators of the function and expression of P-gp and other transporters under pathophysiological conditions[8-14]. NO-mediated nitrosative stress was reported to stimulate the function and expression of P-gp in the blood-brain barrier of streptozotocin-treated diabetic rats[8]. Activation of inductible nitric oxide synthase (iNOS) seemed to explain the increase in the expression and function of intestinal P-gp in interferon-γ-induced human intestinal cells, as evidenced by the fact that coadministration of the iNOS inhibitor L-N^6-(1-iminoethyl)-lysin abrogated the cytokine-mediated increase in P-gp expression and function[9]. LPS-induced upregulation of Abca1 and Abcb1/P-gp in the kidney occurred via alteration of NO production by iNOS; this induction may be attenuated by co-administration of the iNOS inhibitor aminoguanidine[14]. However, contradictory results were also reported. In HT29/HT29-dx cell cultures, nitric oxide production reversed resistance to the P-gp substrate doxorubicin, suggesting that NO decreased the activity of P-gp[10]. N^G-monomethyl-*L*-arginine,

* To whom correspondence should be addressed.
E-mail xdliu@cpu.edu.cn (Xiao-dong LIU);
liulee@cpu.edu.cn (Li LIU)
Received 2011-12-13 Accepted 2012-02-29

a NO synthase inhibitor, markedly blocked cyclosporin A-induced impairment of P-gp function in cocultures of MBEC and rat astrocytes[11]. NO was also reported to be involved in the decreased expression of intestinal P-gp in the early stages of intestinal ischemia and reperfusion[12]. Recently, Nawa *et al* reported that iNOS were involved in downregulation of intestinal P-gp expression in streptozotocin-treated diabetic mice[13]. Further studies, however, showed that iNOS regulated the activity of intestinal P-gp in a bidirectional way, inhibiting their effect at earlier stages of diabetes and intensifying their effect at later stages[15].

The aim of this study was to further investigate the effects of NO on intestinal P-gp activity using the Caco-2 cell model; the Caco-2 cell monolayers have tight junctions, microvilli and various types of enzymes and transporters, thereby resembling the intestinal epithelium. In addition, Caco-2 cells express high levels of P-gp and have been widely used for the study of P-gp function and intestinal absorption[16]. Three different types of NO donors, SNP, SIN-1, and SNAP[8, 17] were used as source of NO. The function of P-gp was assessed using uptake of Rhodamine123 (Rho123) by Caco-2 cells. P-gp protein levels were measured using Western blotting. Our preliminary study showed that the effects of NO on the function of P-gp in Caco-2 cells were dependent on both the exposure time and the concentration of NO donors.

Materials and methods

Materials

Rhodamine123 (Rho123), chelerythrine, wortmannin, SB203580, SNAP (*S*-nitroso-*N*-acetylpenicillamine), 3-morpholinosydnonimine (SIN-1), 2-phenyl-4,4,5,5-tetramethyl-imidazoline-l-oxyl-3-oxide (PTIO), reduced glutathione (GSH) and 1H-[1,2,4]oxadiazolol[4,3-a]quinoxalin-1-one (ODQ) were purchased from Sigma Chemical Co (St Louis, MO, USA). Sodium nitroprusside (SNP), uric acid and ascorbate were purchased from Sinopharm Chemical Reagent Co Ltd (Shanghai, China); reactive oxygen species (ROS) and reactive nitrogen species (RNS) assay kits were purchased from Beyotime Institute of Biotechnology (Nantong, China); anti-P-gp monoclonal antibody C219 was purchased from Calbiochem-Novabiochem (Seattle, WA, USA); Blueranger prestained protein molecular weight marker mix was purchased from Pierce (Rockford, IL, USA); and goat anti-mouse secondary antibodies conjugated with the appropriate horseradish peroxidase and polyclonal anti-β-actin antibodies were purchased from Boshide Biotech Co (Wuhan, China). All other reagents were commercially available and were of analytical grade.

Cell culture

Caco-2 cells were obtained from American Type Culture Collection (Manassas, VA, USA). The cells were maintained at 37 °C in a controlled atmosphere of 5% CO_2 and 90% relative humidity, using DMEM (high glucose) supplemented with 2.5 mmol/L *L*-glutamine, 100 U/L penicillin, 100 U/L streptomycin, 3.7 g/L $NaHCO_3$, 1% nonessential amino acids, and 10% fetal bovine serum (Gibco BRL Co Ltd, USA). The medium was changed every other day. When 80% confluent, the cultured Caco-2 cells were passaged and seeded in 24-well plastic plates (Costar, Cambridge, MA, USA). Cells were used when a significant fraction of the cell population exhibited a colonic phenotype. Cells were co-incubated with the tested agents at designated time periods, and the Rho123 uptake experiment was performed to assess the function of P-gp. The 3-(4,5-dimethyl-2-thiazolyl)-2,5-diphenyl-2H-tetrazolium bromide (MTT) assay showed that none of the tested agents in the study damaged the viability of the cells.

Caco-2 cells treated with NO donors

Krischel *et al*'s experiments using various doses of NO donors (from 0.01 to 5 mmol/L)[18] showed that the effect of low doses (lower than 0.1 mmol/L) was not obvious, whereas high doses (higher than 2 mmol/L) impaired cell viability. Therefore, 0.1 and 2 mmol/L were chosen as representative concentrations for the time-dependent research. Generally, the NO donor SNP was freshly prepared before use. The cultured Caco-2 cells were washed three times with serum-free medium. Then, the cells were incubated in the presence of 0.1 and 2 mmol/L SNP for 2, 4, 6, 8, 24, and 48 h. P-gp function was assessed by measuring the uptake of Rho123 by the cells.

Another experiment was also designed to further assess the changes of P-gp function in Caco-2 cells following 4-h and 24-h incubation times in the presence of several doses of SNP, SNAP and SIN-1. The concentration-dependent effects of SNP on P-gp function were further documented following a 24-h incubation.

Caco-2 cells co-treated with SNP and pharmacological inhibitors

The free radical scavengers ascorbate (antioxidant[8], 2 mmol/L), PTIO (NO scavenger[17], 2 mmol/L), GSH (active against nitrosative stress[17], 2 mmol/L) and uric acid (peroxynitrite scavenger[19], 2 mmol/L) as well as several signal pathway inhibitors: chelerythrine (a PKC inhibitor, 5 μmol/L), wortmannin (a PI3K/Akt inhibitor, 1 μmol/L), SB203580 (a p38 MAPK inhibitor, 10 μmol/L) and ODQ (a specific guanylate cyclase inhibitor, 50 μmol/L)[20, 21] were used to investigate whether these inhibitors reverse the alteration in P-gp function induced by SNP. Caco-2 cells were pretreated with a pharmacological inhibitor for 1 h, then either SNP or normal medium was added and incubated for 4 and 24 h, respectively[22]. The P-gp function in the cells was measured and compared among relevant groups.

Measurement of Rho123 uptake by Caco-2 cells

The P-gp function in cells was measured using the Rho123 uptake experiment. Uptake experiments were performed according to the method previously reported[23]. In brief, treated cells were washed and preincubated in pH 7.4 Hanks' balanced salt solution (HBSS) at 37 °C for 30 min, then 1 mL HBSS containing 100 ng/mL Rho123 was added to initiate the uptake of Rho123. After incubation for 2 h, the uptake was stopped by rinsing the cells three times with ice-cold HBSS,

and 0.5 mL of purified water was added to each incubated well. Cells were lysed by three freeze-thaw cycles, and the protein concentrations were measured using the Bradford method (1976)[24]. The sensitivity of Rho123 uptake as an indicator of P-gp activity was verified using the P-gp inhibitor cyclosporin A (0.625–2.5 μg/mL), which significantly increased the intracellular accumulation of Rho123.

The concentrations of Rho123 in cells were determined by HPLC[25]. The lowest limit of quantitation of Rho123 in cells was 0.002 ng/μg protein. The yields were higher than 85%. The relative standard derivations of intra day and inter day data were lower than 10%. The linear range of Rho123 in cells was 0.002–0.064 ng/μg protein.

Determination of the intracellular levels of ROS and RNS

The levels of intracellular ROS (iROS) and intracellular RNS (iRNS) were measured according to the manufacturer's instructions of the ROS and RNS assay kits. Briefly, Caco-2 cells were incubated with SNP for different times, then cells were rinsed three times with PBS buffer (including 1% BSA and 10 mmol/L HEPES) and treated with 2′,7′-dichlorofluorescin-diacetate (DCFH-DA, 10 μmol/L) and 4-amino-5-methylamino-2′,7′-difluorofluorescein (DAF-FM DA, 10 μmol/L) for 30 min, the intracellular DCFH was oxidized to DCF by ROS while the intracellular DAF-FM was nitrosated to DAF by RNS. Cells were washed 5 times with cold PBS. DCF was used as an indicator of ROS; it was detected with a fluorescence detector at an excitation wavelength of 488 nm and an emission wavelength of 525 nm. DAF was used as an indicator of RNS and was detected at an excitation wavelength of 495 nm and emission wavelength of 515 nm.

Western blotting analysis

Protein expression of P-gp in Caco-2 cells was assessed using Western blotting according to a previously described method[25, 26]. Briefly, following 4-h and 24-h exposures to SNP (0.1 and 2 mmol/L), the Caco-2 cells were lysed in ice-cold lysis buffer containing 10 mmol/L Tris-HCl (pH 7.5), 1 mmol/L EGTA, 1 mmol/L $MgCl_2$, 1 mmol/L mercaptoethanol, 1% glycerol, and a protease inhibitor cocktail containing 1 mmol/L dithiothreitol, and 2 mmol/L phenylmethylsulfonylfluoride (Sigma Chemical Co, Ltd, St Louis, MO, USA) for 30 min. The cells were then ultrasonicated five times for 10 s in an ice bath. Samples were then centrifuged at 500×*g* for 10 min at 4 °C. The supernatant was transferred to a new tube and centrifuged at 15000×*g* for 60 min at 4 °C. The supernatant (cytosolic proteins such as β-actin) and the pellet (membrane proteins such as P-gp) were both collected and stored at -80 °C until use. Protein concentrations were measured by the Bradford method. Samples were reconstituted in SDS-polyacrylamide gel electrophoresis sample loading buffer and were boiled for 5 min to denature the protein. The protein samples were separated on an 8% SDS-polyacrylamide gel and were transferred onto a polyvinylidene difluoride membrane (Millipore Corporation). After blotting, the membrane was blocked with 10% bovine serum albumin in Tris-buffered saline-Tween 20 (TBS-T) for 1 h at 37 °C. Immunoblots were incubated with the primary monoclonal antibody to P-gp (1:200; C219) or β-actin (1:800; Bioworld Technology, St Louis Park, MN, USA) for 24 h at 4 °C. The membrane was washed (10 min×4), incubated with the secondary antibody, horseradish peroxidase-conjugated goat anti-mouse IgG (1:800; Boster Biological Technology, Wuhan, China) for 1 h at 37 °C and then washed three times with TBS-T. The signals were detected using an enhanced chemiluminescence kit (Pierce Chemical). The P-gp protein band intensity was normalized to that of β-actin.

Statistical analysis

Results were expressed as the mean±standard deviation (SD). The overall differences between groups were determined by one-way of analysis of variance (ANOVA). If analysis indicated significance, the differences between groups were estimated using the Student-Newman-Keuls multiple comparison *post-hoc* test. *P* values of less than 0.05 indicated a significant difference.

Results

Alteration in P-gp function and expression induced by NO donors

Caco-2 cells were incubated with two concentrations (0.1 and 2 mmol/L) of SNP for designated time periods (2, 4, 6, 8, 24, and 48 h), and Rho123 uptake by the cells was measured (Figure 1). The results demonstrated that the effect of SNP on Rho123 uptake was dependent on the SNP concentration and the incubation time. Short-term exposure to SNP increased cellular Rho123 uptake in a concentration-dependent manner. Maximum induction (115% and 140% of Rho123 uptake in control cells) occurred after 4-h of incubation. In contrast, long-term (24- and 48-h) exposure to SNP resulted in a decrease in cellular Rho123 uptake. The decrease of Rho123 by low concentrations (0.1 mmol/L) of SNP was more profound than that by high concentrations (2 mmol/L). To investigate whether alteration in cellular Rho123 uptake was the result of expression of P-gp, the levels of P-gp were measured (Figure 2). As

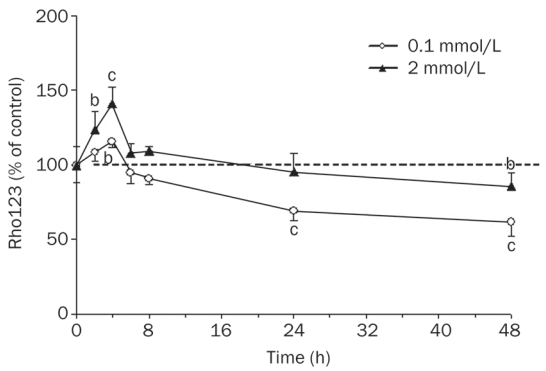

Figure 1. Effects of SNP on P-gp function following different incubation time periods. Caco-2 cells were incubated with low (0.1 mmol/L) and high (2 mmol/L) concentrations of SNP for 2, 4, 6, 8, 24, and 48 h. P-gp function was measured using cellular Rho123 uptake. Cells incubated with drug-free medium served as a control. Mean±SD (n=4). $^bP<0.05$, $^cP<0.01$ *vs* control.

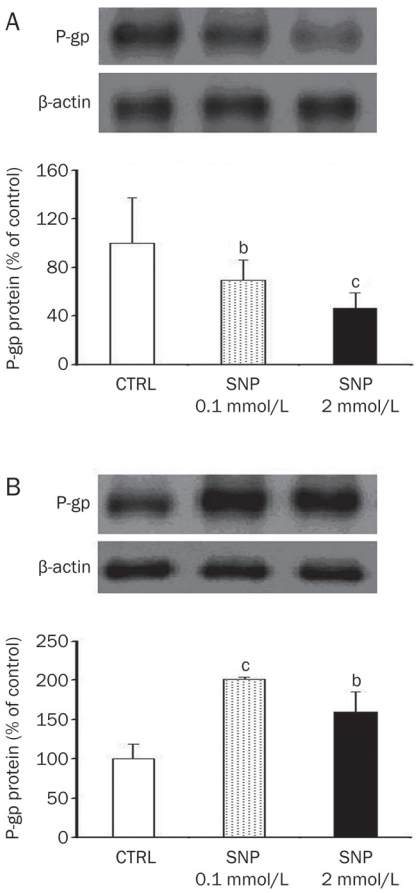

Figure 2. Effects of a 4-h exposure (A) and a 24-h exposure (B) to SNP on P-gp protein levels in Caco-2 cells. Caco-2 cells were incubated with 0.1 or 2 mmol/L SNP for 4 and 24 h, respectively, and the levels of P-gp in the cells were measured using Western blotting. Cells incubated with drug-free medium served as a control. Mean±SD (n=3–4). $^{b}P<0.05$, $^{c}P<0.01$ *vs* control.

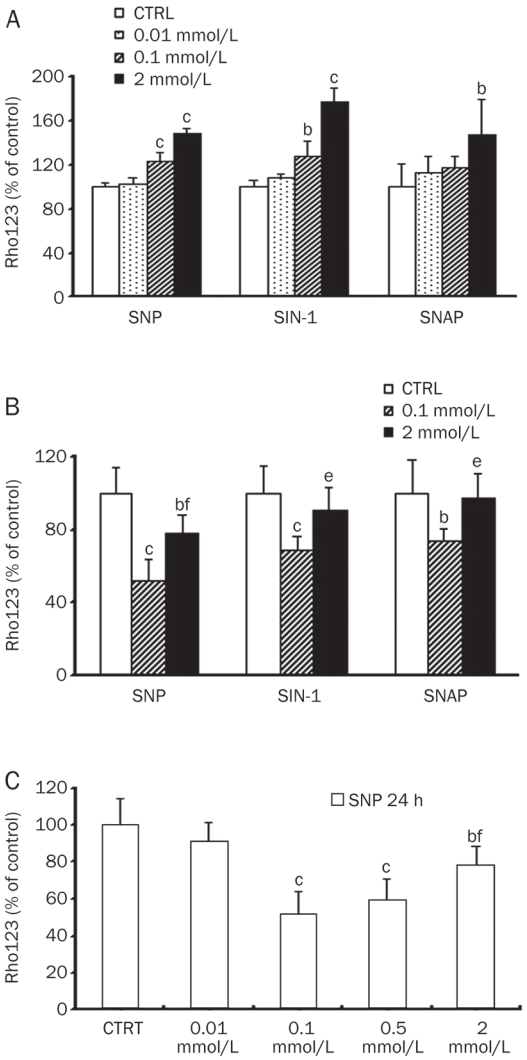

Figure 3. Effects of a 4-h exposure (A), a 24-h exposure (B) to SNP, SIN-1 and SNAP or a 24-h exposure (C) to different levels of SNP on P-gp function in Caco-2 cells. Caco-2 cells were incubated with the tested agents for designated times. P-gp function was assessed by measuring cellular Rho123 uptake. Cells incubated with drug-free medium served as a control. Mean±SD (n=4). $^{b}P<0.05$, $^{c}P<0.01$ *vs* control. $^{e}P<0.05$, $^{f}P<0.01$ *vs* 0.1 mmol/L SNP.

expected, 4-h of exposure to SNP decreased P-gp expression in a concentration-dependent manner, whereas 24-h of exposure to SNP induced P-gp expression in a biphasic manner.

To verify that the phenomenon induced by SNP came from NOx rather than other species derived from SNP, the effects of different types of NO donors on P-gp function were investigated following 4-h and 24-h incubations. The three donors have different structures, which release NO at different rates and by different mechanisms. SIN-1, a NO donor that releases both NO and O_2^-, is usually used as peroxynitrite donor[27]. SNAP is an *S*-nitrosothiol NO donor with a half-life of approximately 4 h[28]. Similar to the findings with SNP, 4-h of exposure to SIN-1 or SNAP decreased the efflux activity of P-gp in a concentration-dependent manner (Figure 3A), and 24-h of exposure to SIN-1 or SNAP exerted biphasic regulation effects (Figure 3B). Effects of a series of SNP concentrations on the efflux activity of P-gp were also measured following 24-h of incubation (Figure 3C). The results showed that the effect of SNP on basal P-gp activity was normally distributed. The maximal stimulation occurred at 0.1 mmol/L SNP; at higher SNP concentrations, the stimulatory effect gradually decreased (Figure 3C). Concentrations over 2 mmol/L were not tested because of cell toxicity.

Temporal profile of intracellular ROS and RNS level after exposure to SNP

iROS and iRNS levels were measured following exposure to 0.1 and 2 mmol/L of SNP for different times (Figure 4). The results showed that ROS was produced concomitantly with

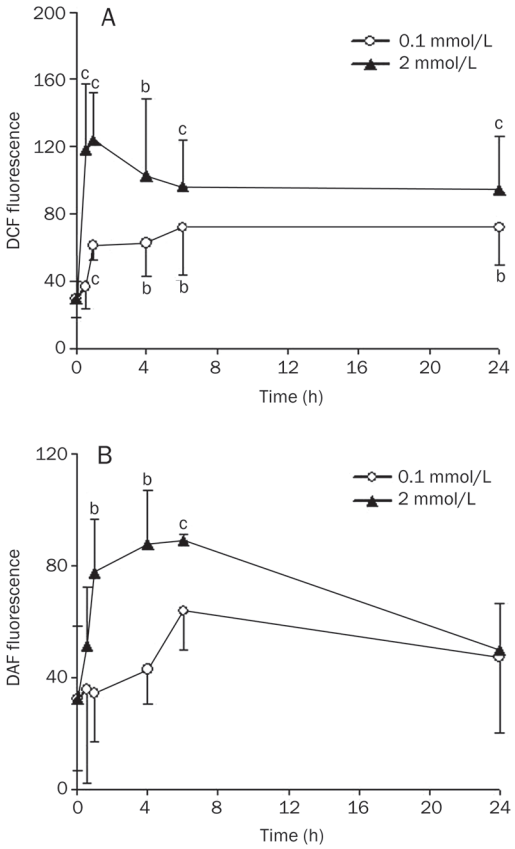

Figure 4. Effects of SNP on intracellular ROS (A) and RNS (B) following different incubation times. Caco-2 cells were exposed to 0.1 or 2 mmol/L SNP for 0.5, 1, 4, 6, or 24 h, and iROS and iRNS levels were assessed according to the instructions of the respective assay kits. Cells incubated with drug-free medium served as a control. Mean±SD (n=4). ^{b}P<0.05, ^{c}P<0.01 *vs* control.

the nitric oxide released by SNP in Caco-2 cells. Short-term exposure to SNP significantly increased iROS and iRNS, and iROS and iRNS were sustained at relatively high levels for the first 6 h. Following 24 h of exposure to SNP, the iROS and iRNS levels were still higher than in the control cells.

Effect of free radical scavengers on P-gp function induced by SNP

Effects of several free radical scavengers on P-gp function induced by SNP were investigated. The results showed that 2 mmol/L ascorbate, GSH and uric acid significantly reversed alteration in P-gp function by 24 h of exposure to SNP, whereas the nitric oxide scavenger PTIO had no effect (Figure 5B), indicating that the alteration in P-gp function did not result from a direct effect of NO itself but from the indirect effects of NO-derived oxidative and nitrosative stress. However, neither VC, GSH, UA nor PTIO could attenuate the impairment of P-gp function after only 4 h of exposure to SNP (Figure 5A), treatment with GSH even showed a trend toward enhancing the impaired P-gp function. Higher doses of these free radical scavengers caused cell toxicity. None of the above

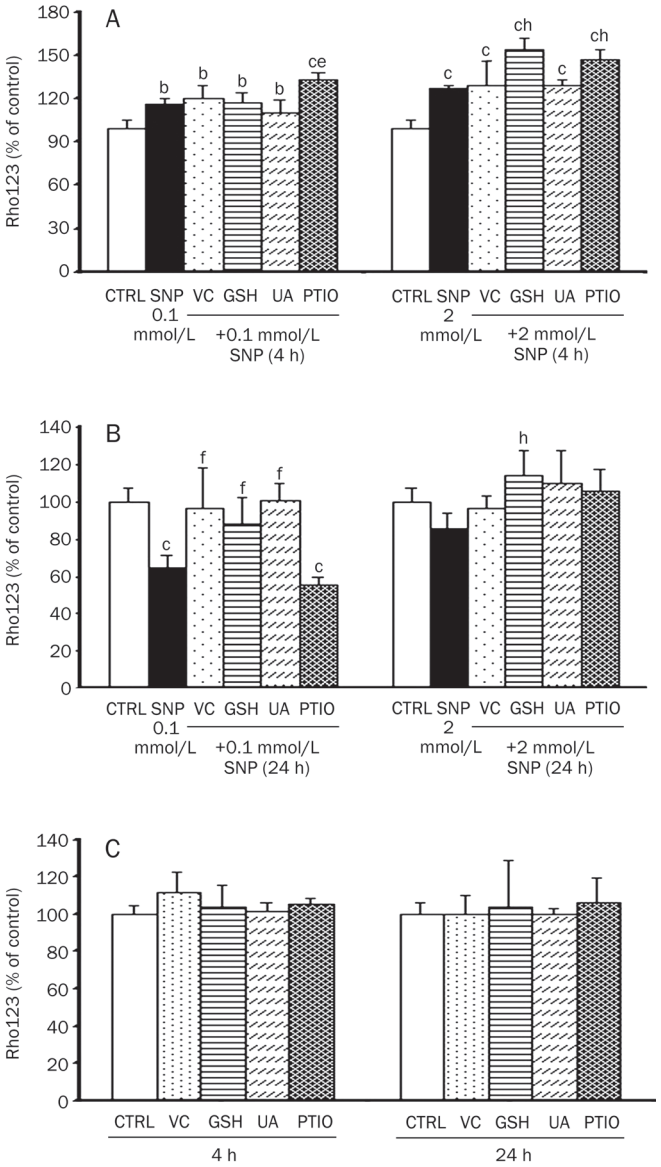

Figure 5. Effects of free radical scavengers on short-term inhibition and long-term stimulation of P-gp function induced by exposure to SNP in Caco-2 cells. Caco-2 cells were co-incubated with SNP (0.1 and 2 mmol/L) in the presence of ascorbate (VC, 2 mmol/L), GSH (2 mmol/L), uric acid (UA, 2 mmol/L), or PTIO (2 mmol/L) for 4 h (A) and 24 h (B). (C) represents the 4-h and 24-h effects of the free radical scavengers alone on P-gp function. Cells incubated with drug-free medium served as a control. P-gp function was measured using cellular Rho123 uptake. Cells incubated with drug-free medium served as a control. Mean±SD (n=4). ^{b}P<0.05, ^{c}P<0.01 *vs* control; ^{e}P<0.05, ^{f}P<0.01 *vs* 0.1 mmol/L SNP. ^{h}P<0.05, ^{i}P<0.01 *vs* 2 mmol/L SNP.

radical scavengers alone had a significant influence on P-gp function (Figure 5C).

Effects of signal pathway inhibitors on the alteration of P-gp function by SNP

The cGMP/PKG pathway is a typical pathway that is downstream of the NO modulation system. The soluble guanylate

cyclase inhibitor ODQ was used to determine the association between the cGMP/PKG pathway and the alteration in P-gp function by SNP. ODQ did not reverse the alteration in P-gp function by 4-h or 24-h of exposure to 2 mmol/L SNP (Figure 6). This result indicated that the changes in P-gp activity by SNP are independent of the cGMP/PKG pathway, which is consistent with a previous report[10]. However, the compounds wortmannin (a PI3K/Akt inhibitor), chelerythrine (a PKC inhibitor) and SB203580 (a p38 MAPK inhibitor) significantly reversed the alteration in P-gp function induced by 24-h of exposure to SNP (Figure 6B), implying that the alteration in the function of P-gp by a 24-h exposure to SNP involved the PI3K/Akt, PKC, and MAPK pathways. In contrast, none of the three pharmacological inhibitors could reverse the inhibitory effect of a 4-h exposure to SNP on P-gp function (Figure 6A); in fact, the PI3K/Akt inhibitor wortmannin further decreased P-gp activity. None of the above pharmacological inhibitors alone had a significant influence on P-gp function (Figure 6C).

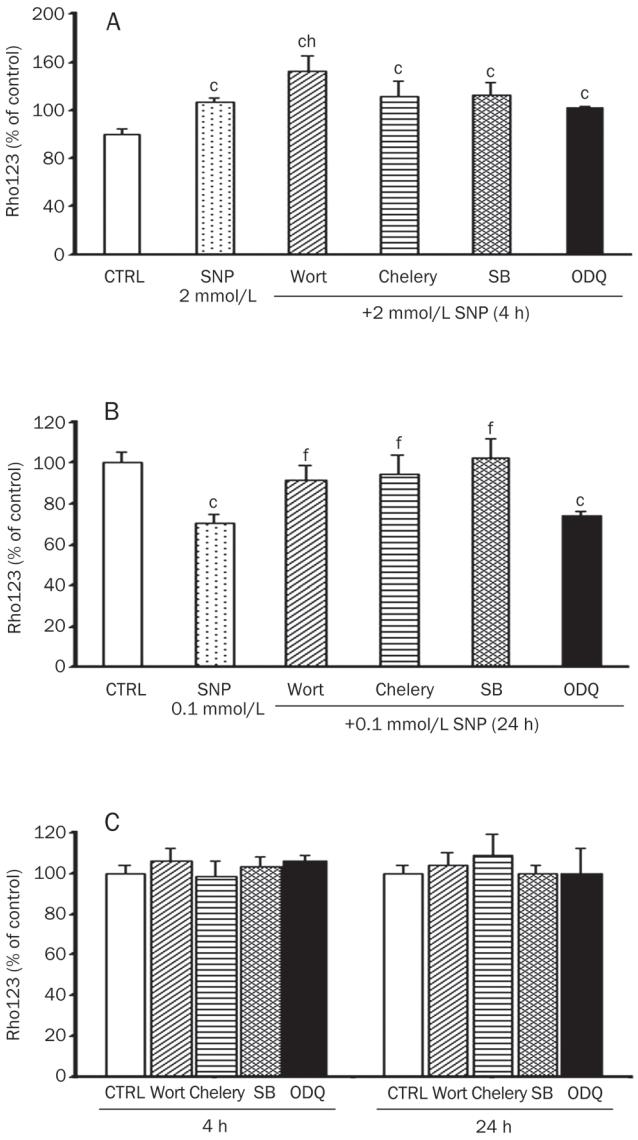

Figure 6. Effects of several pharmacological inhibitors on short-term inhibition and long-term stimulation of P-gp function induced by exposure to SNP in Caco-2 cells. Caco-2 cells were co-incubated with SNP in the presence of wortmannin (Wort, 1 μmol/L), chelerythrine (Chelery, 5 μmol/L), SB203580 (SB, 10 μmol/L) or ODQ (50 μmol/L) for 4 h (A) and 24 h (B). (C) represents the 4-h and 24-h effects of inhibitors alone on P-gp function. Cells incubated with drug-free medium served as a control. P-gp function was measured using cellular Rho123 uptake. Mean±SD (n=4). ^{b}P<0.05, ^{c}P<0.01 *vs* control. ^{e}P<0.05, ^{f}P<0.01 *vs* 0.1 mmol/L SNP. ^{h}P<0.05, ^{i}P<0.01 *vs* 2 mmol/L SNP.

Discussion

Accumulating evidence clearly demonstrates a link between NOx (NO and its redox-reactive derivatives) and the activity of P-gp, although the published results are often contradictory[8, 10, 12–14]. The present study was designed to investigate the effects of NO and its redox-reactive derivatives (NOx) on the expression and function of P-gp in Caco-2 cells using three different NOx donors. P-gp function was quantitatively assessed by measuring the cellular uptake of the P-gp substrate Rho123. Alteration of the intracellular accumulation of this compound directly correlated with the altered activity of this efflux system, which is expressed in the apical membrane of Caco-2 cells. The main finding was that the effects of the NO donor SNP on the function and expression of P-gp were dependent on incubation time. Short-term exposure to SNP impaired expression and function of P-gp in a concentration-dependent manner, whereas long-term exposure to SNP biphasically enhanced the expression and function of P-gp.

The intracellular accumulation of Rho123 in Caco-2 cells was measured following incubation with two concentrations of SNP (0.1 and 2 mmol/L). The results showed that cellular uptake of Rho123 increased with incubation time at early time-points (2 and 4 h), peaked at 4 h, then declined gradually (Figure 1) with increased incubation time. It was also observed that long-term exposure to SNP caused biphasic regulation of P-gp function. The stimulatory effect of 0.1 mmol/L SNP was more profound than that of 2 mmol/L SNP. Western blot data showed that the altered function of P-gp in Caco-2 cells was in agreement with the alteration in P-gp protein levels, indicating that the altered function of P-gp partly came from altered P-gp protein levels.

To exclude a direct role of SNP in P-gp function and expression levels, two other donors, SIN-1 and SNAP, which possess different structures and NO release rates, were also used to investigate the roles of NO donors. A similar pattern of alteration in P-gp function was observed, suggesting that the alteration in P-gp activity resulted from NO and its reactive derivates. Biphasic regulation of P-gp function by SNP in Caco-2 cells was further verified using a 24-h exposure to different concentrations of SNP (Figure 3C).

NO is a short-lived reactive molecule: when it is released, it rapidly reacts with its specific biological target or reacts with oxygen or superoxide to generate ROS and RNS, which subsequently react with biological targets[28]. The sGC/cGMP pathway is considered a typical downstream pathway of

NO; NO activates sGC (soluble guanylate cyclase) to produce cGMP (cyclic GMP), which regulates a series of physiological responses[29, 30, 31]. Our results showed that the sGC inhibitor ODQ did not reverse the alteration of P-gp function induced by NO donors, suggesting that the regulation of P-gp function by NO donors is independent of the sGC/cGMP pathway. This finding was supported by previous studies that used doxorubicin accumulation in HT29/HT29-dx cells[10]. In addition, the specific NO scavenger PTIO did not reverse the SNP-induced alteration of P-gp function, indicating that the effect of SNP on P-gp function occurred via an NO-independent mechanism[29]. This result agreed with previous studies performed in isolated perfused rat livers[32]. Furthermore, a significant increase in intracellular ROS (iROS) and RNS (iRNS) in Caco-2 cells was observed at early stages of SNP exposure, which indicated that iROS and iRNS were involved in the SNP-induced impairment of P-gp function. Although, the decrease in folate transporter function induced by 10 μmol/L SNAP was reversible with sufficient (10 mmol/L) ascorbate, GSH, or NO scavengers[33], however these results showed that VC, GSH, UA and PTIO did not alleviate the impairment of P-gp function following a 4-h exposure to 0.1 and 2 mmol/L SNP (Figure 5A); this lack of effect was most likely due to insufficient dosing of the reversal agents (2 mmol/L) at 0.1 and 2 mmol/L NO donors. Higher doses of the reversal agents were not used because simultaneous exposure to SNP and higher doses of reversal agents led to significant cell damage. However, these scavengers significantly reversed the SNP-induced stimulation of P-gp after a 24-h exposure to SNP, suggesting that the increase in both the activity and expression of P-gp by long-term exposure to NO donors resulted from the comprehensive effects of oxidative stress and nitrosative stress. This conclusion was consistent with previous reports[8] in MBEC cells.

NOx activates diverse signaling pathways to regulate gene expression[20]. The MAPK signaling pathway, the PKC signal pathway and the PI3K/Akt pathways have been reported to be activated by NOx[20–23, 33, 34]. Whether or not NOx altered intestinal efflux activity by regulating these signal pathways was also studied using the corresponding pharmacological inhibitors wortmannin (a PI3K inhibitor), SB203580 (a p38 MAPK inhibitor), and chelerythrine (a PKC inhibitor). The results observed with these inhibitors were similar to the effects of free radical scavengers: although the three inhibitors did not alleviate the impairment of P-gp function induced by a 4-h exposure to 2 mmol/L SNP, they reversed the P-gp stimulation induced by long-term exposure to 0.1 mmol/L SNP. These results suggest that a 24-h exposure to NOx donors stimulated the expression and activity of P-gp via the PI3K/Akt, PKC and p38 MAPK pathways.

The pattern of changes in P-gp activity and protein expression in response to NO donors is certainly complex, as short-term exposure to NO donor decreased P-gp function and expression, whereas long-term exposure to NO donors elevated P-gp function and expression. Similar patterns have been found for MRP2 in renal proximal tubules exposed to certain tubular nephrotoxicants[35] and in P-gp in rat brain capillaries exposed to TNF (tumor necrosis factor)-α and ET (endothelin-1)[36]. These findings seem to partly explain the contradictory reports on the regulation of P-gp by NOx when different doses or incubation times were used[8, 10, 37].

The present results indicate that the effects of NO donors on P-gp function and expression were dependent on exposure time. Short-term exposure to NO donors led to a significant decrease in P-gp function and expression, whereas long-term exposure to NO donors stimulated P-gp function and expression. The regulation of P-gp function and expression by NO donors occurred via a NO-independent mechanism.

Acknowledgements

This work was supported by the National Natural Science Foundation of China (No 81072693 and 81102503), and supported by funding for Innovative Research Team in Institution of Jiangsu Higher Education.

Author contribution

Ru DUAN and Xiao-dong LIU designed the experiments and analyzed the data; Ru DUAN wrote the paper; Xiao-dong LIU and Li LIU revised the paper; Ru DUAN, Nan HU, Hai-yan LIU, Jia LI, Li LIU, Hai-fang GUO, and Can LIU performed the research.

References

1 Brady JM, Cherrington NJ, Hartley DP, Buist SC, Li N, Klaassen CD. Tissue distribution and chemical induction of multiple drug resistance genes in rats. Drug Metab Dispos 2002; 30: 838–44.
2 Marchetti S, Mazzanti R, Beijnen JH, Schellens JH. Concise review: Clinical relevance of drug drug and herb drug interactions mediated by the ABC transporter ABCB1 (MDR1, P-glycoprotein). Oncologist 2007; 12: 927–41.
3 Fromm MF. Importance of P-glycoprotein for drug disposition in humans. Eur J Clin Invest 2003; 33: 6–9.
4 Liu H, Zhang D, Xu X, Liu X, Wang G, Xie L, *et al*. Attenuated function and expression of P-glycoprotein at blood-brain barrier and increased brain distribution of phenobarbital in streptozotocin-induced diabetic mice. Eur J Pharmacol 2007; 561: 226–32.
5 Zhang LL, Lu L, Jin S, Jing XY, Yao D, Hu N, *et al*. Tissue-specific alterations in expression and function of P-glycoprotein in streptozotocin-induced diabetic rats. Acta Pharmacol Sin 2011; 32: 956–66.
6 Laouari D, Yang R, Veau C, Blanke I, Friedlander G. Two apical multidrug transporters, P-gp and MRP2, are differently altered in chronic renal failure. Am J Physiol Renal Physiol 2001; 280: 636–45.
7 Blokzijl H, Vander Borght S, Bok LI, Libbrecht L, Geuken M, van den Heuvel FA, *et al*. Decreased P-glycoprotein (P-gp/MDR1) expression in inflamed human intestinal epithelium is independent of PXR protein levels. Inflamm Bowel Dis 2007; 13: 710–20.
8 Maeng HJ, Kim MH, Jin HE, Shin SM, Tsuruo T, Kim SG, *et al*. Functional induction of P-glycoprotein in the blood-brain barrier of streptozotocin-induced diabetic rats: evidence for the involvement of nuclear factor-kappaB, a nitrosative stress-sensitive transcription factor, in the regulation. Drug Metab Dispos 2007; 35: 1996–2005.
9 Dixit SG, Zingarelli B, Buckley DJ, Buckley AR, Pauletti GM. Nitric oxide mediates increased P-glycoprotein activity in interferon-{gamma}-stimulated human intestinal cells. Am J Physiol Gastrointest Liver

Physiol 2005; 288: G533–40.
10 Riganti C, Miraglia E, Viarisio D, Costamagna C, Pescarmona G, Ghigo D, *et al*. Nitric oxide reverts the resistance to doxorubicin in human colon cancer cells by inhibiting the drug efflux. Cancer Res 2005; 65: 516–25.
11 Dohgu S, Yamauchi A, Nakagawa S, Takata F, Kai M, Egawa T, *et al*. Nitric oxide mediates cyclosporine-induced impairment of the blood-brain barrier in cocultures of mouse brain endothelial cells and rat astrocytes. Eur J Pharmacol 2004; 505: 51–9.
12 Takizawa Y, Kishimoto H, Kitazato T, Tomita M, Hayashi M. Effects of nitric oxide on mucosal barrier dysfunction during early phase of intestinal ischemia/reperfusion. Eur J Pharm Sci 2011; 42: 246–52.
13 Nawa A, Fujita Hamabe W, Tokuyama S. Inducible nitric oxide synthase-mediated decrease of intestinal P-glycoprotein expression under streptozotocin-induced diabetic conditions. Life Sci 2010; 86: 402–9.
14 Heemskerk S, van Koppen A, van den Broek L, Poelen GJ, Wouterse AC, Dijkman HB, *et al*. Nitric oxide differentially regulates renal ATP-binding cassette transporters during endotoxemia. Pflugers Arch 2007; 454: 321–34.
15 Nawa A, Fujita-Hamabe W, Tokuyama S. Regulatory action of nitric oxide synthase on ileal P-glycoprotein expression under streptozotocin-induced diabetic condition. Biol Pharm Bull 2011; 34: 436–8.
16 Meunier V, Bourrié M, Berger Y, Fabre G. The human intestinal epithelial cell line Caco-2; pharmacological and pharmacokinetic applications. Cell Biol Toxicol 1995; 11: 187–94.
17 Uchiyama T, Matsuda Y, Wada M, Takahashi S, Fujita T. Functional regulation of Na^+-dependent neutral amino acid transporter ASCT2 by S-nitrosothiols and nitric oxide in Caco-2 cells. FEBS Lett 2005; 579: 2499–506.
18 Krischel V, Bruch-Gerharz D, Suschek C, Kröncke KD, Ruzicka T, Kolb-Bachofen V. Biphasic effect of exogenous nitric oxide on proliferation and differentiation in skin derived keratinocytes but not fibroblasts. J Invest Dermatol 1998; 111: 286–91.
19 Kean RB, Spitsin SV, Mikheeva T, Scott GS, Hooper DC. The peroxynitrite scavenger uric acid prevents inflammatory cell invasion into the central nervous system in experimental allergic encephalomyelitis through maintenance of blood-central nervous system barrier integrity. J Immunol 2000; 165: 6511–8.
20 Hemish J, Nakaya N, Mittal V, Enikolopov G. Nitric oxide activates diverse signaling pathways to regulate gene expression. J Biol Chem 2003; 278: 42321–9.
21 Barancík M, Bohácová V, Kvackajová J, Hudecová S, Krizanová O, Breier A. SB203580, a specific inhibitor of p38-MAPK pathway, is a new reversal agent of P-glycoprotein-mediated multidrug resistance. Eur J Pharm Sci 2001; 14: 29–36.
22 Saksena S, Goyal S, Raheja G, Singh V, Akhtar M, Nazir TM, *et al*. Upregulation of P-glycoprotein by probiotics in intestinal epithelial cells and in the dextran sulfate sodium model of colitis in mice. Am J Physiol Gastrointest Liver Physiol 2011; 300: 1115–23.
23 Liu H, Liu X, Jia L, Liu Y, Yang H, Wang G, *et al*. Insulin therapy restores impaired function and expression of P-glycoprotein in blood-brain barrier of experimental diabetes. Biochem Pharmacol 2008; 75: 1649–58.
24 Bradford MM. A rapid and sensitive method for the quantitation of microgram quantities of protein utilizing the principle of protein-dye binding. Anal Biochem 1976; 72: 248–54.
25 Liu H, Xu X, Yang Z, Deng Y, Liu X, Xie L. Impaired function and expression of P-glycoprotein in blood-brain barrier of streptozotocin-induced diabetic rats. Brain Res 2006; 1123: 245–52.
26 Zhang J, Zhou F, Wu X, Gu Y, Ai H, Zheng Y, *et al*. 20(S)-ginsenoside Rh2 noncompetitively inhibits P-glycoprotein *in vitro* and *in vivo*: a case for herb-drug interactions. Drug Metab Dispos 2010; 38: 2179–87.
27 Feelisch M. The use of nitric oxide donors in pharmacological studies. Naunyn Schmiedebergs Arch Pharmacol 1998; 358: 113–22.
28 Thomas DD, Ridnour LA, Isenberg JS, Flores-Santana W, Switzer CH, Donzelli S, *et al*. The chemical biology of nitric oxide: implications in cellular signaling. Free Radic Biol Med 2008; 45: 18–31.
29 Feelisch M. Nitric oxide and cyclic GMP in cell signaling and drug development. N Engl J Med 2006; 355: 2003–11.
30 Pfeifer A, Ruth P, Dostmann W, Sausbier M, Klatt P, Hofmann F. Structure and function of cGMP-dependent protein kinases. Rev Physiol Biochem Pharmacol 1999; 135: 105–49.
31 Espey MG, Miranda KM, Thomas DD, Wink DA. Distinction between nitrosating mechanisms within human cells and aqueous solution. J Biol Chem 2001; 276: 30085–91.
32 Parasrampuria R, Mehvar R. Divergent effects of nitric oxide donors on the biliary efflux transporters in isolated perfused rat livers: nitric oxide-independent inhibition of ABC transporters by sodium nitroprusside. Drug Metab Lett 2011; 5: 64–72.
33 Smith SB, Huang W, Chancy C, Ganapathy V. Regulation of the reduced-folate transporter by nitric oxide in cultured human retinal pigment epithelial cells. Biochem Biophys Res Commun 1999; 257: 279–83.
34 Katayama K, Yoshioka S, Tsukahara S, Mitsuhashi J, Sugimoto Y. Inhibition of the mitogen-activated protein kinase pathway results in the down-regulation of P-glycoprotein. Mol Cancer Ther 2007; 6: 2092–102.
35 Terlouw SA, Graeff C, Smeets PH, Fricker G, Russel FG, Masereeuw R, *et al*. Short- and long-term influences of heavy metals on anionic drug efflux from renal proximal tubule. J Pharmacol Exp Ther 2002; 301: 578–85.
36 Bauer B, Hartz AM, Miller DS. Tumor necrosis factor alpha and endothelin-1 increase P-glycoprotein expression and transport activity at the blood-brain barrier. Mol Pharmacol 2007; 71: 667–75.
37 Robertson SJ, Mokgokong R, Kania KD, Guedj AS, Hladky SB, Barrand MA. Nitric oxide contributes to hypoxia-reoxygenation-induced P-glycoprotein expression in rat brain endothelial cells. Cell Mol Neurobiol 2011; 31: 1103–11.

Acta Pharmacologica Sinica (2012) 33: 775–782
 1671-4083/12 $32.00
www.nature.com/aps

Original Article

Melatonin reduces acute lung inflammation, edema, and hemorrhage in heatstroke rats

Wen-shiann WU[1], Ming-ting CHOU[1], Chien-ming CHAO[2], Chen-kuei CHANG[3], Mao-tsun LIN[3, 4], Ching-ping CHANG[5, *]

[1]*Department of Cardiology, Chi Mei Medical Center, and The Center of General Education, Chia Nan University of Pharmacy & Science, Tainan, Taiwan, China;* [2]*Departments of Surgery and Intensive Care Medicine, Chi Mei Medical Center, Liouying, Tainan, Taiwan;* [3]*Graduate Institute of Disease Prevention and Control, Taipei Medical University and Department of Surgery, Shuan-Ho Hospital, Taipei, Taiwan, China;* [4]*Department of Medical Research, Chi Mei Medical Center, Tainan, Taiwan, China;* [5]*Department of Biotechnology, Southern Taiwan University, Tainan, Taiwan, China*

Aim: To assess the therapeutic effect of melatonin on heat-induced acute lung inflammation and injury in rats.
Methods: Heatstroke was induced by exposing anesthetized rats to heat stress (36 °C, 100 min). Rats were treated with vehicle or melatonin (0.2, 1, 5 mg/kg) by intravenous administration 100 min after the initiatioin of heatstroke and were allowed to recover at room temperature (26 °C). The acute lung injury was quantified by morphological examination and by determination of the volume of pleural exudates, the number of polymorphonuclear (PMN) cells, and the myeloperoxidase (MPO) activity. The concentrations of tumor necrosis factor, interleukin (IL)-1β, IL-6, and IL-10 in bronchoalveolar fluid (BALF) were measured by ELISA. Nitric oxide (NO) level was determined by Griess method. The levels of glutamate and lactate-to-pyruvate ratio were analyzed by CMA600 microdialysis analyzer. The concentrations of hydroxyl radicals were measured by a procedure based on the hydroxylation of sodium salicylates leading to the production of 2,3-dihydroxybenzoic acid (DHBA).
Results: Melatonin (1 and 5 mg/kg) significantly (i) prolonged the survival time of heartstroke rats (117 and 186 min *vs* 59 min); (ii) attenuated heatstroke-induced hyperthermia and hypotension; (iii) attenuated acute lung injury, including edema, neutrophil infiltration, and hemorrhage scores; (iv) down-regulated exudate volume, BALF PMN cell number, and MPO activity; (v) decreased the BALF levels of lung inflammation response cytokines like TNF-alpha, interleukin (IL)-1β, and IL-6 but further increased the level of an anti-inflammatory cytokine IL-10; (vi) reduced BALF levels of glutamate, lactate-to-pyruvate ratio, NO, 2,3-DHBA, and lactate dehydrogenase.
Conclusion: Melatonin may improve the outcome of heatstroke in rats by attenuating acute lung inflammation and injury.

Keywords: free radicals; heat stroke; melatonin; acute lung injury; Wistar rats; tumor necrosis factor alpha; interleukins; nitric oxide

Acta Pharmacologica Sinica (2012) 33: 775–782; doi: 10.1038/aps.2012.29; published online 21 May 2012

Introduction

Heatstroke can be defined as a systemic condition of excessive hyperthermia (body core temperature above 40 °C) associated with a systemic inflammatory response that leads to multiple organ dysfunction, predominantly in the brain (*eg*, delirium, convulsion, and coma)[1, 2]. Heatstroke is the third most common cause of fatal brain injury in the world[3]. More than three quarters of studied heatstroke patients develop multiple organ dysfunction, the most common of which is acute respiratory distress syndrome clinically manifested as inflammatory lung injury of very rapid onset[4]. Indeed, acute lung inflammation and injury can be induced in a rat heatstroke model[5, 6].

* To whom correspondence should be addressed.
E-mail jessica@mail.stut.edu.tw
Received 2012-01-02 Accepted 2012-03-12

Melatonin, the main product of the pineal gland, is found in high concentrations in other body fluids and tissues[7, 8] and has anti-oxidant and anti-inflammatory actions[9–12]. We have evaluated the prophylactic effect of melatonin in heatstroke rats and showed that the systemic delivery of melatonin immediately before the start of heat stress significantly prolongs the survival time of heatstroke rats[13]. However, it is not known whether melatonin can be used as a therapeutic agent for heatstroke resuscitation.

The present study had two purposes. First, experiments were conducted to assess the effect of melatonin administered immediately after the onset of heatstroke on the survival time of heatstroke rats. Second, we attempted to assess the temporal profile of acute lung inflammation and injury in heatstroke rats treated with melatonin or vehicle. In our previous study[13], prophylactic doses of melatonin (0.2–5.0

mg/kg, intravenously) were effective in preventing the occurrence of heatstroke. The same dosage of melatonin was used in the present study to test its therapeutic action.

Materials and methods

Animals

Adult male Wistar rats (weighing 226–248 g) were obtained from the Animal Resource Center of the Republic of China National Science of Council (Taipei, Taiwan). The animals were housed four to a cage at ambient temperature (Ta) of 26±0.5 °C with a 12-h light/dark cycle. Pelleted rat chow and tap water were available *ad libitum*. The rats were allowed to become acclimated for at least 1 week. The experimental protocol was approved by the Animal Ethic Committee of Chi Mei Medical Center (Tainan, Taiwan) under the Guidelines of the National Science Council of the Republic of China (Taipei, Taiwan). Animal care and experiments were conducted according to the Guide for the Care and Use of Laboratory Animals published by the US National Institutes of Health (publication No 85–23, revised 1996). In all experiments, adequate anesthesia — via a single intraperitoneal dose of urethane (1.4 g/kg of body weight) — was maintained for approximately 480 min to abolish the corneal reflex and pain reflexes induced by tail pinching. At the end of the experiments, control rats and rats that had survived heatstroke were killed with an overdose of urethane.

Surgery and monitoring of physiological parameters

The right femoral artery and vein of rats were cannulated with polyethylene tubing (PE50) under urethane anesthesia for blood pressure monitoring and drug administration, respectively. The body core temperature (Tco) was monitored continuously by a thermocouple, and mean arterial pressure (MAP) was monitored continuously with a pressure transducer.

Induction of heatstroke

The Tco of the anesthetized animals was maintained at approximately 37 °C with an infrared light lamp, except in the heat stress experiments. Heatstroke was induced by placing the animals in a folded heating pad at 36 °C controlled by circulating hot water. The time at which the MAP started to drop and the time at which MAP dropped to a value of approximately 50 mmHg were found to be 100 and 140 min, respectively, after the start of heat stress[13]. At 100 min, the heating pad was removed, and the animals were allowed to recover at room temperature (26 °C)[13]. Survival time values (the interval between the 100-min time point and death) were determined. Our previous results showed that the vehicle-treated heated rats had both hyperthermia (~40 °C Tco) and hypotension (~50 mmHg) at 140 min, suggesting the occurrence of heatstroke[13].

Preparation of the melatonin solution

Melatonin (Sigma, St Louis, MO, USA) was dissolved in a minimum volume of ethanol (0.5 mL) and diluted to the desired concentration with normal saline. In the vehicle-treated heatstroke group, an intravenous dose of vehicle solution (1 mL of ethanol-normal saline solution per kilogram of body weight) was administered 120 min after the onset of heat stress. In the melatonin-treated heatstroke group, an intravenous dose of melatonin solution (0.2–5 mg of melatonin in 1 mL of ethanol-normal saline solution per kilogram of body weight) was administered 120 min after the start of heat stress.

Experimental groups

Animals were assigned randomly to one of three groups. The normothermic control group was treated with an intravenous dose of vehicle solution and exposed to a Ta of 26 °C. The vehicle-treated heatstroke group was treated with the same dose of vehicle solution 120 min after the initiation of heat exposure (36 °C for 100 min). The third group of rats was treated with an intravenous dose of melatonin (0.2, 1.0, or 5.0 mg/kg) solution 120 min after the onset of heat stress. The last two groups of rats were exposed to heat stress (36 °C) for exactly 100 min to induce heatstroke and were then allowed to recover at room temperature (26 °C). In all groups, the physiological parameters and survival time were observed for up to 480 min (or to the end of the experiments).

Lung morphology

At the end of the experiments, the animals were killed, and the lungs not used for lavage were excised en bloc. Lung tissues were fixed in 10% buffered formalin for 24 h and then embedded in paraffin and cut into 3-μm thick sections. Sections were stained with hematoxylin and eosin, and images were taken with an Olympus BX51 microscope with a 40×objective. The lung injury scoring method of Su *et al*[14, 15] was modified and applied to quantify changes in lung architecture visible by light microscopy. The degree of microscopic injury was scored on the basis of the following variables: alveolar and interstitial edema, neutrophil infiltration, and hemorrhage. The severity of injury was graded for each variable: no injury=0; injury to 25% of the field=1; injury to 55% of the field=2; injury to 75% of the field=3; and diffuse injury=4. All samples were analyzed on a scaled grading system by a pathologist who was blinded to the experimental protocol and the region of sampling. A total of three slides prepared using each lung sample were randomly screened, and the mean was taken as the representative value of the sample. For presentation, we chose typical examples that were observed in all preparations of the same treatment.

Determination of the volume of pleural exudates and the number of polymorphonuclear (PMN) cells

The chest was carefully opened, and the plural cavity was washed with 2 mL of saline solution with heparin (5 U/mL) and indomethacin (10 μg/mL). The exudates and the washing solution were removed by aspiration, and the total volume was measured. The results were calculated by subtracting the volume injected (2 mL) from the total volume recovered. Cells were counted with the aid of a hemocytometer, and the PMN

populations were found to contain at least 95% PMN cells as demonstrated by cytospin and differential stain analysis (vital Trypan Blue stain).

Measurements of the levels of cytokines, glutamate, lactate/pyruvate ratio, lactate dehydrogenase (LDH), nitric oxide (NO) metabolites, and 2,3-dihydroxybenzoic acid (2,3-DHBA) in bronchoalveolar fluid (BALF)

In separate experiments, the lungs were lavaged by the installation of 5 mL saline solution at room temperature through a PE tube (2.0 mm in diameter) onto the trachea. BALF was obtained 140 min after the start of heat stress or at the equivalent time for normothermic controls. The 5 mL of saline installed into the lung was withdrawn. After centrifugation at 830×*g* for 10 min, the BALF supernatant was collected for measurement.

The concentrations of tumor necrosis factor-alpha (TNF-α), interleukin-1β (IL-1β), IL-6, and IL-10 in the BALF were determined using the double antibody sandwich ELISA (R&D systems, Minneapolis, MN, USA) according to the manufacturer's instructions. Optical densities were read on a plate reader. The concentrations of these cytokines in the samples were calculated from the standard curve multiplied by the dilution factor and expressed as pg/mL.

To determine the glutamate levels and lactate-to-pyruvate ratio, 5-μL aliquots of the samples were injected onto a CMA600 microdialysis analyzer (Carnegie Medicine, Stockholm, Sweden) for measurement[16]. It should be stressed that BALF samples were not re-used for the determination of markers of oxidative/nitrosative stress.

Nitric oxide (NO) is an unstable molecule that is easily degraded into nitrite and nitrate ions[17]. These stable NO metabolites have been reported to reflect the levels of regional NO production/release. Nitrite and nitrate levels were measured using an HPLC-NO detector system (ENO-10; Eicom) as reported previously[18]. In brief, nitrite and nitrate were separated on a reverse-phase column (NO-PAK, 4.6 mm×50 mm; Eicom), and nitrate was reduced to nitrite by passage through a reduction column (NO-RED; Eicom). Nitrite was determined as the Azo Dye compound formed by the Griess reaction using a spectrophotometer. These oxidative NO products were also evaluated as NO.

The concentrations of hydroxyl radicals were measured by a modified procedure based on the hydroxylation of sodium salicylates by hydroxyl radicals leading to the production of 2,3-DHBA and 2,5-DHBA[19]. A Ringer's solution containing 0.5 mmol/L sodium salicylate was perfused through the microdialysis probe at a constant flow rate (1.2 μL/min). An all-time reverse phase C_{18} column (150 mm×1 mm internal diameter, particle size 5 μm; BAS) was used to separate the DHBA moieties, and the mobile phase consisted of a mixture of 0.1 mol/L chloroacetic acid, 26.87 nmol/L disodium EDTA, 688.16 nmol/L sodium octylsulfate and 10% acetonitrile (pH 3.0). The retention times of 2,3-DHBA and 2,5-DHBA were 8.1 and 6.0 min, respectively.

Measurements of myeloperoxidase (MPO) activity in lung tissue

MPO activity, an index of PMN cell accumulation, was determined as previously described[20]. Lung tissues were homogenized in a solution containing 0.5% hexa-decyl-trimethyl-ammonium bromide dissolved in 10 mmol/L potassium phosphate buffer (pH 7.0) and centrifuged for 30 min at 20 000×*g* at 4 °C. An aliquot of the supernatant was then allowed to react with a solution of 1.6 mmol/L tetra-methyl-benzedrine and 0.1 mmol/L H_2O_2. The rate of change in absorbance was measured by spectrophotometry at 650 nm. MPO activity was defined as the quantity of enzyme needed to degrade 1 μmol/mL of peroxide at 37 °C and was expressed in ng/mg protein of wet tissue.

Statistical analysis

All data are expressed as the mean±SD. A one-way analysis of variance with Tukey's multiple comparisons test was used for BALF or lung markers and physiological parameters. Significant differences were established if $P<0.05$. For all statistical analyses, SPSS software version 10.0 (SPSS Inc, Chicago, IL, USA) was used.

Results

Melatonin therapy attenuates hyperthermia and hypotension and improves survival during heatstroke

Table 1 summarizes the survival time for vehicle- and melatonin-treated rats during heatstroke. The melatonin-treated heatstroke rats had significantly higher survival time values compared with the vehicle-treated rats ($P<0.05$): the survival times were 56–62 min ($n=6$) for vehicle-treated rats and 178–194 min ($n=6$) for melatonin (5 mg/kg)-treated rats.

Figure 1 shows the effect of heat exposure (36 °C for 100 min) on both Tco and MAP in rats treated with vehicle or melatonin (0.2–5 mg/kg). As shown in Figure 1, 40 min after the termination of heat exposure in the vehicle-treated group,

Table 1. Effects of heat exposure (36 °C for 100 min) on survival time in rats treated with vehicle or melatonin immediately after the initiation of heat exposure. Except for the normothermic controls, data are presented as the mean±SD. $n=6$. [b]$P<0.05$ compared with Group 1; [e]$P<0.05$ compared with Group 2.

Treatment group	Survival time (min)
1. Normothermic controls	>480
2. Vehicle-treated heatstroke rats*	59±3[b]
3. Melatonin (0.2 mg/kg)-treated heatstroke rats*	65±3
4. Melatonin (1 mg/kg)-treated heatstroke rats*	117±5[e]
5. Melatonin (5 mg/kg)-treated heatstroke rats*	186±8[e]

Group 1 rats were sacrificed approximately 480 min after the initiation of the experiment (or at the end of the experiment) by an over-dose of anesthetic; otherwise, they should survive more than 480 min.

* For the groups exposed to 36 °C, the heat stress was withdrawn at 100 min, and the rats were allowed to recover at room temperature (26 °C).

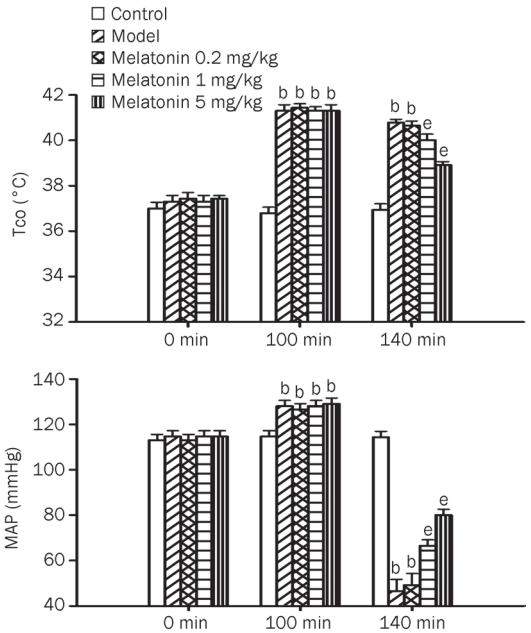

Figure 1. Core temperature (Tco, A) and mean arterial pressure (MAP, B) values for normothermic controls, vehicle-treated heatstroke rats, melatonin (0.2 mg/kg)-treated heatstroke rats, melatonin (1 mg/kg)-treated heatstroke rats, and melatonin (5 mg/kg)-treated heatstroke rats. The values were obtained at 0, 100, or 140 min after the initiation of heat exposure in heatstroke rats or the equivalent times in normothermic controls. All heatstroke groups had heat exposure (36 °C) withdrawn at exactly 100 min and were then allowed to recover at room temperature (26 °C). Bars are the mean±SD of 6 rats for each group. $^{b}P<0.05$ compared with normothermic controls; $^{e}P<0.05$ compared with vehicle-treated heatstroke rats.

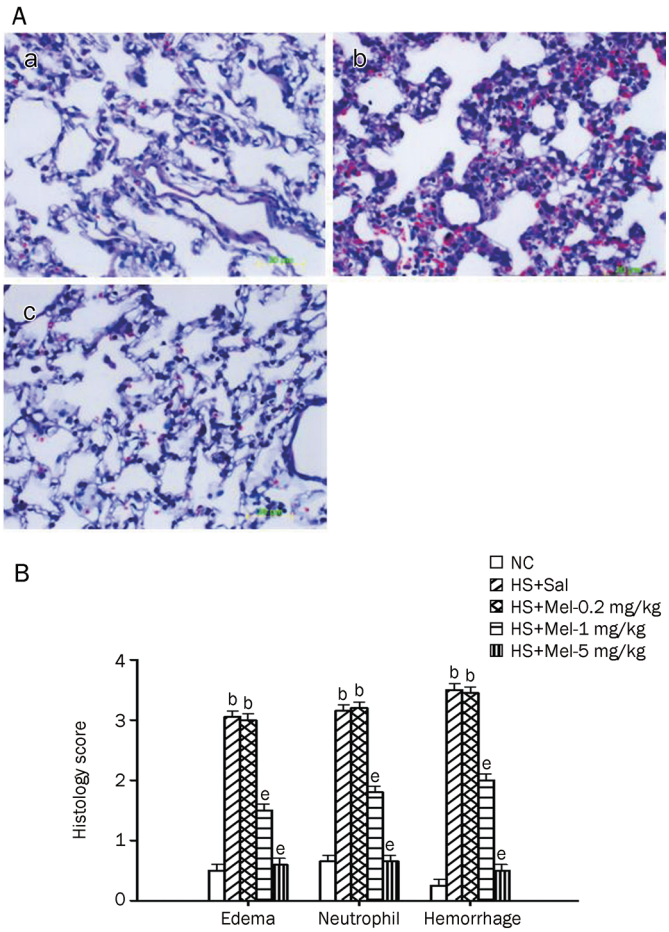

Figure 2. Histological examination of lung tissue from normothermic controls (NC), vehicle-treated heatstroke rats (HS+Sal), melatonin (0.2 mg/kg)-treated heatstroke rats (HS+Mel-0.2 mg/kg), melatonin (1 mg/kg)-treated heatstroke rats (HS+Mel-1 mg/kg), and melatonin (5 mg/kg)-treated heatstroke rats (HS+Mel-5 mg/kg). (A) Representative lung microscopic image from an NC rat (a), an HS+Sal rat (b), and an HS+Mel-5 mg/kg rat (c). The HS+Sal rats had interstitial edema, neutrophil accumulation and hemorrhage. The lung pathological changes that occurred during heatstroke were significantly attenuated by melatonin (1–5 mg/kg) ($P<0.05$). (B) The level of edema, neutrophils infiltration, and hemorrhage score. Data are expressed as the mean±SD. $n=6$. $^{b}P<0.05$ compared with the NC group; $^{e}P<0.05$ compared with the vehicle-treated heatstroke group (HS+Sal).

the MAP values were significantly lower than those of the normothermic controls ($P<0.05$). In contrast, the Tco values in the vehicle-treated heatstroke rats were significantly higher than those of the normothermic controls. Heatstroke-induced hyperthermia and hypotension were significantly and dose-dependently attenuated by melatonin therapy (1–5 mg/kg).

Melatonin therapy reduces acute lung injury during heatstroke

Figure 2 summarizes the effects of heat exposure on acute lung injury scores in rats treated with vehicle or with melatonin (0.2–5 mg/kg). A typical example of hematoxylin-eosin staining of the lung is depicted in Figure 2A. The images of the lungs that were not lavaged in the histology revealed that all the injury scores, including edema, neutrophil infiltration, and hemorrhage scores, were significantly increased in the vehicle-treated heatstroke group compared with the normothermic controls (Figure 2B). However, when compared with the vehicle-treated group, the animals of the melatonin (1–5 mg/kg)-treated heatstroke group had significantly lower injury scores (Figure 2B).

Melatonin therapy down-regulates exudate volume, BALF PMN cell number, and lung MPO activity during heatstroke

Figure 3 summarizes the effects of heat exposure on exudate volume, the number of PMN cells in the BALF, and lung MPO activity of normothermic controls, vehicle-treated heatstroke rats, and melatonin (0.2–5 mg/kg)-treated heatstroke rats. At 140 min after the start of heat exposure, the exudate volume, number of PMN cells in the BALF, and the lung MPO activity were greater in vehicle-treated heatstroke rats than in the normothermic controls. However, all these indicators of acute pleurisy were greatly attenuated by melatonin therapy.

Melatonin up-regulates BALF IL-10 levels but down-regulates BALF TNF-α, IL-1β, and IL-6 levels during heatstroke

Figure 4 summarizes the BALF IL-10, TNF-α, IL-1β, and IL-6 levels among the three experimental groups. Compared with

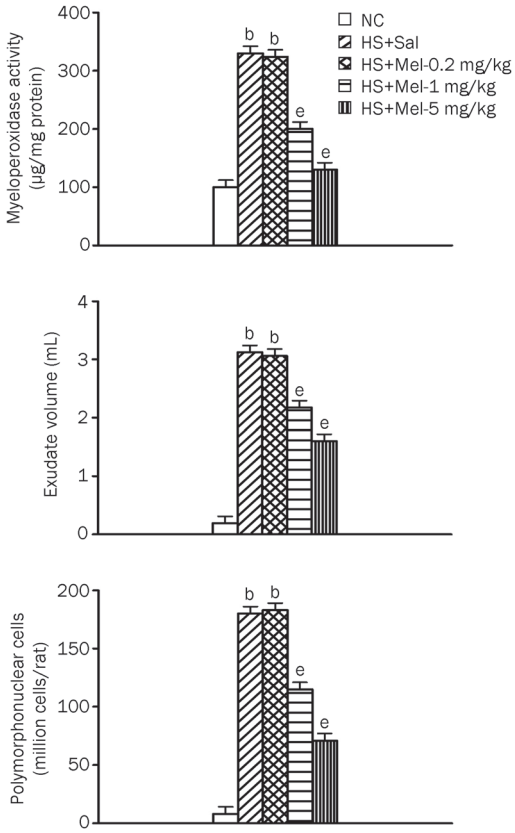

Figure 3. Exudate volume, number of PMN cells and MPO activity in lung tissues from NC, HS+Sal, HS+Mel (0.2 mg/kg), HS+Mel (1 mg/kg), and HS+Mel (5 mg/kg) rats. Data are expressed as mean±SD. n=6. ^{b}P<0.05 compared with the NC group; ^{e}P<0.05 compared with the HS+Sal group.

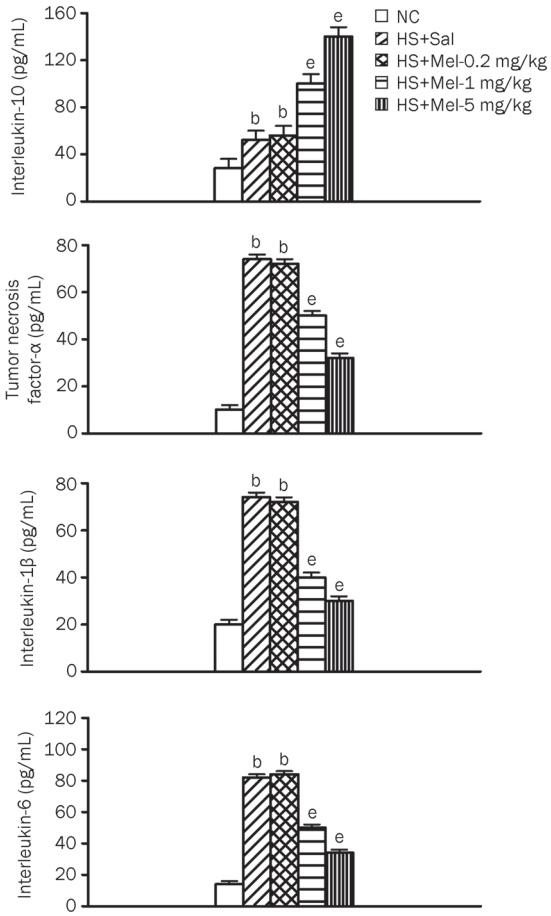

Figure 4. Interleukin-10, tumor necrosis factor-alpha, interleukin-1β, and interleukin-6 levels in BALF from the NC, HS+Sal, HS+Mel (0.2 mg/kg), HS+Mel (1 mg/kg), and HS+Mel (5 mg/kg) rat. Data are expressed as the mean±SD. n=6. ^{b}P<0.05 compared with the NC group; ^{e}P<0.05 compared with the HS+Sal group.

the normothermic controls, vehicle-treated heatstroke rats had significantly higher levels of IL-10, TNF-α, IL-1β, and IL-6 at 140 min after the onset of heat stress. The increase in the BALF levels of TNF-α, IL-1β, and IL-6 during heatstroke was significantly reduced by melatonin therapy (1–5 mg/kg). However, compared with vehicle-treated rats, melatonin therapy (1–5 mg/kg) further enhanced the BALF levels of heat-induced IL-10.

Melatonin therapy down-regulates the BAL levels of glutamate, NO, lactate-to-pyruvate ratio, 2,3-DHBA, and LDH during heatstroke

Figure 5 shows the levels of glutamate, NO, lactate-to-pyruvate ratio, 2,3-DHBA, and LDH in the BALF among the three experimental groups. Compared with normothermic controls, vehicle-treated heatstroke rats had significantly higher levels of all these markers 140 min after the start of heat stress. These increases were significantly reduced by melatonin therapy (1–5 mg/kg).

Discussion

On the level of the whole organism, severe heat stress (42–43 °C for ~70 min) caused hyperthermia (i.e., body core temperature >40 °C), hypotension (mean arterial pressure <50 mmHg), intracranial hypertension, splanchnic vasoconstriction, and hypoxia, which might facilitate the leakage of endotoxin from the intestine to the systemic circulation and result in excessive activation of PMN cells and endothelial cells[1, 2, 21]. In this study, mild heat stress (36 °C for 100 min) also caused hyperthermia, hypotension, and many aspects of heatstroke reactions, described below. This indicates that the MAP value of ~50 mmHg and hyperthermia (>40 °C body core temperature) used in the present study are sufficient to represent heat shock.

Endotoxin causes multiple organ dysfunction, including acute lung injury[22]. During acute lung injury, acute lung inflammation is characterized by the local recruitment and activation of PMNs[23] and the release of proinflammatory mediators[24, 25], proteases, and reactive oxygen and nitrogen species[26, 27]. These reactions lead to alveolar-capillary damage, with high permeability lung edema and alteration of lung mechanics, and result in severe gas exchange abnormalities[28]. Endotoxin can stimulate the overproduction of a variety of

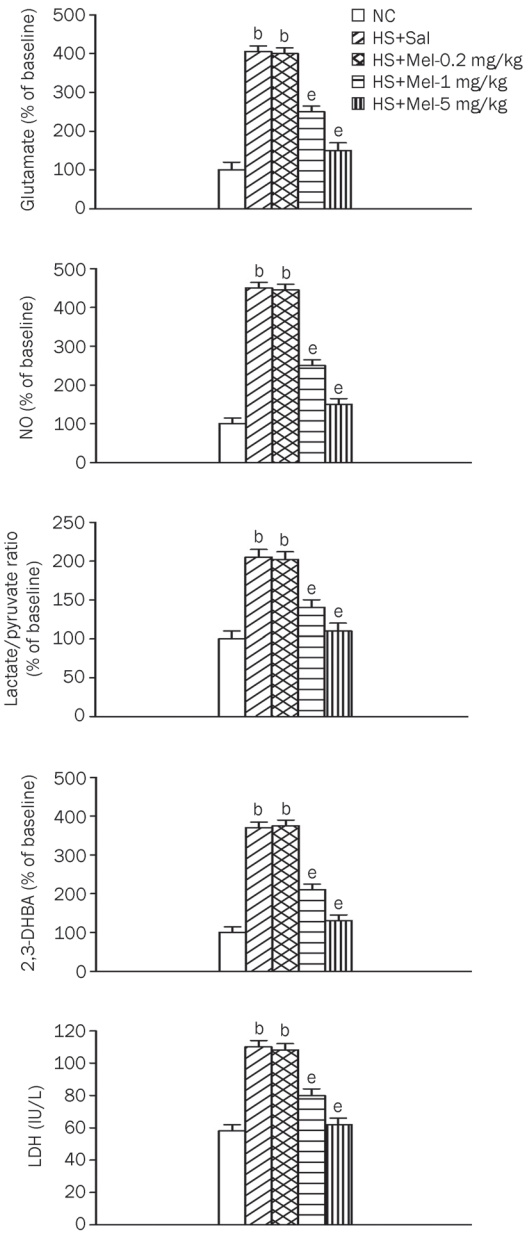

Figure 5. Glutamate, lactate-to-pyruvate ratio, lactate dehydrogenase (LDH), nitric oxide metabolites (NO), and 2,3-dihydroxybenzoic acid (2,3-DHBA) levels in BALF from the NC, HS+Sal, HS+Mel (0.2 mg/kg), HS+Mel (1 mg/kg), and HS+Mel (5 mg/kg) rats. Data are expressed the mean±SD. n=6. ^{b}P<0.05 compared with the NC group; ^{e}P<0.05 compared with the HS+Sal group.

proinflammatory mediators, such as TNF-α, IL-1β, IL-6, and NO[29]. Concurrently, IL-10, an anti-inflammatory cytokine, is induced to limit the net inflammatory response in the lungs[30]. The pleiotropic transcription factor nuclear-kappa B (NF-κB) also plays a crucial role in regulating the expression of cytokines, chemokines, adhesion molecules, and other mediators[22, 31].

Like endotoxin-induced septic shock, heatstroke rats showed (i) increased lung activity of MPO (an indicator for PMN cell infiltration); (ii) increased exudate volume and PMN cell numbers (indicators of acute pleurisy); (iii) increased BALF levels of proinflammatory cytokines, such as TNF-α and IL-1β, and the anti-inflammatory cytokine IL-10; (iv) increased BALF levels of glutamate and the lactate-to-pyruvate ratio (cellular ischemia markers), the toxic oxidizing radicals NO and 2,3-DHBA, and LDH (an indicator of toxic organ injury); and (v) increased acute lung edema, neutrophil infiltration, and hemorrhage scores.

This study provides the first data showing the beneficial effects of melatonin on acute lung inflammation and injury in heatstroke rats. Our results clearly indicate that melatonin treatment significantly (i) reduced acute lung injury, including edema, neutrophil infiltration, and hemorrhage scores; (ii) decreased acute pleurisy; (iii) decreased BALF levels of proinflammatory cytokines, a cellular ischemia marker, and ischemic and oxidative damage markers; and (iv) reduced lung MPO activity in rats during heatstroke. In conclusion, heatstroke causes acute lung inflammation and injury, and melatonin has a beneficial effect against acute lung inflammation and injury in heatstroke. Therefore, melatonin has a therapeutic potential in the clinical treatment of lung inflammation and injury.

Our results are partly consistent with previous findings obtained from different disease models. For example, melatonin reduces acute lung injury in endotoxemic rats[22] or in sleep-deprived mice[32] by attenuating pulmonary inflammation and inhibiting NF-κB activation[22]. Melatonin protects against acute lung injury caused by radiation therapy in a rat model[26]. Additionally, oral melatonin attenuates acute lung injury caused by the inhalation of aerosolized pancreatic fluids in rats by reducing lung inflammation and airway hyperactivity[10]. Leukocyte rolling and adhesion to the microcirculation in rats is inhibited by melatonin[27]. Melatonin attenuates paraquet-induced acute lung toxicity in rats by inhibiting oxidative damage[28]. Melatonin is efficient in ameliorating ischemia/reperfusion injury of the intestine and lung in rats by inhibiting both oxidative and nitrosative stress in these organs[33]. Together, these observations led us to conclude that melatonin might attenuate heatstroke-induced acute lung injury in rats by inhibiting pulmonary inflammation, NF-κB activation, and oxidative and nitrosative stress in the lung. Of course, the hypothesis warrants further verification in future studies.

It has been shown that the BALF levels of pro-inflammatory cytokines, such as IL-1β, are elevated in patients with adult respiratory distress syndrome[34]. An overproduction of TNF-α is also noted in endotoxin-induced lung inflammation[35]. Both our previous[6] and present results confirm that the inflammatory process (*eg*, heat-induced acute pleurisy) leads to the overproduction of pro-inflammatory cytokines, such as TNF-alpha, IL-1β, and IL-6, in the BALF. Our results further show that the increased BALF levels of both IL-1β and TNF-α during experimental heatstroke can be reduced by melatonin. In addition, BALF IL-10 levels in heatstroke are elevated by melatonin. IL-10 can attenuate both IL-1β and TNF-α production[36]. Therefore, melatonin may attenuate acute lung

inflammation during heatstroke by stimulating IL-10 production and inhibiting the production of proinflammatory cytokines, including IL-1β and TNF-α, in the BALF.

The above-mentioned pro-inflammatory cytokines lead to the release of large amounts of the toxic oxidizing radicals, such as NO, superoxide anion (O_2^-), and hydroxyl radicals, from neutrophils, macrophages, and monocytes, which causes multiple organ injury via the peroxidation of membrane lipids, the oxidative damage of proteins and DNA[37], or the augmentation of local tissue injury[38]. This systemic inflammatory response would result in the sequestration of polymorphonuclear cells in the lung and liver, which would lead to vascular dysfunction and multiple organ dysfunction[39]. In the present study, melatonin therapy may have caused the attenuation of acute lung injury in heatstroke by reducing the overproduction of pro-inflammatory cytokines, toxic oxidizing radicals, the sequestration of polymorphonuclear cells, and organ damage markers in lung tissues.

Both glutamate and the lactate-to-pyruvate ratio are markers of cellular ischemia[40, 41]. Our data show that the excessive elevation of both glutamate levels and the lactate-to-pyruvate ratio in the BALF occurred during heatstroke, suggesting that heat stress causes lung ischemia. We further demonstrate that heat-induced lung ischemia can be attenuated by melatonin.

It should be stressed that our previous results demonstrated that systemic administration of melatonin immediately before the onset of heatstroke significantly prolongs the survival time of rats[13]. In the present study, the delivery of melatonin immediately after the onset of heatstroke also significantly prolonged survival time. The results indicate that melatonin can be used as both a prophylactic and a therapeutic agent for experimental heatstroke. As shown by our previous and present results, the time to death of heatstroke rats treated with melatonin was prolonged, but all the animals eventually died. In fact, these animals were under general urethane anesthesia. To verify that there was durable improvement in survival, unanesthetized, unrestrained animals with or without melatonin treatment should be exposed to heat stress.

In summary, the present study provides the data showing that the occurrence of pulmonary edema, inflammation, and ischemic and oxidative damage caused by heatstroke in rats can be attenuated by melatonin therapy.

Key messages

Heatstroke rats display acute lung edema, inflammation, and injury. Melatonin therapy significantly attenuated heat-induced acute lung edema, inflammation, and injury.

Abbreviations

Tco, core body temperature; Ta, ambient temperature; MAP, mean arterial pressure; PMN, polymorphonuclear; LDH, lactate dehydrogenase; NO, nitric oxide; DHBA, dihydroxybenzoic acid; BALF, bronchoalveolar fluid; TNF-α, tumor necrosis factor-alpha; IL-1β, interleukin-1β; IL-6, interleukin-6; IL-10, interleukin-10; MPO, myeloperoxidase.

Author contribution

Mao-tsun LIN and Ching-ping CHANG helped to draft the manuscript or to critically revise it. Furthermore, Chen-kuei CHANG, Mao-tsun LIN, Wen-shiann WU, Ming-ting CHOU,and Chien-ming CHAO participated in the design, coordination and data acquisition of the study. Wen-shiann WU and Ching-ping CHANG participated in the statistical analysis.

References

1 Bouchama A, Knochel JP. Heat stroke. N Engl J Med 2002; 346: 1978–88.
2 Chang CK, Chang CP, Chiu WT, Lin MT. Prevention and repair of circulatory shock and cerebral ischemia/injury by various agents in experimental heatstroke. Curr Med Chem 2006; 13: 3145–54.
3 Sharma HS, Westman J. Brain function in hot environment. Progress in brain research, vol 115. Elsevier, Amsterdam, 1998. p 1–516.
4 Varghese GM, John G, Thomas K, Abraham OC, Mathai D. Predictors of multi-organ dysfunction in heatstroke. Emerg Med J 2005; 22: 185–7.
5 Yang HH, Chang CP, Cheng JT, Lin MT. Inhibition of acute lung inflammation and injury is a target of brain cooling after heatstroke injury. J Trauma 2010; 69: 805–12.
6 Yang HH, Chang CP, Cheng JT, Lin MT. Attenuation of acute lung inflammation and injury by whole body cooling in a rat heatstroke model. J Biomed Biotechnol 2009; 2009: 768086.
7 Menendez-Pelaez A, Reiter RJ. Distribution of melatonin in mammalian tissues: the relative importance of nuclear versus cytosolic localization. J Pineal Res 1993; 15: 59–69.
8 Reiter RJ, Tan DX. What constitutes a physiological concentration of melatonin? J Pincal Res 2000; 34: 79–80.
9 Galano A, Tan DX, Reiter RJ. Melatonin as a natural ally against stress: a physicochemical examination. J Pineal Res 2011; 51: 1–16.
10 Chen CF, Wang D, Reiter RJ, Yeh DY. Oral melatonin attenuates lung inflammation and airway hyperreactivity induced by inhalation of aerosolized pancreatic fluid in rats. J Pineal Res 2011; 50: 46–53.
11 Manda K, Ueno M, Anzai K. AFMK, a melatonin metabolite, attenuates X-ray-induced oxidative damage to DNA, proteins and lipids in mice. J Pineal Res 2007; 42: 386–93.
12 Hardeland R, Backhaus C, Fadavi A. Reactions of the NO redox forms NO+, *NO and HNO (protonated NO-) with the melatonin metabolite N1-acetyl-5-methoxykynuramine. J Pineal Res 2007; 43: 382–8.
13 Lin XJ, Mei GP, Liu J, Li YL, Zuo D, Liu SJ, *et al*. Therapeutic effects of melatonin on heatstroke-induced multiple organ dysfunction syndrome in rats. J Pineal Res 2011; 50: 436–44.
14 Li Z, Gao C, Wang Y, Liu F, Ma L, Deng C, *et al*. Reducing pulmonary injury by hyperbaric oxygen preconditioning during simulated high altitude exposure in rats. J Trauma 2011; 71: 673–9.
15 Su X, Bai C, Hong Q, Zhu D, He L, Wu J, *et al*. Effect of continuous hemofiltration on hemodynamics, lung inflammation and pulmonary edema in a canine model of acute lung injury. Intensive Care Med 2003; 29: 2034–42.
16 Chou YT, Lai ST, Lee CC, Lin MT. Hypothermia attenuates circulatory shock and cerebral ischemia in experimental heatstroke. Shock 2003; 19: 388–93.
17 Yamada K, Nabeshima T. Simultaneous measurement of nitrite and nitrate levels as indices of nitric oxide release in the cerebellum of conscious rats. J Neurochem 1997; 68: 1234–43.
18 Togashi H, Mori K, Ueno K, Matsumoto M, Suda N, Saito H, *et al*.

Consecutive evaluation of nitric oxide production after transient cerebral ischemia in the rats hippocampus using *in vivo* brain microdialysis. Neurosci Lett 1998; 240: 53–7.
19 Yang CY, Lin MT. Oxidative stress in rats with heatstroke-induced cerebral ischemia. Stroke 2002; 33: 790–4.
20 Mullane KM, Kraemer R, Smith B. Myeloperoxidase activity as a quantitative assessment of neutrophil infiltration into ischemic myocardium. J Pharmacol Methods 1985; 14: 157–67.
21 Hall DM, Buettner GR, Oberley LW, Xu L, Matthes RD, Gisolfi CV. Mechanisms of circulatory and intestinal barrier dysfunction during whole body hyperthermia. Am J Physiol Heart Circ Physiol 2001; 280: H509–21.
22 Shang Y, Xu SP, Wu Y, Jiang YX, Wu ZY, Yuan SY, *et al*. Melatonin reduces acute lung injury in endotoxemic rats. Chin Med J 2009; 122: 1388–93.
23 Chignard M, Balloy V. Neutrophil recruitment and increased permeability during acute lung injury induced by lipopolysaccharide. Am J Physiol Lung Cell Mol Physiol 2000; 279: L1083–90.
24 Wright RM, Ginger LA, Kosila N, Elkins ND, Essary B, McManaman JL, *et al*. Mononuclear phagocyte xanthine oxidoreductase contributes to cytokine-induced acute lung injury. Am J Respir Cell Mol Biol 2004; 30: 479–90.
25 Shinbori T, Walczak H, Krammer PH. Activated T killer cells induce apoptosis in lung epithelial cells and the release of pro-inflammatory cytokine TNF-alpha. Eur J Immunol 2004; 34: 1762–70.
26 Haddad IY, Pataki G, Hu P, Galliani C, Beckman JS, Matalon S. Quantitation of nitrotyrosine levels in lung sections of patients and animals with acute lung injury. J Clin Invest 1994; 94: 2407–13.
27 Matthay MA, Geiser T, Matalon S, Ischiropoulos H. Oxidant-mediated lung injury in the acute respiratory distress syndrome. Crit Care Med 1999; 27: 2028–30.
28 Liu D, Zeng BX, Shang Y. Decreased expression of peroxisome proliferator-activated receptor gamma in endotoxin-induced acute lung injury. Physiol Res 2006; 55: 291–9.
29 Liu D, Zeng BX, Zhang SH, Wang YL, Zeng L, Geng ZL, *et al*. Rosiglitazone, a peroxisome proliferator-activated receptor-gamma agonist, reduces acute lung injury in endotoxemic rats. Crit Care Med 2005; 33: 2309–16.
30 Pedreira PR, García-Prieto E, Parra D, Astudillo A, Diaz E, Taboada F, *et al*. Effects of melatonin in an experimental model of ventilator-induced lung injury. Am J Physiol Lung Cell Mol Physiol 2008; 295: L820–7.
31 Ali S, Mann DA. Signal transduction via the NF-kappaB pathway: a targeted treatment modality for infection, inflammation and repair. Cell Biochem Funct 2004; 22: 67–79.
32 Lee YD, Kim JY, Lee KH, Kwak YJ, Lee SK, Kim OS, *et al*. Melatonin attenuates lipopolysaccharide-induced acute lung inflammation in sleep-deprived mice. J Pineal Res 2009; 46: 53–7.
33 Kesik V, Guven A, Vurucu S, Tunc T, Uysal B, Gundogdu G, *et al*. Melatonin and 1400 W ameliorate both intestinal and remote organ injury following mesenteric ischemia/reperfusion. J Surg Res 2009; 157: e97–105.
34 Pugin J, Ricou B, Steinberg KP, Suter PM, Martin TR. Proinflammatory activity in bronchoalveolar lavage fluids from patients with ARDS, a prominent role for interleukin-1. Am J Resp Crit Care Med 1996; 153: 1850–6.
35 Xing Z, Jordana M, Kirpalani H, Driscoll KE, Schall TJ, Gauldie J. Cytokine expression by neutrophils and macrophages *in vivo*: endotoxin induces tumor necrosis factor-alpha, macrophage inflammatory protein-2, interleukin-1 beta, and interleukin-6 but not RANTES or transforming growth factor-beta 1 mRNA expression in acute lung inflammation. Am J Resp Cell Molec Biol 1994; 10: 148–53.
36 Oberholzer A, Oberholtz C, Moldawer LL. Cytokine signaling-regulation of the immune response in normal and critically ill states. Crit Care Med 2000; 28: N3–12.
37 Feihl F, Wasber B, Liaudet L. Is nitric oxide overproduction the target of choice for the management of septic shock? Pharmacol Ther 2001; 91: 179–213.
38 Kim PK, Deutscheman CS. Inflammatory responses and mediators. Surg Clin North Am 2000; 80: 885–94.
39 Neviere RR, Cepinskas G, Madorin WS, Hoque N, Karmazyn M, Sibbald WJ, *et al*. LPS pretreatment ameliorates peritonitis-induced myocardial inflammation and dysfunction: role of myocytes. Am J Physiol 1999; 277: H885–92.
40 Persson L, Hillered L. Chemical monitoring of neurosurgical intensive care patients using intracerebral microdialysis. J Neurosurg 1992; 76: 72–80.
41 Hillered L, Persson L. Neurochemical monitoring of the acutely injured human brain. Scand J Clin Lab Invest Suppl 1999; 229: 9–18.

Acta Pharmacologica Sinica (2012) 33: 783–790
 1671-4083/12 $32.00
www.nature.com/aps

Original Article

Characterization of the immune responses elicited by baculovirus-based vector vaccines against influenza virus hemagglutinin

Zhi-peng HU, Juan YIN, Yuan-yuan ZHANG, Shu-ya JIA, Zuo-jia CHEN, Jiang ZHONG*

Department of Microbiology and Microbial Engineering, School of Life Sciences, Fudan University, Shanghai 200433, China

Aim: To compare the specific immune responses elicited by different baculovirus vectors in immunized mice.
Methods: We constructed and characterized two recombinant baculoviruses carrying the expression cassette for the H5N1 influenza virus hemagglutinin (HA) gene driven by either an insect cell promoter (vAc-HA) or a dual-promoter active both in insect and mammalian cells (vAc-HA-DUAL). Virus without the HA gene (vAc-EGFP) was used as a control. These viruses were used to immunize mice subcutaneously and intraperitoneally. The production of total and specific antibodies was determined by ELISA and competitive ELISA. Cytokine production by the spleen cells of immunized mice was studied using the ELISPOT assay.
Results: Both the vAc-HA and vAc-HA-DUAL vectors expressed HA proteins in insect Sf9 cells, and HA antigen was present in progeny virions. The vAc-HA-DUAL vector also mediated HA expression in virus-transduced mammalian cell lines (BHK and A547). Both vAc-HA and vAc-HA-DUAL exhibited higher transduction efficiencies than vAc-EGFP in mammalian cells, as shown by the expression of the reporter gene egfp. Additionally, both vAc-HA and vAc-HA-DUAL induced high levels of HA-specific antibody production in immunized mice; vAc-HA-DUAL was more efficient in inducing IFN-γ and IL-2 upon stimulation with specific antigen, whereas vAc-HA was more efficient in inducing IL-4 and IL-6.
Conclusion: Baculovirus vectors elicited efficient, specific immune responses in immunized mice. The vector displaying the HA antigen on the virion surface (vAc-HA) elicited a Th2-biased immune response, whereas the vector displaying HA and mediating HA expression in the cell (vAc-HA-DUAL) elicited a Th1-biased immune response.

Keywords: baculovirus; H5N1 avian influenza; hemagglutinin; immune response; vector vaccine

Acta Pharmacologica Sinica (2012) 33: 783–790; doi: 10.1038/aps.2012.23; published online 7 May 2012

Introduction

The H5N1 avian influenza virus is a highly contagious virus that causes significant morbidity and mortality worldwide. It infects not only avian species but also humans. Over 565 human cases have been reported, of which 331 cases were fatal[1]. New prophylactic and therapeutic strategies are essential for pandemic influenza preparedness[2].

The baculovirus *Autographa californica* multiple nucleopolyhedrovirus (AcMNPV) has been widely used to overexpress recombinant proteins in insect cells. Recently, it has also been found to enter mammalian cells efficiently and without viral replication. Modified AcMNPV can express exogenous genes in mammalian cells when controlled by promoters active in mammalian cells. The list of mammalian cells permissive to baculovirus transduction has expanded rapidly[3]. Because of its excellent biosafety and high efficiency in gene delivery, baculovirus is believed to have great potential as a novel vector for gene therapy and vaccine development[3, 4].

Two basic approaches have been explored to develop baculovirus as a vaccine vector. One approach is to insert the expression cassette of the target antigen into the viral genome so that the recombinant virus can produce the antigen inside the host cells. The second approach is to display the antigen on the virion surface. Both approaches have been shown to elicit efficient immune responses against target antigens *in vivo*[5–8].

In the current study, two recombinant baculoviruses were constructed, one displaying the influenza virus HA protein only on the virion surface, and the other both displaying HA and mediating HA expression in mammalian cells. Although both viruses elicited efficient responses in immunized mice, they showed different biases with regard to Th1 and Th2 balance. Our results provide new insight into the immune responses elicited by baculovirus vectors and indicate that

* To whom correspondence should be addressed.
E-mail jzhong@fudan.edu.cn
Received 2011-12-05 Accepted 2012-02-29

baculoviruses can be used as efficient vectors for vaccine development[9, 10].

Materials and methods

Construction of recombinant baculovirus vectors

The pFB-EGFP plasmid was constructed as follows. The enhanced green fluorescence protein gene (*egfp*), driven by the tandemly arranged promoters of baculovirus p10 and CMV IE1, was digested from pFB-GR using *Xba* I and inserted into the *Xba* I site of pFastBac1 (Invitrogen, Carlsbad, CA, USA). The full-length HA gene from the H5N1 highly pathogenic avian influenza virus was constructed from the HA gene sequence of A/Vietnam/1203/2004 (GenBank accession No AY818135) by annealing synthetic oligonucleotides and amplifying with PCR. The full-length gene was verified by DNA sequencing; it was then inserted into pFB-EGFP between the *Bam*H I and *Sal* I sites downstream of the baculovirus polyhedrin promoter to generate the plasmid pFB-HA.

The pFB-HA-DUAL plasmid was constructed by inserting the CMV IE1 promoter into the *Bam*H I site between the polyhedrin promoter and the HA coding sequence in pFB-HA. The CMV IE1 promoter was generated by PCR using pFB-EGFP as the template and the primers 5′-GGCGGATCCCGTTACATAACTTACGGTAAATGGCCCGCCTGGC-3′ and 5′-GCCGGATCCCGGTGTCTTCTATGGAGGTCAAAACAGCGTGG-3′.

Virus and cells

The recombinant baculoviruses, vAc-EGFP, vAc-HA, and vAc-HA-DUAL, were generated from the plasmids, pFB-EGFP, pFB-HA, and pFB-HA-DUAL, respectively, using the Bac-to-Bac system (Invitrogen) according to the manufacturer's instructions. Viruses were grown in *Spodoptera frugiperda* (Sf9) cells at a Multiplicity of Infection (MOI) of 0.1 (plaque forming units/cell) and harvested 4 d post-infection. Virus titers were determined by end-point dilution assay in Sf9 cells[11]. Viruses in the supernatant were concentrated by centrifugation at 40 000×*g* for 1 h; pellets were suspended in PBS and further purified by 25%–60% sucrose gradient ultracentrifugation at 100 000×*g* for 1 h. To determine the distribution of HA proteins, purified virions were treated with an equal volume of 1% Triton X-100 for 15 min to disrupt the viral envelope, and the viral nucleocapsids were collected by centrifugation at 50 000×*g* for 1 h.

Sf9 cells were cultured at 27 °C in TNM-FH medium (Sigma-Aldrich, St Louis, MO, USA) supplemented with 10% fetal bovine serum (FBS), 100 μg/mL streptomycin and 100 U/mL penicillin. Baby hamster kidney (BHK) and human lung (A549) cell lines were cultured in Dulbecco's modified Eagle's medium (DMEM, Invitrogen) supplemented with 10% FBS, 100 μg/mL streptomycin, and 100 U/mL penicillin at 37 °C and 5% CO_2.

Baculovirus transduction of mammalian cells

BHK or A549 cells were seeded in 24-well plates and cultured until the cells reached approximately 70%–80% confluence. Then, the culture medium was removed, and the cells were washed three times with PBS (pH 7.4). The baculovirus inoculum was added to the cells to an MOI of 200, and the cells were incubated for 2 h at 37 °C. Virus was removed, fresh medium was added, and the cells were incubated at 37 °C for another 24 h before the expression of HA was examined[12–14].

Western blot analysis

Total protein from cell or virus samples was separated using 10% sodium dodecyl sulfate-polyacrylamide gel electrophoresis (SDS-PAGE) and transferred to polyvinylidene difluoride (PVDF) membranes. Mouse antibody against HA (H5-specific, 1:5000 dilution, USBiological, Swampscott, MA, USA) and alkaline phosphatase-conjugated goat anti-mouse IgG (1:30 000 dilution, Sigma-Aldrich) were used as the primary and secondary antibodies, respectively. Blots were developed with NBT and BCIP.

Flow cytometry

BHK or A549 cells were transduced with baculovirus at an MOI of 10 for BHK cells and an MOI of 100 for A549 cells as described above, then cultured for 24 h. The cells were detached by trypsinization, washed twice with PBS and analyzed for green fluorescence by flow cytometry (Becton Dickinson FACS Calibur). A minimum of 10 000 events were collected and analyzed for each sample. Data were analyzed using the CELLQUEST software. Representative results from at least three independent experiments are shown.

Immunization of mice

Six- to eight-week-old female BALB/c mice (Animal Center, Shanghai Institutes for Biological Science, Shanghai, China) were randomly divided into three groups with 8 mice per group (n=8). The mice were immunized twice, separated by 14 d, both subcutaneously and intraperitoneally, with 1×10^9 pfu of recombinant baculovirus per inoculum. Immunized mice were housed in the SPF animal facility at Fudan University (Shanghai, China) under constant conditions of 23±1 °C, 40%±5% humidity and a 12 h:12 h light/dark cycle, with free access to pellet food and tap water. All animal experiments were performed in accordance with the Guide for the Care and Use of Laboratory Animals and were approved by the Ethics Committee for Animal Care and Use of Fudan University. One week following the second immunization, serum samples were collected from the retro-orbital plexus for serological testing and antibody assay; the mice were sacrificed, and splenocytes were harvested for ELISPOT assay.

Enzyme-linked immunosorbent assay (ELISA) and competitive ELISA

The expressed amount of HA-specific antibody in immunized mice was determined by competitive ELISA using an H5-subtype HA detection kit (AXIOM, Burstadt, Germany) and the negative and positive control samples provided by the kit. The levels of total IgG and IgA in the mice were also determined using ELISA kits (ADI, San Antonio, TX, USA).

All steps were performed according to the manufacturer's instructions. The antibody concentrations in the samples were calculated from standard curves.

Splenocytes were harvested from the mice one week after the second immunization and cultured in 24-well plates (1×10^6/well) at 37°C and 5% CO_2 in the presence of one of the following: an HA-specific peptide (a 14-mer peptide from the middle region of HA, 5 μg/mL, Biodesign, catalog number R88640), a non-specific peptide (a 16-mer peptide from the middle region of neuraminidase, 5 μg/mL, Biodesign, catalog number R88440) or plant hemagglutinin (PHA, 2.5 μg/mL). A control of untreated splenocytes was also included. After 72 h of incubation, the culture supernatant was harvested, and the level of IFN-γ and IL-4 in the supernatant was determined using mouse IFN-γ and IL-4 immunoassay ELISA kits (Dakewei, Shenzhen, China) according to the manufacturer's instructions. The concentrations of IFN-γ and IL-4 in the samples were determined using standard curves.

ELISPOT assay

The number of splenocytes producing cytokines upon antigen stimulation was determined using the ELISPOT assay (U-CyTech, Netherlands) according to the manufacturer's instructions. Briefly, 96-well plates were coated overnight at 4 °C with 100 μL per well of specific antibody against the cytokines of interest (IFN-γ, IL-2, IL-4, or IL-6). The plates were washed three times with sterile and pyrogen-free PBS and blocked with blocking buffer for 1 h at 37°C. The splenocytes from immunized mice were added to the wells (1×10^5/well) in RPMI-1640 containing either the HA peptide, the NA peptide or PHA as described above. Mock-stimulated and blank controls were included. The cells were cultured for 24 h at 37°C, 5% CO_2 and 100% humidity. Cultured cells were washed twice with PBS and 5 times with wash buffer (PBS with 0.05% Tween-20). Then, 100 μL of properly diluted (1:10) biotinylated detection antibodies was added to each well, and the plate was incubated for 1 h at 37 °C. After washing both sides of the PVDF membrane 5 times with wash buffer, 100 μL of properly diluted (1:10) streptavidin-HRP solution was added to each well, and the plate was incubated for 1 h at 37 °C. The plate was washed as described above and developed for 25 min at room temperature in the dark with the peroxidase substrate AEC. The reaction was stopped by thoroughly rinsing both sides of the PVDF membrane with deionized water. The plates were air dried at room temperature, and the spots were counted using an immunospot image analyzer. The blank control consistently demonstrated fewer than 10 SFC (spot forming cells) per 10^6 splenocytes.

Statistical analysis

Means from at least 3 replicates are shown along with error bars representing the standard deviations. Animal experiments were repeated at least twice for each treatment. Student's *t*-test was used to compare humoral or cellular immune responses between different groups, and *P*-values less than 0.05 were considered statistically significant .

Results

Construction of recombinant viruses

Recombinant baculoviruses for the expression of H5N1 influenza virus HA protein in insect cells (vAc-HA), or in both insect cells and mammalian cells (vAc-HA-DUAL), were constructed. Both viruses contained an *egfp*-gene expression cassette for both insect and mammalian cells. The control virus, vAc-EGFP, contained the egfp gene but not the HA gene. The genomic structure of the three recombinant viruses is shown in Figure 1.

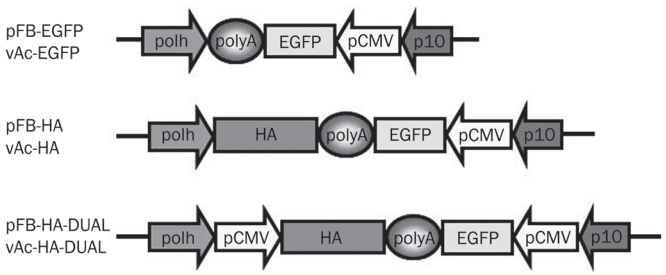

Figure 1. Schematic illustration of recombinant baculoviruses. The EGFP and HA expression cassettes were inserted in the polyhedrin locus.

Presence of HA on the viral envelope

Western blotting using anti-HA monoclonal antibodies revealed a protein of approximately 72 kDa in Sf9 cells infected by vAc-HA and vAc-HA-DUAL (Figure 2A). By contrast, no HA protein was observed in cells infected by vAc-EGFP. Mock-treated cells were uninfected.

Virions produced by the recombinant baculoviruses were purified from the medium of infected Sf9 cells and examined for the presence of HA protein using Western blotting. As shown in Figure 2B, HA proteins were found in vAc-HA and vAc-HA-DUAL virions but not in vAc-EGFP virions. When the virions were treated with Triton X-100 to dissolve the viral envelopes, HA proteins were no longer present (Figure 2B), indicating that the HA proteins were localized to the viral envelope.

Baculovirus-mediated HA expression in mammalian cells

The recombinant baculoviruses vAc-EGFP, vAc-HA, and vAc-HA-DUAL were used to transduce BHK cells at an MOI of 100. Green fluorescence was observed in cells transduced by all three viruses 24 h post-transduction (pt) (data not shown). As expected, Western blot analysis using anti-HA antibodies demonstrated HA expression only in BHK cells transduced with vAc-HA-DUAL (Figure 2C). The HA protein was partially cleaved to HA1 (55 kDa) and HA2 in BHK cells.

Growth curves for recombinant baculoviruses

The growth kinetics of recombinant baculoviruses in Sf9 cells were assayed, and the results are shown in Figure 3. Recombinant viruses expressing HA on their envelopes (vAc-HA and vAc-HA-DUAL) grew slower than the control virus (vAc-

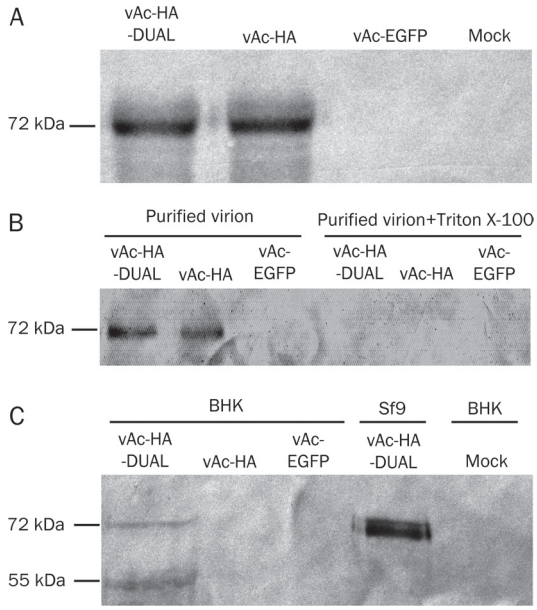

Figure 2. Expression of HA protein cells and its presence in the virion. (A) HA protein expressed in Sf9 cell. Total cellular extracts from Sf9 cells infected with vAc-HA-DUAL, vAc-HA, and vAc-EGFP were analyzed with SDS-PAGE and Western blot. Uninfected Sf9 cells were used as a mock control. (B) Localization of HA in the envelop of vAc-HA and vAc-HA-DUAL virus particles. Purified virion and virion treated with Triton X-100 to remove the envelop were examined for HA protein with Western blot. (C) Expression of the HA protein in baculovirus-transduced BHK cells. Sf9 cells infected with vAc-HA-DUAL and untransduced BHK cells were used as positive or negative controls, respectively. The HA protein expressed in BHK cells was partially cleaved to HA1 and HA2.

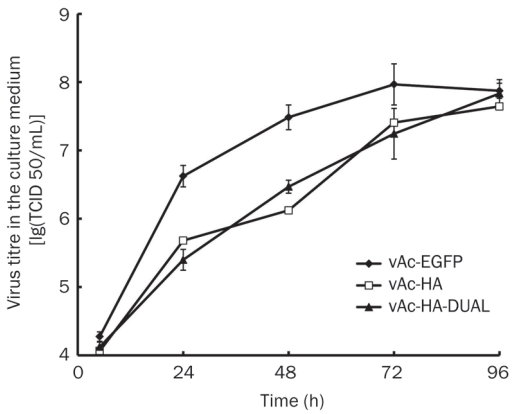

Figure 3. Virus growth curves in Sf9 cells. Sf9 cells were infected with vAc-EGFP, vAc-HA, and vAc-HA-DUAL at MOI 1. Each data point represents the mean value of 3 replicates.

EGFP), with a lag time of approximately 24 h. However, the recombinants reached similar titers as vAc-EGFP late in the infection (96 h post-infection). Extensive syncytium formation was also observed in Sf9 cells infected with vAc-HA and vAc-HA-DUAL (data not shown).

Transduction efficiency of the HA-displaying baculoviruses

BHK and A549 cells were transduced with recombinant baculoviruses at an MOI of 10 and 100, respectively. The cells were analyzed for green fluorescence using flow cytometry 36 h pt. As shown in Figure 4, the percentages of EGFP-positive cells in BHK cells transduced by vAc-HA and vAc-HA-DUAL were both twice as high as in cells transduced by vAc-EGFP. Similar differences were observed between HA-displaying recombinant viruses and the control virus in A549 cells. In both cell lines, similar percentages of EGFP-positive cells were observed with vAc-HA and vAc-HA-DUAL. These results indicate that the HA protein on the surface of recombinant baculoviruses preserved its native activity and contributed to viral entry into mammalian cells.

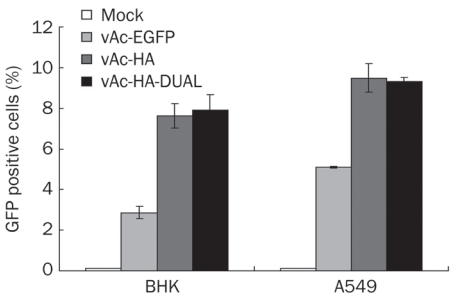

Figure 4. Transduction efficiency of HA-displaying baculoviruses. BHK and A549 cells were transduced with baculoviruses at MOI of 10 and 100, respectively, collected at 24 h post transduction, and analyzed by flow cytometry for EGFP expression.

Antibody responses in mice immunized with recombinant baculoviruses

Mice were vaccinated twice (d 1 and d 15) with recombinant baculoviruses and specific serum antibodies against HA were measured on d 21 using a competitive ELISA; higher ELISA readings indicate lower levels of anti-HA antibodies. As shown in Figure 5, HA-specific antibodies were produced in mice immunized with vAc-HA and vAc-HA-DUAL. No significant difference in antibody levels was observed between the two viruses, and no significant levels of HA-specific antibodies were observed in vAc-EGFP-immunized mice.

The levels of total serum IgA and IgG in immunized mice were also determined (Figure 6). vAc-HA and vAc-HA-DUAL induced 3–4 times more IgA and IgG than vAc-EGFP, and vAc-HA elicited 20% more IgA and IgG than vAc-HA-DUAL. The reason for these differences remains to be elucidated.

Production of Th1 and Th2 cytokines by splenocytes from immunized mice

The splenocytes from immunized mice were examined for the production of Th1 (IFN-γ and IL-2) and Th2 cytokines (IL-4

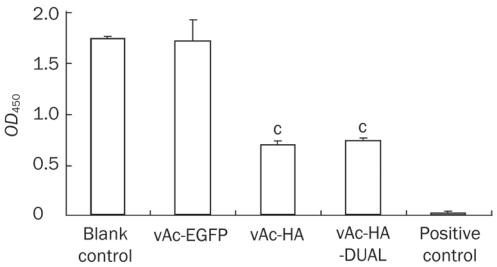

Figure 5. HA-specific antibody in serum of baculovirus-immunized mice. Sera of mice were immunized with vAc-HA-DUAL, vAc-HA, and vAc-EGFP were collected 21 d after the first immunization. The titers of HA specific antibody were measured by ELISA. According to the manufacturer's instruction, higher OD means negative results. Negative control and Positive control were provided by the kit. $^{c}P<0.01$.

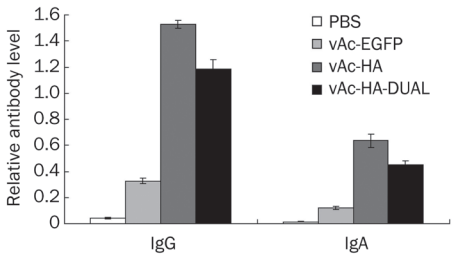

Figure 6. Total IgG and IgA antibody in immunized mice. Mice were immunized with vAc-HA-DUAL, vAc-HA, vAc-EGFP, or PBS. Sera of immunized mice from different groups were collected 21 d after the first immunization. The titers of total IgG and IgA antibodies were determined by ELISA.

and IL-6) using ELISPOT and ELISA. As shown in Figures 7A and 7B, after stimulating with the specific antigen (a 14-mer HA peptide), the number of IFN-γ-secreting splenocytes was 20- and 40-fold higher in mice immunized with vAc-HA and vAc-HA-DUAL than in vAc-EGFP-immunized mice, respectively. Similarly, the number of IL-4-secreting splenocytes was approximately 40- and 20-fold higher in vAc-HA and vAc-HA-DUAL mice than in vAc-EGFP mice, respectively. No differences were observed when the splenocytes were treated with an unrelated 16-mer peptide from influenza virus neuraminidase or with PHA. The results again showed that the recombinant baculoviruses elicited strong HA-specific immune responses in mice.

Furthermore, twofold more splenocytes produced IFN-γ in mice immunized with vAc-HA-DUAL compared with mice immunized with vAc-HA (Figure 7A) whereas twofold more cells produced IL-4 in the vAc-HA group than in the vAc-HA-DUAL group (Figure 7B). This difference was supported by results indicating that the level of IFN-γ was higher in splenocyte cultures from mice immunized with vAc-HA-DUAL compared with mice immunized with vAc-HA, and the level of IL-4 was higher in the vAc-HA group than in the vAc-HA-DUAL group (Figures 8A and 8B). Similar results were observed in separate experiments measuring the number of splenocytes producing IL-2 and IL-6 after antigen stimulation. The number of cells producing IL-2 in the vAc-HA-DUAL group was approximately 3-fold higher than in the vAc-HA group (Figure 7C) whereas the number of cells producing IL-6 was 2-fold higher in the vAc-HA group than in the vAc-HA-DUAL group (Figure 7D). These results demonstrated that

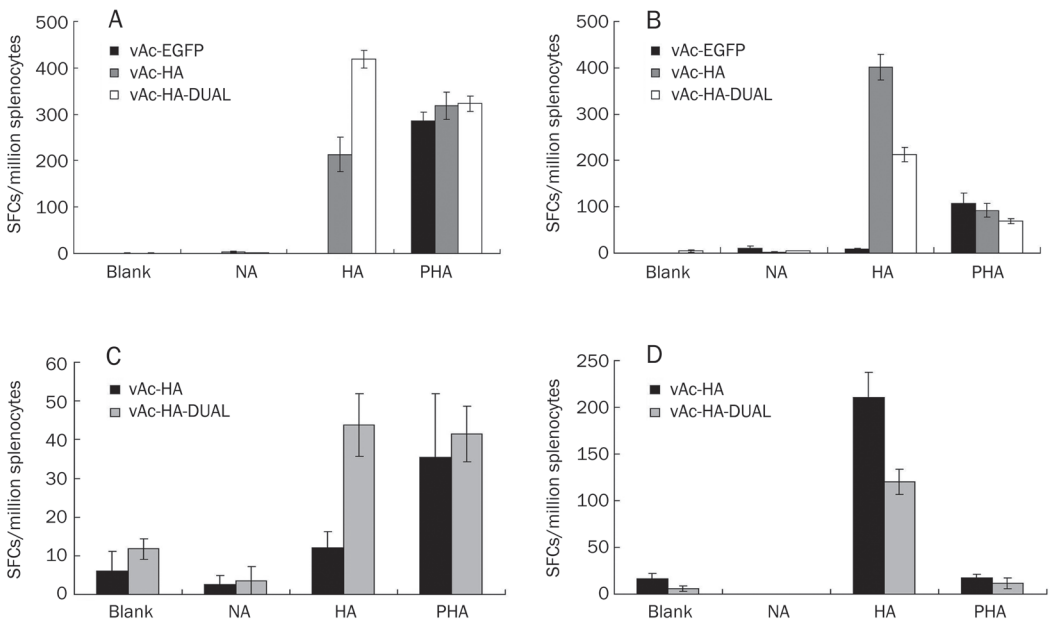

Figure 7. Number of splenocytes from baculovirus-immunized mice that produced various cytokines upon antigen stimualtion. The splenocytes of immunized mice were obtained after two immunizations and stimulated with antigen-specific peptide (HA, 14 mer), an unrelated peptide (NA, 16 mer) or plant hemaglutinin (PHA, positive control). Cytokine-producing cells were assayed with ELISPOT. Un-stimulated control (Blank) and no-cell control were also included. (A) IFN-γ; (B) IL-4; (C) IL-2; (D) IL-6.

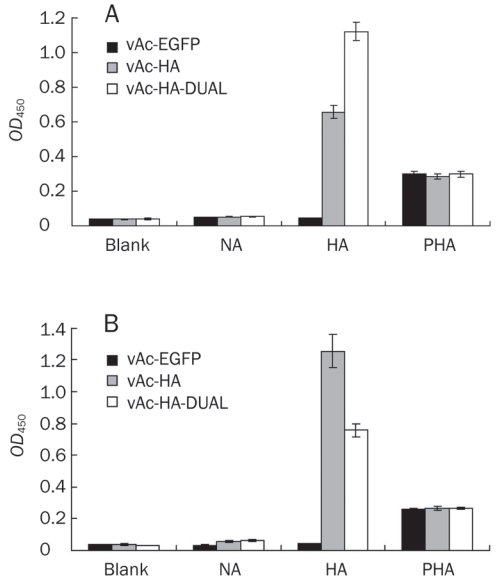

Figure 8. Cytokine production by splenocytes from baculovirus-immunized mice. Splenocytes from mice immunized with vAc-EGFP, vAc-HA, or Ac-HA-DUAL were isolated one week after second immunization and stimulated *in vitro* with peptides of HA or NA, or PHA for 72 h. The level of IFN-γ (A) and IL-4 (B) in the supernatant was analyzed by ELISA.

although both vAc-HA-DUAL and vAc-HA efficiently elicited specific immune responses, they had different biases in Th1 and Th2 responses. Specifically, vAc-HA-DUAL elicited a Th1-biased response whereas vAc-HA elicited a Th2-biased response.

Discussion

In the present study, two different recombinant baculovirus vectors were constructed and compared for their potential to induce immune responses in animals. These recombinant viruses contained the expression cassette for the H5N1 influenza virus HA gene allowing protein production in either insect cells (vAc-HA) or in both insect and mammalian cells (vAc-HA-DUAL). Both viruses mediated HA protein production in infected insect Sf9 cells at similar levels. HA is believed to have been transported to the surface of infected insect cells based on the observation that chicken red blood cells attached to the surface of the Sf9 cells infected by HA-expressing viruses, but not to mock-infected cells[15] or cells infected by control virus (data not shown). This is consistent with results showing that HA proteins were present in the viral envelopes of vAc-HA and vAc-HA-DUAL and confirms previous results that HA-transportation signals were properly recognized by insect cells[16].

The expression and surface display of HA proteins appeared to slow down the rate of viral replication in insect cells as indicated by the kinetics of budding virus production. This reduction was most likely due to the presence of HA on the virion envelope and the surface of infected cells that diluted GP64, the baculovirus major envelope protein, and thus affected viral entry and/or assembly and budding[17, 18]. However, the effect seems to be limited, as the virus titer caught up at the late stage of virus infection.

On the other hand, the presence of HA on the virion surface increased the transduction efficiency of baculoviruses in mammalian cells. The percentage of cells expressing the reporter gene (*egfp*) was 2 times higher in A549 cells transduced by HA-displaying virus than A549 cells transduced by the control virus (vAc-EGFP). As expected, HA proteins were efficiently expressed in mammalian cells transduced by vAc-HA-DUAL but not by vAc-HA[19–21].

In vAc-HA-DUAL, the expression of the egfp reporter and HA genes was driven by two hybrid promoters, composed either of the baculovirus p10 and mammalian CMV promoters, or by the baculovirus polyhedrin and CMV promoters, respectively (Figure 1). Although the transcription mediated by these hybrid promoters requires further detailed characterization, they both appeared highly effective in insect and mammalian cells[22, 23].

The recombinant baculoviruses were tested for their potential as vector vaccines to elicit immune responses against HA in mice. Because vAc-HA and vAc-HA-DUAL displayed HA proteins on the virion surface, they might act primarily as a particle vaccine. However, vAc-HA-DUAL could also work as a DNA vaccine because it could mediate HA protein expression when it entered the cells. Thus, the two virus vectors were expected to induce different immune responses.

In mice injected with vAc-HA and vAc-HA-DUAL, significant levels of HA-specific antibodies were produced. These HA-specific antibody levels were similar for both viruses, most likely indicating the same efficiency of antigen presentation for the two viruses. No HA-specific antibodies were detected in mice injected with the control virus vAc-EGFP. However, the levels of total IgG and IgA were much higher in mice injected with vAc-HA compared with mice injected with vAc-HA-DUAL. Very low levels of total IgG and IgA were detected in the control group. The reason for this result remains unclear.

Moreover, splenocytes from the immunized mice were cultured *in vitro* to test their ability to produce IFN-γ, IL-2, IL-4, and IL-6 upon stimulation with antigens consisting of an HA-specific peptide. The predominant cytokines that resulted were found to be different in mice immunized with the different baculoviruses. In mice immunized with vAc-HA, more splenocytes secreted IL-4 and IL-6 than IFN-γ and IL-2, and the level of IL-4 in the culture medium was higher than the level of IFN-γ. These results suggest that vAc-HA induced a Th2-biased immune response in mice, which is consistent with the behavior of vAc-HA as a particle protein vaccine. Our results were also similar to those of previous studies using baculovirus as a vaccine vector and the surface-display approach[8].

On the other hand, vAc-HA-DUAL not only presented the HA protein on the virion surface but also expressed HA protein in transduced cells. Although the transduction efficiency *in vivo* was difficult to evaluate, the pattern of immune responses elicited by the vAc-HA-DUAL vector, as compared

with that elicited by vAc-HA, indicated that the HA protein was likely to have been produced *in vivo*. Unlike vAc-HA, more splenocytes from immunized mice produced IFN-γ and IL-2 than the Th2 cytokines IL-4 and IL-10, and the level of IFN-γ was higher than that of IL-4 in the culture medium, suggesting a Th1-biased immune response. In addition, vAc-HA-DUAL was also found to be more effective in inducing HA-specific CD4+ and CD8+ T-cell responses *in vitro* (data not shown).

In recent years, baculoviruses have been intensively studied as potential vaccine vectors. In addition to its high biosafety, easy handling, efficient protein production in insect cells and other advantages, baculovirus vaccine vectors have low pre-existing immunity in humans and animals and the ability to elicit innate immunity. AcMNPV was found to have strong adjuvant properties. It could also activate dendritic cell (DC)-mediated innate immunity through MyD88/TLR9-dependent and MyD88/TLR9-independent pathways, which might help to improve the efficacy of baculovirus vector vaccines[24]. In fact, AcMNPV was shown to induce antiviral activity in mammalian cells and confer protection against lethal encephalomyocarditis virus and influenza virus infections in mice[25, 26].

Several recent studies have shown that baculovirus transduction vectors tend to elicit a Th1-biased immune reaction against the target antigen when the antigen was only expressed in the transduced cells and was not presented on the virions. Evidence has shown that a baculovirus vector with a mammalian expression cassette producing proteins from a SARS-like coronavirus could elicit a Th1-dominant immune response in mice[6, 13–16]. A similar approach has been used to develop vaccines against pseudorabies virus. High proportions of Ig2a IgG and high levels of IFN-γ were found, indicating a Th1-type immune response. Studies using baculovirus capable of displaying circumsporozoite proteins from plasmodium on the virion surface and expressing the same protein in transduced mammalian cells demonstrated that the baculovirus induced a mixed Th1/Th2 response, resulting in strong protection against infection[27, 28]. By comparing a baculovirus vector that could only display HA with a vector that could both display and express HA, we showed that different biases in Th1 and Th2 immune responses were induced. The balance between Th1 and Th2 responses mounted against an infectious agent can influence both the control of the pathogen and immunopathology. Humoral immune responses are essential for immunity against viral infections, but they may not be sufficient to clear the virus[6]. T cell responses, especially Th1-mediated cellular immunity, may also play a crucial role in long-term protection in some cases. Thus, the information provided here might be helpful for the design of effective baculovirus-based vaccines in the future.

Acknowledgements

This investigation received support from the National Natural Science Foundation of China (30770079) and the National Science and Technology Major Project for Drug Discovery (2009ZX09303).

Author contribution

Jiang ZHONG and Zhi-peng HU designed the research; Zhi-peng HU, Juan YIN, Yuan-yuan ZHANG, Shu-ya JIA, and Zuo-jia CHEN performed the research; Zhi-peng HU and Jiang ZHONG analyzed the data; and Zhi-peng HU and Jiang ZHONG wrote the paper.

References

1 World Health Organization. Geneva: The Association; c2003-2011 [updated 2011 Aug 19; cited 2011 Oct 2]. WHO Global Influenza Programme; Available from: http://www.who.int/influenza/human_animal_interface/H5N1_cumulative_table_archives/en/index.html
2 Chen MW, Cheng TG, Huang XY, Jan JT, Ma SH, Yu AL, *et al*. A onsensus–hemagglutinin-based DNA vaccine that protects mice against divergent H5N1 influenza viruses. Proc Natl Acad Sci U S A 2008; 105: 13538–43.
3 Hu YC. Baculovirus as a highly efficient expression vector in insectand mammalian cells. Acta Pharmacol Sin 2005; 26: 405–16.
4 Ghosh S, Parvez MK, Banerjee K, Sarin SK, Hasnain SE. Baculovirus as mammalian cell expression vector for gene therapy: an emerging strategy. Mol Ther 2002; 6: 5–11.
5 He F, Madhan S, Kwang J. Baculovirus vector as a delivery vehicle for influenza vaccines. Expert Rev Vaccines 2009; 8: 455–67.
6 Bai B, Lu X, Meng J, Hu Q, Mao P, Lu B, *et al*. Vaccination of mice with recombinant baculovirus expressing spike or nucleocapsid protein of SARS-like coronavirus generates humoral and cellular immune responses. Mol Immunol 2008; 45: 868–75.
7 Wang S, Fang L, Fan H, Jiang Y, Pan Y, Luo R, *et al*. Construction and immunogenicity of pseudotype baculovirus expressing GP5 and M protein of porcine reproductive and respiratory syndrome virus. Vaccine 2007; 25: 8220–7.
8 Lu L, Yu L, Kwang J. Baculovirus surface-displayed hemagglutinin of H5N1 influenza virus sustains its authentic cleavage, hemagglutination activity, and antigenicity. Biochem Biophys Res Commun 2007; 358: 404–9.
9 Kost TA, Condreay JP. Recombinant baculoviruses as expression vectors for insect and mammalian cells. Curr Opin Biotechnol 1999; 10: 428–33.
10 Kost TA, Condreay JP. Recombinant baculoviruses as mammalian cell gene delivery vectors. Trends Biotechnol 2002; 20: 173–80.
11 O'Reilly DR, Miller LK, Luckow VA. Baculovirus expression vectors. A laboratory manual, 1994. Oxford University Press, Oxford, UK.
12 Song J, Liang C, Chen X. Transduction of avian cells with recombinant baculovirus. J Virol Methods 2006; 135: 157–62.
13 Leisy DJ, Lewis TD, Leong JA, Rohrmann GF. Transduction of cultured fish cells with recombinant baculoviruses. J Gen Virol 2003; 84: 1173–8.
14 Wagle M, Jesuthasan S. Baculovirus-mediated gene expression in zebrafish. Mar Biotechnol 2003; 5: 58–63.
15 Ping W, Ge J, Li S, Zhou H, Wang K, Feng Y, *et al*. Baculovirus-mediated gene expression in chicken primary cells. Avian Dis 2006; 50: 59–63.
16 Jin R, Lv Z, Chen Q, Quan Y, Zhang H, Li S, *et al*. Safety and immunogenicity of H5N1 influenza vaccine based on baculovirus surface display system of *Bombyx mori*. PLoS One 2008; 3: e3933.
17 Ojala K, Mottershead DG, Suokko A, Oker-Blom C. Specific binding of baculoviruses displaying gp64 fusion proteins to mammalian cells. Biochem Biophys Res Commun 2001; 284: 777–84.
18 Zhou J, Blissard GW. Display of heterologous proteins on gp64null baculovirus virions and enhanced budding mediated by a vesicular

stomatitis virus *Gstem construct*. J Virol 2008; 82: 1368–77.
19 Raty JK, Airenne KJ, Marttila AT, Marjomaki V, Hytonen VP, Lehtoainen P, *et al*. Enhanced gene delivery by avidin-displaying baculovirus. Mol Ther 2004; 9: 282–91.
20 Kitagawa Y, Tani H, Limn CK, Matsunaga TM, Moriishi K, Matsuura Y. Ligand directed gene targeting to mammalian cells by pseudotype baculoviruses. J Virol 2005; 79: 3639–52.
21 Ge J, Huang Y, Hu X, Zhong J. A surface modified baculovirus vector with improved gene delivery to B-lymphocytes. J Biotechnol 2007; 129: 367–72.
22 Mahonen AJ, Airenne KJ, Purola S, Peltomaa E, Kaikkonen MU, Riekkinen MS, *et al*. Post-transcriptional regulatory element boosts baculovirus-mediated gene expression in vertebrate cells. J Biotechnol 2007; 131: 1–8.
23 Keil GM, Klopfleisch C, Giesow K, Blohm U. Novel vectors for simultaneous high-level dual protein expression in vertebrate and insect cells by recombinant baculoviruses. J Virol Methods 2009; 160: 132–7.
24 Abe T, Hemmi H, Miyamoto H, Moriishi K, Tamura S, Takaku H, *et al*. Involvement of the Toll-like receptor 9 signaling pathway in the induction of innate immunity by baculovirus. J Virol 2005; 79: 2847–58.
25 Gronowski AM, Hilbert DM, Sheehan KCF, Garotta G, Schreiber RD. Baculovirus stimulates antiviral effects in mammalian cells. J Virol 1999; 73: 9944–51.
26 Abe T, Takahashi H, Hamazaki H, Miyano-Kurosaki N, Matsuura Y, Takaku H. Baculovirus induces an innate immune response and confers protection from lethal influenza virus infection in mice. J Immunol 2003; 171: 1133–9.
27 Strauss R, Huser A, Ni S, Tuve S, Kiviat N, Sow P, *et al*. Baculovirus based vaccination vectors allow for efficient induction of immune responses against plasmodium falciparum circumsporozoite protein. Mol Ther 2007; 15: 193–202.
28 Yoshida S, Araki H, Yokomine T. Baculovirus-based nasal drop vaccine confers complete protection against malaria by natural boosting of vaccine-induced antibodies in mice. Infect Immun 2010; 78: 595–602.

Acta Pharmacologica Sinica (2012) 33: 791–797
 1671-4083/12 $32.00
www.nature.com/aps

Original Article

Protective effects of tiopronin against high fat diet-induced non-alcoholic steatohepatitis in rats

Jian-qing WANG[1, 2], Yu-hong ZOU[3], Cheng HUANG[1], Chao LU[4], Lei ZHANG[1], Yong JIN[1], Xiong-wen LÜ[1], Li-ping LIU[2], Jun LI[1, *]

[1]School of Pharmacy, Anhui Key Laboratory of Bioactivity of Natural Products, Anhui Medical University, Hefei 230032, China; [2]Second Hospital of Anhui Medical University, Hefei 230601, China; [3]Department of Biology, Center of Regenerative Biology and Medicine, Indiana University-Purdue University, Indianapolis, IN 46202, USA; [4]First Hospital of Anhui Medical University, Hefei 230022, China

Aim: To study the protective effects of tiopronin against high fat diet-induced non-alcoholic steatohepatitis in rats.
Methods: Male Sprague-Dawley rats were given a high-fat diet for 10 weeks. The rats were administered tiopronin (20 mg/kg) or a positive control drug ursodeoxycholic acid (UDCA, 15 mg/kg) via gavage daily from week 5 to week 10. After the rats were sacrificed, serum levels of alanine aminotransferase (ALT), aspartate aminotransferase (AST), total cholesterol (TC), triglyceride (TG), free fatty acids (FFA), high-density lipoprotein (HDL-C) and low-density lipoprotein (LDL-C), and liver homogenate FFA, superoxide dismutase (SOD), glutathione peroxidase (GSH-Px) and malondialdehyde (MDA) were measured using commercial analysis kits. The expression levels of CYP2E1 mRNA and protein were determined using RT-PCR and immunoblot assays, respectively.
Results: Tiopronin significantly lowered both the serum ALT and AST levels, while only the serum ALT level was lowered by UDCA. Tiopronin significantly decreased the serum and liver levels of TG, TC and FFA as well as the serum LDL-C level, and increased the serum HDL-C level, while UDCA decreased the serum and liver TC levels as well as the serum LDL-C level, but did not change the serum levels of TG, FFA and HDL-C. Tiopronin apparently ameliorated the hepatocyte degeneration and the infiltration of inflammatory cells in the livers, but UDCA did not affect the pathological features of the livers. Both tiopronin and UDCA ameliorated the mitochondrial abnormality in the livers. The benefits of tiopronin were associated with increased SOD and GSH-Px activities, and with decreased MDA activity and CYP2E1 expression in the livers.
Conclusion: Tiopronin exerts protective effects against non-alcoholic steatohepatitis in rats, which may be associated with its antioxidant properties and regulation of lipid metabolism.

Keywords: tiopronin; ursodeoxycholic acid; non-alcoholic steatohepatitis; antioxidant; lipid metabolism; mitochondria; CYP2E1

Acta Pharmacologica Sinica (2012) 33: 791–797; doi: 10.1038/aps.2012.19; published online 30 Apr 2012

Introduction

Non-alcoholic fatty liver disease (NAFLD) is emerging as a common medical problem and is recognized as a cause of potentially progressive liver damage. Within the spectrum of NAFLD, non-alcoholic steatohepatitis (NASH) is considered the critical turning point at which point NAFLD progresses to more advanced stages such as hepatic fibrosis, cirrhosis and even hepatocellular carcinoma.

The pathogenesis of NAFLD is complex, multifactorial and poorly understood. Currently, the popular theory on NASH pathogenesis is the "two-hit" hypothesis[1] in which the first hit leads to hepatic steatosis, which makes the liver vulnerable to the second hit. In this stage, steatosis is mediated by an increase in dietary fat intake, the liberation of free fatty acids from adipose tissue, insufficient hepatic lipid secretion and the development of insulin resistance[2]. The second hit, which leads to steatohepatitis, is mediated by increased oxidative stress subsequent to lipid peroxidation as well as the induction of pro-inflammatory cytokine expression.

Gradual weight loss is the only therapeutic strategy established to be effective in treating NASH. It has been proven that lifestyle modification and regular physiological exercise will regulate the individual's body weight and improve NASH and the associated metabolic syndrome[3–5]. However, if there is no change in the course of disease after adequate lifestyle changes, pharmacological interventions should be considered, especially for those patients at a high risk of progression. There is generally consistent evidence from clinical trials indicating that certain pharmacological agents may be effective in the treatment of NASH.

Tiopronin [N-(2-mercaptopropionyl)-glycine], a chemical compound with a free thiol group, is an oxygen free radi-

* To whom correspondence should be addressed.
E-mail lijun@ahmu.edu.cn
Received 2011-11-02 Accepted 2012-02-08

cal that has been used clinically in the treatment of several disorders linked to abnormal free radical production[6–8]. Tiopronin is readily absorbed after oral administration and is generally reported to be a well-tolerated drug[8]. The oral administration of 600 mg of tiopronin daily was associated with improvement in liver function in patients with viral chronic hepatitis[9, 10]. It has also been reported that tiopronin is able to reduce fat levels in the liver after acute or prolonged ethanol administration[11]. The histologic characteristics of NAFLD resemble those of alcoholic fatty liver disease (AFLD), which suggests that both diseases may have a similar pathogenesis and benefit from similar therapies. Tiopronin was used in the treatment of hepatic steatosis in certain clinical trials[12, 13]. Most of these studies have been uncontrolled and open label with a duration of 1 year or less. Only a few have evaluated the effect of treatment on liver histology. Therefore, this study was designed to evaluate the protective effects of tiopronin on high-fat-diet-induced NASH in rats and its mechanism of action.

Ursodeoxycholic acid (UDCA) is a hydrophilic biliary acid known to possess antioxidant properties and cytoprotective, anti-apoptotic, membrane stabilizing and immunomodulative effects[14–16]. It is suggested that UDCA treatment may improve aminotransferase and adiponectin levels as well as the grade of steatosis in NASH patients[17–20]. UDCA was also reported to enhance the therapeutic effects of a low-caloric diet in a rat model of NASH[21]. Thus, it served as a positive control drug in this study.

Materials and methods

Experimental model and drug treatment

Male Sprague-Dawley rats weighing 180–200 g were obtained from the Experimental Animal Center of Anhui Medical University. The study protocol was approved by the ethics committee of Anhui Medical University. Rats were housed in plastic cages with room temperature of 22±1 °C under a 12-h light:dark cycle and were provided with standard rodent chow and water *ad libitum*. Rats were given a normal diet for 1 week to adapt to vivarium conditions and then randomly divided into four groups (n=10 per group): a normal control group, a high-fat diet group, a high-fat diet with tiopronin (20 mg/kg) treatment group and a high-fat diet with UDCA (15 mg/kg) treatment group. The NASH model was induced by high-fat emulsion as previously reported[22]. Briefly, rats were orally treated with the high-fat emulsion (10 mL/kg) at 8:00 AM. each day for 10 weeks, with the exception of the normal control group, which received an equal volume of saline alone. In the treatment groups, 20 mg/kg of tiopronin (Henan Xinyi Pharmaceutical Co, Ltd) or 15 mg/kg of UDCA (Sigma-Aldrich, St Louis, MO, USA) was given via gavage daily at 6:00 PM from the 5th week in rats fed a high-fat diet. UDCA and tiopronin were suspended in 0.5% CMC-Na solution. The normal control and high-fat diet groups were given an equal volume of 0.5% CMC-Na solution. Rats were sacrificed after 10 weeks. Blood samples were collected from the aorta ventralis. The livers were immediately removed and weighed. Specimens of isolated rat livers were fixed in 10% formalin or frozen in liquid nitrogen until use.

Analytical procedures

The serum levels of alanine aminotransferase (ALT), aspartate aminotransferase (AST), total cholesterol (TC), triglyceride (TG), free fatty acids (FFA), high-density lipoprotein (HDL-C), low-density lipoprotein (LDL-C), liver homogenate FFA, superoxide dismutase (SOD), glutathione peroxidase (GSH-Px) and malondialdehyde (MDA) were determined using commercial analysis kits obtained from the Jiancheng Institute of Biotechnology (Nanjing, China) and the Furui Institute of Biotechnology (Beijing, China). Hepatic concentrations of TC and TG were also measured after chloroform–methanol extraction[23].

Semi-quantitative reverse transcription-polymerase chain reaction (RT-PCR)

Total RNA was extracted from rat liver tissues using TRIzol reagent (Invitrogen). The first-strand cDNA was synthesized from total RNA using the Thermoscript RT-PCR synthesis kit (Fermentas) according to the manufacturer's instructions. RT-PCR was carried out under the standard protocol using the following primers: β-actin (forward: 5′-TGGAATCCTGTGGCATCCATGAAAC-3′; reverse: 5′-ACGCAGCTCAGTAACAGTCCG-3′); CYP2E1 (forward: 5′-CCTAGCGCACATGGCGGTTCT-3′; reverse: 5′-GCCTCCCTTTGGATGCGGGC-3′). PCR was performed, using the ABI9700, at 94 °C for 2 min, followed by 30–33 cycles of amplification at 94 °C for 36 s, 52 °C for 36 s and 72 °C for 1 min. The band intensities were measured by a densitometer, and the results were normalized with β-actin. The results were repeated in at least three independent experiments under each condition, while each cDNA template was extracted from at least six samples per group.

Immunoblot analysis

Liver tissue was homogenized in RIPA lysis buffer. Samples were then centrifuged at 15000×g for 15 min. Supernatants from each sample were added to a gel-loading buffer and boiled for 5 min. Proteins in loading buffer were subjected to electrophoresis in a 10% SDS-polyacrylamide gel for 3 h. Proteins in the gel were transferred electrophoretically onto a polyvinylidene fluoride membrane (Immobilon-P; Millipore Corp, Bedford, MA, USA) and blocked in 5% nonfat powdered milk in PBS overnight at 4 °C. The membranes were then incubated for 2 h with rabbit polyclonal antibody against mouse CYP2E1 (Millipore Corp, Bedford, MA, USA) (1:2500 dilutions) or β-actin (Beijing Biosynthesis Biotechnology Inc, Beijing, China) (1:2000 dilutions) at room temperature. After four washes in PBS containing 0.05% Tween-20, the membranes were incubated with goat anti-rabbit IgG antibody for 1 h. The membranes were then washed four times in PBS containing 0.05% Tween-20. The signal was visualized using an enhanced chemiluminescence (ECL) detection kit from Pierce (Pierce Biotechnology, Inc, Rockford, IL, USA). Each band of immunoblotting was scanned, and its intensity was analyzed

by Image J software.

Morphological evaluation

For histopathological analysis, liver specimens fixed in 10% neutral-buffered formalin were embedded in paraffin, sliced at 5-μm thickness, and stained with hematoxylin and eosin (HE) to detect the degree of hepatic steatosis and inflammation and necrosis. The pathological changes were assessed and photographed under an Olympus BX-51 microscope. Fatty change was graded according to the percentage of hepatocytes containing macrovesicular fat (grade 1: 0%–25%; grade 2: 26%–50%; grade 3: 51%–75%; grade 4, 76%–100%)[24]. The degree of inflammation and necrosis was expressed as the mean of 10 different fields within each slide. Each slide was then classified on a scale of 0–3 (0: normal; 1: mild; 2: moderate; 3: severe)[25].

For ultrastructural analysis, 1-mm^3 samples were fixed in glutaraldehyde (2.5%), post-fixed in osmium tetraoxide (2%) and embedded in Spurr's resin. Sections were stained with uranyl acetate (2%, *w*/*v*) and lead citrate prior to analysis with electron microscopy (Zeiss EM 109; Oberkochen, Germany). Morphometric measurement of the mitochondrial surface area was performed on the five largest mitochondria per photograph using an image analysis and measuring system (Image Pro Plus V 5.2)[24].

Statistical analysis

Data are expressed as the mean±SD, and the statistical analysis was performed using Student's *t*-test. The Mann-Whitney rank-sum test was used to analyze the degree of histopathological liver steatosis and inflammation. $P<0.05$ was considered to be significant.

Results

Serum aminotransferase activities

The rats with NASH induced by a high-fat diet developed hepatic damage as evidenced by the increased serum levels of AST and ALT. The administration of tiopronin significantly reduced the AST and ALT activities compared with the model group, while UDCA only decreased serum ALT levels (Table 1).

Table 1. Effects of tiopronin on liver function in rat fed with high fat diet. n=10. Mean±SD. $^cP<0.01$ *vs* normal diet. $^eP<0.05$, $^fP<0.01$ *vs* high fat.

Groups	Dose (mg/kg)	ALT (U/L)	AST (U/L)
Normal diet	–	33.59±4.15	44.88±5.36
High fat	–	65.40±7.03^c	85.58±7.84^c
High fat+tiopronin	20	51.60±7.11^f	56.00±4.05^f
High fat+UDCA	15	58.70±5.66^e	78.20±8.82

Serum and liver lipid metabolism

To investigate the possible role of tiopronin in lipid metabolism, which is the key factor in fatty liver formation, the levels of TG, TC, FFA, HDL-C, and LDL-C were analyzed. As shown in Tables 2 and 3, the increased serum and liver levels of TG, TC, and FFA as well as serum LDL-C levels were significantly suppressed, whereas the decreased serum HDL-C level was obviously elevated by tiopronin treatment in rats fed a high-fat diet. Compared with model group rats, UDCA lowered serum and liver TC levels as well as serum levels of LDL-C but did not change serum levels of TG, FFA, and HDL-C (Tables 2 and 3).

Table 3. Effects of tiopronin on liver lipid content in rat fed with high fat diet. n=10. Mean±SD. $^cP<0.01$ *vs* normal diet. $^eP<0.05$, $^fP<0.01$ *vs* high fat. TG, triglyceride; TC, total cholesterol; FFA, free fatty acids.

Groups	Dose (mg/kg)	Liver TG (mmol/g liver weight)	Liver TC (mmol/g liver weight)	Liver FFA (mmol/g liver weight)
Normal diet	–	1.49±0.09	0.24±0.03	0.50±0.05
High fat	–	2.29±0.16^c	1.16±0.18^c	1.47±0.10^c
High fat+tiopronin	20	1.64±0.16^e	0.95±0.14^e	1.05±0.87^f
High fat+UDCA	15	2.06±0.32	0.93±0.19^e	1.37±0.11^e

Lipid peroxidation and antioxidative enzyme levels

Oxidative stress has been focused upon as a common pathogenic mechanism in various liver diseases and is considered to play a major role in the pathogenesis of NASH as well[1]. In Table 4, the antioxidant activities of tiopronin were estimated by measuring the hepatic MDA content and levels of SOD and GSH-Px activity. The high-fat diet increased liver MDA levels but decreased liver levels of SOD and GSH-Px activity compared with those observed in the normal control group.

Table 2. Effects of tiopronin on serum lipid metabolism parameters in rat fed with high fat diet. n=10. Mean±SD. $^cP<0.01$ *vs* normal diet. $^eP<0.05$, $^fP<0.01$ *vs* high fat. TG, triglyceride; TC, total cholesterol; FFA, free fatty acids; HDL-C, high-density lipoprotein; LDL-C, low-density lipoprotein.

Groups	Dose (mg/kg)	Serum TG (mmol/L)	TC (mmol/L)	FFA (mmol/L)	HDL-C (mmol/L)	LDL-C (mmol/L)
Normal diet	–	1.61±0.10	1.94±0.30	0.40±0.07	1.41±0.11	0.28±0.08
High fat	–	2.80±0.29^c	3.92±0.42^c	1.30±0.11^c	1.17±0.16^c	1.13±0.13^c
High fat+tiopronin	20	1.90±0.22^f	3.05±0.40^f	1.00±0.08^f	1.34±0.16^e	0.90±0.09^f
High fat+UDCA	15	2.44±0.46	3.55±0.34^e	1.21±0.10	1.30±0.17	1.04±0.15

Table 4. Effects of tiopronin on hepatic lipid peroxidation and antioxidative enzyme activities in rat fed with high fat diet. n=10. Mean±SD. ^{c}P<0.01 *vs* normal diet. ^{e}P<0.05, ^{f}P<0.01 *vs* high fat.

Groups	Dose (mg/kg)	MDA (nmol/mg)	SOD (U/mg)	GSH-Px (U/mg)
Normal diet	–	4.81±0.74	23.72±2.90	25.02±4.08
High fat	–	12.10±1.42^{c}	7.82±1.43^{c}	16.77±2.05^{c}
High fat+tiopronin	20	7.99±0.83^{f}	18.75±3.55^{f}	20.58±3.06^{f}
High fat+UDCA	15	10.21±1.86^{e}	9.30±1.96	19.49±2.30^{e}

Tiopronin treatment significantly reversed these values. These results suggest that the imbalance between oxidative stress generation and antioxidant formation could occur after rats were fed a high-fat diet. Tiopronin may prevent this pathological process, indicating its therapeutic and preventive effect on NASH induced by the ingestion of a high-fat diet (Table 4).

Histological analysis

Rats fed high-fat diet for 10 weeks not only developed a high degree of hepatic steatosis with severe cytoplasmic vacuoles and swelling of the hepatocytes but also exhibited more prominent inflammation, which was corroborated by morphological evidence of an abundance of inflammatory cells (Figure 1B), whereas no histological abnormalities were observed in normal control rats (Figure 1A). Hepatocyte degeneration and the infiltration of inflammatory cells were all apparently ameliorated in the rats treated with tiopronin (Figure 1C). UDCA treatment did not affect the histological features of the liver (Table 5 and Figure 1D).

Ultrastructural analysis of morphological changes in the mitochondria

Accumulating evidence indicates that mitochondrial dysfunction plays a key role in the physiopathology of NASH[26]. In this study, mitochondria in the livers of rats fed a high-fat diet exhibited degenerative changes such as mitochondrial swelling, matrix rarefication and cristae loss. These changes were ameliorated by tiopronin and UDCA treatment (Table 5 and Figure 2).

Hepatic CYP2E1 expression

Previous studies showed that alterations of CYP2E1 contributed to NASH[27]. Therefore, we analyzed the effect of tiopronin on the expression of CYP2E1 in the rat liver with NASH. During the 10 weeks of dietary treatment, mRNA and protein levels of CYP2E1 in the rat liver were significantly increased. In contrast, tiopronin treatment reduced the expression of CYP2E1 in rats fed a high-fat diet (Figures 3 and 4).

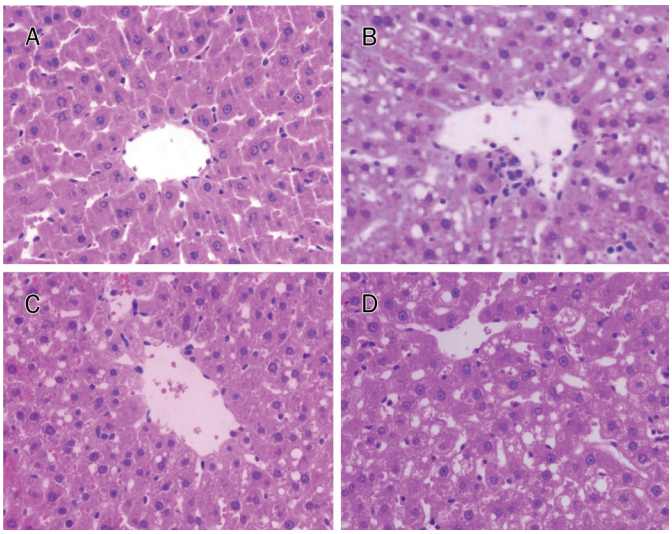

Figure 1. Histological images of liver tissues from rats in which steatohepatitis was induced by a high-fat emulsion reveal the anti-steatohepatitis effects of tiopronin. There were no histological abnormalities observed in rats fed a normal diet (A). Rats fed high-fat diet for 10 weeks developed a high degree of steatosis and inflammation (B). Hepatocyte degeneration and the infiltration of inflammatory cells were all apparently ameliorated by tiopronin treatment in rats fed high-fat diet (C). UDCA treatment did not affect the histological features of the liver in the rats fed high-fat diet (D). The magnification is ×400.

Discussion

This study reveals that tiopronin, which contains an SH-group and is generally considered an antioxidant, protects against the accumulation of lipid in the rat liver induced by a high-fat diet. The protective effect of tiopronin is mediated through the downregulation of TG, TC, FFA, and LDL-C and the elevation of HDL-C. Histological examination showed that the histological changes associated with liver injury were also remarkably ameliorated after tiopronin treatment. These results demonstrate that tiopronin has protective effects against steatohepatitis induced by a high-fat diet in rats.

Although steatosis represents a form of lipotoxicity, its pathogenesis remains poorly understood. Free fatty acids

Table 5. Average histological grades of steatosis, inflammation and mitochondrial surface area in rat fed with high fat diet. n=10. Mean±SD. ^{c}P<0.01 *vs* normal diet. ^{e}P<0.05, ^{f}P<0.01 *vs* high fat.

Parameter	Normal diet	High fat	High fat+tiopronin	High fat+UDCA
Steatosis	1.00±0.00	3.77±0.43^{c}	1.96±0.28^{f}	3.24±0.45
Inflammation	0	1.80±0.29^{c}	0.57±0.27^{f}	1.55±0.25
Mitochondrial area (μm^2)	0.31±0.02	0.91±0.04^{c}	0.54±0.04^{f}	0.73±0.04^{f}

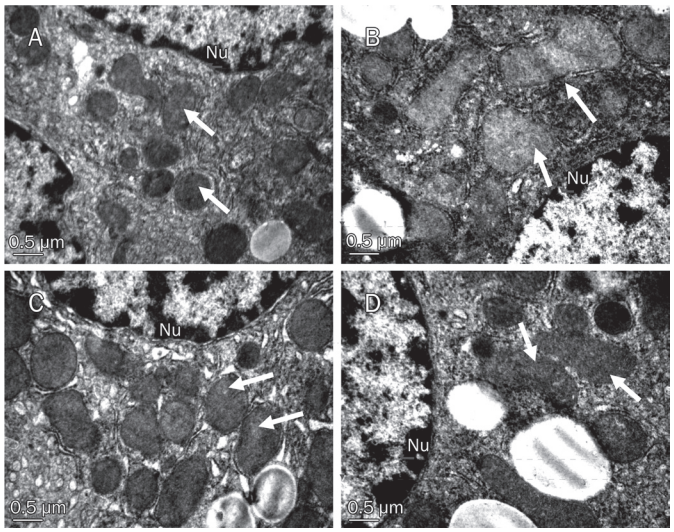

Figure 2. Electron microscopy of hepatic mitochondria. Mitochondria in the rats fed the high-fat emulsion diet showed degenerative changes with mitochondrial swelling, rarefied matrices and cristae loss (B) (arrows). These changes were prominent in most of the mitochondria in the rats fed the high-fat emulsion diet but were rare in the mitochondria in the normal diet-fed rats (A). These changes were also ameliorated by tiopronin (C) and UDCA (D) treatment in the rats fed a high-fat diet. The magnification is ×15 000.

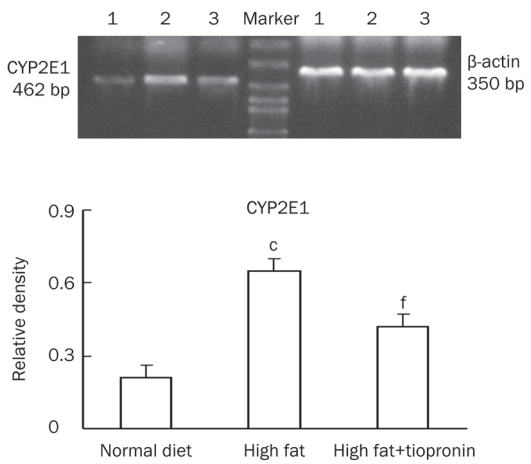

Figure 3. The effect of tiopronin on hepatic CYP2E1 mRNA expression in rats fed a high-fat diet. The mRNA levels were normalized to those of β-actin. RT-PCR analysis reveals that the mRNA expression of CYP2E1 was significantly increased in rats fed a high-fat diet. In contrast, tiopronin treatment reduced the expression of CYP2E1 in rats fed a high-fat diet. Data are expressed as the mean±SD (n=6). ^{c}P<0.01 *vs* normal diet. ^{f}P<0.01 *vs* high fat. 1, normal diet; 2, high fat; 3, high fat+tiopronin.

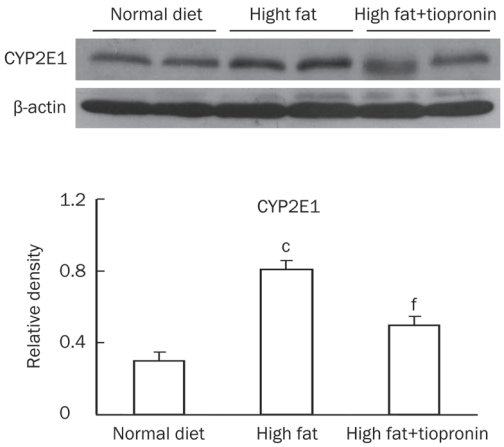

Figure 4. Effect of tiopronin on hepatic CYP2E1 protein expression in rats fed a high-fat diet. The protein was corrected by β-actin. Immunoblot analysis showed that the protein expression of CYP2E1 was significantly increased in rats fed a high-fat diet. In contrast, tiopronin treatment reduced the expression of CYP2E1 in rats fed a high-fat diet. Data are expressed as the mean±SD (n=6). ^{c}P<0.01 *vs* normal diet. ^{f}P<0.01 *vs* high fat.

(FFAs) appear to be important mediators of lipotoxicity, both as potential cellular toxins and by inducing lipid over-accumulation[28]. Furthermore, FFAs not only promote hepatic lipotoxicity via a lysosomal pathway[29] but are also the most important source of reactive oxygen species (ROS)[30, 31]. Some studies suggest that the excessive accumulation of saturated FFAs in liver cells directly induces mitochondrial dysfunction and oxidative stress[32]. Mitochondrial abnormality plays a role in the onset and progression of NASH in correlation with oxidative stress[33]. In this study, FFA levels in both the serum and liver were reduced by tiopronin treatment, and mitochondrial morphological changes were also reproduced in rats fed a high-fat diet. These results indicate that tiopronin may be a potential candidate to protect against the steatohepatitis induced by a high-fat diet.

Oxidative stress and alterations in the pro-oxidant-antioxidant balance are commonly implicated as the 'second hit' in the steatotic liver, which promotes the progression from steatosis to steatohepatitis[1]. The proinflammatory, pro-fibrogenic effects of the aldehyde end-products of lipid peroxidation (MDA and 4-hydroxynonenol) potentially account for all of the typical histological features observed in NAFLD[34]. It has been shown that MDA, an index of lipid peroxidation and oxidative stress, damages cells and tissues. SOD is responsible for neutralizing the most common free radical, which is known as superoxide. It also aids the body's utilization of copper, zinc and manganese. GSH-Px, along with SOD, is one of the body's endogenous antioxidants and is well known to protect liver cells against oxidative damage through chemical or enzymatic reactions. It has also been reported that tiopronin, like glutathione, is able to protect against ethanol-induced fatty liver by preventing fat accumulation and mitochondrial injury. This increases the proportion of reactive SH groups in the mitochondrial membrane[9, 11, 13]. In this study, the markers of oxidative stress included increased hepatic MDA content and decreased levels of SOD and GSH-Px. Tiopronin successfully reversed these changes. These data suggest that the therapeutic effects of tiopronin against steato-

hepatitis in rats may be associated with preventing the development of oxidative stress and mitochondrial abnormalities.

Although different studies point to the damaged respiratory chain as a main source of mitochondrial ROS in NASH, some data suggest that the ectopic expression of cytochrome P450 2E1 (CYP2E1) in mitochondria could also play a role in ROS overproduction. Previous studies have shown that CYP2E1 is the major catalyst for the formation of lipid peroxides in mice[35]. CYP2E1 has been shown to play a key role in the pathogenesis of alcoholic liver injury, including alcoholic steatohepatitis[36]. Its pathogenic role in NASH has also been recognized in both animal experiments and human studies[27, 37]. A recent study has also shown that tiopronin exerts its hepatoprotective activity against isoniazid-induced hepatotoxicity by reducing free radical generation in addition to its role as a scavenger via the inhibition of hepatic CYP2E1[38]. In this study, the protein expression of CYP2E1 was also significantly decreased by tiopronin treatment in rats fed a high-fat diet. To summarize, tiopronin exerts its protective activity against steatohepatitis by preventing oxidative stress through the inhibition of hepatic CYP2E1.

In conclusion, our current investigation for the first time shows that the protective effects of tiopronin on NASH are associated with the regulation of lipid metabolism and the amelioration of mitochondrial abnormalities through the prevention of oxidative stress as well as the inhibition of hepatic CYP2E1 expression. These results have shed some light on the clinical therapeutic potential of tiopronin in treating NASH.

Acknowledgements

The research presented in this paper was financially supported by the National Natural Science Foundation of China (No 30873081 and 81072686) and Natural Science Foundation of Anhui Province (No 1208085QH143).

Author contribution

Jun LI, Yu-hong ZOU, and Jian-qing WANG designed research; Jian-qing WANG and Cheng HUANG performed research; Chao LU and Lei ZHANG contributed new reagents or analytic tools; Yong JIN, Xiong-wen LÜ, and Li-ping LIU analyzed data; Jian-qing WANG wrote the paper; and Yu-hong ZOU and Cheng HUANG revised the paper.

References

1 Day CP, James OF. Steatohepatitis: a tale of two "hits"? Gastroenterology 1998; 114: 842–5.
2 Te Sligte K, Bourass I, Sels JP, Driessen A, Stockbrugger RW, Koek GH. Non-alcoholic steatohepatitis: review of a growing medical problem. Eur J Intern Med 2004; 15: 10–21.
3 Huang MA, Greenson JK, Chao C, Anderson L, Peterman D, Jacobson J, *et al*. One-year intense nutritional counseling results in histological improvement in patients with non-alcoholic steatohepatitis: a pilot study. Am J Gastroenterol 2005; 100: 1072–81.
4 Stratopoulos C, Papakonstantinou A, Terzis I, Spiliadi C, Dimitriades G, Komesidou V, *et al*. Changes in liver histology accompanying massive weight loss after gastroplasty for morbid obesity. Obes Surg 2005; 15: 1154–60.
5 Luyckx FH, Lefebvre PJ, Scheen AJ. Non-alcoholic steatohepatitis: association with obesity and insulin resistance, and influence of weight loss. Diabetes Metab 2000; 26: 98–106.
6 Dioguardi N, Ideo G, De Franchis R, Ronchi G. Controlled clinical trial of 2-mercapto-propionyl-glycine in chronic hepatopathies. Minerva Med 1976; 67: 676–81.
7 Ichikawa H, Imaizumi K, Tazawa Y, Obara Y, Ishikawa Y, Tobari I, *et al*. Effect of tiopronin on senile cataracts. A double-blind clinical study. Ophthalmologica 1980; 180: 293–8.
8 Sany J, Combe B, Verdie-Petibon D, Tagemouati A, Daures JP. Long-term tolerability of tiopronin (Acadione) in the treatment of rheumatoid arthritis. Apropos of 140 personal cases. Rev Rhum Mal Osteoartic 1990; 57: 105–11.
9 Ichida F, Shibasaki K, Takino T, Suzuki H, Fujisawa K, Inoue K, *et al*. Therapeutic effects of tiopronin on chronic hepatitis: a double-blind clinical study. J Int Med Res 1982; 10: 325–32.
10 Kim ES, Glisson BS. Treatment of metastatic head and neck cancer: chemotherapy and novel agents. Cancer Treat Res 2003; 114: 295–314.
11 Hirayama C, Kishimoto Y, Wakushima T, Murawaki Y. Mechanism of the protective action of thiol compounds in ethanol-induced liver injury. Biochem Pharmacol 1983; 32: 321–5.
12 Yilong C. Clinical evaluation on the effect of tiopronin in nonalcoholic steatohepatitis. China Modern Doctor 2008; 46: 37–8.
13 Surrenti C, Arcangeli A, Casini A. The antisteatosic activity of 2-MPG (Thiola). Study with the (BSF) dynamic test and with liver biopsy before and after the treatment. Minerva Med 1978; 69: 4251–6.
14 Ljubuncic P, Tanne Z, Bomzon A. Ursodeoxycholic acid suppresses extent of lipid peroxidation in diseased liver in experimental cholestatic liver disease. Dig Dis Sci 2000; 45: 1921–8.
15 Buko VU, Lukivskaya OY, Zavodnik LV, Sadovnichy VV, Petushok NE, Tauschel ND. Antioxidative effect of ursodeoxycholic acid in the liver of rats with oxidative stress caused by gamma-irradiation. Ukr Biokhim Zh 2002; 74: 88–92.
16 Chang CY, Argo CK, Al-Osaimi AM, Caldwell SH. Therapy of NAFLD: antioxidants and cytoprotective agents. J Clin Gastroenterol 2006; 40: S51–60.
17 Balmer ML, Siegrist K, Zimmermann A, Dufour JF. Effects of ursodeoxycholic acid in combination with vitamin E on adipokines and apoptosis in patients with nonalcoholic steatohepatitis. Liver Int 2009; 29: 1184–8.
18 Georgescu EF, Georgescu M. Therapeutic options in non-alcoholic steatohepatitis (NASH). Are all agents alike? Results of a preliminary study. J Gastrointestin Liver Dis 2007; 16: 39–46.
19 Laurin J, Lindor KD, Crippin JS, Gossard A, Gores GJ, Ludwig J, *et al*. Ursodeoxycholic acid or clofibrate in the treatment of non-alcohol-induced steatohepatitis: a pilot study. Hepatology 1996; 23: 1464–7.
20 Dufour JF, Oneta CM, Gonvers JJ, Bihl F, Cerny A, Cereda JM, *et al*. Randomized placebo-controlled trial of ursodeoxycholic acid with vitamine in nonalcoholic steatohepatitis. Clin Gastroenterol Hepatol 2006; 4: 1537–43.
21 Fan JG, Zhong L, Tia LY, Xu ZJ, Li MS, Wang GL. Effects of ursodeoxycholic acid and/or low-calorie diet on steatohepatitis in rats with obesity and hyperlipidemia. World J Gastroenterol 2005; 11: 2346–50.
22 Zou Y, Li J, Lu C, Wang J, Ge J, Huang Y, *et al*. High-fat emulsion-induced rat model of nonalcoholic steatohepatitis. Life Sci 2006; 79: 1100–7.
23 Folch J, Lees M, Sloane Stanley GH. A simple method for the isolation and purification of total lipides from animal tissues. J Biol Chem 1957; 226: 497–509.

24 Kirsch R, Clarkson V, Shephard EG, Marais DA, Jaffer MA, Woodburne VE, *et al*. Rodent nutritional model of non-alcoholic steatohepatitis: species, strain and sex difference studies. J Gastroenterol Hepatol 2003; 18: 1272–82.
25 Avni Y, Shirin H, Aeed H, Shahmurov M, Birkenfeld S, Bruck R. Thioacetamide-induced hepatic damage in a rat nutritional model of steatohepatitis. Hepatol Res 2004; 30: 141–7.
26 Begriche K, Igoudjil A, Pessayre D, Fromenty B. Mitochondrial dysfunction in NASH: causes, consequences and possible means to prevent it. Mitochondrion 2006; 6: 1–28.
27 Weltman MD, Farrell GC, Liddle C. Increased hepatocyte CYP2E1 expression in a rat nutritional model of hepatic steatosis with inflammation. Gastroenterology 1996; 111: 1645–53.
28 Mavrelis PG, Ammon HV, Gleysteen JJ, Komorowski RA, Charaf UK. Hepatic free fatty acids in alcoholic liver disease and morbid obesity. Hepatology 1983; 3: 226–31.
29 Feldstein AE, Werneburg NW, Canbay A, Guicciardi ME, Bronk SF, Rydzewski R, *et al*. Free fatty acids promote hepatic lipotoxicity by stimulating TNF-alpha expression via a lysosomal pathway. Hepatology 2004; 40: 185–94.
30 Halliwell B. Free radicals, antioxidants, and human disease: curiosity, cause, or consequence? Lancet 1994; 344: 721–4.
31 Morris AA. Mitochondrial respiratory chain disorders and the liver. Liver 1999; 19: 357–68.
32 Li Z, Berk M, McIntyre TM, Gores GJ, Feldstein AE. The lysosomal-mitochondrial axis in free fatty acid-induced hepatic lipotoxicity. Hepatology 2008; 47: 1495–503.
33 Kojima H, Sakurai S, Uemura M, Fukui H, Morimoto H, Tamagawa Y. Mitochondrial abnormality and oxidative stress in nonalcoholic steatohepatitis. Alcohol Clin Exp Res 2007; 31: S61–6.
34 Uzun MA, Koksal N, Kadioglu H, Gunerhan Y, Aktas S, Dursun N, *et al*. Effects of N-acetylcysteine on regeneration following partial hepatectomy in rats with nonalcoholic fatty liver disease. Surg Today 2009; 39: 592–7.
35 Leclercq IA, Farrell GC, Field J, Bell DR, Gonzalez FJ, Robertson GR. CYP2E1 and CYP4A as microsomal catalysts of lipid peroxides in murine nonalcoholic steatohepatitis. J Clin Invest 2000; 105: 1067–75.
36 Lieber CS. Cytochrome P-4502E1: its physiological and pathological role. Physiol Rev 1997; 77: 517–44.
37 Chalasani N, Gorski JC, Asghar MS, Asghar A, Foresman B, Hall SD, *et al*. Hepatic cytochrome P450 2E1 activity in nondiabetic patients with nonalcoholic steatohepatitis. Hepatology 2003; 37: 544–50.
38 Yue J, Dong G, He C, Chen J, Liu Y, Peng R. Protective effects of thiopronin against isoniazid-induced hepatotoxicity in rats. Toxicology 2009; 264: 185–91.

Acta Pharmacologica Sinica (2012) 33: 798–808
 1671-4083/12 $32.00
www.nature.com/aps

Original Article

Roles of vimentin and 14-3-3 zeta/delta in the inhibitory effects of heparin on PC-3M cell proliferation and B16-F10-luc-G5 cells metastasis

Yan PAN[1], Li-jun ZHONG[2], Hong ZHOU[1], Xin WANG[1], Kui CHEN[1], Hao-peng YANG[1], Yilixiati XIAOKAITI[1], Aikebaier MAIMAITI[1], Ling JIANG[1], Xue-jun LI[1, *]

[1]*State Key Laboratory of Natural and Biomimetic Drugs, Department of Pharmacology, School of Basic Medical Sciences, Peking University and Institute of System Biomedicine, Peking University, Beijing 100191, China*; [2]*Center of Medical Analysis, Peking University, Beijing 100191, China*

Aim: To investigate the inhibitory effects of heparin on PC-3M cells proliferation *in vitro* and B16-F10-luc-G5 cells metastasis in Balb/c nude mice and identify the protein expression patterns to elucidate the action mechanism of heparin.
Methods: Human prostate cancer PC-3M cells were incubated with heparin 0.5 to 125 μg/mL for 24 h. The proliferation of PC-3M cells was assessed by MTS assay. BrdU incoporation and Ki67 expression were detected using a high content screening (HCS) assay. The cell cycle and apoptosis of PC-3M cells were tested by flow cytometry. B16-F10-luc-G5 cardinoma cells were injected into the lateral tail vein of 6-week old male Balb/c nude mice and heparin 30 mg/kg was administered iv 30 min before and 24 h after injection. The metasis of B16-F10-luc-G5 cells was detected by bioluminescence assay. Activated partial thromboplastin time (APTT) and hemorheological parameters were measured on d 14 after injection of B16-F10-luc-G5 carcinoma cells in Balb/c mice. The global protein changes in PC-3M cells and frozen lung tissues from mice burdened with B16-F10-luc-G5 cells were determined by 2-dimensional gel electrophoresis and image analysis. The protein expression of vimentin and 14-3-3 zeta/delta was measured by Western blot. The mRNA transcription of vimentin, transforming growth factor (TGF)-β, E-cadherin, and α_v-integrin was measured by RT-PCR.
Results: Heparin 25 and 125 μg/mL significantly inhibited the proliferation, arrested the cells in G_1 phase, and suppressed BrdU incorporation and Ki67 expression in PC-3M cells compared with the model group. But it had no significant effect on apoptosis of PC-3M cells. Heparin 30 mg/kg markedly inhibits the metastasis of B16-F10-luc-G5 cells on day 8. Additionally, heparin administration maintained relatively normal red blood hematocrit but had no influence on APTT in nude mice burdened with B16-F10-luc-G5 cells. Thirty of down-regulated protein spots were identified after heparin treatment, many of which are related to tumor development, extracellular signaling, energy metabolism, and cellular proliferation. Vimentin and 14-3-3 zeta/delta were identified in common in PC-3M cells and the lungs of mice bearing B16-F10-luc-G5 carcinoma cells. Heparin 25 and 125 μg/mL decreased the protein expression of vimentin and 14-3-3 zeta/delta and the mRNA expression of α_v-integrin. Heparin 125 μg/mL decreased *vimentin* and *E-cadherin* mRNA transcription while increased *TGF-β* mRNA transcription in the PC-3M cells, but the differences were not significant. Transfection of vimentin-targeted siRNA for 48 h significantly decreased the BrdU incoporation and Ki67 expression in PC-3M cells.
Conclusion: Heparin inhibited PC-3M cell proliferation *in vitro* and B16-F10-luc-G5 cells metastasis in nude mice by inhibition of vimentin, 14-3-3 zeta/delta, and α_v-integrin expression.

Keywords: heparin; cell growth; proteome; vimentin; 14-3-3 zeta/delta; α_v-integrin

Acta Pharmacologica Sinica (2012) 33: 798–808; doi: 10.1038/aps.2012.42

Introduction

Despite the progress made over decades of research, cancer remains a major threat to human health with significant morbidity and mortality. In the development of new anti-tumor treatments, multi-targeting drugs continue to emerge as investigators search for candidates among currently available agents. Drugs with a long history of safe clinical use are especially attractive for testing their efficacy against cancer, which may be outside of the scope of their original application. In addition to its anti-coagulant activity, heparin is known to have suppressive effects on multiple biologic functions, such as hypertension[1], inflammation[2], and cellular proliferation[3].

* To whom correspondence should be addressed.
E-mail xjli@bjmu.edu.cn
Received 2012-02-14 Accepted 2012-03-30

Heparin is a polysulfated glycosaminoglycan with a highly negative charge. Two trials (FAMOUS and MALT) previously studied the effect of unfractionated heparin (UFH)[4] or low molecular weight heparin (LMWH)[5] in patients with small cell lung cancer. In both of these studies, a statistically significant survival advantage was observed in patients randomized to chemotherapy plus UFH or LMWH relative to patients who received chemotherapy alone. While several clinical studies strongly support an anti-cancer activity of heparin, especially LMWH, many questions remain unresolved[6]. For example, it is still unknown whether and how heparin modulates survival of carcinoma cells, although a number of biological properties have been postulated to explain the effects of heparin on the malignant process.

In this investigation, we addressed the potential inhibitory effects of heparin on growth of human prostate cancer cells (PC-3M) and metastasis of B16-F10-luc-G5 carcinoma cells in Balb/c nude mice with single dose and twice injection way and monitoring with living imaging technology. For the spontaneous hemorrhage is the main side effects of heparin, we also evaluated the systemic bleeding parameters of activated partial thromboplastin time (APTT) and hemorheological parameters of whole blood viscosity, elongation index (EI), orientation index (OI) and hematocrit of red blood cells, which are related greatly with tumor metastasis. By using a proteomic approach, we also identified proteins significantly associated with the anti-tumor and anti-metastatic effects of heparin to explore its new molecular mechanisms.

Materials and methods

Materials

DMEM medium, fetal bovine serum (FBS), penicillin and streptomycin were purchased from GIBCO (Grand Island, NY, USA). BrdU and Ki67 Cell Proliferation Kit for high content screening (HCS) was from Cellomics, Inc (Pittsburgh, PA, USA). B16-F10-Luc-G5 was from Caliper Life Sciences (Hopkinton, MA, USA). The vimentin specific antibody was from Beijing Biosynthesis Biotechnology (Beijing, China). Heparin sodium salt from porcine intestinal mucosa was purchased from Sigma-Aldrich, Inc (Saint Louis, MO, USA).

Cell culture

PC-3M cells were cultured in DMEM medium containing 10% heat-inactivated FBS, 100 U/mL penicillin and 100 μg/mL streptomycin in a humidified incubator with 5% CO_2 in air at 37 °C. B16-F10-Luc-G5 cells were cultured in DMEM medium containing 10% heat-inactivated FBS, 100 U/mL penicillin and 100 μg/mL streptomycin in a humidified incubator with 5% CO_2 in air at 37 °C.

Cell proliferation

PC-3M cells were cultured in 96-well plates. When the cells reached approximately 70% confluency, different doses of heparin (0, 0.5, 1, 5, 25, and 125 μg/mL) were added to the culture and incubated for 24 h. Every group has six wells. Each independent experiment was performed three times. MTS assays were then conducted using the CellTiter96 Aqueous Non-Radioactive Cell Proliferation Assay kit (Promega Corp, Madison, WI, USA), according to the manufacturer's instructions. Absorbance was measured at a wavelength of 490 nm, and the absorbance values of treated cells were calculated as a percentage of the absorbance of untreated cells.

Cell cycle and apoptosis analysis

For flow cytometric analysis of DNA content, heparin was added to PC-3M cells in the mid-logarithmic phase. After 24 h, cells were collected, pelleted, washed with phosphate-buffered saline (PBS) and resuspended in PBS containing 20 mg/L propidium iodide (PI, Sigma, St Louis, MO, USA) and 1 g/L ribonuclease A (RNAase A). Fixed cells for each experimental condition were examined by flow cytometry.

For analysis of apoptosis after incubation with heparin for 24 h, PC-3M cells (1×10^6 cells per treatment condition) were fixed and stained with 5 mL Annexin V-FITC (BD PharMingen, San Diego, CA) and 5 mL PI. Flow cytometric analysis was performed on 1×10^4 cells per sample and analyzed using a FACS Calibur (Becton Dickinson, Franklin Lakes, NJ) with a single laser emitting excitation light at 488 nm.

Multiparametric proliferation assay with a HCS analyzer

The 5-bromo-2'-deoxyuridine (BrdU) and Ki67 Cell Proliferation Kit for HCS reagent kit was used for simultaneous quantification of DNA replication and Ki67 proliferation marker in the same cell. It allows direct measurements of BrdU incorporation and Ki67 expression using a fixed end-point assay based on immunofluorescence detection in cells grown on standard high-density microplates. The primary antibodies were directed toward BrdU and Ki67 (mouse monoclonal and rabbit polyclonal antibodies, respectively) and secondary antibodies were conjugated with DyLight Fluor 488 (green) and DyLight Fluor 549 (orange). Cells were stained and fixed, and total cells per well of the microplates were analyzed using an ArrayScan HCS system (Cellomics Inc., Pittsburgh, PA, USA).

In vivo metastasis

B16-F10-luc-G5 cells that had been engineered to stably express firefly luciferase (Xenogen Corporation, Alameda, CA, USA) were injected into the lateral tail vein (5×10^6 cells/100 μL/mouse) of 6-week-old BALB/c nude mice. Mice were anesthetized and given 150 mg/g of *D*-luciferin in PBS by intraperitoneal injection. Bioluminescence was imaged with a charge-coupled device camera (IVIS; Xenogen) at 10 min after injection. Mice were anesthetized using 1%–3% isoflurane (Abbott Laboratories, Chicago, IL, USA). Bioluminescence from relative optical intensity was defined manually, and data were expressed as photon flux normalized to background photon flux, which was defined from relative optical intensity obtained from a control mouse not injected with luciferin. Animal handling and procedures were approved by the Peking University Health Science Center Institutional Animal Care and Use Committee. All animal studies conformed to the principles outlined in the Declaration of Helsinki.

Activated partial thromboplastin time (APTT) and hemorheological measurements

On day 14, blood specimens of BALB/c nude mice injected with B16-F10-luc-G5 cells were collected by retro-orbital bleeding after anesthesia with ether. Anesthesia was achieved by placing the mouse in a container containing cotton wool soaked in ether. The anesthetic plane was assessed by pinching the toe, tail or ear of the animal. The respiration rate was even and the color of the mucus membranes was bright pink. As the blood was collected, there was no evidence of pain observed in the animals. Whole blood with sodium citrate anticoagulant (9:1), centrifuged at 3000 r/min for 10 min, and upper plasma was used to detect APTT. APTT was measured in 50 μL plasma using C2000-4 Type Coagulometer (Beijing Precil Instrument Co, Ltd). Whole blood with sodium citrate anticoagulant was used for hemorheological measurements. Whole blood viscosity was detected in 800 μL of blood by using a viscosity meter (LBY-N6C, Precil Group, Beijing, China). Red blood cell deformability was determined by measuring the elongation index (EI) and orientation index (OI) using an ektacytometer (LBY-BX2 Precil Group, Beijing, China). Blood samples diluted with polyvinyl pyrolidone (PVP) were added to the base plate of the instrument. The EI and OI values were measured under stress rates of 100/s and 1000/s. Hematocrit of red blood cells was measured by aspirating blood into a capillary tube, sealing off the end of the tube and then centrifuging it at 10 000 r/min for 5 min. The height of the red blood cells deposited at the bottom end of the tube was recorded.

Two-dimensional gel electrophoresis (2-DE) and image analysis

Monolayers of PC-3M cells were treated with or without heparin (125 μg/mL) for 24 h. Cells were harvested using homemade scrapers. The resulting pellets were resuspended in 100 mL of solubilization buffer containing 40 mmol/L Tris, 8 mol/L urea, 4% *w/v* CHAPS, 60 mmol/L DTT and 1 mmol/L PMSF. After three freeze-thaw cycles, samples were centrifuged at 17 000×*g* for 15 min, and the supernatants were collected. Another pair of samples tested were the frozen mice lung tissues, which were thawed at room temperature before total proteins were extracted as mentioned above and the protein concentration measured by the Bradford method. First dimension isoelectric focusing (IEF) was performed using linear immobilized pH gradient readystrips (24 cm, pH 3–10, Bio-Rad Laboratories, Inc, Hercules, CA, USA). Protein samples (500 μg) from each group were solubilized in rehydration buffer [8 mol/L urea, 4% CHAPS, 65 mmol/L DTT, 0.2% Bio-Lyte (Bio-Rad) and 0.001% bromothymol blue] to a volume of 125 mL and allowed to incubate at room temperature for 30 min. After positive rehydration for 12 h at 50 V, IEF was run at 20 °C in the following steps: 250 V linear for 30 min, 500 V rapid for 30 min, 4000 V linear for 3 h, 4000 V rapid until 20 000 V. The IEF strips were then equilibrated by serial incubation (15 min) in equilibration buffer (6 mol/L urea, 2% SDS, 0.375 mol/L Tris-HCl at pH 8.8, 20% glycerol and 20 mg/mL DTT) and in equilibration buffer containing 2.5% iodoacetamide instead of DTT. Subsequently, the samples were separated in the second dimension on 12% polyacrylamide gels at 80 V for 10 min and then at 110 V for 50–60 min. Gels were stained with Coomassie Blue. The differentially expressed protein spots were excised manually from the sodium dodecyl sulphate-polyacrylamide gel (SDS-PAGE) and subjected to in-gel tryptic digestion.

Mass spectrometry identification of proteins

Proteins of interest were analyzed by nanoelectrospray with a hybrid quadrupole time-of-flight (Q-TOF) mass spectrometer (Waters, Milford, MA, USA). The peptide mixture was carried out on a Waters Capillary liquid chromatography system including three pumps, A, B, and C (Waters). Fused silica tubing were packed with Symmetry 300^{TM} C18, 3.5 mm spherical particles with a pore diameter of 1008 (Waters). The flow rate was set at 2.5 mL/min. Samples were injected at a flow rate of 20 mL/min.

Western blot analysis

Equal amounts of protein were analyzed by SDS–PAGE on a 10% polyacrylamide gel for vimentin and 14-3-3 zeta/delta and transferred to a polyvinylidene difluoride membrane (Millipore Corp, Bedford, MA, USA). The membrane with blotted proteins was blocked for 1 h with blocking buffer containing 5% non-fat dry milk and 0.05% Tween 20 in Tris-buffered saline (TBS-T), followed by incubation with vimentin antibody diluted (1:100) in blocking buffer overnight at 4 °C. The membrane was then washed three times with TBS-T for 30 min and incubated at room temperature for 1 h with diluted (1:2000) secondary AP-labeled IgG (Santa Cruz Biotechnology, Santa Cruz, CA, USA). Blots were extensively washed in TBST buffer and detection was done using the NBT/BCIP reaction (Amersco, NJ, USA) [7].

Ribonucleic acid isolation and reverse transcription–polymerase chain reaction (RT-PCR)

Total RNA was isolated using Trizol reagent (Invitrogen, Groningen, the Netherlands). First-strand cDNAs were generated from RNA samples by reverse transcription using oligo (dT). The following primers were used to amplify fragments of *β-actin*: 5′-ATCATGTTTGAGACCTTCAACA-3′ (sense) and 5′-CATCTCTTGCTCGAAGTCCA-3′ (antisense); transforming growth factor *(TGF)-β*: 5′-CAAGTGGACATCAAC GGTGAGG-3′ (sense) and 5′-TGGCCATGAGAAGCAGGAAAGG-3′ (antisense); *vimentin*: 5′-GACAATGCGTCTCTGGCACGTCTT-3′ (sense) and 5′-TCCTCCGCCTCCTGCAGGTTCTT-3′ (antisense); a_v*-integrin*: 5′-GACTGTGTGGAAGACAATGTCTGTAAACCC-3′ (sense) and 5′-CCAGCTAAGAGTTGAGTTCCAGCC-3′ (antisense); *E-cadherin*: 5′-TGGAGGAATTCTTGCTTTGC-3′ (sense) and 5′-CGTACATGTCAGCCAGCTTC-3′ (antisense).

Short interfering ribonucleic acid (siRNA) transfection

siRNA duplexes used in this study were bought from Santa Cruz, to interfere with vimentin expression. Non-silencing

siRNA (5′-UUAAGUAGCUUGGCCUUGATdT-3′ and 5′-UCAAGGCCAAGCUACUUAATdT-3′) was used as the negative controls. siRNA duplexes were transfected into HUVECs with siRNA transfection reagent (Polyplus-transfection Inc, San Marcos, CA, USA), according to the manufacturer's instructions. After transfection for 48 h, cells were subjected to multiparametric proliferation assay with a HCS analyzer.

Statistical analysis

Data were expressed as means±standard error of mean (SEM). Statistical significance of differences between means was determined by one-way analysis of variance (ANOVA) followed by Dunnett's test (Graphpad Prism 5 software). $P< 0.05$ was considered to be statistically significant.

Results

Effect of heparin on PC-3M cell viability and cell cycle

As estimated by the MTS assay, cell viability decreased dose dependently after 24 h of exposure to heparin at different concentrations (0.5, 1, 5, 25, and 125 μg/mL) (Figure 1A). Heparin 5, 25, and 125 μg/mL arrested cells in the G_1 phase and influence DNA synthesis, with a significant effect at 125 μg/mL ($P<0.05$, Figure 1B). Correspondingly, cells in the S phase decreased with increasing doses of heparin.

Effect of heparin on apoptosis of PC-3M cells

Annexin V^+ and PI^- staining represented early apoptotic cells, and Annexin V^+ and PI^+ staining represented late apoptotic and necrotic cells. Although the apoptotic cells were slightly elevated in the 125 μg/mL heparin treated group compared with the vehicle treated group, the difference was not significant (control: 1.55%±0.19% *vs* 5 μg/mL heparin: 1.44%±0.06%, 25 μg/mL heparin: 2.21%±0.08%, 125 μg/mL heparin: 5.91%±0.15%) (Figure 1C).

Effect of heparin on BrdU incorporation and Ki67 expression in PC-3M cells

BrdU incorporation and Ki67 activation in PC-3M cells were measured simultaneously in the same cells as described in Methods. As an alternative to [^{3}H]thymidine, BrdU, a thymidine analog, enables detection of DNA replication in actively proliferating cells using a monoclonal antibody directed against BrdU and fluorophore-conjugated secondary antibody. In addition, Ki67 antigen-positive cells can provide a specific and accurate indication of proliferating cells. As determined by HCS, we found that heparin suppressed BrdU incorporation and Ki67 expression in PC-3M cells compared to the control group, with statistically significant differences seen at the dosage of 125 μg/mL (Figure 1D).

Heparin inhibits B16-F10-luc-G5 cell lung metastasis in Balb/c nude mice

Balb/c nude mice were implanted with B16-F10-luc-G5 carcinoma cells by tail vein injection and systemically treated with vehicle (model), 30 mg/kg heparin intravenously 30 min before B16-F10-luc-G5 carcinoma cell injection and 24 h after B16-F10-luc-G5 carcinoma cell injection. From day 2, the growth of B16-F10-luc-G5 tumor burden over time in representative Balb/c nude mice was measured by *in vivo* imaging. By this analysis, progression of tumors in the whole body of mice and lung tissue was delayed and reduced in the 30 mg/kg heparin treatment group, and the growth of the primary tumor was reduced significantly from day 8 onward when detected from the ventral (A, B, C) and dorsal (D, E, F) views ($P<0.01$, Figure 2).

Heparin influences APTT and hemorheological parameters of Balb/c nude mice burdened with B16-F10-luc-G5 cells

At the 100/s and 1000/s shear rate, heparin could obviously decrease the whole blood viscosity, and there were significant differences when the tumor burdened (model) group was compared with the normal group or the heparin treated group ($P<0.01$, Table 1). Factors influencing whole blood viscosity were measured including red blood hematocrit, EI and OI. We also found that in the model group, red blood hematocrit, EI and OI were decreased significantly compared with the normal group ($P<0.01$) at the 100/s shear rate. At the shear rate of 1000/s in the model group, OI was decreased significantly compared with the normal group ($P<0.01$), but no significant difference was detected for EI. Additionally, heparin maintained relatively normal red blood hematocrit, with EI and OI at the 100/s shear rate and OI at the 1000/s shear rate being significantly different with the model group ($P<0.01$, Table 1). We had not found the difference in APTT between normal Balb/c nude mice with those burdened with B16-F10-luc-G5 cells; and heparin had also no influence on APTT of Balb/c nude mice burdened with B16-F10-luc-G5 cells.

Comparative proteomic analysis of PC-3M cells with or without heparin treatment

To explore the molecular mechanisms by which heparin exerts

Table 1. Effect of heparin on activated partial thromboplastin time (APTT) and hemorheological parameters in Balb/c nude mice burdened with B16-F10-luc-G5 cells. Mean±SEM. n=5. $^cP<0.01$ *vs* model.

Drug	Hematocrit (%)	Elongation Index		Orientation Index		Whole blood viscocity (mPa/s)		APTT (s)
		100/s	1000/s	100/s	1000/s	100/s	1000/s	
Normal	39±3.99^c	36.61±5.58^c	66.9±4.16	8.2±0.74^c	10.1±1.15^c	7.77±0.64^c	3.54±0.47^c	28.6±4.35
Model	21±4.60	28.2±2.69	64.2±3.58	4.94±0.69	5.03±0.24	12.19±2.28	4.58±0.02	27.11±3.13
Heparin	44±4.55^c	37.6±4.60^c	65.6±4.80	8.54±0.83^c	9.34±0.91^c	8.06±0.13^c	3.88±0.11^c	29.02±4.08

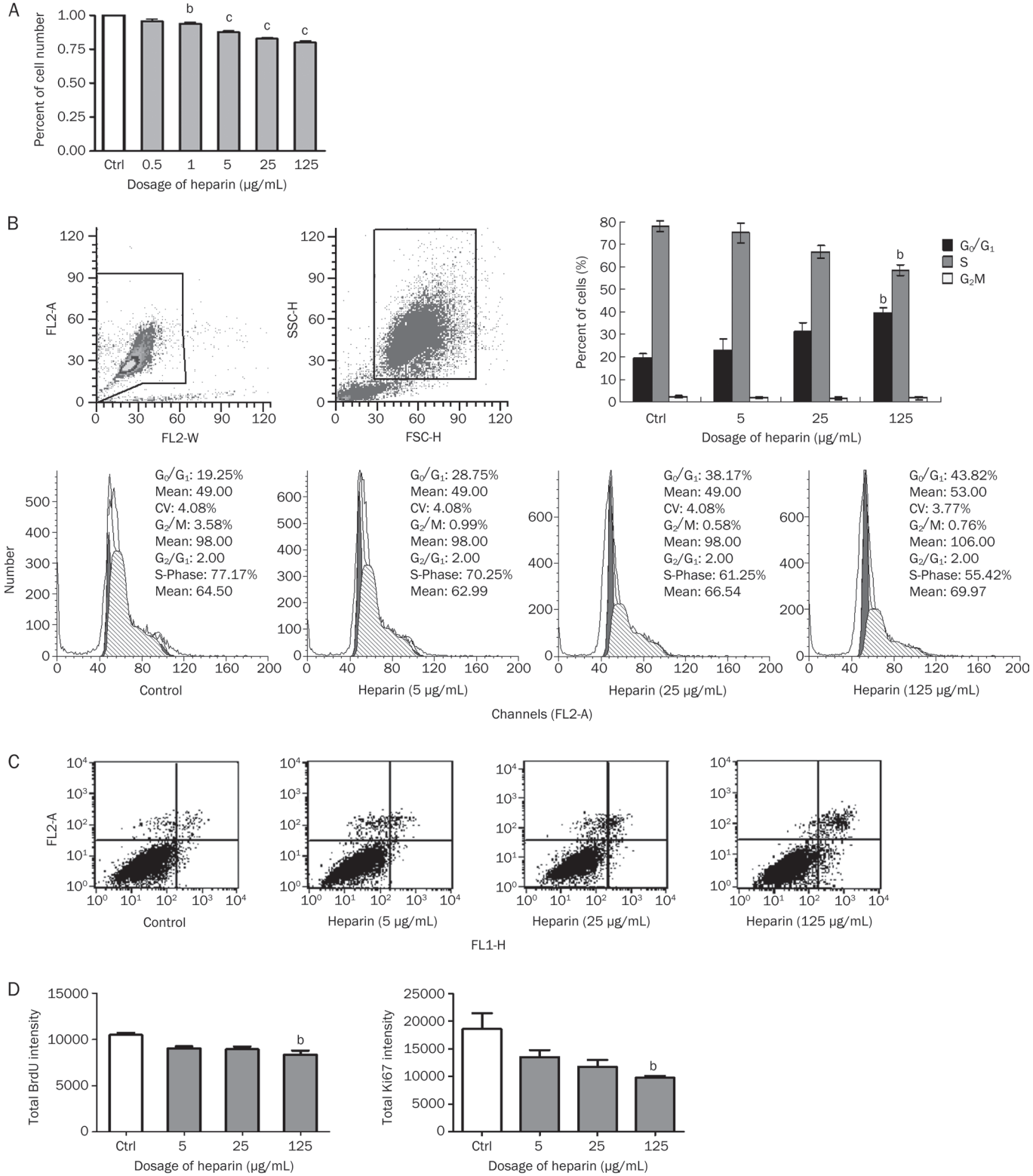

Figure 1. Heparin inhibits PC-3M cell growth. (A) MTS assays demonstrated a heparin-induced, dose-dependent decrease in PC-3M cell growth. (B) Flow cytometry showed that heparin treatment (5, 25, and 125 μg/mL, 24 h) resulted in marked cell cycle changes. (C) Flow cytometric analysis by Annexin V and PI double staining showed that heparin treatment (5, 25, and 125 μg/mL, 24 h) induced mild cell apoptosis. (D) HCS analysis showed that heparin suppressed BrdU incorporation and Ki67 expression in PC-3M cells. A total of 3000 cells were plated per well and incubated for 24 h before treatment with 5, 25, and 125 μg/mL heparin for 24 h. Control wells were treated with PBS per well. BrdU incorporation and Ki67 expression were measured simultaneously. Mean±SEM. n=6. ^{b}P<0.05, ^{c}P<0.01 compared with control. Each independent experiment was performed three times.

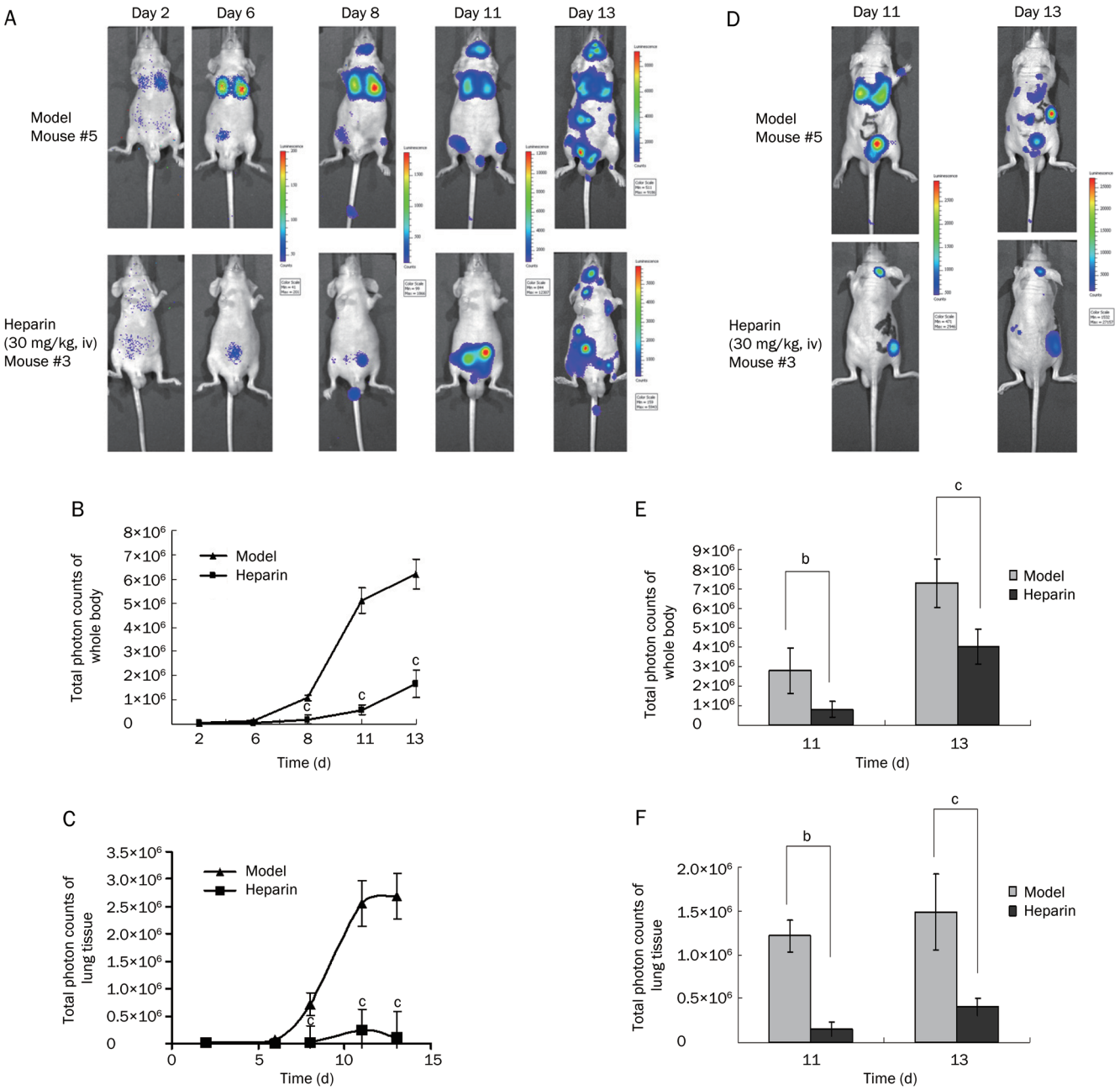

Figure 2. *In vivo* imaging of B16-F10-luc-G5 cell-derived tumors in mice. The cells (5×10^6) were injected intravenously through the tail vein of male BALB/c nude mice. Mice were imaged *in vivo* from the ventral (A) and dorsal (D) views between 2 to 14 days after the injection. Shown are images of one representative control (saline) animal and one representative heparin-treated mouse. Images were set on a pseudocolor scale to show relative bioluminescent changes over time. Metastatic signals reappeared on the day following administration of control mice with vehicle and multiple signals developed on day 6. *In vivo* imaging confirmed metastases in lungs (highest signal), ileum, jaws and skin (lower signal). Mice administered heparin (30 mg/kg, 30 min before and 24 h after tumor cell injection via the tail vein) showed significant reduction of pulmonary metastatic nodules. B, C, E, F show the statistical analysis of the total photon counts of whole body (B, E) or lung tissue (C, F) of BALB/c nude mice burdened with B16-F10-luc-G5 cells from the ventral (B, C) and dorsal (E, F) views. Mean±SEM. n=3. $^bP<0.05$, $^cP<0.01$ compared with the vehicle-treated control group.

anti-tumor and anti-proliferative effects in PC-3M cells, we compared the protein expression patterns in heparin treated (125 μg/mL) and untreated cells. 2-DE analysis showed generally similar protein expression patterns in the heparin treated and untreated PC-3M cells (Figure 3A, B). The protein spots were analyzed by PDQuest software, and 83 protein spots were significantly decreased in heparin treated versus untreated PC-3M cells ($P<0.05$, Supporting information). Thirty of these obviously decreased spots after heparin treatment were identified by Q-TOF analysis (Table 2).

Table 2. Thirty of the significantly decreased spots after heparin treatment in PC-3M cells identified by Q-TOF analysis and search of the Mascot database.

Protein spot	Protein name	Mass	Score	Matches	Sequences	emPAI
1	Anterior gradient protein 2 (AGR2)	20 024	497	27 (17)	8 (6)	3.06
2	Adenylate kinase isoenzyme 1 (KAD1)	21 735	190	9 (5)	6 (5)	1
3	GTP-binding nuclear protein Ran (RAN)	24 579	694	29 (24)	12 (10)	3.63
4	14-3-3 protein zeta/delta 1433Z_HUMAN	27 899	89	1 (1)	1 (1)	0.12
5	Heterogeneous nuclear ribonucleoprotein D0 (HNRPD_HUMAN)	38 581	65	2 (2)	1 (1)	0.09
6	Heterogeneous nuclear ribonucleoprotein A3 (ROA3_HUMAN)	39 799	170	6 (5)	4 (3)	0.14
7	ATP synthase subunit alpha, mitochondrial (ATPA_HUMAN)	59 828	240	24 (13)	13 (8)	0.53
8	ATP synthase subunit alpha, mitochondrial ATPA_HUMAN	59 828	29	2 (1)	2 (1)	0.98
9	Annexin A11ANX11_HUMAN	54 697	724	19 (16)	8 (7)	0.57
10	Vimentin	55 123	1 124	51 (29)	21 (14)	1.84
11	Dihydrolipoyl dehydrogenase, mitochondrial DLDH_HUMAN	54 713	283	12 (10)	6 (4)	1.23
12	Prelamin-A/C LMNA_HUMAN	74 380	1 332	45 (38)	27 (22)	1.11
13	Dihydrolipoyllysine-residue succinyltransferase component of 2-ox oglutarate dehydrogenase complex, mitochondrial ODO2_HUMAN	49 067	225	6 (4)	4 (2)	0.91
14	Stress-70 protein, mitochondrial GRP75_HUMAN	73 920	163	5 (4)	5 (4)	0.08
15	Stress-70 protein, mitochondrial GRP75_HUMAN	73 920	149	3 (3)	2 (2)	0.09
16	L-lactate dehydrogenase B chain LDHB_HUMAN	36 900	193	6 (5)	5 (4)	0.46
17	T-complex protein 1 subunit zeta TCPZ_HUMAN	58 444	343	12 (9)	5 (4)	0.39
18	Heat shock protein beta-1 HSPB1_HUMAN	22 826	1 172	36 (27)	12 (10)	4.91
19	T-complex protein 1 subunit gamma TCPG_HUMAN	61 066	103	4 (3)	3 (2)	1.55
20	Pyruvate kinase isozymes M1/M2 KPYM_HUMAN	58 470	88	3 (2)	3 (2)	1.21
21	RuvB-like 2 RUVB2_HUMAN	51 296	262	9 (7)	6 (5)	0.45
22	Phosphoglycerate mutase 1 PGAM1_HUMAN	28 900	420	17 (11)	7 (7)	1.67
23	Elongation factor Tu, mitochondrial EFTU_HUMAN	49 852	1 519	42 (31)	15 (11)	1.79
24	Heat shock protein HSP 90-alpha HS90A_HUMAN	85 006	1 345	41 (31)	26 (20)	1.48
25	Heat shock protein 75 kDa, mitochondrial TRAP1_HUMAN	80 345	285	4 (4)	1 (1)	0.04
26	Heat shock protein HSP 90-beta HS90B_HUMAN	83 554	352	7 (5)	3 (2)	0.12
27	Endoplasmin ENPL_HUMAN	92 696	139	3 (2)	3 (2)	0.11
28	Peptidyl-prolyl *cis-trans* isomerase F, mitochondrial PPIF_HUMAN	22 368	288	9 (5)	7 (4)	0.67
29	Beta-enolase ENOA_HUMAN	47 481	3 394	86 (64)	29 (21)	6.49
30	Voltage-dependent anion-selective channel protein 1 VDAC1_HUMAN	30 868	1 502	40 (33)	13 (11)	2.78

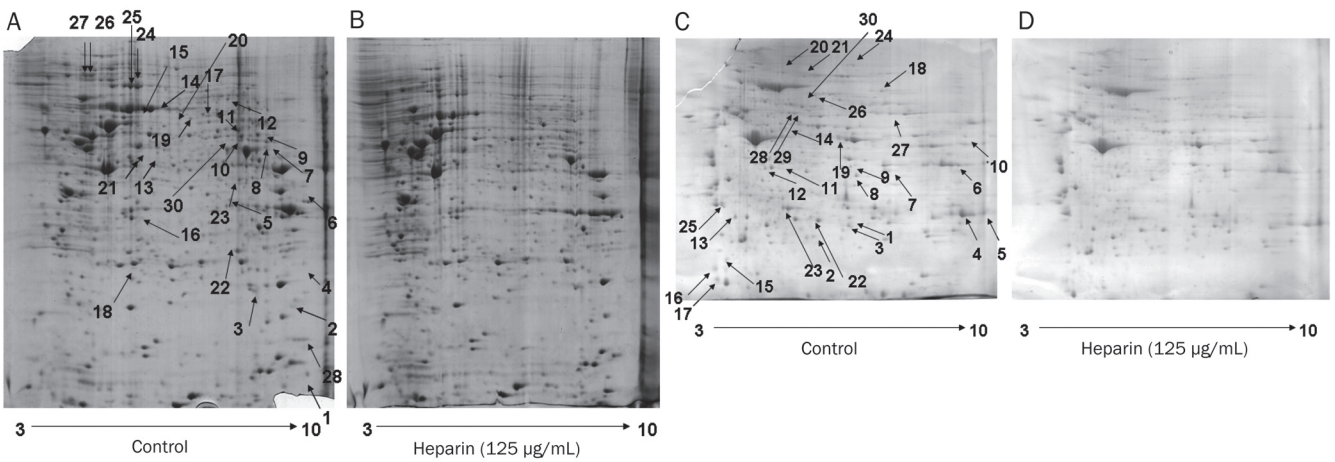

Figure 3. 2-DE analysis of protein expression in PC-3M cells and lungs of mice burdened with B16-F10-luc-G5 cells with or without heparin treatment. Representative 2-DE maps of proteins in PC-3M cell lysis without (A) or with heparin treatment (B). Representative 2-DE maps of proteins in lysed lung tissues of mice bearing B16-F10-luc-G5 cells without (C) or with (D) heparin administration. Approximately 500 μg of total protein were focused on linear immobilized pH gradient strips (pH 3–10, 24 cm) before separating on a 12% sodium dodecyl sulphate–polyacrylamide gel and staining with Coomassie blue for detecting protein spots. The experiment was performed three times.

Comparative proteomic analysis of lungs of mice bearing B16-F10-luc-G5 cells with or without heparin administration

To further elucidate the possible novel molecular mechanisms by which heparin might exert its anti-tumor and anti-metastasic effects in Balb/c nude mice burdened with B16-F10-luc-G5 cells, we compared protein expression patterns in the lungs of heparin-treated and untreated (control) mice. 2-DE analysis showed generally similar protein expression patterns in the heparin-treated and untreated groups (Figure 3C and 3D). Among them, 30 obviously different spots (indicated by arrows) were identified by using Q-TOF analysis (Table 3).

Effect of heparin on expression levels of 14-3-3 zeta/delta, vimentin, E-cadherin, TGF-β, and α_v-integrin in PC-3M cells

After comparing the 2-DE results from PC-3M cells and lungs of mice burdened with B16-F10-luc-G5 cells, we found 14-3-3 zeta/delta and vimentin protein spots were identified in common. Then, our Western blot analysis confirmed that heparin could dose-dependently decrease the protein expression of 14-3-3 zeta/delta and vimentin, and there were significant differences at 25 and 125 μg/mL (Figure 4A). Cytoskeleton protein vimentin is involved in tumor mobility, adhesion, and epithelial to mesenchymal transition (EMT). Vimentin also co-localizes with $\alpha_v\beta_3$-integrin (focal contacts) when tumor cell moved and thought as an important marker of tumor cell EMT, along with E-cadherin, TGF-β. To determine whether E-cadherin, TGF-β and α_v-integrin are transcriptionally regulated by heparin, RT–PCR analysis was performed on heparin treated PC-3M cells. *Vimentin* and *E-cadherin* mRNA decreased at the high dosage of heparin, while *TGF-β* mRNA increased with heparin treatment in the PC-3M cells (Figure 4B), although the differences were not significant. Expression of *a_v-integrin* mRNA in PC-3M cells decreased with heparin 25 and 125 μg/mL treatment (Figure 4C).

The effect of vimentin-targetted siRNA on PC-3M cell proliferation

When PC-3M cells were transfected with siRNA against the vimentin gene for 48 h, the expression of vimentin in cells was partially reduced by 35% in comparison to the controls ($P<0.05$; Figure 5A) and the BrdU incorporation and Ki67 activation in PC-3M cells was reduced significantly compared with the control ($P<0.05$; Figure 5B).

Table 3. Thirty of the significantly decreased spots after heparin administration in lung tissue of Balb/c nude mice burdened with B16-F10-luc-G5 cells identified by Q-TOF analysis and search of the Mascot database.

Protein spot	Protein name	Mass	Score	Matches	Sequences	emPAI
1	Carbonyl reductase [NADPH]	26 056	335	15 (9)	7 (5)	1.32
2	14-3-3 protein zeta/delta	27 925	370	15 (11)	10 (7)	2.08
3	Hemoglobin subunit beta-1	15 944	79	1 (1)	1 (1)	0.21
4	Selenium-binding protein 1	53 051	72	4 (3)	3 (2)	0.13
5	Elongation factor 1-beta	24 849	344	5 (4)	3 (3)	0.46
6	Phosphoglycerate mutase 2	28 980	350	29 (21)	10 (8)	2.31
7	Carbonyl reductase [NADPH] 2	26 056	662	34 (23)	12 (7)	1.96
8	Troponin I, fast skeletal muscle	21 515	268	26 (15)	9 (5)	2.68
9	Hemoglobin subunit alpha	15 133	165	6 (6)	3 (3)	0.84
10	Carbonic anhydrase 3	29 633	144	31 (11)	8 (5)	1.34
11	Triosephosphate isomerase	32 684	65	25 (7)	10 (4)	0.47
12	Transcription factor BTF3	22 017	34	9 (1)	4 (1)	0.33
13	HIV Tat-specific factor 1 homolog	86 644	27	1 (0)	1 (0)	0.04
14	Transgelin	22 618	19	4 (0)	3 (0)	0.15
15	Filamin A-interacting protein 1-like	130 263	15	2 (0)	1 (0)	0.03
16	Monoglyceride lipase	33 708	64	13 (3)	7 (2)	0.46
17	Fructose-bisphosphate aldolase A	39 787	45	3 (1)	3 (1)	0.17
18	Creatine kinase M-type	43 246	36	25 (2)	10 (1)	0.16
19	Advanced glycosylation end product-specific receptor	42 984	19	2 (0)	1 (0)	0.08
20	Beta-enolase	47 337	31	9 (1)	8 (1)	0.07
21	Fatty acid-binding protein, epidermal	15 470	19	1 (1)	1 (1)	0.22
22	40S ribosomal protein SA	32 931	28	3 (1)	3 (1)	0.1
23	Myosin light chain 3	22 521	635	41 (30)	14 (11)	3.6
24	Serum albumin	70 700	302	25 (17)	12 (7)	0.44
25	Vimentin	53 712	24	1 (0)	1 (0)	0.06
26	Phosphoglycerate mutase 1	28 928	217	19 (11)	7 (4)	0.92
27	Adenylate kinase isoenzyme 1	21 640	49	21 (3)	8 (3)	0.78
28	Pyruvate dehydrogenase protein X component, mitochondrial	54 250	39	3 (2)	3 (2)	0.13
29	Myosin regulatory light chain 2, skeletal muscle isoform	19 057	44	18 (2)	4 (2)	0.38
30	Dynein heavy chain 12, axonemal	3 587 387	31	1 (1)	1 (1)	0.01

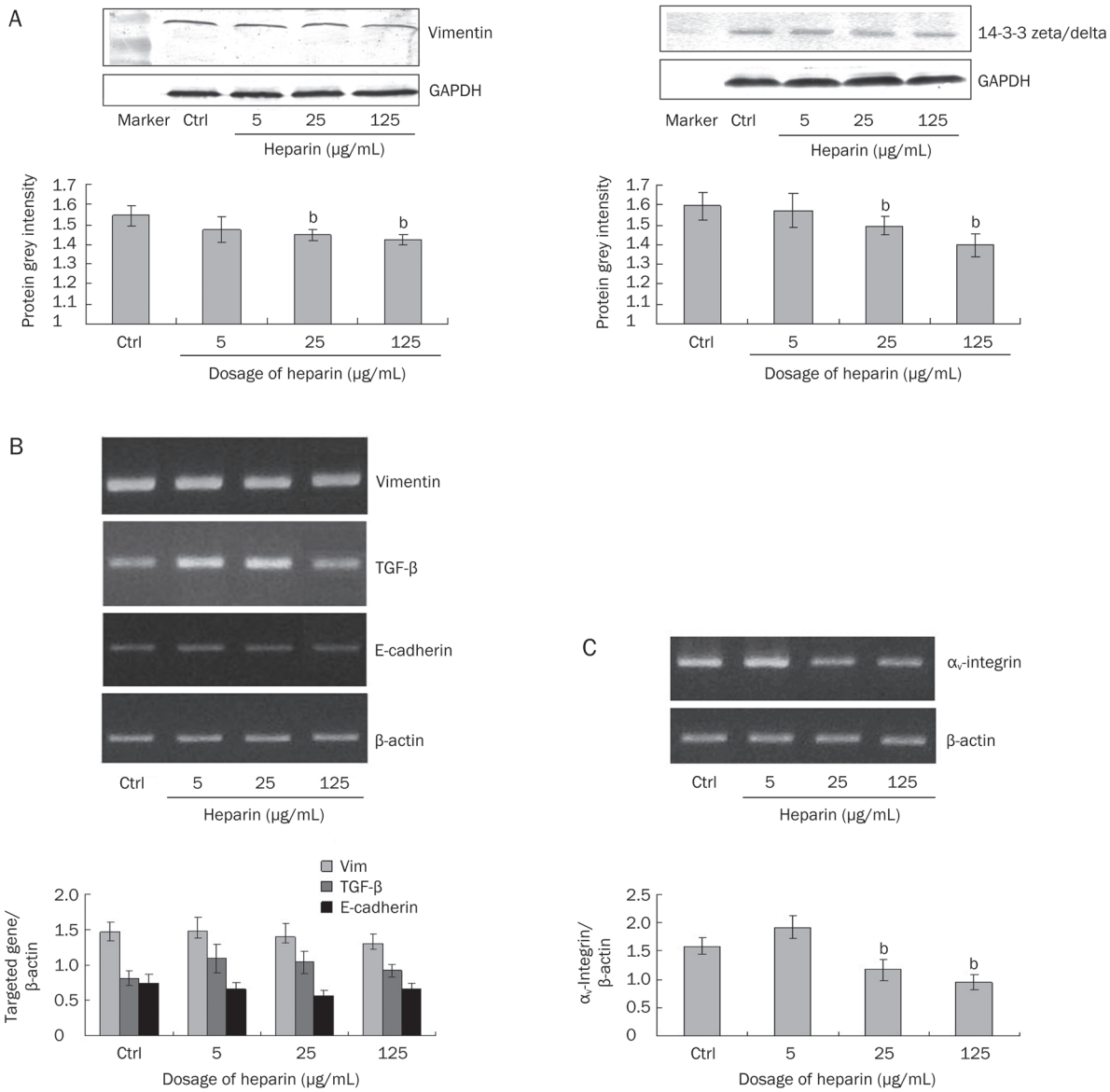

Figure 4. Effects of heparin on protein expression of vimentin and 14-3-3 zeta/delta (A) and mRNA expression of vimentin, TGF-β, E-cadherin, and α_v-integrin (B, C) in PC-3M cells. Mean±SEM. n=3. $^bP<0.05$ *vs* the vehicle-treated control group. Each independent experiment was performed three times.

Discussion

In the experimental metastasis model, B16F10-luc-G5 tumor cells stably expressing firefly luciferase injected intravenously in the tail vein develop into pulmonary metastasis and are easily detected *in vivo* over time. We obtained results similar to that of others[8–10] in that a single administration of heparin 30 min before injection of tumor cells into the tail vein could significantly inhibit this lung metastasis. In our study, with a second administration of heparin at 24 h after tumor cell injection, the lung metastasis could be significantly inhibited throughout the 14-day experimental period. APTT data showed that this injection of heparin was safe. As blood disorders (*ie*, low hematocrit) have been reported in cancer patients, we also analyzed hemorheological paremeters in Balb/c nude mice burdened with B16-F10-luc-G5 cells. Erythrocyte deformability and hematocrit were decreased, while the whole blood viscosity was increased in the model group compared to those of normal subjects[11, 12]. The observation that heparin could maintain the normal levels of these blood parameters and also inhibit metastasis as mentioned above indicated that the influence of heparin on circulating cells was related to its inhibition of tumor development.

The effect of heparin on tumors includes interference with cancer-induced hypercoagulation, cancer cell proliferation, degradation of the extra-cellular matrix (involving the heparan sulfate chains of cell surface and extracellular matrix proteoglycans), angiogenesis, selectin-mediated binding of platelets and cancer cells, growth factors and their receptors, hepara-

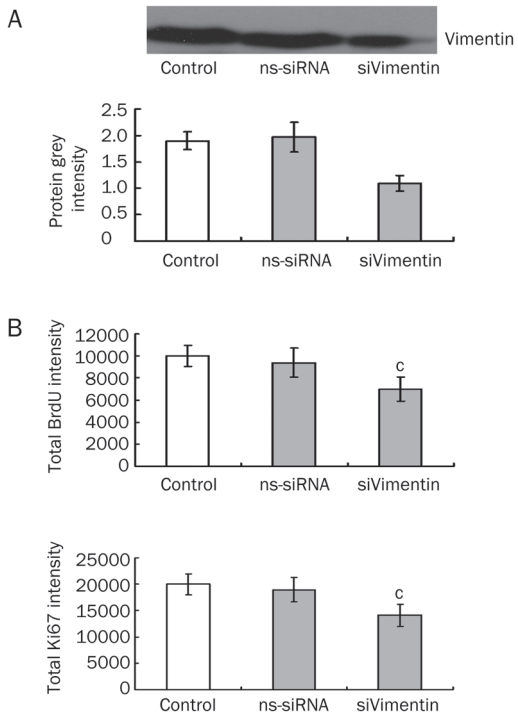

Figure 5. siRNA interferes with vimentin expression in PC-3M cells. Non-silencing siRNA (ns-siRNA) was used as a negative control. Vimentin-targeted siRNA (siVimentin) was transfected into PC-3M for 48 h; the total protein was extracted with protein lysis buffer and protein concentrations were measured using the Bradford protein assay. Cell lysates were analyzed by Western blotting (A). The effect of this vimentin knockdown on BrdU incorporation and Ki67 expression (B) in PC-3M cells. A total of 3000 cells were plated per well and incubated for 24 h. Mean±SEM. n=6. ^{c}P<0.01 compared with control. Each independent experiment was performed three times.

nase, tumor progression, and metastasis[13,14]. Heparin was proposed to have a role in maintaining the effects of chemotherapeutic drugs, as both UFH and LMWH have been shown to act as chemotherapy sensitizers[4, 5]. In our evaluation of the influence of heparin on tumor cell proliferation, cell cycle and apoptosis, we found that it could inhibit proliferation of PC-3M tumor cells and arrest them in the G_0/G_1 phase. Heparin has been reported to induce apoptosis in tumor cells mediated by caspase-3, caspase-8, Fas, and Bcl-2[15]. In this study, we did not find a significant influence of heparin on tumor cell apoptosis, although there was a slight increase in number of apoptotic PC-3M cells treated with heparin (125 μg/mL).

To gain a global overview of protein changes in response to heparin treatment, we utilized the 2-DE method to evaluate PC-3M cells and lungs of mice bearing B16-F10-luc-G5 cells. Our 2-DE analysis identified 60 different down-regulated proteins in PC-3M tumor cells and lungs after heparin treatment. The functions of those differentially expressed proteins are related to cell structure and movement (*eg*, fascin, transgelin, filamin, myosin, vimentin, dynein), cell growth and apoptosis (*eg*, anterior gradient protein 2, pyruvate kinase isozymes M1/M2, enolase, 14-3-3 zeta/delta), energy metabolism (*eg*, adenylate kinase isoenzyme 1, ATP synthase subunit alpha, dihydrolipoyllysine-residue succinyltransferase component of 2-ox oglutarate dehydrogenase complex), nuclear activity regulation (*eg*, GTP-binding nuclear protein Ran) and several chaperones in the control of cell proliferation (*eg*, stress-70 protein, T-complex protein 1, heat shock protein HSP 90, heat shock protein 75 and endoplasmin).

After comparing the 2-DE results from PC-3M cells and lungs of mice burdened with B16-F10-luc-G5 cells, we found five protein spots which were identified in common: adenylate kinase isoenzyme 1, 14-3-3 protein zeta/delta, vimentin, phosphoglycerate mutase 1 and β-enolase.

Previously, based on the hypothesis that heparin regulates vimentin in the tumor-endothelium interaction and the finding of endothelial 2-DE experiment that vimentin expression altered greatly by low molecular weight heparin, we demonstrated that vimentin partly plays a role in the anti-metastatic effects of low molecular weight heparin[16]. In the present study, we further analyzed and confirmed the down-regulated expression of vimentin, which was also one of the proteins influenced by heparin and identified in both the PC-3M cells and lungs of mice burdened with B16-F10-luc-G5 cells, along with 14-3-3 zeta/delta. The 14-3-3 zeta/delta belongs to a family of highly conserved proteins that play important roles in a wide range of cellular processes including apoptosis, cell cycle progression, and signal transduction. 14-3-3 proteins regulate the cell cycle and prevent apoptosis by controlling the nuclear and cytoplasmic distribution of signaling molecules with which they interact. In our pharmacodynamics studies about heparin on PC-3M tumor cells, we found that heparin have obviously inhibitory effects on tumor growth, proliferation and cell cycle. Additionally, the 14-3-3 dimer can bind to vimentin polypeptides and regulate Raf activation by EGF[17], 14-3-3 protein plays an organizing role in the intermediate filament network[18], and its overexpression has been found in multiple cancers. 14-3-3 zeta and delta both have been identified as biomarkers for poor prognosis, therapy and chemoresistance in multiple tumor types[19, 20]. Thus, vimentin and 14-3-3 are of interest as their protein expression levels were found to be significantly decreased by heparin in PC-3M cells. Our results of vimentin-targetted siRNA showed that partial knockdown of vimentin in PC-3M could reduce the ability of PC-3M cells proliferation. The inhibitory effects of heparin on structural organization of vimentin play an important role in its anti-tumor and anti-metastasis function. Meaningfully, activation of an Akt-14-3-3 zeta signaling pathway in promoting a multidrug-resistant phenotype has been associated with vimentin-dependent invasive behavior in diffuse large B-cell lymphoma cells[21]. These proteins may account for the effect of heparin as a chemotherapy sensitizer, but further research on the role of 14-3-3 and vimentin in multi-drug resistance to anti-tumor agents should be undertaken.

In recent years, the cytoskeleton protein vimentin has gained attention for its roles in cell migration, adhesion, EMT, and signal transduction. In cancer-related studies, vimentin

has been found to be mainly involved in tumor mobility[22, 23]. Vimentin has been shown to co-localize with $\alpha_v\beta_3$-integrin (focal contacts)[24]. Moreover, through integrin-linked kinase, integrin can regulate expression and function of vimentin. The levels of vimentin and integrin play a key role in tissue homeostasis as well, and their hyperexpression leads to tumorigenesis[25, 26]. We detected and observed that the mRNA expression levels of α_v-integrin and vimentin could be mediated by heparin treatment.

In conclusion, our study has demonstrated multiple effects of heparin on tumors, consistent with previous studies that have identified heparin as an anti-cancer drug with diverse targets. These effects of heparin involve the inhibition of 14-3-3 zeta/delta, vimentin and α_v-integrin expression.

Acknowledgements

This work was supported by the National Natural Science Foundation of China (No 81020108031, 30572202, 30973558, 30772571, 30901815, 30901803), the Major Specialized Research Fund from the Ministry of Science and Technology in China (No 2009ZX09103-144), Research Fund from Ministry of Education of China (111 Projects No B07001) and Scientific Research Foundation for the Returned Overseas Chinese Scholars, State Education Ministry.

Author contribution

Yan PAN, Hong ZHOU, and Xue-jun LI designed research; Yan PAN, Li-jun ZHONG, Kui CHEN, Hao-peng YANG, Yilixiati XIAOKAITI, Aikebaier MAIMAITI, and Ling JIANG performed research; Yan PAN, Xin WANG, and Li-jun ZHONG analyzed data; Yan PAN and Xue-jun LI wrote the paper.

References

1 Mandal AK, Lyden TW, Saklayen MG. Heparin lowers blood pressure biological and clinical perspectives. Kidney Int 1995; 47: 1017–24.
2 Neison RM, Cecconi O, Roberts G, Aruffo A, Linhard RJ, Bcvilaqua MP. Heparin oligosaccharides bind L- and P-selection and inhibit acute inflammation. Blood 1993; 82: 3253–61.
3 Li HL, Ye KH, Zhang HW, Luo YR, Ren XD, Xiong AH, *et al*. Effect of heparin on apoptosis in human nasopharyngeal carcinoma CNE2 cells. Cell Res 2001; 4: 311–5.
4 Lebeau B, Chastang C, Brechot JM, Capron F, Dautzenberg B, Delaisements C, *et al*. Subcutaneous heparin treatment increases survival in small cell lung cancer. Cancer 1994; 1: 38–45.
5 Altinbas M, Coskun HS, Er O, Ozkan M, Eser B, Unal A, *et al*. A randomized clinical trial of combination chemotherapy with and without low-molecular-weight heparin in small cell lung cancer. J Thromb Haemost 2004; 8: 1266–71.
6 Niers TM, Klerk CP, DiNisio M, Van Noorden CJ, Büller HR, Reitsma PH, *et al*. Mechanisms of heparin induced anti-cancer activity in experimental cancer models. Crit Rev Oncol Hematol 2007; 3: 195-207.
7 Pan Y, Iwata F, Wang D, Muraguchi M, Ooga K, Ohmoto Y, *et al*. Identification of aquaporin-5 and lipid rafts in human resting saliva and their release into cevimeline-stimulated saliva. Biochim Biophys Acta 2009; 1: 49–56.
8 Boeryd B. Effect of heparin and plasminogen inhibitor (EACA) in brief and prolonged treatment on intravenously injected tumor cells. Acta Pathol Microbiol Scand 1966; 68: 347–54.
9 Hagmar B, Boeryd B. Disseminating effect of heparin on experimental tumor metastases. Pathol Eur 1969; 4: 274–82.
10 Maat B. Extrapulmonary colony formation after intravenous injection of tumor cells into heparin-treated animals. Br J Cancer 1978; 3: 369–76.
11 Ramakrishnan S, Grebe R, Singh M, Schmid-Schönbein H. Evaluation of hemorheological risk factor profile in plasmacytoma patients. Clin Hemorheol Microcirc 1999; 20: 11–9.
12 Rickles FR, Falanga A. Molecular basis for the relationship between thrombosis and cancer. Thromb Res 2001; 6: V215–24.
13 Mousa SA, Petersen LJ. Anti-cancer properties of low-molecular-weight heparin: preclinical evidence. Thromb Haemost 2009; 102: 258–67.
14 Casu B, Vlodavsky I, Sanderson RD. Non-anticoagulant heparins and inhibition of cancer. Pathophysiol Haemost Thromb 2008; 36: 195–203.
15 Erduran E, Tekelioglu Y, Gedik Y, Bektaş I, Hacisalihoglu S. *In vitro* determination of the apoptotic effect of heparin on lymphoblasts using DNA analysis and measurements of Fas and Bcl-2 proteins by flow cytometry. Pediatr Hematol Oncol 2004; 5: 383–91.
16 Pan Y, Lei TL, Teng B, Liu JH, Zhang JZ, An Y, *et al*. Role of vimentin in inhibitory effects of low molecular weight heparin on PC-3M adhesion to and migration through endothelium. J Pharmacol Exp Ther 2011; 339: 82–92.
17 Tzivion G, Luo ZJ, Avruch J. Calyculin A-induced vimentin phosphorylation sequesters 14-3-3 and displaces other 14-3-3 partners *in vivo*. J Biol Chem 2000; 275: 29772–8.
18 Satoh J, Yamamura T, Arima K. The 14-3-3 protein epsilon isoform expressed in reactive astrocytes in demyelinating lesions of multiple sclerosis binds to vimentin and glial fibrillary acidic protein in cultured human astrocytes. Am J Pathol 2004; 165: 577–92.
19 Yang X, Cao W, Zhang L, Zhang W, Zhang X, Lin H. Targeting 14-3-3zeta in cancer therapy. Cancer Gene Ther 2012; 19: 153–9.
20 Neal CL, Yu D. 14-3-3ζ as a prognostic marker and therapeutic target for cancer. Expert Opin Ther Targets 2010; 14: 1343–54
21 Maxwell SA, Cherry EM, Bayless KJ. Akt, 14-3-3ζ, and vimentin mediate a drug-resistant invasive phenotype in diffuse large B-cell lymphoma. Leuk Lymphoma 2011; 52: 849–64.
22 Shirahata A, Sakata M, Sakuraba K, Goto T, Mizukami H, Saito M, *et al*. Vimentin methylation as a marker for advanced colorectal carcinoma. Anticancer Res 2009; 29: 279–81.
23 Vora HH, Patel NA, Rajvik KN, Mehta SV, Brahmbhatt BV, Shah MJ, *et al*. Cytokeratin and vimentin expression in breast cancer. Int J Biol Markers 2009; 23: 38–46.
24 Tsuruta D, Jones JC. The vimentin cytoskeleton regulates focal contact size and adhesion of endothelial cells subjected to shear stress. J Cell Sci 2003; 116: 4977–84.
25 Zhang X, Fournier MV, Ware JL, Bissell MJ, Yacoub A, Zehner ZE. Inhibition of vimentin or beta1 integrin reverts morphology of prostate tumor cells grown in laminin-rich extracellular matrix gels and reduces tumor growth *in vivo*. Mol Cancer Ther 2009; 3: 499–508.
26 Bhattacharya R, Gonzalez AM, Debiase PJ, Trejo HE, Goldman RD, Flitney FW, *et al*. Recruitment of vimentin to the cell surface by beta3 integrin and plectin mediates adhesion strength. J Cell Sci 2009; 122: 1390–400.

Acta Pharmacologica Sinica (2012) 33: 809–816
 1671-4083/12 $32.00
www.nature.com/aps

Original Article

Anti-CHMP5 single chain variable fragment antibody retrovirus infection induces programmed cell death of AML leukemic cells *in vitro*

Hai-rong WANG[1, #], Zhen-yu XIAO[2, 3, #], Miao CHEN[1, #], Fei-long WANG[1, #], Jia LIU[2, 3], Hua ZHONG[2, 3], Ji-hua ZHONG[2, 3], Ren-rong OU-YANG[2, 3], Yan-lin SHEN[4], Shu-ming PAN[1, *]

[1]Emergency Department, Xin-Hua Hospital, Shanghai Jiao Tong University School of Medicine, Shanghai 200092, China; [2]Department of Hematology, Ren-Ji Hospital, Shanghai Jiao Tong University School of Medicine, Shanghai 200127, China; [3]Shanghai Institute of Hematology, Shanghai 200025, China; [4]Department of Pharmacy, Xin-Hua Hospital, Shanghai Jiao Tong University School of Medicine, Shanghai 200092, China

Aim: Over-expressed CHMP5 was found to act as oncogene that probably participated in leukemogenesis. In this study, we constructed the CHMP5 single chain variable fragment antibody (CHMP5-scFv) retrovirus and studied the changes of programmed cell death (PCD) of AML leukemic cells after infection by the retrovirus.
Methods: The anti-CHMP5 KC14 hybridoma cell line was constructed to generate monoclonal antibody of CHMP5. The protein expression of CHMP5 was studied using immunofluorescence analysis. pMIG-CHMP5 scFv antibody expressible retroviral vector was constructed to prepare CHMP5-scFv retrovirus. AML leukemic U937 cells were infected with the retrovirus, and programmed cell death was studied using confocal microscope, FCM and Western blot.
Results: We obtained a monoclonal antibody of CHMP5, and found the expression of CHMP5 was up-regulated in the leukemic cells. After U937 cells were infected with CHMP5-scFv retrovirus, CHMP5 protein was neutralized. Moreover, the infection resulted in a significant increase in apoptosis and necrosis of U937 cells. In U937 cells infected with CHMP5-scFv retrovirus, apoptosis-inducing factor (AIF)-mediated caspase-independent necrotic PCD was activated, but autophagic programmed cell death was not observed. Neither the intrinsic nor extrinsic apoptotic PCD pathway was activated. The granzyme B/perforin-mediated caspase-dependent apoptotic PCD pathway was not activated.
Conclusion: CHMP5-scFv retrovirus can neutralize the abnormally high levels of the CHMP5 protein in the cytosol of AML leukemic U937 cells, thereby inducing the programmed cell death of the leukemic cells via AIF-mediated caspase-independent necrosis and apoptosis.

Keywords: leukemia; CHMP5; monoclonal antibody; single chain variable fragment antibody (scFv); retrovirus; programmed cell death; apoptosis; necrosis; autophagy; apoptosis-inducing factor (AIF)

Acta Pharmacologica Sinica (2012) 33: 809–816; doi: 10.1038/aps.2012.38; published online 21 May 2012

Introduction

In adults, acute myeloid leukemia (AML) is by far the most common type of acute leukemia. It is a cancer of the bone marrow and is characterized by a mutation in a hematopoietic stem or progenitor cell, which develops into the accumulation of highly proliferative dysfunctional and immature myeloid cells. These abnormal cells eventually dominate hematopoietic niches, such as the bone marrow, and result in abnormal peripheral blood counts due to high number of myeloblasts. Over the past several decades, improvements in chemotherapeutic regimens and supportive care have resulted in significant but modest progress in treating AML, but AML remains a fatal disease for most patients[1]. A better molecular definition and the elucidation of the physiopathology of AML combined with the development of new and targeted therapies may result in a better prognosis for patients with AML in the future.

The human charged multivesicular body protein 5 (CHMP5) is a member of the CHMP family of coiled-coil proteins[2]. The multivesicular body (MVB) is a particular type of late endosomes, which are crucial intermediates in the internalization

# These authors contributed equally to this work.
* To whom correspondence should be addressed.
E-mail panshuming@live.com
Received 2012-02-09 Accepted 2012-03-23

of nutrients, ligands and receptors through the endolysosomal system. It plays a crucial role in sorting membrane proteins that are destined for degradation or routing to the lysosome[3, 4]. These proteins, such as activated growth-factor, hormone and cytokine receptors, are internalized into vesicles forming an MVB, the contents of the MVB are then transferred to lysosomes for degradation[2, 5, 6]. CHMP5 is responsible for the final conversion of late endosomal MVB to lysosomes and plays a critical role in the downregulation of signaling pathways through receptor degradation[2, 7].

Functional analyses of CHMP5 are performed using an RNAi and protein overexpression strategy in our lab. We found CHMP5 is an anti-apoptotic gene[8], which is consistent with previous findings by Shahmoradgoli *et al*[9]. Moreover, our data confirmed previous findings showing that CHMP5 is significantly increased in *de novo* or relapsed acute myeloid leukemia, indicating that it may participate in leukemogenesis[8, 9]. Immunofluorescence experiments using a monoclonal antibody produced by our lab suggested that the CHMP5 protein was expressed at low levels in the cytosol of 293T cells and normal blood mononuclear cells from healthy volunteers. Interestingly, the CHMP5 protein was highly expressed in the cytosol of AML leukemic cells (unpublished data). These findings indicate that highly expressed CHMP5 protein may participate in leukemogenesis, and the abnormal expression of the CHMP5 protein may be a target for gene therapy.

Recently, recombinant antibodies targeting tumor-associated antigens (TAAs) or tumor-specific antigens (TSAs), gene therapy and immunomodulators have transformed the traditional chemotherapy based only on anticancer drugs. TAAs or TSAs are proteins or other molecular species that are expressed in a specific tumor type that can be targeted for diagnostic and immunotherapy purposes[10]. Tumor-specific recombinant antibodies have been employed in diagnosis and therapy, such as the anti-CD20 monoclonal antibody (McAb), either as single agents or in combination with chemotherapy. These agents have resulted in large improvements in non-Hodgkin's lymphoma survival rates. The main pitfalls of utilizing antibodies to tumor-specific antigens in cancer diagnosis and therapy are the immune response to non-human antibodies and the large size of antibodies, which hinders their access to the large tumors or into cells[10].

The first single chain variable fragment antibody (scFv) was developed in 1988. An scFv is an antibody composed of heavy- and light-chain variable regions that are joined by an interchain polypeptide linker. The scFv is one of the smallest fragments to be produced that shows equivalent binding affinity to the parent Fab (fragment antigen-binding) fragment[11, 12]. ScFv can be conjugated to different types of molecules, such as radioisotopes and toxins, or expressed as an intracellular antibody (intrabody) in a specific intracellular compartment, where it can interfere with the function of the targeted antigen at the level of a specific domain[13]. Human single chain antibody fragments offer the advantage of being expressed as a single polypeptide, and their small size means that they can serve as a highly safe, selective and effective diagnostic and therapeutical tool[10, 14–20]. The scFv on target molecules within cells or intrabodies provides a useful tool for research as well as for control of diseases such as human immunodeficiency virus type 1 infection and other diseases[13, 15, 16, 21].

As we mentioned previously, the expression of the anti-apoptotic protein CHMP5 was dramatically up-regulated in the cytosol of AML leukemic cells, which was distinct from the expression in normal mononuclear cells. Infecting AML leukemic cells with an anti-CHMP5 scFv retrovirus may induce programmed cell death by neutralizing the excess anti-apoptotic CHMP5 protein.

Materials and methods

Cell culture and transfection

Human HEK293T (human embryonic kidney) cells and U937 cells were obtained from the Shanghai Institute of Hematology (Shanghai, China). The anti-CHMP5 KC14 hybridoma cell line was constructed by our lab. The cells were cultured in RPMI-1640 supplemented with 10% (*v*/*v*) fetal bovine serum (FBS), 100 U/mL penicillin and 100 μg/mL streptomycin at 37 °C and 5% (*v*/*v*) CO_2. The media for culturing the hybridoma cell line KC14 contained 1×HAT (Hypoxathine, Aminopterin and Thymidine).

Generation of the anti-CHMP5 hybridoma cell line and preparation of the anti-CHMP5 monoclonal antibody

Antheprot 4.3 was used to select three antigenic epitopes of the CHMP5 protein. These antigenic epitopes were synthesized and used to generate the CHMP5 polyclonal antibody. Western blot analysis revealed that the polyclonal antibody derived from the KC14 antigenic epitope performed best. The amino acid sequence of KC14 was N′-KAK PKA PPP SLT DC-C′. The hybridoma was constructed according to Ball *et al*[22]. Briefly, we conjugated the KC14 peptide to bovine serum albumin (BSA). BALB/c mice were immunized against the synthetic peptide of the CHMP5 protein. The spleen cells of the mice were fused with Sp2/0 mouse myeloma cells. The titers of the monoclonal antibody (McAb) were tested by ELISA.

Cloning of the VH and VL regions from the KC14 hybridoma

Total RNA extracted from the KC14 hybridoma was converted into cDNA using reverse transcriptase. PCR was performed with mouse primers for VL and VH. The primers were designed according to references[23, 24]. The VL sense primer was: 5′-CCT CTA GAG ACA TTG TG-3′; the VL antisense primer was: 5′-GCC CTT GGC TCG AGT TTT-3′; the VH sense primer was: 5′-ATG AGT CCT GAA CTA ACC TTG AAT C-3′; and the VH antisense primer was: 5′-TCA TTC TAG CCC TTT CCC TGT AGC C-3′. PCR products were purified, TOPO-TA was cloned into the T-vector, and the recombinant vector was sequenced to obtain DNA sequence of VL and VH.

pBabe-CHMP5 scFv antibody retroviral expression vector construction

The pBabe-puro retroviral vector was obtained from the

Shanghai Institute of Hematology (Shanghai, China). We first inserted the VL sequences into pBabe to generate the pBabe-VL recombinant vector. The VL sense primer included restriction sites for the endonuclease *Bam*H I, and the antisense primer included restriction sites for the endonuclease *Eco*R I. PCR was performed using cDNA of the KC14 hybridoma cells to obtain VL sequences. The purified PCR products and the pBabe-Puro retroviral vector were digested with restriction enzymes *Bam*H I and *Eco*R I, respectively. The DNA Ligation Kit Ver 2.0 (Takara, Tokyo, Japan) was used to ligate the VL sequences with pBabe to produce the pBabe-VL recombinant vector. Subsequently, we chemically synthesized a linker oligonucleotide. The sense sequence of linker was 5′-AAT TCG GTG GTG GTG GAT CCG GTG GTG GTG GTT CTG GCG GCG GCG GCT CCG-3′ and the antisense sequence of linker was 5′-*TCG AC*G GAG CCG CCG CCG CCA GAA CCA CCA CCA CCG GAT CCA CCA CCA CCG-3′. The underlined portion shows the *Eco*R I site. After annealing with its counterpart oligonucleotide, the *Eco*R I sticky end may form at the 5′ terminal end of the linker dsDNA. The *Sal* I site is shown in italics. After annealing with its counterpart oligonucleotide, the *Sal* I sticky end may form at the 3′ terminal end of the linker dsDNA. After the pBabe-VL recombinant vector was cut with the *Eco*R I and *Sal* I restriction enzymes, the linker dsDNA was introduced to form the pBabe-VL-linker recombinant vector. Subsequently, both VH sense and antisense primers were added with restriction sites for the endonuclease *Sal* I and VH was introduced into pBabe-VL-linker to form the pBabe-CHMP5 scFv antibody retroviral expression vector.

pMIG-CHMP5 scFv antibody retroviral expression vector construction

The pMIG-GFP retroviral vector, gag/pol and VSV-G were obtained from the Shanghai Institute of Hematology (Shanghai, China). Because the pBabe-CHMP5 scFv antibody retroviral expression vector did not contain the GFP (green fluorescence protein) sequence, it was difficult for us to evaluate the infection efficiency after transient transfection. Therefore, we utilized the pMIG-GFP retroviral vector to construct pMIG-CHMP5 scFv antibody retroviral expression vector. The primer pairs 5′-tac gtt *aga tct* ATG ACC CAG TCT CCT GCT-3′ and 5′-tag att *gtt aac* GCA TTC TAG CCC TTT CCC-3′ were used, and the pBabe-CHMP5 scFv antibody retroviral expression vector served as the DNA template for PCR to obtain the CHMP5 scFv sequence. The purified PCR products and the pMIG-GFP retroviral vector were digested with the *Bgl* I and *Hpa* I restriction enzymes, respectively. The DNA Ligation Kit Ver 2.0 was used to ligate the CHMP5 scFv sequence with pMIG to generate the pMIG-CHMP5 scFv antibody retroviral expression vector.

pMIG-CHMP5 scFv retrovirus preparation and infection

To prepare the virus, 293T cells were cotransfected with the empty pMIG vector or the pMIG-CHMP5 scFv antibody retroviral expression plasmid and gag/pol and VSV-G using the FuGENE 6 transfection reagent (Roche, USA)[25, 26]. One day after transfection, the medium was changed, and collection of the virus-containing medium began on d 2. The medium was filtered through a 0.22-μm filter. U937 cells were then infected with the retroviral supernatants. The clones expressing the desired genes were sorted by a flowcytometer (FCM), and the GFP-positive cells were selected[26].

Immunofluorescence analysis

Our CHMP5 McAb was used to detect the CHMP5 protein in U937 cells by immunofluorescence after infected by the scFv retrovirus. The cells were incubated with primary antibodies and the anti-mouse secondary antibody was CY3-conjugated. The images were captured by confocal laser scanning microscope (Carl Zeiss, ObErkochen, Germany). To avoid experimental error, non-infected U937 cells served as the control and the parameters of the microscope were fixed in each experiment. The typical field of the microscope was selected by the operator of the confocal laser scanning microscope.

Programmed cell death (PCD) analysis

The cells were stained with annexin-allophycocyanin (APC)/7-amino-actinomycin (7-AAD) (BD PharMingen, San Jose, CA, USA) and evaluated using FCM. APC was optimized for FL-4 fluorescence on a flowcytometer, and 7-AAD fluorescence was detected in the far red range of the spectrum (650 nm long-pass filter)[8]. The results were represented as the percentage of both annexin V-APC$^+$/7-AAD$^-$ and annexin V-APC$^+$/7-AAD$^+$ cells. For confocal microscopy, the excitation wavelength of annexin V-APC was 633 nm and the emission wavelength was 700–780 nm[8]. The excitation wavelength of 7-AAD was 543 nm and the emission wavelength was 560–615 nm. A total of 200 cells were counted, and the results were calculated based on the percentages of both annexin V-APC$^+$/7-AAD$^-$ and annexin V-APC$^+$/7-AAD$^+$ cells.

Western blot was performed using PCD-associated antibodies. The Granzyme B, microtubule-associated protein 1 light chain 3 (LC-3) and Caspase 9 antibodies were purchased from Cell Signal Technology (MA, USA); AIF and Caspase 3 antibodies were purchased from Epitmics (CA, USA); antibodies against PARP were purchased from Santa Cruz Biotechnology (CA, USA); anti-Caspase 8 was purchased from BD Pharmingen (CA, USA).

Changes in CHMP5 gene and protein expression after scFv retrovirus infection

The changes in gene and protein expression of CHMP5 in U937 cells after scFv retrovirus infection were studied. Reverse transcription polymerase chain reaction (RT-PCR) was performed, and the CHMP5 primers were: 5′-TGC TCA AGA TGA ACC GAC TCT-3′ and 5′-GTG GGA ACA CCT TCT GGA AT-3′. The β-actin primers were: 5′-TCG ACA ACG GCT CCG GCA T-3′ and 5′-AAG GTG TGG TGC CAG ATT TTC-3′. The polyclonal antibody against CHMP5 that was used for Western blot analysis was purchased from Abcam (Cambridge, UK).

Statistical analysis

All statistics were performed using SAS 6.12 software. Data were expressed as mean±SD from three independent experiments. The statistical significance was determined using *t*-test to compare groups of data. *P* values <0.05 were considered to be statistically significant.

Results

Identification of anti-CHMP5 monoclonal antibody

Because a monoclonal antibody of CHMP5 was not commercially available and we needed to obtain the VL and VH sequence of anti-CHMP5 hybridoma cells, we constructed hybridoma cells and produced our own CHMP5 monoclonal antibody. After we obtained the monoclonal antibody of CHMP5, both Western blot analysis and immunofluorescence studies verified that McAb functioned as expected (Figure 1). The U937 group consisted of U937 cells that were not transfected with plasmids. The sh Con group consisted of U937 cells that were transfected with short-hairpin RNA (shRNA) control plasmids. The sh-CHMP5 group was composed of cells with RNA interference-mediated CHMP5 inhibition[8]. We found that our monoclonal antibody could detect an approximately 28 kDa band in the U937 and sh Con groups by Western blot analysis; however, this band was very weak in the sh-CHMP5 group. The reduction in the density of the band was consistent with the changes in CHMP5 expression, indicating that this McAb could be utilized to detect CHMP5 protein by Western blot (Figure 1A). The McAb immunofluorescence (IF) results also confirmed that we had successfully prepared the McAb. Figure 1B–1D show the immunofluorescence results of the U937, sh Con and sh-CHMP5 groups, respectively. The figure shows the merged by red and blue fluorescence images. The red fluorescence (CY3) represents CHMP5 protein, and the blue fluorescence represents the DAPI (diamidino-phenyl-indole) signal, which labeles the nucleus. We found that the red fluorescence signal of the CHMP5 protein was highly expressed throughout cytosol (Figure 1A and 1B), but the red fluorescence signal decreased after CHMP5 was inhibited by RNA interference (Figure 1C). The change in red fluorescence was consistent with the changes in CHMP5 expression, indicating that this McAb may be utilized for immunofluorescence.

VL and VH cloning

The detailed DNA sequencing results of the cloned VL and VH of the scFv were supplied in the supplemental data.

IgBLAST and Nucleotide blast (http://blast.ncbi.nlm.nih.gov/Blast.cgi) were employed, and we confirmed that the sequences of VL and VH we obtained represented the variable region. VL shares 98% identity (281/288) to the *Mus musculus* strain C57BL/6J chromosome 6 genomic contig (NT 039353.7). At this site, the *Mus musculus* light chain gene Igk-V21-12 is represented (GeneID: 667914). The VH was on the *Mus musculus* strain 129/SvJ chromosome 12 unlocalized genomic contig (NT 114985.2), and this site included the *Mus musculus* heavy chain gene Igh-VX24 (GeneID: 195176). The VH appeared to be the composite of two fragments, and each fragment showed high similarity (98% and 100%, respectively) to Igh-VX24.

Changes in CHMP5 protein expression after scFv retrovirus infection

The non-infected U937 group showed CHMP5 protein expression (red fluorescence) distributed throughout the cytosol. The GFP protein could not be detected because it was not infected (Figure 2). The scFv-Con group (U937 cells were infected by empty pMIG-GFP) displayed GFP expression, indicating that the retrovirus had successfully infected U937 cells, and we could note that the expression of the CHMP5 protein was similar to the level observed in the U937 cells (Figure 2). The scFv-virus group (U937 cells infected with the pMIG-CHMP5 scFv retrovirus) showed GFP expression, indicating that the virus had successfully infected U937 cells. We found that the red fluorescence decreased dramatically, and the remaining red fluorescence appeared to exist as particulates in cytosol (Figure 2).

Changes in programmed cell death after scFv retrovirus infection

By FCM, we found that the apoptosis rate was 1.60%±0.24% in U937 group, and 1.81%±0.11% and 10.19%±0.46% in the scFv-Con and scFv-CHMP5 groups, respectively. There were

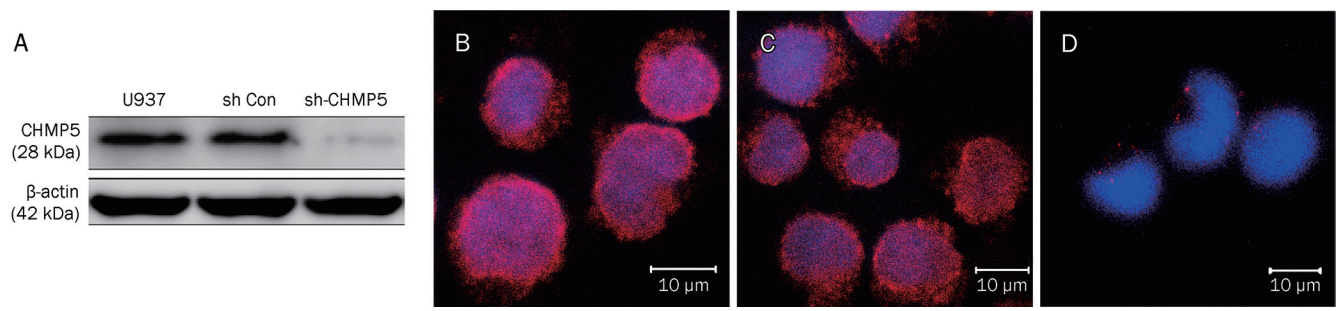

Figure 1. The efficiency of CHMP5 monoclonal antibody. (A) The CHMP5 McAb was able to detect the CHMP5 protein by Western blot. When CHMP5 was inhibited by sh-CHMP5, the band was nearly undetectable; the McAb could detect the CHMP5 band in the control groups, in which CHMP5 was not inhibited. (B) In untranfected U937 cells, the red fluorescence signal of the CHMP5 protein was relatively highly expressed throughout cytosol. (C) In the sh Con group, the red fluorescence signal of the CHMP5 protein was similar to untranfected U937 cells. (D) The red fluorescence signal of CHMP5 protein decreased dramatically in the sh-CHMP5 group.

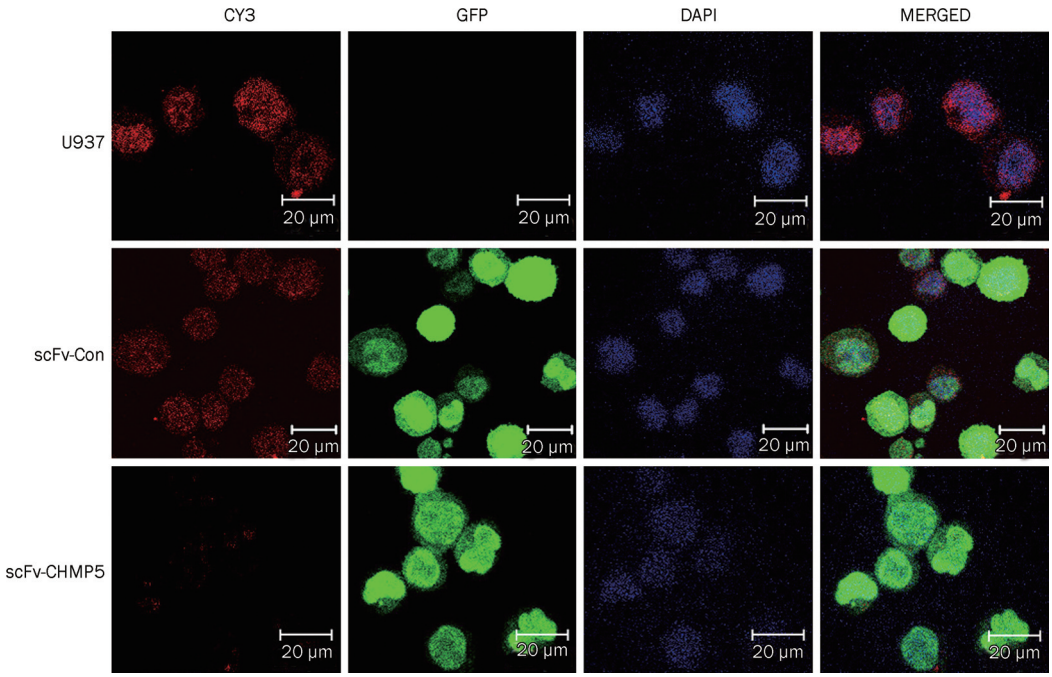

Figure 2. Immunofluorescence after scFv retrovirus infection. The U937 group consisted of cells not infected by the retrovirus, the scFv-Con group consisted of U937 cells infected by control retrovirus, and the scFv-CHMP5 group consisted of U937 cells infected by scFv retrovirus. CHMP5 was represented by the CY3 red fluorescence signal, the green fluorescence signal represented GFP, and DAPI was depicted by the blue fluorescence signal. The merged images represent the fusion of the red, green and blue fluorescence images. The expression of CHMP5 was similar in the U937 group and scFv-Con group; however, the signal of CHMP5 decreased dramatically in the scFv-CHMP5 group.

no statistically significant differences between the U937 and scFv-Con groups (P=0.1217). There was a statistically significant difference between the scFv-Con and scFv-CHMP5 groups (P=0.0015) (Figure 3A). The apoptosis rate increased approximately 5 times following the scFv retrovirus infection. We used confocal microscopy to further demonstrate that the apoptosis rate was 3.27% in the U937 group, 3.54% in the scFv-Con group and 12.36% in the scFv-CHMP5 group, in agreement with the FCM results (Figure 3B–3D). We also found that the percentage of 7-AAD single-stained cells increased, which was likely necrosis[27, 28] (Figure 3D).

After we showed that the scFv retrovirus infection could induce U937 leukemic cells to undergo apoptosis, Western blot analysis was applied to study the changes in the apoptotic pathway. The autophagic and necrotic programmed cell death pathways were also examined. We found that after U937 cells were infected by the scFv retrovirus, the expression of AIF and cleaved Caspase 3 increased (Figure 4). PARP was the substrate of the activated Caspase 3, and we found that PARP decreased and its cleavage increased after scFv retrovirus infection. Granzyme B (Gran B), proCaspase 8, cleaved Caspase 8 and cleaved Caspase 9 showed no obvious changes.

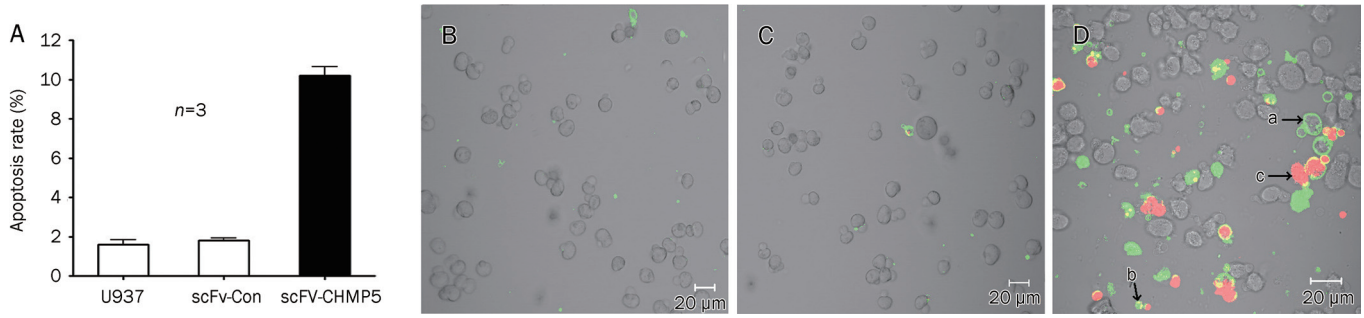

Figure 3. Apoptosis assessment after scFv retrovirus infection. (A) The apoptosis rate increased after infected by the scFv retrovirus and showed a statistically significant difference between the scFv-Con and scFv-CHMP5 groups, P<0.05 (n=3). (B) A typical confocal microscope field of the U937 group. (C) A typical confocal microscope field of the scFv-Con group. (D) A typical confocal microscope field of the scFv-CHMP5 group. (a) A typical annexin V-APC$^+$/7-AAD$^-$ apoptotic cell at an early stage. (b) A typical annexin V-APC$^+$/7-AAD$^+$ apoptotic cell at a later stage; we could view the karyorrhexis and apoptotic body. (c) Karyopyknosis, which is indicative of necrosis.

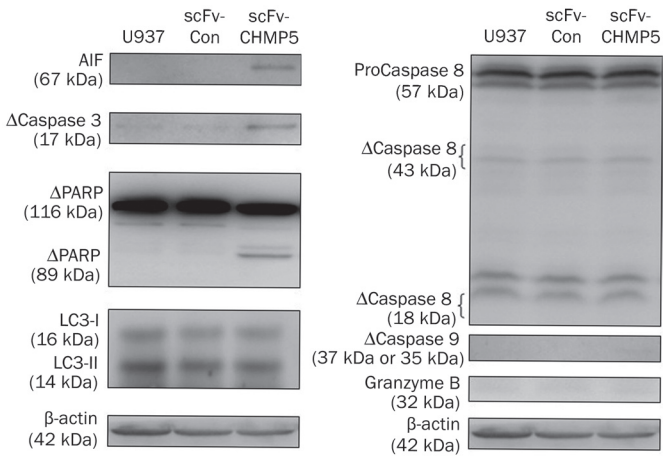

Figure 4. Expression of PCD-related factors detected by Western blot. After U937 cells were infected by scFv retrovirus, we found that the amount of AIF protein and cleaved Caspase 3 increased, and PARP, which was the substrate of activated Caspase 3, was cleaved. However, the levels of Granzyme B (Gran B), proCaspase 8, cleaved Caspase 8 and cleaved Caspase 9 were not changed. Neither the conversion of LC3-I to LC3-II nor an increase of LC3-II was observed. Δ indicated the cleaved protein.

Neither the conversion of LC3-I to LC3-II nor the increase of LC3-II was observed after scFv retrovirus infection (Figure 4).

CHMP5 gene and protein changes after scFv retrovirus infection

To detect whether scFv retrovirus infection could affect the gene expression in U937 cells, reverse transcript PCR was used. We found the gene expression was not altered after scFv retrovirus infection. The change in CHMP5 protein expression after scFv retrovirus infection was also studied by Western blot using a polyclonal antibody purchased from Abcam. We found that the protein expression was also not changed after scFv retrovirus infection (Figure 5).

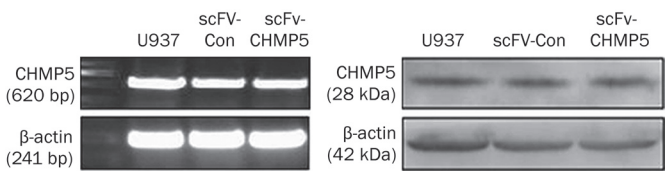

Figure 5. Changes in CHMP5 gene and protein expression after scFv retrovirus infection. (A) We did not observe gene expression changes. (B) We found that the protein expression was not changed after scFv retrovirus infection.

Discussion

As we have mentioned previously, immunofluorescence experiments using a monoclonal antibody produced by our lab suggested that the CHMP5 protein was expressed at relatively low levels in the cytosol of 293T cells and normal blood mononuclear cells from healthy volunteers. Conversely, the CHMP5 protein was highly expressed in the cytosol of AML leukemic cells (unpublished data). Moreover, our studies are consistent with previous studies which show that CHMP5 is an anti-apoptotic gene[8, 9]. Furthermore, in agreement with these previous studies, we found that the CHMP5 gene expression is significantly increased in *de novo* or relapsed AML, indicating that it may participate in leukemogenesis[8, 9]. As shown in Figure 1, after CHMP5 is inhibited by RNA interference in the AML leukemic cell line, U937, the expression of the CHMP5 protein is significantly decreased, and the leukemic cells are induced to undergo apoptosis[8]. These findings indicate that highly expressed CHMP5 protein in the cytosol may participate in leukemogenesis, and it may be a target for gene therapy.

The scFv to target molecules within cells provide a useful tool for research as well as for the control of diseases[13, 15, 16, 21]. To produce a scFv-CHMP5, the hybridoma cells should be created, and subsequently the VL and VH variable region from the RNA of hybridoma cells must be obtained[29]. Immunofluorescence revealed that when the U937 cells were infected by the scFv-CHMP5 retrovirus, the red fluorescence of the CHMP5 protein decreased dramatically. Because the VL and VH variable regions of the CHMP5 scFv are generated from the RNA of hybridoma cells, which are also used to produce the McAb of CHMP5, the antigenic site of CHMP5 is shared and recognized by scFv and McAb. Immunofluoresence with this monoclonal antibody shows a decrease of red fluorescence (CHMP5 protein) after scFv retrovirus infection. This reduction may be explained by two potential scenarios; after the CHMP5 protein is neutralized by the scFv, the amount of CHMP5 protein in cytosol is not altered or CHMP5 is degraded. Both the gene and protein expression level of CHMP5 are studied, and the results indicate its gene expression level and the amount of CHMP5 protein in cytosol are not altered after being neutralized by scFv (Figure 5). Notably, we find little red fluorescence remains in the cytosol after scFv-virus infection, and this red fluorescence appears to be in the particulates in the cytosol. Ward *et al* has reported that the CHMP5 protein is likely to be found in vesicles, which are thought to be lysosome and MVB[7]. Consistent with this observation, we suggest that the CHMP5 protein, which has been neutralized by scFv, is in cytosol, whereas the remaining CHMP5 protein is localized to the lysosome and MVB.

Recently, apoptosis was classified as type I programmed cell death[30]. Our previous study had found that both the Granzyme B/Perforin-mediated apoptotic and AIF-mediated necrotic programmed cell death pathways are activated during CHMP5 deficiencies, whereas the autophagic programmed cell death is not activated (unpublished data). Therefore, these PCD pathways were studied in U937 cells after scFv retrovirus infection. In general, activation of Caspase 9 results in the initiation of the intrinsic pathway, whereas activation of Caspase 8 results in the initiation of the extrinsic pathway[31]. Activation of either pathway leads to activation of the downstream Caspase 3 and Caspase 7. We find that Caspase 3 is activated after U937 cells are infected by scFv retrovirus, indicating the

apoptotic PCD pathway is activated. Neither Caspase 8 nor Caspase 9 is activated, indicating that neither intrinsic and extrinsic apoptotic PCD pathways are activated. To our surprise, the granzyme B/perforin-mediated Caspase-dependent apoptotic PCD pathway is also not activated. Although the apoptosis-inducing protein, AIF, increased after scFv retrovirus infection, AIF is thought to activiate Caspase-independent necrotic PCD pathways. That is, it is considered to be unable to active Caspase 3[32, 33]. It appears that an additional uncommon Caspase-dependent apoptotic PCD pathway is activated, or this may indicate that AIF can active Caspase 3.

AIF-induced apoptosis now is reported to be Caspase-independent necroptosis[32], and necrosis is thought to be type III programmed cell death[30]. Increasing evidence shows that necrosis is a highly orchestrated type of PCD[32, 33]. Upon activation of PCD, AIF is released from the mitochondria and translocated into the nucleus to induce phosphatidylserine exposure, chromatin condensation and DNA fragmentation[27, 28]. We find that AIF increases after scFV retrovirus infection in U937 cells. Phosphatidylserine exposure can be detected by annexin V, and we find that both phosphatidylserine exposure and chromatin condensation can be found in U937 cells after scFV retrovirus infection (Figure 3D), indicating that AIF-mediated caspase-independent necrosis is activated.

Recently, autophagy has also been shown to be a genetically programmed and regulated process by which cells undergo self-elimination. It is classified as type II programmed cell death[30]. In mammals, the conversion of the microtubule-associated protein 1 light chain 3 (LC3) from LC3-I (free form) to LC3-II (phosphatidylethanolamine-conjugated form) or the increase of LC3-II is a key step in autophagy[34]. We find that neither the conversion of protein LC3-I to LC3-II nor the amount of LC3-II is increased. These findings indicate that autophagic programmed cell death is not observed in U937 cells after scFV virus infection.

In conclusion, we find that the scFv-CHMP5 virus can neutralize the abnormally high levels of the CHMP5 protein in the cytosol of AML leukemic U937 cells, thereby inducing leukemic cells to undergo programmed cell death via AIF-mediated caspase-independent necrosis and apoptosis. Althought this is a pilot report, our findings provide a potential method to treat AML.

Abbreviations

AML, acute myeloid leukemia; CHMP5, charged multivesicular body protein 5; MVB, multivesicular body; ESCRT, endosomal sorting complex required for transport; scFv, single chain variable fragments antibody; PCD, programmed cell death; AIF, apoptosis inducing factor.

Acknowledgements

This work was supported by the National Natural Science Foundation of China (30670881 and 81000212), the Shanghai Municipal Health Bureau (2009Y031) and a cooperative project of the Renji-Foundation Medical School (ZD0704). We would like to thank Dr Qiang-su GUO from the Key Laboratory for Reproductive Medicine, Shanghai Jiao Tong University School of Medicine, for his technical assistance.

Author contribution

Hai-rong WANG designed research, performed research and wrote the paper; Zhen-yu XIAO, Miao CHEN, Fei-long WANG, Jia LIU, Hua ZHONG, Ji-hua ZHONG, and Yan-lin SHEN performed research and analyzed data; Ren-rong OU-YANG and Shu-ming PAN analyzed data and revised the paper.

Supplementary information

Supplementary tables are available at Acta Pharmacologica Sinica website of NPG.

References

1 Jabbour EJ, Estey E, Kantarjian HM. Adult acute myeloid leukemia. Mayo Clin Proc 2006; 81: 247–60.
2 Shim JH, Xiao C, Hayden MS, Lee KY, Trombetta ES, Pypaert M, *et al*. CHMP5 is essential for late endosome function and down-regulation of receptor signaling during mouse embryogenesis. J Cell Biol 2006; 172: 1045–56.
3 Katzmann DJ, Odorizzi G, Emr SD. Receptor downregulation and multivesicular-body sorting. Nat Rev Mol Cell Biol 2002; 3: 893–905.
4 Raiborg C, Rusten TE, Stenmark H. Protein sorting into multivesicular endosomes. Curr Opin Cell Biol 2003; 15: 446–55.
5 Raiborg C, Stenmark H. The ESCRT machinery in endosomal sorting of ubiquitylated membrane proteins. Nature 2009; 458: 445–52.
6 Wollert T, Hurley JH. Molecular mechanism of multivesicular body biogenesis by ESCRT complexes. Nature 2010; 464: 864–9.
7 Ward DM, Vaughn MB, Shiflett SL, White PL, Pollock AL, Hill J, *et al*. The role of LIP5 and CHMP5 in multivesicular body formation and HIV-1 budding in mammalian cells. J Biol Chem 2005 280: 10548–55.
8 Wang HR, Gu CH, Zhu JY, Han JY, Zhong H, Chen FY, *et al*. PNAS-2: a novel gene probably participating in leukemogenesis. Oncology 2006; 71: 423–9.
9 Shahmoradgoli M, Mannherz O, Engel F, Heck S, Krämer A, Seiffert M, *et al*. Antiapoptotic function of charged multivesicular body protein 5: a potentially relevant gene in acute myeloid leukemia. Int J Cancer 2011; 128: 2865–71.
10 Accardi L, Di Bonito P. Antibodies in single-chain format against tumour-associated antigens: present and future applications. Curr Med Chem 2010; 17: 1730–55.
11 Huston JS, Levinson D, Mudgett-Hunter M, Tai MS, Novotný J, Margolies MN, *et al*. Protein engineering of antibody binding sites: recovery of specific activity in an anti-digoxin single-chain Fv analogue produced in *Escherichia coli*. Proc Natl Acad Sci U S A 1988; 85: 5879–83.
12 Kortt AA, Malby RL, Caldwell JB, Gruen LC, Ivancic N, Lawrence MC, *et al*. Recombinant anti-sialidase single-chain variable fragment antibody. Characterization, formation of dimer and higher-molecular-mass multimers and the solution of the crystal structure of the single-chain variable fragment/sialidase complex. Eur J Biochem 1994; 221: 151–7.
13 Pérez-Martínez D, Tanaka T, Rabbitts TH. Intracellular antibodies and cancer: new technologies offer therapeutic opportunities. Bioessays 2010; 32: 589–98.

14 Lu RM, Chang YL, Chen MS, Wu HC. Single chain anti-c-Met antibody conjugated nanoparticles for *in vivo* tumor-targeted imaging and drug delivery. Biomaterials 2011; 32: 3265–74.
15 Marasco WA, Haseltine WA, Chen SY. Design, intracellular expression, and activity of a human anti-human immunodeficiency virus type 1 gp120 single-chain antibody. Proc Natl Acad Sci U S A 1993; 90: 7889–93.
16 Levy-Mintz P, Duan L, Zhang H, Hu B, Dornadula G, Zhu M, *et al*. Intracellular expression of single-chain variable fragments to inhibit early stages of the viral life cycle by targeting human immunodeficiency virus type 1 integrase. J Virol 1996; 70: 8821–32.
17 Mabry R, Snavely M. Therapeutic bispecific antibodies: The selection of stable single-chain fragments to overcome engineering obstacles. IDrugs 2010; 13: 543–9.
18 ten Cate B, Bremer E, de Bruyn M, Bijma T, Samplonius D, Schwemmlein M, *et al*. A novel AML selective TRAIL fusion protein that is superior to Gemtuzumab Ozogamicin in terms of *in vitro* selectivity, activity and stability. Leukemia 2009; 23: 1389–97.
19 Olafsen T, Betting D, Kenanova VE, Salazar FB, Clarke P, Said J, *et al*. Recombinant anti-CD20 antibody fragments for small-animal PET imaging of B-cell lymphomas. J Nucl Med 2009; 50: 1500–8.
20 Geng SS, Feng J, Li Y, Sun Y, Gu X, Huang Y, *et al*. Binding activity difference of anti-CD20 scFv-Fc fusion protein derived from variable domain exchange. Cell Mol Immunol 2006; 3: 439–43.
21 Accardi L, Donà MG, Mileo AM, Paggi MG, Federico A, Torreri P, *et al*. Retinoblastoma-independent antiproliferative activity of novel intracellular antibodies against the E7 oncoprotein in HPV 16-positive cells. BMC Cancer 2011; 11: 17.
22 Ball RK, Siegl B, Quellhorst S, Brandner G, Braun DG. Monoclonal antibodies against simian virus 40 nuclear large T tumour antigen: epitope mapping, papova virus cross-reaction and cell surface staining. EMBO J 1984; 3: 1485–91.
23 Lou Q, Kelleher RJ Jr, Sette A, Loyall J, Southwood S, Bankert RB, *et al*. Germ line tumor-associated immunoglobulin VH region peptides provoke a tumor-specific immune response without altering the response potential of normal B cells. Blood 2004; 104: 752–9.
24 Lu M, Gong XG, Yu H, Li JY. Cloning, expression, purification, and characterization of LC-1 ScFv with GFP tag. J Zhejiang Univ Sci B 2005; 6: 832–7.
25 Welm AL, Kim S, Welm BE, Bishop JM. MET and MYC cooperate in mammary tumorigenesis. Proc Natl Acad Sci U S A 2005; 102: 4324–9.
26 Wang L, O'Leary H, Fortney J, Gibson LF. Ph^+/VE-$cadherin^+$ identifies a stem cell like population of acute lymphoblastic leukemia sustained by bone marrow niche cells. Blood 2007; 110: 3334–44. .
27 Susin SA, Lorenzo HK, Zamzami N, Marzo I, Snow BE, Brothers GM, *et al*. Molecular characterization of mitochondrial apoptosis-inducing factor. Nature 1999; 397: 441–6.
28 Lee JH, Yang HS, Park KW, Kim JY, Lee MK, Jeong IY, *et al*. Mechanisms of thiosulfinates from *Allium tuberosum* L-induced apoptosis in HT-29 human colon cancer cells. Toxicol Lett 2009; 188: 142–7.
29 Colcher D, Pavlinkova G, Beresford G, Booth BJ, Batra SK. Single-chain antibodies in pancreatic cancer. Ann N Y Acad Sci 1999; 880: 263–80.
30 Portt L, Norman G, Clapp C, Greenwood M, Greenwood MT. Anti-apoptosis and cell survival: a review. Biochim Biophys Acta 2011; 1813: 238–59. .
31 Klener P Jr, Andera L, Klener P, Necas E, Zivný J. Cell death signalling pathways in the pathogenesis and therapy of haematologic malignancies: Overview of apoptotic pathways. Folia Biol (Praha) 2006; 52: 34–44.
32 Delavallée L, Cabon L, Galán-Malo P, Lorenzo HK, Susin SA. AIF-mediated caspase-independent necroptosis: a new chance for targeted therapeutics. IUBMB Life 2011; 63: 221–32.
33 Boujrad H, Gubkina O, Robert N, Krantic S, Susin SA. AIF-mediated programmed necrosis: a highly regulated way to die. Cell Cycle 2007; 6: 2612–9.
34 Kabeya Y, Mizushima N, Ueno T, Yamamoto A, Kirisako T, Noda T, *et al*. LC3, a mammalian homologue of yeast Apg8p, is localized in autophagosome membranes after processing. EMBO J 2000; 19: 5720–8.

Acta Pharmacologica Sinica (2012) 33: 817–822
 1671-4083/12 $32.00
www.nature.com/aps

Original Article

E-cadherin promotes proliferation of human ovarian cancer cells *in vitro* via activating MEK/ERK pathway

Ling-ling DONG[1], Lian LIU[1, 2, *], Chun-hong MA[2], Ji-sheng LI[1], Chao DU[2], Shan XU[1], Li-hui HAN[2], Li LI[1], Xiu-wen WANG[1]

[1]*Department of Chemotherapy, Cancer Center, Qilu Hospital, Shandong University, Ji'nan 250012, China;* [2]*Institute of Immunology, School of Medicine, Shandong University, Ji'nan 250012, China*

Aim: E-cadherin is unusually highly expressed in most ovarian cancers. This study was designed to investigate the roles of E-cadherin in the carcinogenesis and progression of ovarian cancers.
Methods: Human ovarian adenocarcinoma cell line SKOV-3 was examined. E-cadherin gene CDH1 in SKOV-3 cells was knocked down via RNA interference (RNAi), and the resultant variation of biological behavior was observed using CCK-8 and colony formation experiment. E-cadherin-mediated Ca^{2+}-dependent cell-cell adhesion was used to study the mechanisms underlying the effects of E-cadherin on the proliferation and survival of SKOV-3 cells. The expression levels of E-cadherin, extracellular signal-related kinase (ERK), phosphorylated ERK (P-ERK) were measured using Western blot assays.
Results: Transfection with CDH1-siRNA for 24–96 h significantly suppressed the growth and proliferation of SKOV-3 cells. E-cadherin-mediated calcium-dependent cell-cell adhesion of SKOV-3 cells resulted in a rapid increase of P-ERK, but did not modify the expression of ERK protein. The phosphorylation of ERK in the cells was blocked by pretreatment with the MEK1 specific inhibitor PD98059 (50 μmol/L), but not by the PI3K inhibitor wortmannin (1 μmol/L) or PKA inhibitor H89 (10 μmol/L).
Conclusion: E-cadherin may function as a tumor proliferation enhancer via activating the MEK/ERK pathway in development of ovarian epithelial cancers.

Keywords: ovarian cancer; E-cadherin; proliferation; mitogen-activated protein kinase kinase (MEK); extracellular signal-related kinase (ERK); RNA interference

Acta Pharmacologica Sinica (2012) 33: 817–822; doi: 10.1038/aps.2012.30; published online 30 Apr 2012

Introduction

Cadherins are a family of cell surface glycoproteins that mediate calcium-dependent intercellular adhesion, and are involved in cell differentiation and morphogenesis[1, 2]. E-cadherin is a 120 kDa transmembrane protein, encoded by the *CDH1* gene at 16q22.1. E-cadherin can not only help establish calcium-dependent cell-cell contact through its extracellular domain, but also link the extracellular environment to the contractile cytoskeleton inside cells by the interaction of its short intracellular tail with catenins, which in turn bind to actin filaments and play an important role in certain nuclear responses[3–5].

E-cadherin has been generally regarded as a tumor suppressor in various malignancies, such as lung, gastric, laryngeal, pancreatic, and bladder cancers. This is based on the fact that E-cadherin can prevent tumorigenesis, invasion, and metastasis via promoting cell-cell adhesions and inhibiting epithelial-mesenchymal transition (EMT)[6–11]. However, a growing body of studies has recently emerged to challenge this view. For instance, E-cadherin is reported to be necessary for anchorage-independent growth and suppression of apoptosis in oral squamous cancer cells[12]. Expression of the E-cadherin-catenin cell adhesion complex is shown to be vital for disease progression in primary squamous cell carcinomas of the head and neck and their nodal metastases[13]. Most importantly, E-cadherin appears to function differently in the development of ovarian cancers. E-cadherin is not expressed by the normal human ovarian surface epithelium (OSE), whereas it can be detected in the OSE located in the deep clefts, inclusion cysts, and invaginations[14], where over 90% of the ovarian cancers arise[15]. E-cadherin expression has been found in malignant ovarian tumors of all stages and its level is significantly higher in ovarian cancer tissues than in normal ovarian tissues[14, 16, 17]. Furthermore, when introduced into OSE, E-cadherin stimulates the secretion of the ovarian cancer-associated marker CA125 and the anchorage-independent growth *in vitro* and

* To whom correspondence should be addressed.
E-mail lianliu@sdu.edu.cn
Received 2011-09-30 Accepted 2012-03-09

induces the growth, invasion, and metastasis of adenocarcinoma[18, 19].

The above results suggest that the up-regulation of E-cadherin may be an early event in the initial development of ovarian epithelial cancers, which is opposite to its hypothesized role as a tumor suppressor. However, the mechanism that how E-cadherin plays its role during the development of ovarian cancer still remains unclear. Moreover, contradictory data have suggested that E-cadherin could inhibit tumor cell growth by suppressing phosphatidylinositol 3-kinase (PI3K)/Akt signaling in ovarian cancer cells[20]. In the present study, to determine the possible functions of E-cadherin in ovarian cancer cells, we knocked down the *CDH1* gene expression via RNA interference (RNAi) in the SKOV-3 ovarian cancer cells. We also established an E-cadherin-mediated calcium-dependent cell-cell adhesion model by a method described before[21], to detect its role and related signaling mechanism in the regulation of ovarian cancer cell growth and proliferation.

Materials and methods

Cell culture and reagents

The human ovarian adenocarcinoma cell line, SKOV-3, was kept in our laboratory and maintained in RPMI-1640 (Gibco, Paisley, UK) supplemented with 10% fetal calf serum (Gibco) at 37 °C in a 5% CO_2 humidified atmosphere. To establish the calcium-dependent cell-cell adhesion model, SKOV-3 cells were serum starved overnight, and then were suspended in serum-free medium containing 4 mmol/L EGTA for 30 min to disrupt the calcium-dependent and E-cadherin-mediated cell-cell contacts. Thereafter, intercellular interactions were allowed to reestablish while the cells were re-suspended in fresh $CaCl_2$ solution (final concentration of $CaCl_2$, 1.8 mmol/L) for different periods ranging from five to thirty minutes. To block the function of certain kinases in signaling transduction experiments, cells were pretreated with kinase inhibitors before EGTA treatment. The SKOV-3 cells transfected by plasmids including siRNA targeting E-cadherin were treated in the same way as above 48 h after transfection.

The MEK1 inhibitor, PD98059, was purchased from Cell Signaling Technologies (Danvers, MA, USA). The PKA inhibitor, H89, was from Upstate Biotechnology (Boston, MA, USA). The PI3K inhibitor, wortmannin, was from Santa Cruz Biotechnology (Santa Cruz, CA, USA). The mouse anti-human E-cadherin monoclonal antibody and mouse monoclonal antibody to β-actin were purchased from BD Transduction Laboratories (SanJose, CA, USA). Neutralizing antibody to E-cadherin, SHE 78-7, was from Takara (Shiga, Japan). Rabbit polyclonal antibodies to p44/42 ERK, and phosphorylated p44/42 ERK (Thr202/Tyr204), were obtained from Cell Signaling Technologies (Beverly, MA, USA). Rabbit anti-mouse IGG-FITC secondary antibodies were from Zymed Laboratories, Inc (South San Francisco, CA, USA). Lipofectamine 2000 for transfection of small interfering RNA (siRNA) oligonucleotides was obtained from Invitrogen (Carlsbad, CA, USA).

RNA interference (RNAi)

SKOV-3 cells were seeded in 24-well plates 24 h before transfection at a density of 3×10^4 cells/well. Plasmids (1 μg per well) including siRNA targeting E-cadherin were mixed with Lipofectamin 2000 for transfection according to the manufacturer's instructions. The sequence of the double-stranded E-cadherin-specific siRNA was 5′-GGCCTCTACG-GTTTCATAA-3′. The E-cadherin siRNA expressing plasmid and the negative control plasmid HK were purchased from Wuhan Gensil Biotechnology (Wuhan, China) and used directly for transfection.

Immunofluorescence staining

SKOV-3 cells cultured on glass coverslips were washed with PBS, fixed in 4% paraformaldehyde for 20 min at room temperature, and permeabilized with 0.5% Triton X-100 for 10 min at room temperature. The cells were then washed with PBS, sequentially stained with mouse anti-E-cadherin monoclonal antibody (1:100) for 1 h followed by fluorescent isothiocyanate (FITC)-labeled anti-mouse IgG antibody (1:50) (Zymed Laboratories, San Francisco, CA, USA) for 30 min at 37 °C, and mounted for visualization under a Zeiss Axiophot microscope (Carl Zeiss, Thornwood, NY, USA).

Western blot

To test the possible role of E-cadherin, MEK, PI3K and PKA, cells were pretreated with corresponding protein kinase inhibitors such as E-cadherin-specific neutralizing antibody SHE 78-7 (20 μg/mL), MEK1 specific inhibitor PD98059 (50 μmol/L), PI3K inhibitor wortmannin (1 μmol/L) or PKA inhibitor H89 (10 μmol/L) respectively for 30 min before being restored with fresh calcium for 10 min. At different time points after calcium restoration, certain cells were harvested and lysed in TNES buffer: 50 mmol/L Tris-HCl (pH 7.5), 2 mmol/L EDTA, 100 mmol/L NaCl, 1.0 mmol/L sodium orthovanadate, and 1% NP40 containing protease inhibitors (20 μg/mL aprotinin, 20 μg/mL leupeptin, and 1.0 mmol/L phenylmethylsulfonyl fluoride). The amount of protein was quantified by a colorimetric assay (Bio-Rad, Hercules, CA, USA). Fifty micrograms of total proteins from cell lysates were separated by SDS-PAGE and transferred onto a nitrocellulose membrane (Promega). The membrane was blotted in 5% bovine serum albumin (BSA)-Tris TBS containing 0.1% Tween 20 and probed with antibodies against E-cadherin, ERK, phosphorylated ERK (P-ERK) or β-actin (Santa Cruz). The signals were developed by using an enhanced chemiluminescence system (Pierce, Rockford, IL, USA).

Cell proliferation analysis

SKOV-3 cells transfected with *CDH1* siRNA or HK, untransfected cells incubated with or without SHE 78–7 (20 μg/mL) were prepared separately for proliferation assay. The Cell Counting Kit-8 (CCK-8, Dojindo Molecular Technologies, Shanghai, China) was used to measure cell proliferation with an enzyme-labeled minireader (Bio-Rad, Japan) at 450 nm at

24, 48, 72 and 96 h. For the colony-formation assay, approximately 0.5×10^2 cells which had been transfected by plasmids, including the siRNA or HK, were seeded into each well of six-well plates and cultured for two weeks. Certain control cells were incubated simultaneously with SHE 78–7 (20 μg/mL) or PD98059 (50 μmol/L), respectively. Colonies were stained with gentian violet and counted under a microscope. All the experiments were done three times in triplicate wells.

Statistical analysis

All experiments were repeated at least three times. For Western blot, a representative blot from three independent experiments is shown. For numbers of cells and colonies, data were expressed as mean value±standard deviation (SD) and statistically analyzed with student's *t*-test, and a difference was considered significant at $P<0.05$. Data were analyzed using Graphpad Prism 4.

Results

E-cadherin expression was down-regulated markedly after the RNAi targeting *CDH1* gene

We performed RNAi targeting the *CDH1* gene in SKOV-3 cells that had been reported to highly express E-cadherin[22]. We found that the level of E-cadherin was markedly down-regulated in SKOV-3 cells (Figure 1A). As shown in Figure 1B, E-cadherin staining was intense and restricted to cell-cell contacts in HK, the negative group, as the anti-E-cadherin antibody used for immunofluorescence recognized the intracellular tail of E-cadherin. Meanwhile, the fluorescence signal was much weaker after *CDH1* gene was knocked-down via RNA interference (Figure 1B).

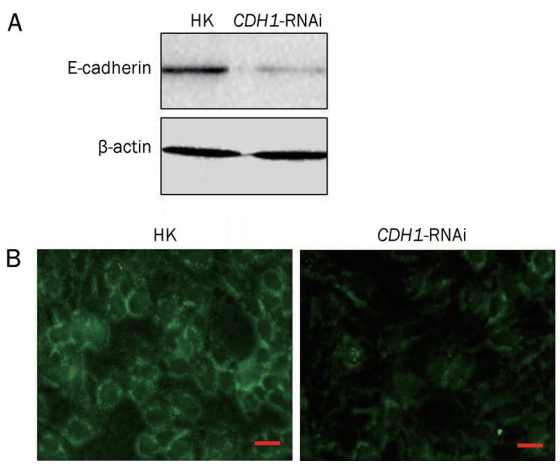

Figure 1. RNA interference of CDH1 gene inhibits E-cadherin expression in SKOV-3 cells. (A) Western blot assay shows that E-cadherin protein level in SKOV-3 cells was markedly reduced 48 h after the transfection of CDH1-siRNA plasmids compared with control plasmid HK. (B) Immunofluorescence staining assay using anti-E-cadherin antibody demonstrates the decrease of E-cadherin protein staining on the cell membrane after RNA interference of *CDH1* (magnification of ×40). The scale bar stands for 20 μm.

Growth and proliferation of SKOV-3 cells was efficiently suppressed after knocking-down of E-cadherin expression

We then studied whether down-regulation of E-cadherin may affect the behavior of SKOV-3 cells, using both CCK8 and colony formation assay. As shown in Figure 2, growth of SKOV-3 cells transfected with *CDH1* siRNA was suppressed at all time points (24, 48, 72, and 96 h) compared to the negative control SKOV-3-HK cells ($P<0.05$ for all). Also as shown in Figure 2, there was marked suppression of cell growth in the positive control cells incubated with SHE 78-7, an E-cadherin neutral antibody, at all time points compared to the SKOV-3-HK cells ($P<0.05$ for all).

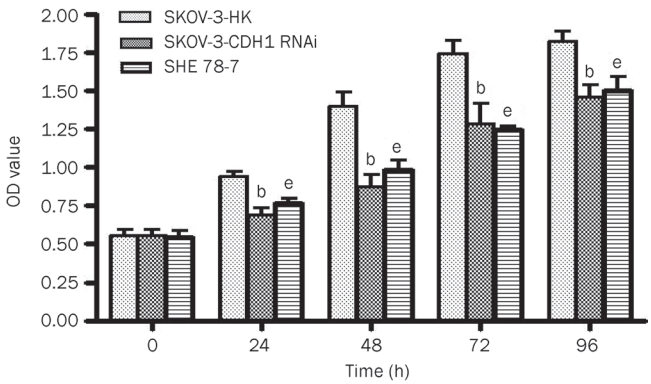

Figure 2. Shutdown of E-cadherin inhibits the proliferation of SKOV-3 cells. After transfection of the *CDH1*-siRNA and the control plasmids, the proliferation ability of SKOV-3 was monitored by CCK8 assay, at 0, 24, 48, 72 and 96 h, respectively. SKOV-3 cells incubated in the presence of SHE 78-7, a neutral antibody of E-cadherin, were treated in the same way. Assay for every time points was repeated 3 times and the mean±SD of the OD reading value was shown in the figure. The difference of OD values between the control group and CDH1-siRNA group or SHE 78-7 group at every time point was analyzed by student's *t*-test. $^bP<0.05$ compared with the HK group. $^eP<0.05$ compared with the CDH1-siRNA group.

Marked inhibition of colony formation ability was also detected. As shown in Figure 3A, colony numbers decreased significantly in the *CDH1*-RNAi group, SHE 78-7 group and PD98059 (a MEK1 specific inhibitor) group in contrast to the HK group respectively ($P<0.01$ for all). The colony numbers in RNAi group were less than both the SHE 78-7 group ($P>0.05$) and PD98059 group ($P<0.05$), but only the latter had a statistical difference (Figure 3B). The size difference of cancer cell colony formed between the two groups (*CDH1*-RNAi *vs* HK) was also noticeable, because the colonies shrank and included much fewer cells after E-cadherin was knocked-down by RNAi (Figure 3C).

E-cadherin promotes ovarian cancer cell proliferation through MEK/ERK signaling pathway

To investigate the underlying mechanism that how E-cadherin functioned to affect the proliferation and survival of ovarian cancer cells, we used a calcium-dependent

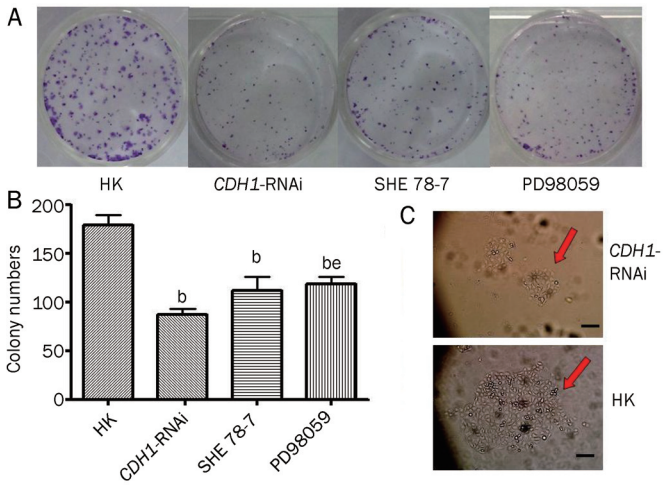

Figure 3. Inhibition of E-cadherin or MEK suppresses the colony formation ability of SKOV-3 cells. (A, B) Representative result and the quantitative analysis of colony formation assay in SKOV-3 cells showed the obviously decreased colony numbers in not only CDH1-siRNA group but also the SHE 78-7 group and PD98059 group, in contrast to the HK group. Mean±SD of three independent experiments was shown. PD98059, a MEK1 inhibitor. $^{b}P<0.05$ compared with the HK group, $^{e}P<0.05$ compared with the *CDH1*-siRNA group. (C) Colony of SKOV3 cells 48 h after transfection with *CHD1*-siRNA plasmid displayed the smaller sizes and contained much less cells compared with HK group, the negative control (magnification of ×10). The scale bar stands for 200 μm.

E-cadherin-mediated cell-cell adhesion model[21]. In SKOV-3 cells, E-cadherin-mediated Ca^{2+}-dependent cell-cell adhesion can be disrupted by a calcium chelator EGTA, and then the cell-cell adhesion can be restored by addition of physiological concentration (1.8 mmol/L) of fresh calcium solution. As shown in Figure 4A, the level of phosphorylated ERK was low in SKOV-3 cells after calcium depletion (Figure 4A, lanes 1 and 2). The restoration of calcium-dependent cell-cell adhesion, however, resulted in a rapid increase on the level of phosphorylated ERK, which lasted for nearly 20 min, and then gradually decreased to the basal level at 30 min after restoration (Figure 4A, lanes 3–6). However, when cells were pretreated with an E-cadherin-specific neutralizing antibody SHE 78-7 (20 μg/mL) for 30 min and then restored with fresh calcium for 10 min, the phosphorylation of ERK could hardly be detected (Figure 4B, lane 7). This result indicated a role of E-cadherin to activate the ERK signaling pathway. Meanwhile, no change was detected in the levels of total ERK protein regardless of any treatments in our experiment (Figure 4A and 4B). These data demonstrates that E-cadherin-mediated calcium-dependent cell-cell adhesions activate ERK signaling by the phosphorylation of ERK, but they do not modify the expression of ERK protein in ovarian cancer cells.

To examine how E-cadherin mediates the activation of ERK, cells were pretreated with several kinase inhibitors separately before restoration of calcium-containing media. As shown in Figure 4B, the phosphorylation of ERK was blocked by the pretreatment of the cells with the MEK1 specific inhibitor PD98059 (Figure 4B, lane 6), while it was not affected by the PI3K inhibitor wortmannin (Figure 4B, lane 4) or PKA inhibitor H89 (Figure 4B, lane 5). To further determine whether MEK activation is also mediated by E-cadherin, we examined the possible alteration of MEK phosphorylation after *CDH1* was knocked-down. The results showed that, the same as the activation of its downstream protein ERK, MEK phosphorylation was both calcium dependent (Figure 4D, lane 3) and E-cadherin dependent, for MEK failed to be activated in the *CDH1*-knocked-down SKOV-3 cells even after calcium restoration (Figure 4D, lane 4). As shown in Figure 4C, no activation of ERK was observed during the disruption and restoration course of cell-cell adhesion after the expression of E-cadherin was suppressed by RNAi. Hence, we suggest that E-cadherin-mediated MEK/ERK activation may act as a major mechanism for ovarian caner cell survival and proliferation.

Discussion

To elucidate the functional implications of the distinct expression pattern of E-cadherin in ovarian cancer cells, we first

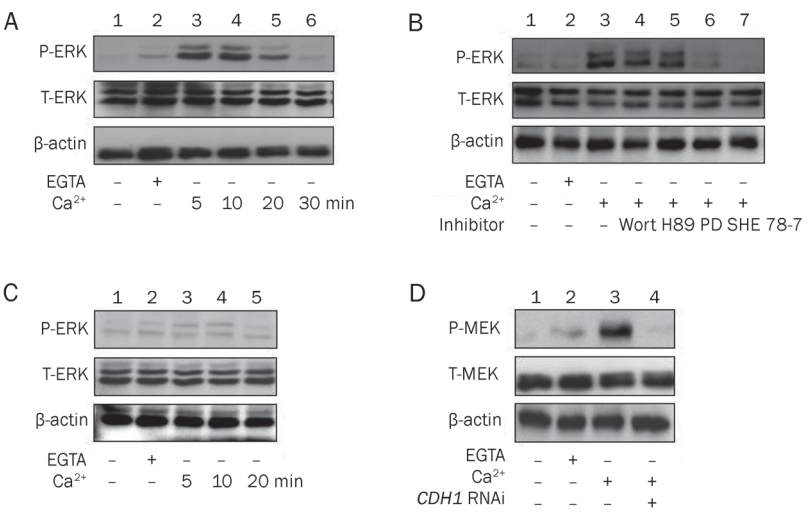

Figure 4. Cell-adhesion-mediated MEK/ERK activation is E-cadherin dependent in SKOV-3 cells. (A) E-cadherin-mediated cell adhesion activates ERK during the time course of calcium restoration in SKOV-3 cells. P-ERK, phosphorylated ERK. T-ERK, total ERK. (B) E-cadherin is required for cell-cell adhesion mediated MEK-ERK activation. Wort, wortmannin (1 μmol/L). H89, PKA inhibitor, 10 μmol/L in concentration. PD, PD98059, MEK1 inhibitor, 50 μmol/L in concentration. SHE 78-7, E-cadherin-specific antibody, 20 μg/mL in concentration. (C, D) After E-cadherin expression was inhibited by siRNA, MEK/ERK failed to be activated after calcium restoration in SKOV-3 cells, for neither ERK (C) nor MEK (D, lane 4) was observed to be phosphorylated. P-MEK, phosphorylated MEK. T-MEK, total MEK.

established a calcium-dependent cell-cell adhesion model in E-cadherin expressing ovarian cancer cell lines such as SKOV-3 and CAOV-3 (data not shown) by a published method[21]. Then we knocked down E-cadherin expression by RNAi to provide a platform to investigate the role of E-cadherin in activating intracellular proliferation and survival-related signals in ovarian cancer cells. We found that down-regulation of E-cadherin expression resulted in marked suppression of survival and of colony formation abilities in ovarian cancer cells. As excessive proliferation and growth are characteristics of malignant cells, we suggest that E-cadherin may play an important role in the growth and proliferation of ovarian carcinoma. It has been previously determined in ovarian cancer that E-cadherin-mediated cellular adhesions and the successive activation of proliferation-related signaling may enhance the transformation of a single layer of normal epithelial cells to neoplastic cells, as well as the stimulation of tumor growth[14]. Therefore, our results suggest that E-cadherin may function as a tumor proliferation enhancer in the development of ovarian epithelial cancers.

Consistently, the up-regulation of E-cadherin expression has been considered as a new epithelial feature for OSE at the early stages of neoplastic transformation[23]. The E-cadherin expression is diminished at later stages of tumor progression as cells de-differentiate and acquire mesenchymal properties associated with a more aggressive phenotype[23–25]. Furthermore, a growing volume of data indicate that cell-cell adhesion mediated by E-cadherin is involved in the suppression of anoikis and maintenance of cellular survival in both epithelial cells, such as normal enterocytes[26], oral squamous carcinoma cells[12] and nonepithelia such as Ewing tumor cells[27]. Instead of distant hematogenous metastasis like most other tumors, regional growth and superficial invasion restricted in the peritoneal cavity are the prominent characteristics of ovarian epithelial cancer. It may result from the formation of E-cadherin-dependent multicellular spheroids, which could manifest a cell-cell adhesion mediated survival and transit to a second anchoring site even in the absence of ascites after detaching from the extracellular matrix (ECM)[28].

Meanwhile, our results convincingly indicate that in SKOV-3 cells the activation of MEK/ERK triggered by cell-cell adhesion is E-cadherin-dependent, evidenced by the fact that both siRNA targeting E-cadherin and its specific neutralizing antibody are able to markedly prevent the phosphorylation of MEK or ERK. We suggest that the activation of proliferation and survival-related signal pathways of E-cadherin may be a ubiquitous phenomenon in ovarian cancer cells. Previously E-cadherin has been reported to activate MEK/ERK in squamous cell carcinoma via physically interacting with and activating EGFR[29]. E-cadherin may also contribute to PI3K-AKT activation by directly engaging the PI3K-p85 regulatory subunit to the adherens junctions of ovarian carcinoma cells[22]. Although in the current study we have no evidence to demonstrate that E-cadherin can directly interact with EGFR or MEK in ovarian cancer cells, our results strongly demonstrated that E-cadherin mediated activation of MEK/ERK exists in many E-cadherin expressing ovarian carcinoma cells such as SKOV-3 and OVCAR-3[17]. Upon activation, MEK/ERK is known to sustain cell survival and proliferation via phosphorylating a series of downstream molecules. The activation of EGFR/MEK/ERK signaling has been demonstrated to support survival in squamous cell carcinoma cells by inducing the anti-apoptotic protein Bcl-2[29]. In addition, MEK/ERK singling has been reported to help cells escape anoikis and maintain anchorage-independent growth in several ovarian cancer cell lines which are deprived of ECM in an *in vitro* environment that intimates the conditions of metastatic cells detached from ovaries and able to survive in the ascites of ovarian cancer patients[30]. These reports may partially explain the underlying mechanism of how E-cadherin promotes ovarian cancer cell survival and proliferation, which may help to clarify the unique role of E-cadherin in ovarian cancer progression. We suggest that E-cadherin plays a pro-oncogenic role during the development and progression of ovary cancer via a cell-cell adhesion activated MEK/ERK signaling pathway, which may serve as a potential therapeutic target to be exploited for ovarian cancer treatment in future.

Although research findings have been accumulating to reveal the ubiquitous expression of E-cadherin and its exact role in ovarian cancers, there are still many opposite opinions[20] as well as lots of unsolved questions. For instance, Sawada reported that loss of E-cadherin promotes ovarian cancer cells metastasis via alpha 5-integrin[31]. Undoubtedly E-cadherin acts as an inhibitor in tumor metastasis, mainly for which it has been traditionally regarded as a tumor suppressor. But the relationship between its proliferation enhancer and metastasis inhibitor roles, in other words, the final counterbalance outcome of its two contrary functions, is still not well-understood. In our colony formation assay, *CDH1* knocked-down SKOV-3 cells had suppressed colony formation ability, even though they 'should' tend to migrate after escaping from the E-cadherin-mediated adhesion of neighbor cells. Similarly in HT29 cells as reported, colony formation ability diminished remarkably after E-cadherin was blocked by SHE 78-7[32]. Consistently, it is reported that Ewing tumor cells transfected by a dominant negative form of E-cadherin plasmid formed fewer and significantly smaller colonies compared with non-transduced cells[27]. Therefore, further research needs to be performed to try to elucidate the exact function of E-cadherin in ovarian cancer development and progression, especially the relationship between its contrary roles in regulating cell mobility and cell viability.

Abbreviations

MEK, mitogen-activated protein kinase kinase; ERK, extracellular signal-related kinase; EGFR, epidermal growth factor receptor; PKA, cAMP-dependent protein kinase A; PI3K, phosphoinositide-3 kinase; OSE, ovarian surface epithelium.

Acknowledgements

This work was supported by the National Natural Science Foundation of China (grant No 30772329 and 81172487), China

Postdoctoral Science Foundation (grant No 20090450153), Grant for Postdoctoral Researchers with Creative Projects of Shandong Province, China (No 200801009) and Natural Science Foundation of Shandong Province, China (grant No ZR2009CM004).

Author contribution

Lian LIU, Chun-hong MA and Li-hui HAN designed the research; Ling-ling DONG, Ji-sheng LI, Chao DU and Shan XU performed the research; Li LI and Xiu-wen WANG contributed analytic tools; Lian LIU and Ji-sheng LI analyzed data and wrote the paper.

References

1 Fang K, Mukhopadhyay T, Shih SH. Retinoic acid modulates epidermal growth factor receptor expression in human lung epithelial cancer cells. J Biomed Sci 1995; 2: 256–62.
2 Kemler R. From cadherins to catenins: cytoplasmic protein interactions and regulation of cell adhesion. Trends Genet 1993; 9: 317–21.
3 Takeichi M. Cadherin cell adhesion receptors as a morphogenetic regulator. Science 1991; 251: 1451–5.
4 Aberle H, Schwartz H, Kemler R. Cadherin-catenin complex: protein interactions and their implications for cadherin function. J Cell Biochem 1996; 61: 514–23.
5 Gottardi CJ, Wong E, Gumbiner BM. E-cadherin suppresses cellular transformation by inhibiting beta-catenin signaling in an adhesion-independent manner. J Cell Biol 2001; 153: 1049–60.
6 Birchmeier W, Weidner KM, Hulsken J, Behrens J. Molecular mechanisms leading to cell junction (cadherin) deficiency in invasive carcinomas. Semin Cancer Biol 1993; 4: 231–9.
7 Birchmeier W. E-cadherin as a tumor (invasion) suppressor gene. Bioessays 1995; 17: 97–9.
8 Birchmeier W, Behrens J. Cadherin expression in carcinomas: role in the formation of cell junctions and the prevention of invasiveness. Biochim Biophys Acta 1994; 1198: 11–26.
9 Thiery JP. Epithelial-mesenchymal transitions in tumour progression. Nat Rev Cancer 2002; 2: 442–54.
10 Mittari E, Charalabopoulos A, Batistatou A, Charalabopoulos K. The role of E-cadherin/catenin complex in laryngeal cancer. Exp Oncol 2005; 27: 257–61.
11 Fearon ER. Connecting estrogen receptor function, transcriptional repression, and E-cadherin expression in breast cancer. Cancer Cell 2003; 3: 307–10.
12 Kantak SS, Kramer RH. E-cadherin regulates anchorage-independent growth and survival in oral squamous cell carcinoma cells. J Biol Chem 1998; 273: 16953–61.
13 Andrews NA, Jones AS, Helliwell TR, Kinsella AR. Expression of the E-cadherin-catenin cell adhesion complex in primary squamous cell carcinomas of the head and neck and their nodal metastases. Br J Cancer 1997; 75: 1474–80.
14 Sundfeldt K, Piontkewitz Y, Ivarsson K, Nilsson O, Hellberg P, Brannstrom M, *et al*. E-cadherin expression in human epithelial ovarian cancer and normal ovary. Int J Cancer 1997; 74: 275–80.
15 Maines-Bandiera SL, Auersperg N. Increased E-cadherin expression in ovarian surface epithelium: an early step in metaplasia and dysplasia. Int J Gynecol Pathol 1997; 16: 250–5.
16 Darai E, Scoazec JY, Walker-Combrouze F, Mlika-Cabanne N, Feldmann G, Madelenat P, *et al*. Expression of cadherins in benign, borderline, and malignant ovarian epithelial tumors: a clinicopathologic study of 60 cases. Hum Pathol 1997; 28: 922–8.
17 Reddy P, Liu L, Ren C, Lindgren P, Boman K, Shen Y, *et al*. Formation of E-cadherin-mediated cell-cell adhesion activates AKT and mitogen activated protein kinase via phosphatidylinositol 3 kinase and ligand-independent activation of epidermal growth factor receptor in ovarian cancer cells. Mol Endocrinol 2005; 19: 2564–78.
18 Auersperg N, Pan J, Grove BD, Peterson T, Fisher J, Maines-Bandiera S, *et al*. E-cadherin induces mesenchymal-to-epithelial transition in human ovarian surface epithelium. Proc Natl Acad Sci U S A 1999; 96: 6249–54.
19 Ong A, Maines-Bandiera SL, Roskelley CD, Auersperg N. An ovarian adenocarcinoma line derived from SV40/E-cadherin-transfected normal human ovarian surface epithelium. Int J Cancer 2000; 85: 430–7.
20 Lau MT, Klausen C, Leung PC. E-cadherin inhibits tumor cell growth by suppressing PI3K/Akt signaling via beta-catenin-Egr1-mediated PTEN expression. Oncogene 2011; 30: 2753–66.
21 Nakagawa M, Fukata M, Yamaga M, Itoh N, Kaibuchi K. Recruitment and activation of Rac1 by the formation of E-cadherin-mediated cell-cell adhesion sites. J Cell Sci 2001; 114: 1829–38.
22 De Santis G, Miotti S, Mazzi M, Canevari S, Tomassetti A. E-cadherin directly contributes to PI3K/AKT activation by engaging the PI3K-p85 regulatory subunit to adherens junctions of ovarian carcinoma cells. Oncogene 2009; 28: 1206–17.
23 Inoue M, Ogawa H, Miyata M, Shiozaki H, Tanizawa O. Expression of E-cadherin in normal, benign, and malignant tissues of female genital organs. Am J Clin Pathol 1992; 98: 76–80.
24 Veatch AL, Carson LF, Ramakrishnan S. Differential expression of the cell-cell adhesion molecule E-cadherin in ascites and solid human ovarian tumor cells. Int J Cancer 1994; 58: 393–9.
25 Davies BR, Worsley SD, Ponder BA. Expression of E-cadherin, alpha-catenin and beta-catenin in normal ovarian surface epithelium and epithelial ovarian cancers. Histopathology 1998; 32: 69–80.
26 Fouquet S, Lugo-Martinez VH, Faussat AM, Renaud F, Cardot P, Chambaz J, *et al*. Early loss of E-cadherin from cell-cell contacts is involved in the onset of Anoikis in enterocytes. J Biol Chem 2004; 279: 43061–9.
27 Kang HG, Jenabi JM, Zhang J, Keshelava N, Shimada H, May WA, *et al*. E-cadherin cell-cell adhesion in ewing tumor cells mediates suppression of anoikis through activation of the ErbB4 tyrosine kinase. Cancer Res 2007; 67: 3094–105.
28 Lengyel E. Ovarian cancer development and metastasis. Am J Pathol 2010; 177: 1053–64.
29 Shen X, Kramer RH. Adhesion-mediated squamous cell carcinoma survival through ligand-independent activation of epidermal growth factor receptor. Am J Pathol 2004; 165: 1315–29.
30 Al-Ayoubi A, Tarcsafalvi A, Zheng H, Sakati W, Eblen ST. ERK activation and nuclear signaling induced by the loss of cell/matrix adhesion stimulates anchorage-independent growth of ovarian cancer cells. J Cell Biochem 2008; 105: 875–84.
31 Sawada K, Mitra AK, Radjabi AR, Bhaskar V, Kistner EO, Tretiakova M, *et al*. Loss of E-cadherin promotes ovarian cancer metastasis via alpha 5-integrin, which is a therapeutic target. Cancer Res 2008; 68: 2329–39.
32 Green SK, Francia G, Isidoro C, Kerbel RS. Antiadhesive antibodies targeting E-cadherin sensitize multicellular tumor spheroids to chemotherapy *in vitro*. Mol Cancer Ther 2004; 3: 149–59.

Acta Pharmacologica Sinica (2012) 33: 823–831
 1671-4083/12 $32.00
www.nature.com/aps

Original Article

Enhancement of cellular uptake and cytotoxicity of curcumin-loaded PLGA nanoparticles by conjugation with anti-P-glycoprotein in drug resistance cancer cells

Wanisa PUNFA[1], Supachai YODKEEREE[1], Pornsiri PITCHAKARN[1], Chadarat AMPASAVATE[2], Pornngarm LIMTRAKUL[1, *]

[1]*Department of Biochemistry, Faculty of Medicine, Chiang Mai University, Chiang Mai 50200, Thailand;* [2]*Department of Pharmaceutical Sciences, Faculty of Pharmacy, Chiang Mai University, Chiang Mai 50200, Thailand*

Aim: To compare the anti-cancer activity and cellular uptake of curcumin (Cur) delivered by targeted and non-targeted drug delivery systems in multidrug-resistant cervical cancer cells.
Methods: Cur was entrapped into poly (*DL*-lactide-co-glycolide) (PLGA) nanoparticles (Cur-NPs) in the presence of modified-pluronic F127 stabilizer using nano-precipitation technique. On the surface of Cur-NPs, the carboxy-terminal of modified pluronic F127 was conjugated to the amino-terminal of anti-P-glycoprotein (P-gp) (Cur-NPs-APgp). The physical properties of the Cur-NPs, including particle size, zeta potential, particle morphology and Cur release kinetics, were investigated. Cellular uptake and specificity of the Cur-NPs and Cur-NPs-APgp were detected in cervical cancer cell lines KB-V1 (higher expression of P-gp) and KB-3-1 (lower expression of P-gp) using fluorescence microscope and flow cytometry, respectively. Cytotoxicity of the Cur-NPs and Cur-NPs-APgp was determined using MTT assay.
Results: The particle size of Cur-NPs and Cur-NPs-APgp was 127 and 132 nm, respectively. The entrapment efficiency and actual loading of Cur-NPs-APgp (60% and 5 μg Cur/mg NP) were lower than those of Cur-NPs (99% and 7 μg Cur/mg NP). The specific binding of Cur-NPs-APgp to KB-V1 cells was significantly higher than that to KB-3-1 cells. Cellular uptake of Cur-NPs-APgp into KB-V1 cells was higher, as compared to KB-3-1 cells. However, the cellular uptake of Cur-NPs and Cur-NPs-IgG did not differ between the two types of cells. Besides, the cytotoxicity of Cur-NPs-APgp in KB-V1 cells was higher than those of Cur and Cur-NPs.
Conclusion: The results demonstrate that Cur-NPs-APgp targeted to P-gp on the cell surface membrane of KB-V1 cells, thus enhancing the cellular uptake and cytotoxicity of Cur.

Keywords: anticancer drug; curcumin; targeting drug delivery; nanoparticle; P-glycoprotein; multidrug resistance; cervical cancer

Acta Pharmacologica Sinica (2012) 33: 823–831; doi: 10.1038/aps.2012.34; published online 14 May 2012

Introduction

Multidrug resistance (MDR) in cancer cells reduces the cytotoxic effects of various anticancer drugs and enhances the ability of cancer cells to actively efflux drugs, leading to a decrease in cellular drug accumulation below toxicity[1]. Although several mechanisms are proposed for drug resistance, the best-studied mechanism of MDR is related to the overexpression of P-glycoprotein (P-gp), a 170 kDa ATP dependent membrane transporter that acts as a drug efflux pump[2]. Overexpression of P-gp in various cancer cells leads to a decrease in the cytotoxicity in a broad spectrum of anticancer drugs including doxorubicin, vincristine, etopoxide and paclitaxel[3]. There have been many studies investigating the ability of P-gp inhibitors to overcome MDR by inhibiting MDR transporters or by suppressing MDR mechanisms. The compounds that would reverse resistance against anticancer drugs are called MDR inhibitors, MDR modulators or chemosensitizers[4]. Many pharmacologic agents from diverse structure classes have been identified as MDR modulators. It has been reported that many agents from natural products and dietary plants also modulate MDR phenotype of cancer cells including the extraction from *Rosmarinus officinalis*, *Momordica charantia*[4, 5], *Stemona aphylla*[6], and including *Curcuma longa*[7, 8].

Curcumin (Cur), a phenolic compound purified from the rhizome of *Curcuma longa*, has a long history of being used as a spice and in traditional medicine. Several studies demon-

* To whom correspondence should be addressed.
E-mail plimtrak@mail.med.cmu.ac.th
Received 2011-11-10 Accepted 2012-02-14

strated that Cur has been shown to display antioxidant, anti-inflammation, anti-diabetes, anti-carcinogenic, anti-tumor invasion and anti-angiogenesis activities[9]. Moreover, our previous findings indicated that Cur down-regulated both MDR1 gene expression and P-gp function[10, 11]. The most compelling and key rationale for the therapeutic use of Cur is its extremely superior safe profile. Cur has been associated with the regression of premalignant lesions of various organs and shows no toxicity to healthy organs at high doses[12]. However, low oral bioavailability, poor pharmacokinetics, insolubility in water[12] and degradability at natural to basic pH conditions are the limited efficiency factors of Cur *in vivo*. The development of novel delivery systems could be one strategy to overcome these problems. One possible way to improve the water solubility and stability of Cur is to entrap it into nanoparticles (NPs)[12].

NPs can target tumors by either the passive or active process. Passive targeting implies that the enhanced permeability and retention effect (EPR effect), which characterizes malignant tissues, allows the passive accumulation of encapsulated drugs to tumor sites[13, 14] . Active targeting involves tagging the drug vehicle with a ligand and allows it to specifically sequester in the targeted tumor[15, 16]. Among the various ligands, such as peptides, carbohydrates, and polymers, monoclonal antibodies are most widely investigated for selectively targeting nanoparticulate drug delivery systems to tumors[17–19]. The P-gp is one such cell-surface target. P-gp-positivity is associated with more aggressive tumor behavior[20] and is a biomarker which overexpresses on the plasma membrane of MDR phenotypes of a variety of cancer cell lines[21], where Cur could be a promising candidate for cancer targeted therapy.

Polymeric nanoparticle-based drugs have been increasingly developed as preferred drug nanocarriers against many diseases. Special focus on the use of particles prepared from poly(DL-lactide-co-glycolic acid) (PLGA)[22], is warranted due to their biocompatibility, biodegradability and high stability in biological fluids[23]. These NPs have proven to be effective carriers for hydrophobic and hydrophilic drugs[24]. Bisht *et al* showed that Cur-loaded NPs could suppress constitutive NF-κB in pancreatic cancer cells[25]. The next previous study again found that Cur-loaded NPs were more active than Cur in suppressing NF-κB activation induced by TNF[26]. These differences could have been due to differential Cur uptake.

Several studies have been reported the evaluations of Cur-loaded PLGA NPs such as the effect in improving oral bioavailability of Cur may be associated with improved water solubility, higher release rate in the intestinal juice, enhanced absorption by improved permeability, inhibition of P-gp-mediated efflux, and increased residence time in the intestinal cavity[12, 17–19, 23]. Thus, encapsulating hydrophobic drugs or medicinal compounds in PLGA polymer is a promising candidate method for sustained and controlled drug delivery with improved bioavailability of Biopharmaceutics Classification System (BCS) class IV, such as Cur[27]. In this study we conjugated anti-P-gp antibody to the surface of biodegradable PLGA-NPs to target P-gp on the surface of MDR cancer cells and Cur was encapsulated to PLGA nanospheres by nanoprecipitation technique. The Cur loaded NPs were then characterized for their actual loading, encapsulation efficiency, particle size, morphology, and then evaluated for their *in vitro* release profiles. Moreover, we compared the cellular uptake and cytotoxicity of targeted and nontargeted Cur-loaded NPs in drug resistant (KB-V1) and drug sensitive (KB-3-1) cervical carcinoma cell lines.

Materials and methods

Materials

Poly(DL-lactide-co-glycolide) (PLGA; lactide to glycolide ratio 50:50), *N*-(3-dimethylaminopropyl)-*N*′-ethylcarbodiimide hydrochloride (EDC), *N*-hydroxy succinimide (NHS) and Pluronic® F127 (Poloxamer 407) were purchased from Sigma Aldrich (St Louis, MO, USA). 4-Dimethylaminopyridine (DMAP) and succinic anhydride were purchased from Fluka Chemie GmbH (Buchs, Switzerland). Dulbecco's modified Eagle's medium (DMEM), penicillin-streptomycin, fetal bovine serum (FBS) and 0.05% trypsin-EDTA were provided by Gibco (Grand Island, NY, USA). Triethylamine and D-Tube™ Dialyzer Midi, MWCO 6–8 kDa, Amicon® Uitra-4 centrifugal Filter Devices (30 K) were supplied by Merck KGaA (Darmstadt, Germany). Acetone, tetrahydrofuran (THF), chloroform, dimethyl sulfoxide (DMSO) and diethyl ether were purchased from Lab Scan (Bangkok, Thailand). PTFE membrane syringe filter (Puradisc13, PTFE; 0.45 μm) was purchased from Whatman (UK). Mouse monoclonal antibody (F4) to P-glycoprotein (P-gp) was purchased from Abcam (Cambridge, UK). Normal mouse IgG1 isotype control was perchased from Santa Cruz (CA, USA).

Cell culture

The multidrug resistant (KB-V1) and drug sensitive (KB-3-1) cervical carcinoma cell lines[8, 10] were generous gifts from Dr Michael M GOTTESMAN (National Cancer Institute, Bethesda, MD, USA). Both cell lines were cultured in DMEM with 10% FBS, 2 mmol/L *L*-glutamine, 50 U/mL penicillin and 50 μg/mL streptomycin and 1 μg/mL of vinblastine was added only to the KB-V1 culture medium. These two-cell lines were maintained in a humidified incubator with an atmosphere comprising 5% CO_2 at 37°C. The expression of P-gp in KB-V1 and KB-3-1 cells was confirmed by Western blot analysis as described in our previous reports[4, 10].

Preparation of poloxamer-carboxylic (Poloxamer-COOH)

Terminal hydroxyl groups on pluronics were first converted to carboxyl groups with a slight modification of the previous procedure described by Guerrouache *et al*[28] and Chittasupho *et al*[29]. Twelve grams of poloxamer (Pluronic® F127) was dissolved in 55 mL tetrahydrofuran (THF), then 122.5 mg of 4-dimethylaminopyridine (DMAP), 135 μL of triethylamine and 1 g of succinic anhydride were added and the mixture was stirred for 48 h at room temperature. The solution was dried by a rotary evaporator, and was then dissolved in 75 mL

of chloroform. The excess succinic anhydride was removed by filtration with a 0.45 μm PTFE membrane syringe filter. The poloxamer-COOH was purified by precipitation for 48 h with ice-cold diethyl ether. The precipitate was dissolved in ethanol, filtered and dried. The product was identified by fourier transform infrared spectrophotometer (Nicolet 470 FT-IR spectrometers, USA).

Preparation of curcumin-encapsulated PLGA nanoparticles (Cur-NPs)

PLGA NPs with encapsulated Cur were formulated by the nanoprecipitation technique[30]. Fifty milligrams of PLGA was dissolved in 7.5 mL acetone containing 500 μg of Cur. One hundred milligrams of poloxamer-COOH was dissolved in 10 mL Deionized (DI) water. Then the PLGA solution was dropwise-added into the poloxamer solution under stirring (400 rounds per minute) overnight. The NPs were then washed twice with DI water, by centrifugation using Amicon filtration device with 30 kDa molecular weight cut off membrane at 4400 rounds per minute for 50 min at 4 °C to obtain Cur-NPs. The resulting NPs were resuspended in 1 mL of sterile DI water.

Preparation of anti-P-gp antibody-conjugated Cur-NPs (Cur-NPs-APgp)

Cur-NPs were conjugated to anti-P-gp antibody through the carbodiimide reaction. Briefly, the NPs were adjusted to pH 5.8, and then incubated with the appropriate amount of NHS (50 mmol/L) and EDC (100 mmol/L) for 30 min. The resulting NHS-activated particles were then centrifuged at 12 000 rounds per minute for 15 min at 4 °C and the supernatant was removed. The NPs were resuspended in 800 μL DI water and 100 μL PBS (pH 7.4), and then 10 μL of anti-P-gp antibody was added under gentle stirring and the solution was then incubated overnight. Cur-NPs-APgp were collected by centrifugation (12 000 rounds per minute for 15 min at 4 °C) and washed 2 times with DI water.

Characterization of NPs

The NPs were characterized for size, zeta potential, and particle distribution by photon correlation spectroscopy (PCS) (Zetasizer, Malvern Instrument, UK).

Fifteen microliters of nanoparticles was dissolved in 25 μL of DI water (2 μg of nanoparticle/mL) and stained with 25 μL of 2% (*w/v*) phosphotungstic acid solution. Five microliters of stained-nanoparticles were dropped on a copper grid and dried by air flow. The morphology of NPs was determined by TEM.

Determination of Cur loading and encapsulation efficiency

The encapsulation efficiency of Cur-NPs was determined by analyzing the supernatant of the final suspension. The NPs and supernatant were separated from each other by centrifugation using an Amicon filtration device with 30 kDa molecular weight cut off membrane at 4400 rounds per minute for 50 min. The remaining Cur in the supernatant was measured by UV-visible spectrophotometer at 425 nm. The concentration of Cur was calculated using the standard curve of Cur in methanol (1–10 μg/mL). The Cur loading content and encapsulation efficiency were calculated as follows:

$$\text{Loading content} = \frac{\text{Amount of Cur in nanoparticle}}{\text{1 mg of nanoparticles}} \quad (1)$$

$$\text{Entrapment efficiency} = \frac{[\text{Cur}]_{\text{total}} - [\text{Cur}]_{\text{filtrate}}}{[\text{Cur}]_{\text{total}}} \times 100 \quad (2)$$

In vitro Cur release

The release of Cur from the NPs was carried out by the dialysis method as previously described[30] with slight modifications. Briefly, 100 μg/mL of Cur-NPs were added in a dialysis tube with a molecular cut off of 6–8 kDa and suspended in 10 mL of release medium (50% *v/v* of ethanol) at 37 °C in shaking incubator at 70 rounds per minute. One milliliter from the release medium was withdrawn at predetermined time interval and replaced with 1 mL of the fresh medium. Finally, Cur in the samples was quantified with a spectrophotometer. The percentage of Cur released from the NPs at various time points was calculated as follows:

$$\text{Cumulative release (\%)} = \frac{\text{Released Cur}}{\text{Total encapsulated Cur}} \times 100$$

Cellular uptake of Cur-NPs-APgp into KB-V1 and KB-3-1 cells

KB-V1 and KB-3-1 (20 000 cells) were seeded on cover slips in 12-well tissue culture plates and incubated at 37 °C, 5% CO_2 in DMEM supplement with 10% FBS, overnight. The cells were then exposed to 10 μg/mL concentrations of Cur-NPs-APgp, Cur-NPs, or Cur-NPs-IgG for 30 and 60 min. Free NPs were removed by being washed 3 times with PBS. The cells were fixed with 4% paraformaldehyde. Cellular uptake of Cur-NPs was determined using a fluorescence microscope.

Specific binding of Cur-NPs-APgp to KB-V1 and KB-3-1 cells

The specific binding of Cur-NPs-APgp was studied by using flow cytometry. KB-V1 and KB-3-1 cells (2×10^5 cells/well) were treated with 5 μmol/L of Cur-NPs-APgp for 5, 30, and 60 min in DMEM without phenol red and incubated at 37 °C. After incubation, the cells were centrifuged at 4400 rounds per minute for 5 min at 4 °C and the cells were washed 2 times with ice cold PBS. The cells were centrifuged at 4400 rounds per minute for 5 min at 4 °C. Then the supernatant was removed and the cell pellet was resuspended with 0.5 mL PBS. The fluorescence intensity was measured by flow cytometer.

Cytotoxicity assay

Cytotoxicity of NPs, NPs-APgp, free Cur, Cur-NPs, and Cur-NPs-APgp against KB-V1 and KB-3-1 cells was evaluated using a colorimetric MTT assay as was described before[31]. Briefly, cells (1×10^3 cells/well) were seeded in a 96-well plates and incubated at 37 °C, 5% CO_2 overnight in DMEM containing 10% FBS. The cells were treated with various concentrations (0–27 μmol/L) of NPs, NPs-APgp, free Cur, Cur-NPs,

and Cur-NPs-APgp for 6 h. Then cell culture supernatant was removed and fresh DMEM containing 10% FBS was added and the cell culture was further incubated for 42 h. For the time interval treatment, the cells were treated with 27 μmol/L of free Cur, Cur-NPs, and Cur-NPs-APgp for 1, 6, or 24 h, after that cultured in the drug free medium for another 23, 18, and 0 h, respectively. At the end of time point, MTT dye (15 μL, 5 mg/mL) was added and incubated for an additional 4 h. The MTT-formazan was dissolved in DMSO and absorbance was measured using a microplate reader at 540 nm with a reference wavelength of 630 nm.

Statistical analysis

All data are presented as mean±SD values. Statistical analyses were conducted with Prism version 5.0 using one-way ANOVA, Dunnett's test or Tukey's test. Statistical significance was concluded with: b, c: $P<0.05$ or 0.01, respectively when compared with control and e, f: $P<0.05$ or 0.01, respectively when compared with free Cur.

Results

Expression of P-gp in KB-V1 and KB-3-1 cells

Western blot analysis for the level of P-gp in KB-V1 and KB-3-1 cells showed that the KB-V1 cells expressed large amount of P-gp while the expression of P-gp in KB-3-1 cells could not be detected (Figure 1).

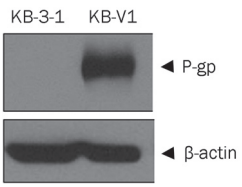

Figure 1. P-gp expression in KB-V1 and KB-3-1 cells determined by Western blot analysis.

Preparation of carboxylated poloxamer (Poloxamer-COOH)

To conjugate anti-P-gp antibody to NPs, the hydroxyl groups of the surfactant and poloxamer were converted to carboxyl groups. The COOH formation was determined by FTIR spectroscopy. The FTIR spectrum showed a strong C=O stretching absorption at 1720 cm^{-1} and a very broad and strong absorption at 3500 cm^{-1}, which indicated the appearance of the hydroxyl of carboxylic acid (Figure 2). These results confirmed the formation of the carboxylated poloxamer. These results were in line with our previous report[32] confirming the partial formation of carboxylated Poloxamer.

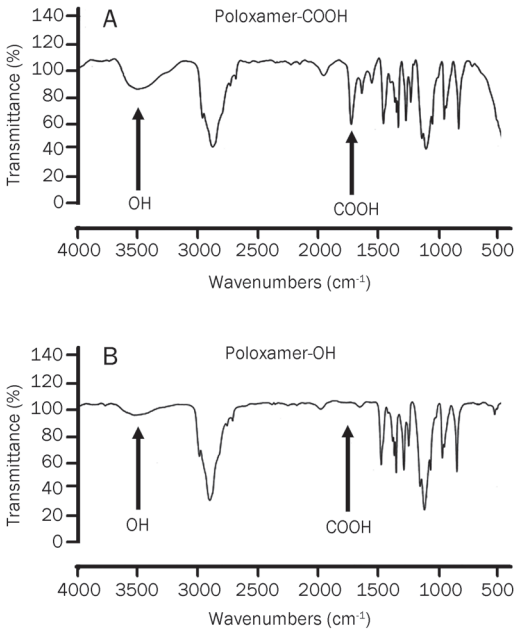

Figure 2. FTIR spectrogram of carboxylated Pluronic F127. Figure A exhibits the carboxylated poloxamer. The FTIR spectrum showed a strong C=O stretching absorption at 1720 cm^{-1} which indicated the appearance of carboxylic acid. Figure B exhibits native Pluronic F127, a very broad and strong absorption at 3500 cm^{-1}, which indicated the appearance of the hydroxyl group.

Size, particle distribution, zeta potential, entrapment efficiency, and actual loading of NPs, Cur-NPs and Cur-NPs-APgp

PLGA NPs were prepared using a nanoprecipitation method. NPs were formed from PLGA, which served as a hydrophobic core to encapsulate the poorly water-soluble Cur. The size, polydispersity (PDI), zeta potential, and actual loading for Cur-NPs and Cur-NPs-APgp are shown in Table 1. The mean diameters of Cur-NPs and Cur-NPs-APgp were 127 and 132 nm, respectively, which were bigger than NPs (111 nm). Moreover, low polydispersity was observed in both Cur-NPs

Table 1. Mean size, zeta potential, polydispersity index (PDI), percent entrapment efficiency (%EE) and actual loading for NPs, Cur-NPs, and Cur-NPs-APgp.

Formation	Size (nm)	Polydispersity	Zeta potential (mV)	EE (%)	Actual loading (μg Cur/mg NP)
NPs	111±5.0	0.245	-23.0	ND	ND
Cur-NPs	127.4±2.2	0.105±2.2	-23.1±1.7	99	7
Cur-NPs-APgp	132.4±1.5	0.091±1.5	-40.3±6.1	60	5

ND=Not determined

and Cur-NP-APgp suggesting a narrow size distribution. The zeta potential of the Cur-NPs and Cur-NPs-APgp were -23.1 and -40.3 mV, respectively. The entrapment efficiency and actual loading of Cur in nanoparticles were determined using equations 1 and 2, as described in the method section. The entrapment efficiency and actual loading of Cur-NPs-APgp (60%, 5 μg Cur/mg NP) were lower than that of Cur-NPs (99%, 7 μg Cur/mg NP).

In addition, with this formulation procedure, the Cur samples encapsulated in NPs were completely dissolved in aqueous solution with no aggregation, unlike those observed in free Cur, which exhibited poor aqueous solubility (Figure 3A).

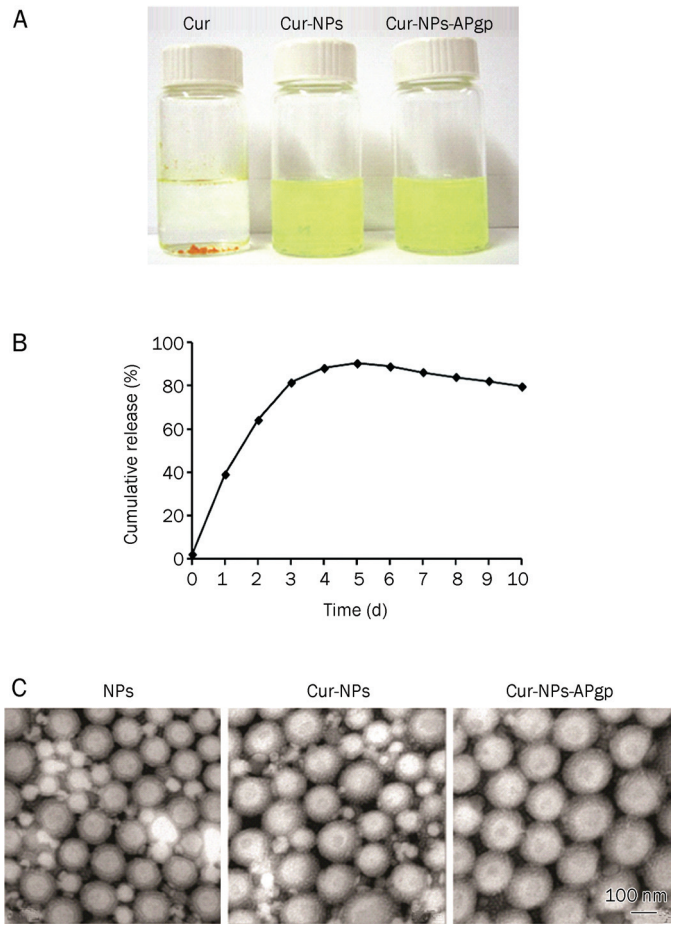

Figure 3. Nano-encapsulation renders Cur completely dispersible in aqueous media. The figure shows solubility of Cur compared with Cur-NPs and Cur-NPs-APgp in aqueous solution (A). *In vitro* Cur release kinetic profile from Cur-NPs in 50% *v/v* of ethanol at 37 °C in shaking incubator at 70 rounds per minute over a period of 10 d (B). Transmission electron microscope image of NPs, Cur-NPs, and Cur-NPs-Apgp, respectively. TEM scanning shows the formation of spherical and smooth particles (C).

In vitro release kinetic profile

Cumulative percentage of Cur released from Cur-NPs is shown in Figure 3B. On the first day, only 40% of Cur was released from the nanoparticles and increased up to 80% on the third days and reached 90% in 5 d, which was a maximum. After that, the sustained-Cur was released at about 80% up to 10 d.

Surface morphology of NPs

The surface morphology of the nanosphere encapsulated Cur was determined by TEM. Figure 3C illustrates a TEM scanning and shows the formation of spherical and smooth particles. The average size of Cur-NPs and Cur-NPs-APgp were 125 nm and 130 nm, respectively, which correlated to that which was observed using photon correlation spectroscopy (Zeta Sizer).

Specific binding of Cur-NPs-APgp to KB-V1 and KB-3-1cells

To determine the specific binding of anti-P-gp antibody conjugated NPs on KB-V1 cells (high expression of P-gp), KB-V1 and KB-3-1 cells were incubated with Cur-NPs-APgp for various time points and then fluorescence intensity was determined by flow cytometry. Figure 4 shows that the interaction of Cur-NPs-APgp to KB-V1 cells was substantially greater than to KB-3-1 cells. The fluorescence intensity in KB-V1 cells was higher than that in the KB-3-1 cells when the cells were

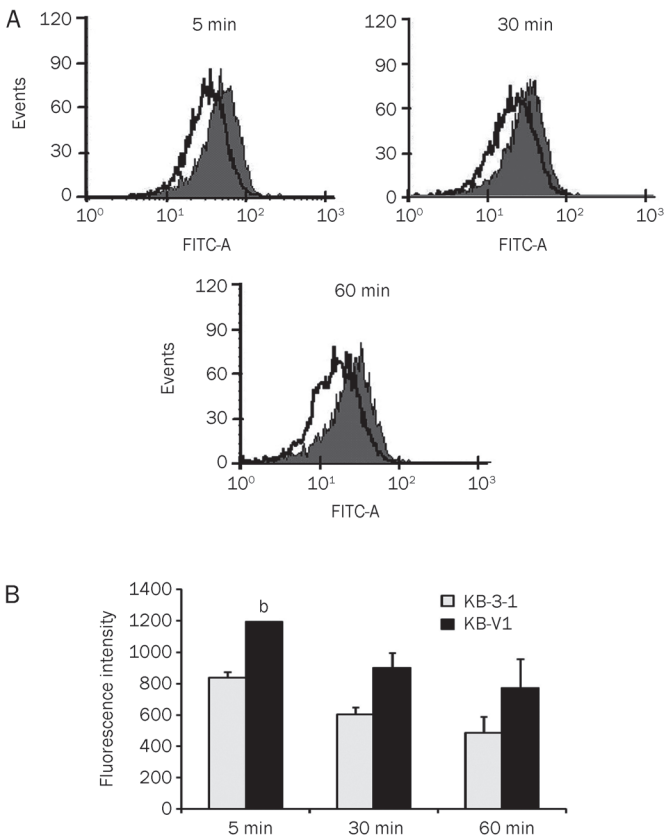

Figure 4. Specific binding of Cur-NPs-APgp to KB-V1 cells determined by FACS. Gray and blank histograms represent Cur-NPs-APgp targeting to KB-V1 and KB-3-1 cells, respectively (A) and show the fluorescence intensity in bar graph (B). All assays have been demonstrated in duplicate and the mean±standard deviations are shown. $^{b}P<0.05$ *vs* KB-3-1 cells.

treated with Cur-NPs-APgp for 5, 30 and 60 min.

Cellular uptake of NPs by KB-V1 and KB-3-1 cells

In order to investigate the cellular uptake of Cur encapsulation in NPs, KB-V1 and KB-3-1 were treated with Cur-NPs, Cur-NPs-APgp, and Cur-NPs-IgG for 30 and 60 min. As shown in Figure 5, the fluorescence intensity of Cur in Cur-NPs-APgp-treated KB-V1 cells was higher than Cur-NPs-APgp-treated KB-3-1 cells at 60 min. In contrast to Cur-NPs-APgp-treated cells, there was no difference in the fluorescence intensity between Cur-NPs and Cur-NPs-IgG treated-KB-V1 and KB-3-1 cells at 60 min (Figure 5B).

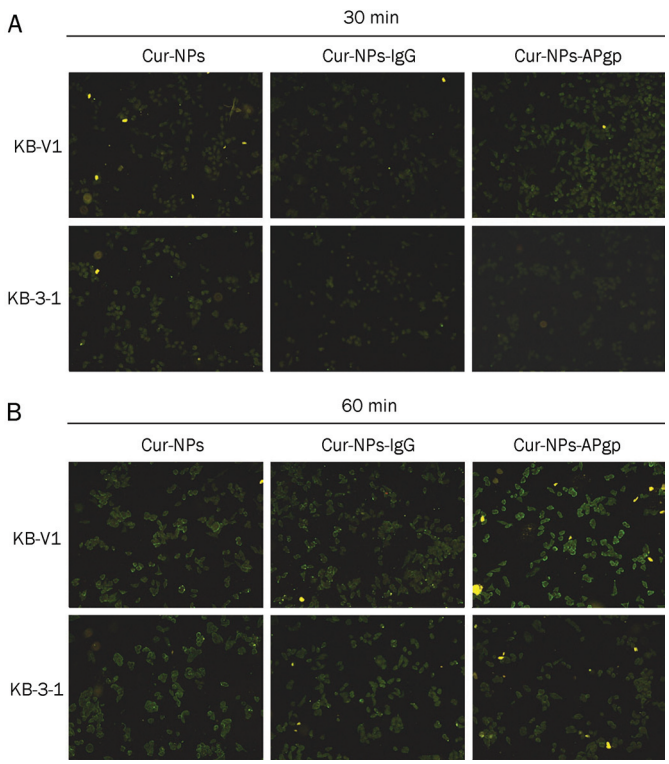

Figure 5. The cellular uptake of Cur-NPs-APgp and Cur-NPs and Cur-NPs-IgG in KB-V1 and KB-3-1 cells. Cells were incubated with 10 μg/mL Cur-NPs-APgp or Cur-NPs and Cur-NPs-IgG for 30 (A) and 60 min (B), and the fluorescence levels were determined by a fluorescence microscope.

Cytotoxicity of nanoparticle to KB-V1 and KB-3-1 cells

To determine the cytotoxicity of NPs, NPs-APgp, free Cur, Cur-NPs and Cur-NPs-APgp, KB-V1 and KB-3-1 cells were treated with NPs, NPs-APgp, free Cur, Cur-NPs, or Cur-NPs-APgp for 6 h and cell viability was then determined by MTT assay. In KB-V1 cells (Figure 6A), Cur-NPs-APgp was found to be the most effective in inducing cancer cell death among three different Cur formations. Free Cur, Cur-NPs, and Cur-NPs-APgp reduced KB-3-1 cell viability in a dose-dependent manner, but the difference did not differ between treatment groups (Figure 6B) and IC_{50} of free Cur, Cur-NPs, and Cur-

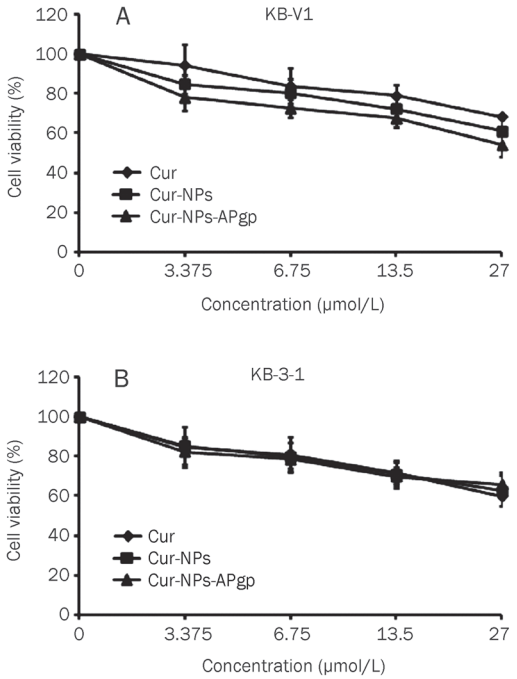

Figure 6. Cytotoxicity of Cur, Cur-NPs, and Cur-NPs-APgp in KB-V1 (A) and KB-3-1 (B) cells. The cells were incubated with the compounds for 6 h, and the cytotoxicity was then determined by MTT assay. All assays have been demonstrated in triplicate and the mean±standard deviations are shown.

NPs-APgp in KB-3-1 and KB-V1 was more than 27 μmol/L, while NPs and NPs-APgp did not reduce cell viability when compared with the control (data not shown). For time interval treatment, the cells were treated with 27 μmol/L of free Cur, Cur-NPs, and Cur-NPs-APgp for 1, 6, or 24 h, after that cultured in the drug free medium for another 23, 18 and 0 h, respectively. The result showed that Cur-NPs-APgp had the most potential to induce cancer cell death among the three different Cur formations. Cur-NPs-APgp at 1 and 6 h showed a significant ability to induce cancer cell death when compared with free Cur and control in KB-V1 cell, while Cur-NPs showed significant ability to induce cancer cell death when compared only with the control, whereas at 24 h both the Cur-NPs and Cur-NPs-APgp showed significant ability to induce cancer cell death when compared with free Cur and the control (Figure 7).

Discussion

Curcumin (Cur), a naturally occurring product, has exhibited potent anti-cancer activities in various models which can be used in cancer therapy[33]. Although Cur showed multiple medicinal benefits, but revealed a low oral bioavailability of Cur[34], which continues to be highlighted as a major challenge in developing its formation for clinical efficacy. Cur encapsulated to nanoparticles is one of the possible ways to increase its solubility and bioavailability[30]. In this direction, various nanocurcumin including liposome, micelles, and biodegrad-

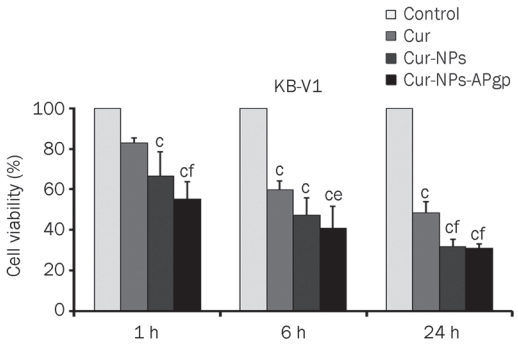

Figure 7. Cytotoxicity of 27 μmol/L Cur, Cur-NPs, and Cur-NPs-APgp in KB-V1 cells. The cells were incubated with the compounds for 1, 6, or 24 h, after that cultured in the drug free medium for another 23, 18, and 0 h, respectively. The cytotoxicity was determined by MTT assay at the end of time point. All assays have been demonstrated in triplicate and the mean±standard deviations are shown. $^{c}P<0.01$ *vs* control; $^{e}P<0.05$, $^{f}P<0.01$ *vs* Cur.

able polymer NPs have been developed and most of them involve passive targeting[35, 36]. However, actively targeting nanocurcumin has not yet been demonstrated. Targeted drug delivery represents a potential approach to further enhance anti-tumor efficacy. P-gp is minimally expressed on normal tissue, but significantly upregulated on MDR cancer cells[37]. Targeted drug delivery to MDR cancer cells is considered a strategy for the increased drug sensitivity of the cancer cells via enhancement of drug accumulation and cellular uptake.

In the current report, we prepared Cur-encapsulated PLGA NPs based on the nanoprecipitation technique. Pluronic is a widely known stabilizer for PLGA-NPs and many other pharmaceutical formations. To conjugate the antibody to the surface of NPs, we converted the hydroxyl groups of pluronic to carboxyl groups and conjugated the anti-P-gp antibody to the surface of NPs using the EDC-NHS carbodiimide reaction. Particles in the 100 to 200 nm range avoid premature clearance by the reticuloendothelial system[16]. We have prepared Cur-NPs and Cur-NPs-APgp with a mean diameter of less than 200 nm and the polydispersity index (PDI) of both was near 0.1. When the PDI value is less than 0.3, this indicated that the distribution of the sample particle size was narrow. These finding demonstrated that the small mean particle size and the uniform particle distribution were observed in Cur-NPs and Cur-NPs-APgp. Our NPs preparation (Cur-NPs) provided smaller size (127 nm) and higher entrapment efficiency (99%) compared to previous study[30] which used emulsion evaporation method. The mean size of the Cur-NPs and Cur-NPs-APgp was confirmed by TEM. The diameter of the particles, observed in TEM (125 and 130 nm, respectively), was smaller than those that were detected by the PCS method. This is due to the fact that the TEM observation of the NPs was done in their dry form (air dried particles). The zeta potential values of Cur-NPs and Cur-NPs-APgp was negative, which is typical of the presence of PLGA terminal carboxylic residues. However, the value of this negative charge is much lower than that of the classical PLGA-NPs, which has been attributed to the presence of the carboxylic group of the pluronic on the surface of the NPs. The entrapment efficiency was lower in Cur-NP-APgp compared to that in Cur-NPs, probably because of the washing of NPs suspension during the antibody conjugation process, which was consistent with the literature that targeted NPs via carbodiimide reaction[38] and the percent conjugation of anti-P-gp antibody on NPs surface was 22% as described in our previous study[32]. Unlike free Cur, Cur-NPs formulations have shown improved solubility in aqueous solution. The prepared particles were further evaluated for *in vitro* Cur releasing. In the present case, considering the solubility of Cur in ethanol, a 50% *v/v* of ethanol was used as the release medium. The release of Cur from Cur-NPs displayed a rapid release in the early phase, and reached a maximum at 5 d of up to 90%, and then gradually slowed down. The sustained Cur release was about 80%, until 10 d.

In order to obtain the antibody conjugated NPs, which are able to target desired cells, the conjugation procedure must preserve the biological activity of targeting ligand. We performed flow cytometry to evaluate the recognition properties of Cur-NPs-APgp to P-gp antigen, and found that the anti-P-gp immunoparticles bound specifically to KB-V1 cells, but exhibited less binding to KB-3-1 negative control cells.

It has been demonstrated that the therapeutic effect of drug-loaded NPs is depended on the internalization and sustained retention of the NPs. By combining the tumor targeting properties of the antibody with NPs, immunoparticles offer the promise of selective drug delivery to tumor cells, increased internalization and an intracellular drug release within targeted cells. Herein, we used Cur as a fluorescence probe to follow the NPs in the cellular uptake experiment. The intensity of Cur-NPs-APgp in KB-V1 was higher than in KB-3-1 cells, while the fluorescence intensity of Cur-NPs and Cur-NPs-IgG between both the cells did not differ. The higher intensity of fluorescence demonstrated the higher amount of Cur-NPs bound or taken up by the cells. To confirm the specificity of NPs conjugated with anti-P-gp antibody, another control using random IgG modified NPs in study of the cellular uptake (Figure 5) showed that IgG-modified nanoparticles did not demonstrate any differences of cellular uptake of Cur in KB-V1 cells compared to KB-3-1 cells. This finding suggested that Cur-NPs-APgp specifically bound to P-gp on KB-V1 cell surface, and enhanced the cellular uptake of Cur-NPs into MDR cancer cells (P-gp overexpressing cancer cells).

We observed significantly higher cytotoxicity of Cur-NPs-APgp treatment in KB-V1 cells when compared to free-Cur, while all three forms of Cur did not show significant cytotoxicity in KB-3-1 cells. When KB-V1 cells were treated with Cur-NPs-APgp at 1 and 6 h, cell death was induced at a greater rate than free Cur and Cur-NPs. These results were consistent with cellular uptake results. The superior cytoxicity of Cur-NPs-APgp in MDR-cancer cells was apparently due to anti-P-gp on the surface of NPs, and could help Cur-NPs-APgp to target KB-V1 cells while rapidly providing an increase of cell internalization efficiency and cytotoxicity in KB-V1 cells.

However, the cytotoxicity of Cur-NPs-APgp and Cur-NPs was not markedly different that might be because of the multiple-NH_2 groups in an antibody and the conjugation of anti-P-gp antibody is not specific to amino-terminus thus has no control on orientation of antibody after the antibody was linked to the NPs. Therefore the accessibility of anti-P-gp antibody on NPs to P-gp probably was reduced. Nevertheless, our study revealed the specificity of Cur-NPs-APgp to KB-V1, P-gp-overexpressed multidrug resistance cell line, and the conjugation of anti-P-gp antibody to Cur-NPs did not decrease their cellular uptake and also cytotoxicity.

The development of the P-gp targeted drug delivery system, Cur-NPs-APgp has shown efficacy in specific binding and internalization to the multidrug resistant cell line (KB-V1), and therefore provide the way to deliver Cur or anti-cancer drugs to targeted cells. Moreover, the formation of Cur-NPs could improve the solubility of Cur, sustain and prolong the release from Cur-NPs *in vitro*. An effective drug delivery system renders Cur induced target cell death, even when used at low doses. For further study, the combination of anti-cancer drugs and nanocurcumin against cancer cells has to be investigated. Additionally, *in vivo* studies are required to determine whether Cur-NPs-APgp are suitable as drug delivery agents, and could be a promising alternative to administered drug delivery systems for cancer therapy.

Acknowledgements

This work was funded by the Royal Golden Jubilee PhD Program of Thailand and the National Nanotechnology Center, National Science and Technology Development Agency of Thailand.

Author contribution

Wanisa PUNFA carried out all experiments, acquisition and analysis of data and wrote the manuscript; Supachai YODKEEREE and Pornsiri PITCHAKARN provided technical support; Chadarat AMPASAVATE provided technical support and some instruments; and Pornngarm LIMTRAKUL designed and supervised the study, and wrote and revised the manuscript. All authors have read and approved the final manuscript.

References

1 Gottesman MM. Mechanisms of cancer drug resistance. Annu Rev Med 2002; 53: 615–27.
2 Szakacs G, Paterson JK, Ludwig JA, Booth-Genthe C, Gottesman MM. Targeting multidrug resistance in cancer. Nat Rev Drug Discov 2006; 5: 219–34.
3 Fujita T, Washio K, Takabatake D, Takahashi H, Yoshitomi S, Tsukuda K, *et al*. Proteasome inhibitors can alter the signaling pathways and attenuate the P-glycoprotein-mediated multidrug resistance. Int J Cancer 2005; 117: 670–82.
4 Limtrakul P, Khantamat O, Pintha K. Inhibition of P-glycoprotein activity and reversal of cancer multidrug resistance by *Momordica charantia* extract. Cancer Chemother Pharmacol 2004; 54: 525–30.
5 Pitchakarn P, Ohnuma S, Pintha K, Pompimon W, Ambudkar SV, Limtrakul P. Kuguacin J isolated from *Momordica charantia* leaves inhibits P-glycoprotein (ABCB1)-mediated multidrug resistance. J Nutr Biochem 2012; 23: 76–84.
6 Chanmahasathien W, Ampasavate C, Greger H, Limtrakul P. Stemona alkaloids, from traditional Thai medicine, increase chemosensitivity via P-glycoprotein-mediated multidrug resistance. Phytomedicine 2011; 18: 199–204.
7 Romiti N, Tongiani R, Cervelli F, Chieli E. Effects of curcumin on P-glycoprotein in primary cultures of rat hepatocytes. Life Sci 1998; 62: 2349–58.
8 Anuchapreeda S, Leechanachai P, Smith MM, Ambudkar SV, Limtrakul PN. Modulation of P-glycoprotein expression and function by curcumin in multidrug-resistant human KB cells. Biochem Pharmacol 2002; 64: 573–82.
9 Singh S, Khar A. Biological effects of curcumin and its role in cancer chemoprevention and therapy. Anticancer Agents Med Chem 2006; 6: 259–70.
10 Chearwae W, Anuchapreeda S, Nandigama K, Ambudkar SV, Limtrakul P. Biochemical mechanism of modulation of human P-glycoprotein (ABCB1) by curcumin I, II, and III purified from Turmeric powder. Biochem Pharmacol 2004; 68: 2043–52.
11 Kunnumakkara AB, Anand P, Aggarwal BB. Curcumin inhibits proliferation, invasion, angiogenesis and metastasis of different cancers through interaction with multiple cell signaling proteins. Cancer Lett 2008; 269: 199–225.
12 Yallapu MM, Gupta BK, Jaggi M, Chauhan SC. Fabrication of curcumin encapsulated PLGA nanoparticles for improved therapeutic effects in metastatic cancer cells. J Colloid Interface Sci 2010; 351: 19–29.
13 Cirstoiu-Hapca A, Buchegger F, Bossy L, Kosinski M, Gurny R, Delie F. Nanomedicines for active targeting: physico-chemical characterization of paclitaxel-loaded anti-HER2 immunonanoparticles and *in vitro* functional studies on target cells. Eur J Pharm Sci 2009; 38: 230–7.
14 Cheng Y, C Samia A, Meyers JD, Panagopoulos I, Fei B, Burda C. Highly efficient drug delivery with gold nanoparticle vectors for *in vivo* photodynamic therapy of cancer. J Am Chem Soc 2008; 130: 10643–7.
15 Noble CO, Kirpotin DB, Hayes ME, Mamot C, Hong K, Park JW, *et al*. Development of ligand-targeted liposomes for cancer therapy. Expert Opin Ther Targets 2004; 8: 335–53.
16 Lei T, Srinivasan S, Tang Y, Manchanda R, Nagesetti A, Fernandez-Fernandez A, *et al*. Comparing cellular uptake and cytotoxicity of targeted drug carriers in cancer cell lines with different drug resistance mechanisms. Nanomedicine 2011; 7: 324–32.
17 Wartlick H, Michaelis K, Balthasar S, Strebhardt K, Kreuter J, Langer K. Highly specific HER2-mediated cellular uptake of antibody-modified nanoparticles in tumour cells. J Drug Target 2004; 12: 461–71.
18 Kocbek P, Obermajer N, Cegnar M, Kos J, Kristl J. Targeting cancer cells using PLGA nanoparticles surface modified with monoclonal antibody. J Control Release 2007; 120: 18–26.
19 Debotton N, Zer H, Parnes M, Harush-Frenkel O, Kadouche J, Benita S. A quantitative evaluation of the molecular binding affinity between a monoclonal antibody conjugated to a nanoparticle and an antigen by surface plasmon resonance. Eur J Pharm Biopharm 2010; 74: 148–56.
20 Ng IO, Liu CL, Fan ST, Ng M. Expression of P-glycoprotein in hepatocellular carcinoma. A determinant of chemotherapy response. Am J Clin Pathol 2000; 113: 355–63.
21 Abolhoda A, Wilson AE, Ross H, Danenberg PV, Burt M, Scotto KW. Rapid activation of MDR1 gene expression in human metastatic sarcoma after *in vivo* exposure to doxorubicin. Clin Cancer Res 1999; 5: 3352–6.
22 Wang G, Uludag H. Recent developments in nanoparticle-based

drug delivery and targeting systems with emphasis on protein-based nanoparticles. Expert Opin Drug Deliv 2008; 5: 499–515.
23 Mukerjee A, Vishwanatha JK. Formulation, characterization and evaluation of curcumin-loaded PLGA nanospheres for cancer therapy. Anticancer Res 2009; 29: 3867–75.
24 Bennewitz MF, Saltzman WM. Nanotechnology for delivery of drugs to the brain for epilepsy. Neurotherapeutics 2009; 6: 323–36.
25 Bisht S, Feldmann G, Soni S, Ravi R, Karikar C, Maitra A. Polymeric nanoparticle-encapsulated curcumin ("nanocurcumin"): a novel strategy for human cancer therapy. J Nanobiotechnology 2007; 5: 3.
26 Anand P, Nair HB, Sung B, Kunnumakkara AB, Yadav VR, Tekmal RR, *et al*. Design of curcumin-loaded PLGA nanoparticles formulation with enhanced cellular uptake, and increased bioactivity *in vitro* and superior bioavailability *in vivo*. Biochem Pharmacol 2010; 79: 330–8.
27 Xie X, Tao Q, Zou Y, Zhang F, Guo M, Wang Y, *et al*. PLGA nanoparticles improve the oral bioavailability of curcumin in rats: characterizations and mechanisms. J Agric Food Chem 2011; 59: 9280–9.
28 Guerrouache M, Karakasyan C, Gaillet C, Canva M, Millot MC. Immobilization of a functionalized poly(ethylene glycol) onto beta-cyclodextrin-coated surfaces by formation of inclusion complexes: Application to the coupling of proteins. J Appl Polym Sci 2006; 100: 2362–70.
29 Chittasupho C, Xie SX, Baoum A, Yakovleva T, Siahaan TJ, Berkland CJ. ICAM-1 targeting of doxorubicin-loaded PLGA nanoparticles to lung epithelial cells. Eur J Pharm Sci 2009; 37: 141–50.
30 Shaikh J, Ankola DD, Beniwal V, Singh D, Kumar MN. Nanoparticle encapsulation improves oral bioavailability of curcumin by at least 9-fold when compared to curcumin administered with piperine as absorption enhancer. Eur J Pharm Sci 2009; 37: 223–30.
31 Wieder ME, Hone DC, Cook MJ, Handsley MM, Gavrilovic J, Russell DA. Intracellular photodynamic therapy with photosensitizer-nanoparticle conjugates: cancer therapy using a 'Trojan horse'. Photochem Photobiol Sci 2006; 5: 727–34.
32 Iangcharoen P, Punfa W, Yodkeeree S, Kasinrerk W, Ampasavate C, Anuchapreeda S, *et al*. Anti-P-glycoprotein conjugated nanoparticles for targeting drug delivery in cancer treatment. Arch Pharm Res 2011; 34: 1679–89.
33 Sa G, Das T. Anti cancer effects of curcumin: cycle of life and death. Cell Div 2008; 3: 14.
34 Anand P, Kunnumakkara AB, Newman RA, Aggarwal BB. Bioavailability of curcumin: problems and promises. Mol Pharm 2007; 4: 807–18.
35 Singh R, Lillard JW Jr. Nanoparticle-based targeted drug delivery. Exp Mol Pathol 2009; 86: 215–23.
36 Gou M, Men K, Shi H, Xiang M, Zhang J, Song J, *et al*. Curcumin-loaded biodegradable polymeric micelles for colon cancer therapy *in vitro* and *in vivo*. Nanoscale 2011; 3: 1558–67.
37 Matheny CJ, Lamb MW, Brouwer KR, Pollack GM. Pharmacokinetic and pharmacodynamic implications of P-glycoprotein modulation. Pharmacotherapy 2001; 21: 778–96.
38 Cirstoiu-Hapca A, Bossy-Nobs L, Buchegger F, Gurny R, Delie F. Differential tumor cell targeting of anti-HER2 (Herceptin) and anti-CD20 (Mabthera) coupled nanoparticles. Int J Pharm 2007; 331: 190–6.

Acta Pharmacologica Sinica (2012) 33: 832–838
 1671-4083/12 $32.00
www.nature.com/aps

Original Article

Pirarubicin inhibits multidrug-resistant osteosarcoma cell proliferation through induction of G_2/M phase cell cycle arrest

Shui-er ZHENG[1, #], Sang XIONG[1, #], Feng LIN[1], Guang-lei QIAO[1], Tao FENG[1], Zan SHEN[1], Da-liu MIN[1], Chun-ling ZHANG[2], Yang YAO[1, *]

[1]*Department of Oncology, Affiliated People's 6th Hospital, Shanghai Jiao Tong University, Shanghai 200233, China;* [2]*Department of Orthopaedics, Affiliated People's 6th Hospital, Shanghai Jiao Tong University, Shanghai 200233, China*

Aim: Pirarubicin (THP) is recently found to be effective in treating patients with advanced, relapsed or recurrent high-grade osteosarcoma. In this study, the effects of THP on the multidrug-resistant (MDR) osteosarcoma cells were assessed, and the underlying mechanisms for the disruption of cell cycle kinetics by THP were explored.
Methods: Human osteosarcoma cell line MG63 and human MDR osteosarcoma cell line MG63/DOX were tested. The cytotoxicity of drugs was examined using a cell proliferation assay with the Cell Counting Kit-8 (CCK-8). The distribution of cells across the cell cycle was determined with flow cytometry. The expression of cell cycle-regulated genes cyclin B1 and Cdc2 (CDK1), and the phosphorylated Cdc2 and Cdc25C was examined using Western blot analyses.
Results: MG63/DOX cells were highly resistant to doxorubicin (ADM) and gemcitabine (GEM), but were sensitive or lowly resistant to THP, methotrexate (MTX) and cisplatin (DDP). Treatment of MG63/DOX cells with THP (200–1000 ng/mL) inhibited the cell proliferation in time- and concentration-dependent manners. THP (50–500 ng/mL) induced MG63/DOX cell cycle arrest at the G_2/M phase in time- and concentration-dependent manners. Furthermore, the treatment of MG63/DOX cells with THP (200–1000 ng/mL) downregulated cyclin B1 expression, and decreased the phosphorylated Cdc2 at Thr^{161}. Conversely, the treatment increased the phosphorylated Cdc2 at Thr^{14}/Tyr^{15} and Cdc25C at Ser^{216}, which led to a decrease in Cdc2-cyclin B1 activity.
Conclusion: The cytotoxicity of THP to MG63/DOX cells may be in part due to its ability to arrest cell cycle progression at the G_2/M phase, which supports the use of THP for managing patients with MDR osteosarcoma.

Keywords: osteosarcoma; multidrug-resistant; pirarubicin; doxorubicin; gemcitabine; methotrexate; cisplatin; cell cycle; G_2/M arrest; cyclin B1; Cdc2; Cdc25C

Acta Pharmacologica Sinica (2012) 33: 832–838; doi: 10.1038/aps.2012.20; published online 14 May 2012

Introduction

Osteosarcoma is the most common malignant primary bone tumor in children, adolescents and young adults. Multiagent chemotherapy, commonly including doxorubicin (ADM), cisplatin (DDP) and high-dose methotrexate (MTX), has improved patient survival from 11% with surgical resection alone to 70% for localized disease. Unfortunately, the long-term survival for the remaining patients with recurrent disease is less than 20%[1–3]. Studies designed to identify novel active agents and implement strategies to overcome chemoresistance will likely be important for improving survival[1].

Recently, pirarubicin (THP), a novel anthracycline derivative of ADM, has been used clinically to treat tumors such as osteosarcoma, breast cancer, lymphoma and acute myeloid leukemia[4–7]. Moreover, THP has shown a greater antitumor activity[8–10] and lower cardiotoxicity[11] than ADM. This may be explained by the higher uptake of THP by tumor cells than ADM and its rapid distribution into the nucleus and subsequent incorporation into deoxyribonucleic acid (DNA)[12–14]. More recently, we found that through retrospective analysis, THP-based chemotherapy regimens were effective and safe as a salvage chemotherapy option for patients with lung metastases, refractory or recurrent high-grade osteosarcoma who previously received adjuvant chemotherapy with high dose-MTX–DDP–ADM–ifosfamide[15, 16]. However, the exact mechanisms by which THP exerts its antitumor effects are not understood. Although previous studies on THP

# These authors contributed equally to this paper.
* To whom correspondence should be addressed.
E-mail zse78106@yahoo.com.cn
Received 2011-11-21 Accepted2012-02-22

have revealed that induction of cell cycle arrest at the G_2 phase may contribute to its action in RPMI-8402 cells[17], the molecular basis of the cell cycle arrest induced by THP remains unclear.

Considering this previous research, we speculated that THP might be a potential chemotherapeutic agent that can circumvent drug resistance in patients with osteosarcoma. However, few studies clearly define the effects of THP on cytotoxicity and multidrug-resistant (MDR) osteosarcoma cells. In this study, we investigated the *in vitro* cytotoxic response of the MDR osteosarcoma cell line MG63/DOX treated with THP and explored the underlying mechanisms THP utilizes to disrupt cell cycle kinetics.

Materials and methods

Reagents

THP was obtained from Wan Le Pharma (Shenzhen, China); ADM and MTX, from Pfizer Pharma (New York, NY, USA); gemcitabine (GEM), from Lilly Pharma (Saint-Cloud, France); and DDP, from Hao Shen Pharma (Nanjing, China). Propidium iodide (PI) was purchased from Sigma Chemicals (St Louis, MO, USA). Cell Counting Kit-8 (CCK-8) was purchased from Dojindo Laboratories (Kumamoto, Japan).

Cell lines and cell culture

The human osteosarcoma parental cell line, MG63, was obtained from the Institute of Biochemistry and Cell Biology, Chinese Academy of Sciences (Shanghai, China). The human MDR osteosarcoma cell line MG63/DOX, which overexpresses P-glycoprotein (P-gp) and was selected in a step-wise manner by exposing drug-sensitive MG63 cells to increasing doses of ADM, was kindly provided by Dr Yoshio ODA (Graduate School of Medical Sciences, Kyushu University, Fukuoka, Japan)[18]. The cells were cultured in Dulbecco's modified Eagle's medium (DMEM; Hyclone, Logan, UT, USA) supplemented with 10% heat-inactivated fetal calf serum (FCS; Si Ji Qing, Hangzhou, China), 100 units/mL penicillin and 100 mg/mL streptomycin (Gibco, Grand Island, NY, USA) in a humidified atmosphere at 37 °C consisting of 5% CO_2. Drugs were initially dissolved in phosphate-buffered saline (PBS) and then serially diluted in culture medium to the desired drug treatment concentrations.

Drug sensitivity and cytotoxicity assays

The effects of THP, ADM, MTX, DDP, and GEM on the proliferation of MG63/DOX and MG63 cells were measured using the CCK-8 colorimetric assay. Briefly, the cells were seeded in a 96-well microtiter plate at 5×10^3 cells/well (100 μL). After 24 h of incubation with fresh medium, 10 μL of the various chemical dilutions at the indicated concentrations of each drug was added to the plates, and the cells were incubated for an additional 24, 48, and 72 h. At the end of drug treatment, 10 μL of CCK-8 was added to each well, and the cells were incubated for 4 h at 37 °C. Absorbance (A) was analyzed on a 96-well Opsys MR Microplate Reader (Thermo Labsystems, Beverly, MA, USA) at 450 nm. All experiments were tested in triplicate and repeated at least three times. The resistance factor (*R* factor) of multidrug-resistant cell line MG63/DOX for a particular drug is defined as the ratio of IC_{50} of MG63/DOX cell to IC_{50} of MG63 cell at 72 h (R<5×: low or no-resistance; R 5–15×: moderate-resistance; R>20×: high-resistance)[19].

Cell cycle analysis

MG63/DOX cells were treated with THP for 24, 48, and 72 h at concentrations of 50, 200, and 500 ng/mL. Control cells were treated with solvent alone for the durations indicated above. Cell cycle was analyzed as previously described[20]. The cells were trypsinized, washed twice with ice cold PBS, fixed in 70% ethanol and stained with propidium iodide (PI; 5 μg/mL PI in PBS containing 0.1% Triton X-100 and 0.2 mg/mL RNase A) in the dark for 30 min at 4 °C. Finally, the cells were analyzed for cell cycle perturbation using a FACSCalibur flow cytometer (Becton-Dickinson, San Diego, CA, USA). Cell fluorescence was measured in duplicate at each time point, and all experiments were performed in triplicate.

Western blot analysis

Cells treated with THP at the indicated concentrations were harvested following 72 h of incubation. Western blotting was performed as described previously[21]. Briefly, 30 μg of protein from whole-cell lysates was separated on a sodium dodecyl sulfate polyacrylamide gel electrophoresis (SDS-PAGE) apparatus and electrotransferred onto polyvinylidene fluoride (PVDF) membranes (Millipore, Bedford, MA, USA). After blocking with 5% (*w*/*v*), non-fat dry milk in Tris-buffered saline for 1 h at room temperature, membranes were incubated overnight at 4 °C with the previously described pretreated antibody diluent according to the one-step Western kit manufacturer's instructions. Primary antibodies were incubated with a horseradish peroxidase antibody for 5 min at room temperature and then diluted (1:1000). The protein bands were visualized using a chemiluminescence imaging system (Bio-Rad, Hercules, CA, USA). All blots are representative of three independent experiments. Primary antibodies assayed were Cyclin B1, Cdc2, p-Cdc2 (Thr^{14}), p-Cdc2 (Tyr^{15}), and p-Cdc2 (Thr^{161}) antibodies (Cell Signaling Technology, Boston, MA, USA); Cdc25C and p-Cdc25C (Ser^{216}) antibodies (Santa Cruz Biotechnology, Inc, Santa Cruz, CA, USA); and β-actin antibody (CoWin Biotech Co, Beijing, China).

Statistical analysis

Data are presented as the mean±SD. The Student's *t*-test was used to analyze the difference between the mean values of the treatment and the control groups. Differences with a *P* value of less than 0.05 were considered statistically significant.

Results

Drug sensitivity

We investigated the effects of THP and chemotherapeutic agents commonly used for osteosarcoma treatment, including ADM, MTX, DDP, and GEM, on the proliferation of MG63/DOX MDR human osteosarcoma cells and their parental

MG63 cells using the CCK-8 colorimetric assay. As shown in Table 1, MG63/DOX cells exhibited high levels of resistance to ADM (*R* factor: 121.6) and GEM (*R* factor: 108.3) but little to no resistance to THP (*R* factor: 3.73), MTX (*R* factor: 4.16) and DDP (*R* factor: 0.91). These results indicate that MG63/DOX cells reveal have a classic MDR phenotype, which has been previously described[18]. Surprisingly, THP had similar inhibitory effects on cell proliferation in both resistant and parental osteosarcoma cells, indicating that MDR osteosarcoma cells are still sensitive to THP.

Table 1. Drug sensitivity of MG63 and MG63/DOX to the commonly used chemotherapeutic agents for osteosarcoma treatment. Mean±SD. *n*=3. [a]*P*>0.05, [b]*P*<0.05, [c]*P*<0.01 compared with MG63 cell group.

Drug	IC_{50} (μg/mL)		*R* factor
	MG63	MG63/DOX	
THP	0.11±0.05	0.41±0.024[b]	3.73
ADM	0.15±0.09	18.24±7.72[c]	121.6
MTX	1.22±0.75	3.86±0.81[b]	4.16
DDP	3.83±0.52	3.48±0.24[a]	0.91
GEM	2.28±0.87	247.0±8.2[c]	108.3

The resistance factor (*R* factor) of multidrug-resistant cell line MG63/DOX for a particular drug is defined as the ratio of IC_{50} of MG63/DOX cell to IC_{50} of MG63 cell at 72 h. *R* factor<5: low or no-resistance; *R* factor 5–15: moderate-resistance; *R* factor >20: high-resistance[19].

THP inhibited proliferation of MG63/DOX cells

The cytotoxic effects of THP on MG63/DOX cells were further measured with the CCK-8 colorimetric assay after the cells were exposed to various concentrations of THP for multiple durations. Cell growth was inhibited in a concentration- and time-dependent manner (Figure 1 and Table 2).

Table 2. Effect of THP on cell growth of MG63/DOX cells. [a]*P*>0.05, [c]*P*<0.01 compared with control.

THP (ng/mL)	Time (h)			
	0	24	48	72
0	0.128±0.031	0.203±0.024	0.329±0.027	0.633±0.056
200	0.100±0.010	0.195±0.013[a]	0.269±0.028[c]	0.412±0.013[c]
500	0.123±0.023	0.186±0.007[a]	0.218±0.012[c]	0.247±0.019[c]
1000	0.090±0.011	0.148±0.014[c]	0.139±0.010[c]	0.096±0.021[c]

THP induced MG63/DOX cells cycle arrest at the G_2/M phase

To examine the mechanism of inhibition of cell growth by THP, cell cycle perturbation was evaluated by flow cytometry after the MG63/DOX cells were exposed to THP at various concentrations for 24, 48, or 72 h. As shown in Figure 2 and Table 3, the fraction of cells in the G_2/M phase increased with the concentration of THP and the duration of treatment. A concurrent reduction in the proportion of cells in G_0/G_1 and S phase was observed. These results demonstrate that THP induced a cycle arrest in MG63/DOX cells at G_2/M phase in a time- and concentration-dependent manner.

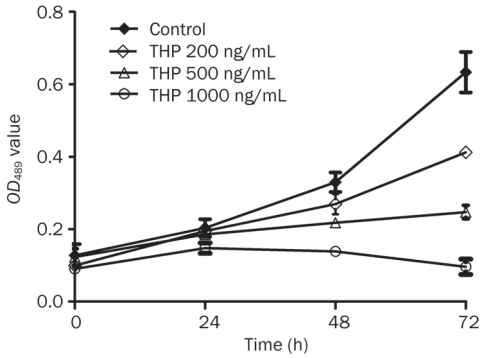

Figure 1. Effect of THP on cell proliferation of MG63/DOX cells. MG63/DOX cells were treated with THP at the indicated concentrations (200, 500, and 1000 ng/mL) for 24–72 h. Cell proliferation was assessed by CCK-8 assay, and cell proliferation values were expressed relative to those of the untreated cells (100% control value). THP inhibited the proliferation of MG63/DOX cells in a time and concentration-dependent manner (reference Table 2). Mean±SD. *n*=3.

Table 3. The effect of THP on cell cycle distribution of MG63/DOX cells. Mean±SD. *n*=3. [b]*P*<0.05, [c]*P*<0.01 compared with control.

Action time	THP (ng/mL)	G_0/G_1 phase (%)	S phase (%)	G_2/M phase (%)
24 h				
	0	16.5±3.54	30.8±0.28	52.7±3.25
	50	17.4±2.56	29.5±0.85	53.1±1.69
	200	5.61±4.51	32.25±3.46	62.1±1.13[b]
	500	12.78±11.01	9.6±13.58	77.65±2.47[c]
48 h				
	0	15.8±2.76	29.7±1.33	52.1±2.14
	50	20.9±1.015	23.47±2.8	55.63±1.79
	200	11±0.78	15.23±3.65	73.77±3.56[c]
	500	6.68±1.98	6.45±1.52	86.88±2.27[c]
72 h				
	0	18.2±1.84	28.3±2.28	53.6±3.76
	50	20.6±4.01	15.66±1.52	63.74±3.35[b]
	200	13.03±2.00	6.53±2.86	80.43±2.6[c]
	500	2.72±0.77	3.07±2.7	94.2±3.41[c]

THP reduced cyclin B1 expression and Cdc2 and Cdc25C activity

To elucidate the molecular basis for THP-induced cell cycle arrest at the G_2/M phase, Cyclin B1, and Cdc2 protein expression was assayed by Western blotting. As shown in Figure 3, the results indicate that protein levels of cyclin B1 decreased after THP treatment in a time- and concentration-dependent manner but that the total protein levels of Cdc2 did not

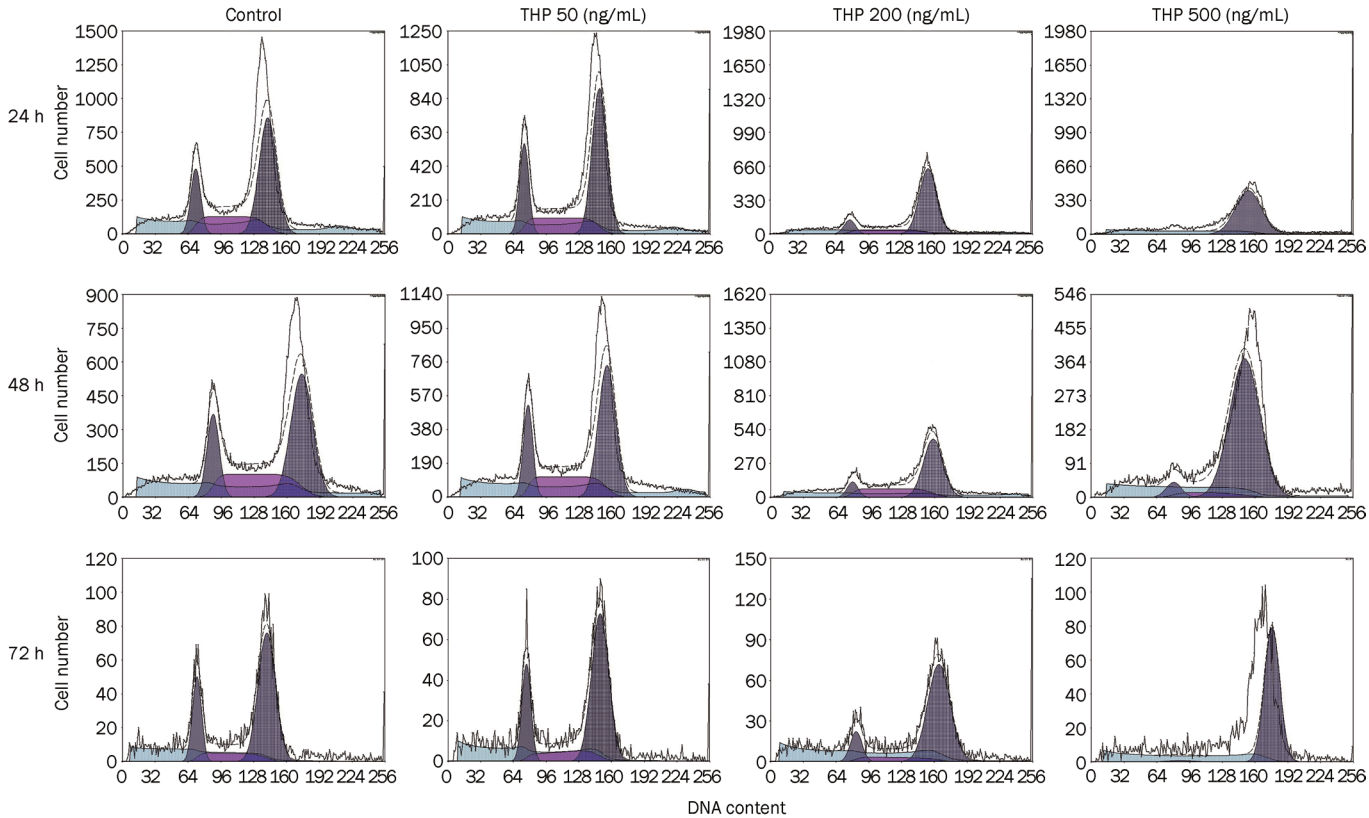

Figure 2. Effect of THP on cell cycle distribution of MG63/DOX cells. MG63/DOX cells were treated with the indicated concentrations (50, 200, and 500 ng/mL) of THP and harvested at 24, 48, or 72 h. DNA content was analyzed by flow cytometry using PI staining. THP induced MG63/DOX cells cycle arrest at the G_2/M phase time and dose-dependently (reference Table 3). A representative profile is shown for each treatment.

change. The Cdc2-cyclin B1 complex was retained in an inactive state by the negative phosphorylation of the residues Thr^{14} and Tyr^{15} on Cdc2 phosphorylated by kinase Wee1 and Myt1, and Cdc2-cyclin B1 activity is increased by the phosphorylation of Cdc2 at Thr^{161}. Therefore, we examined Cdc2 phosphorylation by Western blotting and found that while the protein expression level of Cdc2 was not altered, the phosphorylation of Cdc2 at Thr^{14}/Tyr^{15} [p-Cdc2 (Thr^{14}/Tyr^{15})] was increased and the phosphorylation of Cdc2 at Thr-161 [p-Cdc2 (Thr^{161})] was decreased after THP treatment in a time- and concentration-dependent manner. These data suggest that reduced Cdc2-cyclinB1 activity by THP may account for the G_2/M arrest in our model.

Cdc25C activates Cdc2 by removing inhibitory phosphate groups on Thr^{14} and Tyr^{15}. Because Cdc2 phosphorylation at Thr^{14}/Tyr^{15} was enhanced by THP, we further investigated the effect of THP on Cdc25C expression and phosphorylation at Ser^{216} by Western blotting. We found that the total protein expression levels of Cdc25C were not altered but that the phosphorylation of Cdc25C at Ser^{216} [p-Cdc25C (Ser^{216})] was increased after THP treatment in a time- and concentration-dependent manner (Figure 3). These results suggest that decreased dephosphorylation by Cdc25C is partly responsible for Cdc2 inactivation.

Discussion

Currently, one of the greatest obstacles to improving the survival of patients with osteosarcoma is acquired clinical resistance to chemotherapeutic agents, primarily to the three most widely used agents in the treatment of osteosarcoma — ADM, MTX, and DDP[1, 22, 23]. Cancer cells can utilize a number of different mechanisms to become resistant to one or more chemotherapeutic drugs. Depending on the drug and cellular context, factors such as drug inactivation, drug target mutation, drug target upregulation and downregulation, decreased drug uptake, increased drug elimination and DNA damage repair have all been shown to contribute to both intrinsic and acquired resistant to chemotherapy[1]. ADM is one of the most effective agents for osteosarcoma treatment[1, 22, 23]. Although resistance to ADM in osteosarcoma is likely to be multifactorial, P-gp is thought to be the main resistance mechanism against this agent[1, 24]. Additionally, some retrospective studies[25, 26] have revealed that the overexpression of P-gp may be associated with poor prognosis. THP, a semisynthetic anthracycline glycoside, is a newer generation anthracycline anticancer agent that is reported to have a lower cardiotoxicity than ADM[11]. Changes in structure allow THP to be taken up by tumor cells approximately 170 times faster than ADM and increase the rates at which it distributes into the nucleus and

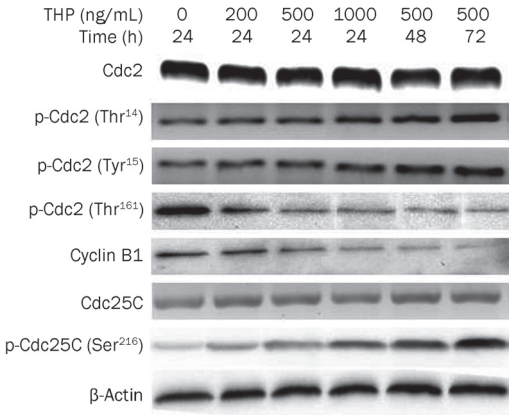

Figure 3. Effects of THP on the protein levels and activity of cell cycle regulatory proteins in MG63/DOX cells. MG63/DOX cells were treated THP at the indicated concentrations (200, 500, and 1000 ng/mL). Cellular proteins were extracted at the indicated time (24, 48, or 72 h) following drug exposure. A total of 30 μg cell extract protein isolated from the drug-treated and untreated MG63/DOX cells was subjected to Western-blotting with antibodies against cyclin B1, Cdc2, p-Cdc2 (Thr^{14}/Tyr^{15}), p-Cdc2 (Thr^{161}), Cdc25C, and p-Cdc25C (Ser^{216}). β-actin was used as a loading control. Densitometry assay showed that the protein levels of cyclin B1 was decreased after THP treatment in time- and concentration-dependantly and the total protein level of Cdc2 was not changed, but the phosphorylation of Cdc2 at Thr14/Tyr15 [p-Cdc2 (Thr^{14}/Tyr^{15})] were increased and the phosphorylation of Cdc2 at Thr^{161} [p-Cdc2 (Thr^{161})] was decreased after THP treatment in a time- and concentration-dependant manner and the total protein level of Cdc25C were not changed, but the phosphorylation of Cdc25C at Ser^{216} [p-Cdc25C (Ser^{216})] was increased after THP treatment in a time and concentration-dependant manner (data not shown). Western blot data presented are representative of those obtained from three separate experiments.

intercalates into DNA[12–14].

On the basis of these considerations, we tested THP for cytotoxicity against MDR osteosarcoma MG63/DOX cells *in vitro*. We found that THP has a marked inhibitory effect on cell proliferation in both resistant and sensitive osteosarcoma cells. These results suggest that THP partially overcomes the resistance caused by overexpression of P-gp and that THP may play an important role in treatment of patients with refractory or recurrent high-grade osteosarcoma. In fact, THP has also shown favorable activity in various types of cancer cells, including P-gp overexpressing breast cancer[27], ADM-resistant lymphoblastoma[28], MG-63 cells[29] and bladder cancers[30] *in vitro*, and has substantial clinical activity against various tumors without severe side effects[4–7,15,16]. Despite the ability of THP to overcome MDR in clinical studies[6, 16, 17], very little is known about THP-induced cytotoxicity and the underlying mechanisms of pirarubicin on MDR osteosarcoma cells. To our knowledge, this is the first study to evaluate the cytotoxicity of THP against human drug-resistant osteosarcoma cells.

In addition, we demonstrated that the effect of THP in resistant MG63/DOX cells is associated with cell cycle arrest at the G_2/M phase in a time- and concentration-dependent manner. Similarly, Takamoto *et al*[17] reported that THP exerted its growth-inhibitory effect by blocking RPMI-8402 cells irreversibly at G_2 and that the G_2 phase accumulation was a cytocidal effect of THP. The eukaryotic cell cycle is strictly regulated by a class of cyclins and cyclindependent kinases (CDKs)[31]. The progression from G_2 to mitosis is controlled by the mitosis-promoting factor, which comprises a complex of Cdc2 (CDK1) and cyclin B[32–35]. During G_2/M transition, CDK1 activation requires an association with cyclin B1 and phosphorylation at Thr^{161} by CDK-activating kinase (CAK), whereas the CDK1/cyclin B complex is kept inactive by phosphorylation on Thr^{14} or Tyr^{15} of CDK1 by kinase Wee1 and Myt1[36]. We found that THP significantly downregulated cyclin B1, p-Cdc2 (Thr^{161}) and upregulated p-Cdc2 (Thr^{14}/Tyr^{15}). Decreased cyclin B1 levels and Cdc2 phosphorylation at Thr^{161} and increased Cdc2 phosphorylation at Thr^{14}/Tyr^{15} may contribute to the THP-induced arrest of MG63/DOX cells at the G_2/M phase and the subsequent blocking of cell cycle progression. Finally, we demonstrated that THP enhanced Cdc25C phosphorylation at the Ser-216 residue in our cell cultured model. The activity of Cdc25C, which is essential for progression into mitosis, is regulated by changes in protein levels, subcellular localization and the phosphorylation state[37]. It is proposed that the checkpoint kinase, Chk1, regulates the interactions between human Cdc25C and 14-3-3 proteins by phosphorylating Cdc25C on serine 216. 14-3-3 proteins, in turn, function to keep Cdc25C out of the nucleus[38]. Therefore, the effect of THP on G_2/M phase arrest in MG63/DOX cells may be partly mediated by Chk1 activation. However, future studies are required to determine whether and how THP affects Chk1 in our model system.

In conclusion, we have demonstrated an encouraging efficacy of THP against human MDR osteosarcoma cells *in vitro*. We also have found, for the first time, that THP could arrest the cell cycle at the G_2/M phase, which was partially associated with the downregulation of cyclin B1, p-Cdc2 (Thr^{161}), and the upregulation of p-Cdc2 (Thr^{14}), p-Cdc2 (Tyr^{15}), and p-Cdc25C (Ser^{216}). The alterations of cell cycle kinetics might contribute to a better understanding of the cytotoxicity induced by THP. These findings also provide a theoretical basis for its potential use in the management of patients with MDR osteosarcoma and suggest that further *in vivo* and prospective clinical studies are warranted.

Acknowledgements

We thank Dr Yoshio ODA for kindly providing the MG63/DOX cell line. This work was supported by grants from National Natural Science Foundation of China (Grant No 81001192 and 81172105) and Shanghai Health Bureau (Grant No 2011171).

Author contribution

Dr Yang YAO designed the research; Dr Shui-er ZHENG designed the research, wrote the paper, analyzed the data and performed the research; Dr Sang XIONG performed the research, analyzed the data, wrote the paper and designed the research; Dr Feng LIN designed the research; Dr Guang-

lei QIAO performed the research and analyzed the data; Dr Tao FENG performed the research; Dr Zan SHEN designed the research; Dr Da-liu MIN performed the research; and Dr Chun-ling ZHANG contributed new reagents.

References

1 Chou AJ, Gorlick R. Chemotherapy resistance in osteosarcoma current challenges and future directions. Expert Rev Anticancer Ther 2006; 6: 1075–85.
2 Hawkins DS, Arndt CA. Pattern of disease recurrence and prognostic factors in patients with osteosarcoma treated with contemporary chemotherapy. Cancer 2003; 98: 2447–56.
3 Chou AJ, Merola PR, Wexler LH, Gorlick RG, Vyas YM, Healey JH, *et al*. Treatment of osteosarcoma at first recurrence after contemporary therapy: the memorial sloan-kettering cancer center experience. Cancer 2005; 104: 2214–21.
4 Shinozaki T, Watanabe H, Yanagawa T, Shirakura K, Takagishi K. Pirarubicin-based versus doxorubicin-based osteosarcoma chemotherapy. Ann Pharmacother 2002; 36: 996–9.
5 Li JJ, Di GH, Tang LC, Yu KD, Hu Z, Liu GY, *et al*. Adjuvant therapy of breast cancer with pirarubicin versus epirubicin in combination with cyclophosphamide and 5-fluorouracil. Breast J 2011; 17: 657–60.
6 Kasahara S, Hara T, Tsurumi H, Goto N, Kitagawa J, Kanemura N, *et al*. Phase II study of the tetrahydropyranyl adriamycin-cyclophosphamide, vincristine, and prednisolone regimen combined with rituximab as first-line treatment for elderly patients with diffuse large B-cell lymphoma. Leuk Lymphoma 2011; 52: 629–34.
7 Kudo K, Kojima S, Tabuchi K, Yabe H, Tawa A, Imaizumi M, *et al*. Prospective study of a pirarubicin, intermediate-dose cytarabine, and etoposide regimen in children with down syndrome and acute myeloid leukemia: the Japanese Childhood AML Cooperative Study Group. J Clin Oncol 2007; 25: 5442–7.
8 Nagai K, Nagasawa K, Sadzuka Y, Tsujimoto M, Takara K, Ohnishi N, *et al*. Relationships between the *in vitro* cytotoxicity and transport characteristics of pirarubicin and doxorubicin in M5076 ovarian sarcoma cells, and comparison with those in Ehrlich ascites carcinoma cells. Cancer Chemother Pharmacol 2002; 49: 244–50.
9 Umezawa H, Takahashi Y, Kinoshita M, Naganawa H, Masuda T, Ishizuka M, *et al*. Tetrahydropyranyl derivatives of daunomycin and adriamycin. J Antibiot (Tokyo) 1979; 32: 1082–4.
10 Tsuruo T, Iida H, Tsukagoshi S, Sakurai Y. 4′-O-tetrahydropyranyladriamycin as a potential new antitumor agent. Cancer Res 1982; 42: 1462–7.
11 Dantchev D, Paintrand M, Hayat M, Bourut C, Mathé G. Low heart and skin toxicity of a tetrahydropyranyl derivate of Adriamycin (THP-ADM) as observed by electron and light microscopy. J Antibiot (Tokyo) 1979; 32: 1085–6.
12 Zou HY, Wu HL, Zhang Y, Li SF, Nie JF, Fu HY, *et al*. Studying the interaction of pirarubicin with DNA and determining pirarubicin in human urine samples: combining excitation — emission fluorescence matrices with second-order calibration methods. J Fluoresc 2009; 19: 955–66.
13 Sridhar KS, Hussein AM, Benedetto P, Ardalan B, Savaraj N, Richman SP. Phase II trial of 4′-0-tetrahydropyranyladriamycin (pirarubicin) in head and neck carcinoma. Cancer 1992; 70: 1591–7.
14 Tsurumi H, Hara T, Goto N, Kanemura N, Kasahara S, Sawada M, *et al*. A phase II study of a THP-COP regimen for the treatment of elderly patients aged 70 years or older with diffuse large B-cell lymphoma. Hematol Oncol 2007; 2: 107–14.
15 Zhao H, Yao Y, Wang Z, Lin F, Sun Y, Yao Y, *et al*. Therapeutic effect of pirarubicin-based chemotherapy for osteosarcoma patients with lung metastasis. J Chemother 2010; 22: 119–24.
16 Qi WX, He AN, Tang LN, Shen Z, Yao Y. Evaluation of pirarubicin-cisplatin chemotherapy in the treatment for refractory and recurrent high-grade osteosarcoma: experience of a single institute. Med Oncol 2011. doi: 10.1007/s12032-011-0021-y.
17 Takamoto S, Ota K. Flow cytometric analysis of the effect of THP-adriamycin on the cell cycle traverse of RPMI-8402 cells — comparison with adriamycin. Gan To Kagaku Ryoho 1986; 13: 1868–75.
18 Oda Y, Matsumoto Y, Harimaya K, Iwamoto Y, Tsuneyoshi M. Establishment of new multidrug-resistant human osteosarcoma cell lines. Oncol Rep 2000; 7: 859–66.
19 Snow K, Judd W. Characterisation of adriamycin- and amsacrine-resistant human leukaemic T cell lines. Br J Cancer 1991; 63: 17–28.
20 Guo JM, Xiao BX, Liu Q, Zhang S, Liu DH, Gong ZH. Anticancer effect of aloe-emodin on cervical cancer cells involves G_2/M arrest and induction of differentiation. Acta Pharmacol Sin 2007; 28: 1991–5.
21 Zheng SE, Yao Y, Dong Y, Lin F, Zhao H, Shen Z, *et al*. Down-regulation of ribosomal protein L7A in human osteosarcoma. J Cancer Res Clin Oncol 2009; 135: 1025–31.
22 Bacci G, Briccoli A, Ferrari S, Longhi A, Mercuri M, Capanna R, *et al*. Neoadjuvant chemotherapy for osteosarcoma of the extremity: long-term results of the Rizzoli's 4th protocol. Eur J Cancer 2001; 37: 2030–9.
23 Chi SN, Conklin LS, Qin J, Meyers PA, Huvos AG, Healey JH, *et al*. The patterns of relapse in osteosarcoma: the Memorial Sloan-Kettering experience. Pediatr Blood Cancer 2004; 42: 46–51.
24 Cagliero E, Ferracini R, Morello E, Scotlandi K, Manara MC, Buracco P, *et al*. Reversal of multidrug-resistance using Valspodar (PSC 833) and doxorubicin in osteosarcoma. Oncol Rep 2004; 12: 1023–31.
25 Serra M, Scotlandi K, Reverter-Branchat G, Ferrari S, Manara MC, Benini S, *et al*. Value of P-glycoprotein and clinicopathologic factors as the basis for new treatment strategies in high-grade osteosarcoma of the extremities. J Clin Oncol 2003; 21: 536–42.
26 Hornicek FJ, Gebhardt MC, Wolfe MW, Kharrazi FD, Takeshita H, Parekh SG, *et al*. P-glycoprotein levels predict poor outcome in patients with osteosarcoma. Clin Orthop 2000; 373: 11–7.
27 Kubota T, Furukawa T, Tanino H, Oura S, Murata H, Yuasa S, *et al*. Pirarubicin might partly circumvent the P-glycoprotein-mediated drug resistance of human breast cancer tissues. Anticancer Res 1998; 18: 967–72.
28 Kunimoto S, Miura K, Umezawa K. Cellular uptake and efflux and cytostatic activity of 4′-O-tetrahydropyranyladriamycin in adriamycin-sensitive and resistant tumor cell lines. J Antibiot (Tokyo) 1984; 37: 1697–702.
29 Liu SY, Song SX, Lin L, Liu X. Molecular mechanism of cell apoptosis by paclitaxel and pirarubicin in a human osteosarcoma cell line. Chemotherapy 2010; 56: 101–7.
30 Maruyama T, Higuchi Y, Suzuki T, Qiu J, Yamamoto S, Shima H. Double short-time exposure to pirarubicin produces higher cytotoxicity against T24 bladder cancer cells. J Infect Chemother 2011; 17: 11–6.
31 Suryadinata R, Sadowski M, Sarcevic B. Control of cell cycle progression by phosphorylation of cyclin-dependent kinase (CDK) substrates. Biosci Rep 2010; 30: 243–55.
32 Yen CY, Chiu CC, Chang FR, Chen JY, Hwang CC, Hseu YC, *et al*. 4beta-Hydroxywithanolide E from Physalis peruviana (golden berry) inhibits growth of human lung cancer cells through DNA damage, apoptosis and G_2/M arrest. BMC Cancer 2010; 10: 46.
33 Stan SD, Zeng Y, Singh SV. Ayurvedic medicine constituent withaferin a causes G_2 and M phase cell cycle arrest in human breast cancer cells. Nutr Cancer 2008; 60: 51–60.

34 Dvory-Sobol H, Cohen-Noyman E, Kazanov D, Figer A, Birkenfeld S, Madar-Shapiro L, *et al*. Celecoxib leads to G_2/M arrest by induction of p21 and down-regulation of cyclin B1 expression in a p53-independent manner. Eur J Cancer 2006; 42: 422–6.

35 Doree M, Hunt T. From Cdc2 to Cdk1: when did the cell cycle kinase join its cyclin partner? J Cell Sci 2002; 115: 2461–4.

36 Taylor WR, Stark GR. Regulation of the G_2/M transition by p53. Oncogene 2001; 20: 1803–15.

37 Lopez-Girona A, Furnari B, Mondesert O, Russell P. Nuclear localization of Cdc25 is regulated by DNA damage and a 14-3-3 protein. Nature 1999; 397: 172–5.

38 Sanchez Y, Wong C, Thoma RS, Richman R, Wu Z, Piwnica-Worms H, *et al*. Conservation of the Chk1 checkpoint pathway in mammals: linkage of DNA damage to Cdk regulation through Cdc25. Science 1997; 277: 1497–501.

Acta Pharmacologica Sinica (2012) 33: 839–844
 1671-4083/12 $32.00
www.nature.com/aps

Original Article

Preclinical assessment of the distribution, metabolism, and excretion of *S*-propargyl-cysteine, a novel H_2S donor, in Sprague-Dawley rats

Yuan-ting ZHENG[1], Jian-hua ZHU[2], Guo MA[1], Qing ZHU[3], Ping YANG[4], Bo TAN[4], Jin-lian ZHANG[1], Hai-xing SHEN[2], Jia-lin XU[1], Yi-zhun ZHU[3], Wei-min CAI[1, *]

[1]Department of Clinical Pharmacy, School of Pharmacy, Fudan University, Shanghai 201203, China; [2]Department of Radiopharmacy, School of Pharmacy, Fudan University, Shanghai 201203, China; [3]Department of Pharmacology, School of Pharmacy and Institute of Biomedical Sciences, Fudan University, Shanghai 201203, China; [4]Analytical and Testing Center, School of Pharmacy, Fudan University, Shanghai 201203, China

Aim: To study the distribution, metabolism and excretion of *S*-propargyl-cysteine (SPRC), a novel hydrogen sulfide (H_2S) donor, after oral administration in rats.
Methods: Adult Sprague-Dawley rats were used. The tissue distribution of [^{35}S] SPRC-derived radioactivity was measured using a liquid scintillation counter. The plasma protein binding of SPRC was examined using 96-well equilibrium dialysis. The excretion of SPRC in urine, bile and feces was analyzed using the LC-MS/MS method. The major metabolites in rat biomatrices were identified using MRM information-dependent, acquisition-enhanced product ion (MRM-IDA-EPI) scans on API 4000QTrap system.
Results: After oral administration of [^{35}S] SPRC at a dose of 75 mg/kg, [^{35}S] SPRC-derived radioactivity displayed broad biological distribution in various tissues of rats, including its target organs (heart and brain) with the highest in kidney. On the other hand, the binding of SPRC to human, rat and dog plasma protein was low. Only 2.18%±0.61% and 0.77%±0.61% of the total SPRC administered was excreted unchanged in the bile and urine. However, neither intact SPRC nor its metabolites were detected in rat feces. The major metabolic pathway *in vivo* (rat bile, urine, and plasma) was *N*-acetylation.
Conclusion: The preliminary results suggest that SPRC possesses acceptable pharmacokinetic properties in rats.

Keywords: hydrogen sulfide (H_2S); *S*-propargyl-cysteine; pharmacokinetics; distribution; metabolism; excretion; disposition

Acta Pharmacologica Sinica (2012) 33: 839–844; doi: 10.1038/aps.2012.15; published online 30 Apr 2012

Introduction

The physiological importance of hydrogen sulfide (H_2S) was first discovered in the mid-1990s. H_2S is now considered to be the third novel gasotransmitter, discovered after nitric oxide and carbon monoxide. Like other gasotransmitters, H_2S is a gaseous small molecule that is freely permeable across membranes. Moreover, the endogenous gas is important in the regulation of vascular tone, myocardial contractility, neurotransmission, insulin secretion, inflammation, longevity, and nociception[1-4]. The garlic-derived organosulfur compounds, known as H_2S donors, have generated interest in the biomedical field. *S*-allylcysteine (SAC), one of the major compounds in aged garlic extract, has been demonstrated to have multiple biological activities, including antibacterial, antifungal, anticancer, antihepatopathic, cardioprotective, and neurotrophic properties[5–8].

S-propargyl-cysteine (SPRC, Figure 1) is an analog of SAC and a novel H_2S donor. Recently, the pharmacological activities of SPRC have been extensively studied. Wang *et al* demonstrated the cardioprotective effects of SPRC using an *in vivo* acute myocardial infarction model in rats and an *in vitro* hypoxic cardiomyocyte model[9]. Further studies revealed that the cardioprotective effect during a myocardial infarction resulted from the modulation of the endogenous levels of H_2S. The release of H_2S might activate signaling cascades

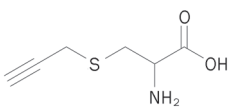

Figure 1. The chemical structure of SPRC.

* To whom correspondence should be addressed.
E-mail weimincai@fudan.edu.cn
Received 2011-12-05 Accepted 2012-01-27

associated with the prevention of oxidative stress[10]. SPRC also attenuated LPS-induced H9c2 cell activation, which would be beneficial for either the prevention or the treatment of cardiovascular inflammatory disease[11]. Furthermore, the protective effects of SPRC in neuroinflammation *in vitro* and *in vivo* indicate therapeutic potential for neurodegenerative diseases, including Alzheimer's disease, Parkinson's disease, ischemic stroke, multiple sclerosis, and amyotrophic lateral sclerosis[12, 13]. Ma *et al* reported that SPRC exhibited anticancer activities in SGC7901 gastric cancer cells and confirmed the *in vivo* antineoplastic effect of SPRC in a nude mice xenograft model[14]. These studies show that SPRC is emerging as a promising H_2S-based therapeutic agent and candidate for future pharmaceutical development.

Preclinical pharmacokinetic characterization of a new drug candidate is an integral part of the drug discovery and development process. Such studies may also provide an in-depth understanding of the drug's mechanism of action. Unfavorable pharmacokinetic properties may lead to drug toxicity, potentially resulting in termination of the program or re-optimization of the chemical structure. Previous studies showed that SPRC was rapidly absorbed and bioavailable in rats[15]. Further studies characterizing the disposition of SPRC *in vivo* are needed to clarify its pharmacokinetic properties. The aim of this study is to investigate the distribution, metabolism, and excretion of SPRC in rats.

Materials and methods

Chemicals and reagents

SPRC was synthesized by reacting *L*-cysteine with propargyl bromide. The product was purified by recrystallization from an ethanol-water solution. The final product was verified by ^{1}H nuclear magnetic resonance spectroscopy. The purity was 99.7%, as measured by high-performance liquid chromatography.

[^{35}S] cysteine (>99% radiochemical purity), Ultima-Gold scintillation fluid, and a Soluene-350 tissue solubilizer were all purchased from Perkin-Elmer Life and Analytical Sciences (Boston, MA). [^{35}S] SPRC (>99% purity) was synthesized by reacting [^{35}S] cysteine with propargyl bromide as described above.

Blank Sprague-Dawley rat plasma was obtained from healthy, drug-free rats. Blank dog plasma was purchased from the Shanghai ChemPartner Co LTD (Shanghai, China). Blank human plasma was kindly provided by the Ruijin Hospital (Shanghai, China). Dialysis membranes used for the experiments had a 12 to 14 kDa molecular mass cutoff and were purchased from HTDialysis, LLC (Gales Ferry, CT, USA). HPLC-grade acetonitrile and methanol were purchased from Fisher Scientific (Pittsburgh, PA, USA). Other reagents used in this study had the highest purity commercially available.

Animal experiments

The experiments were performed in accordance with the Guidelines for Animal Experimentation of Fudan University (Shanghai, China). The protocols used in this study were approved by the Animal Ethics Committee of Fudan University (Shanghai, China). Adult Sprague-Dawley rats (body weight of 200±20 g, half males and half females) were purchased from Sino-British Sipper/BK Lab Animal Ltd (Shanghai, China; animal certificate number: SCXK hu (Shanghai) 2008-0016). The animals were maintained on a 12-h light/dark cycle under controlled conditions (temperature: 20±2 °C, relative humidity: 50%±20%). The rats had free access to food and water throughout the study unless specifically indicated.

In the biliary excretion study, rats were implanted with a cannula that was inserted into the bile duct under anesthesia with diethyl ether, and then allowed to recover before drug administration. Blank bile was collected before administration. Cumulative bile samples were collected during specific time intervals from 0–1, 1–2, 2–3, 3–4, 4–5, 5–6, 6–8, 8–12, and 12–24 h after drug administration.

Animals were housed in metabolic cages to collect urine and feces. Urine and feces were collected separately before dosing and from 0–6, 6–12, 12–24, 24–36, 36–48, and 48–72 h. The feces samples were homogenized with water. These samples were stored at -70°C until they were analyzed.

Analytical method for SPRC

The feces homogenate, bile, or urine samples (20 μL) was precipitated with acetonitrile containing 0.44 μg/mL internal standard. After centrifugation at 12000×*g* for 5 min, 5 μL of the supernatant was used for LC-MS/MS analysis.

SPRC concentrations were quantitated using the LC-MS/MS method. The analytical method has been previously validated and reported for determining the concentration of SPRC in rat plasma[15].

Tissue distribution study of [^{35}S] SPRC-derived radioactivity in rats

The tissue distribution of [^{35}S] SPRC-derived radioactivity was evaluated in Sprague-Dawley rats after an oral administration of 75 mg/kg [^{35}S] SPRC solution (25 μCi/mL, 10 g/L). Animals were euthanized at 0.5 h, 1.5 h, and 6 h after drug administration. Following euthanasia, the rats were exsanguinated, and then plasma and tissues (heart, liver, spleen, lung, kidney, brain, stomach, intestine, and muscle) were collected and homogenized (0.25 g/mL).

Aliquots (400 μL) of the tissue samples were digested in 1 mL of Soluene-350 tissue solubilizer for 3 h at 60 °C. Ultima Gold scintillation fluid (10 mL) was then added to each sample. For plasma samples, 100 μL of plasma was directly mixed with 10 mL of scintillation fluid. All the sample preparations were stored in the dark for 24 h before analysis. All of the radioactivity measurements were made using a Tricarb 2910TR liquid scintillation analyzer (Perkin-Elmer, Wellesley, MA, USA). The tissue radioactivity levels were expressed as a percent injected dose per gram of tissue (%ID/g).

Measurement of the plasma protein binding of SPRC using 96-well equilibrium dialysis

Protein binding of SPRC to human, rat, and dog plasma was

measured using a 96-well microequilibrium Teflon dialysis device (HTDialysis, LLC, Gales Ferry, CT). Dialysis membranes were soaked in distilled water for 20 min and then soaked in 30% (*v*/*v*) ethanol for 15 min. Just prior to use, the membrane was rinsed three times in deionized water and then rinsed once with isotonic sodium phosphate buffer. After assembling the dialysis plates, 110 μL of blank buffer and spiked plasma samples (2, 10, and 50 μg/mL) were added to the receiver and donor side of the equilibrium dialysis block, respectively. The dialysis block was covered with a plastic lid and placed in a shaker (37 °C, 100 r/min) for 6 h. Warfarin was used as a positive control.

SPRC samples from both sides of the chamber were measured using the LC-MS/MS method. Percent binding was calculated using the following equation:

$$\text{Bound } \% = 100 \times ([\text{Donor}] - [\text{Receiver}]) / [\text{Donor}]$$

Metabolite identification using LightSight software

Preliminary metabolites in rat biomatrices were identified using MRM information-dependent, acquisition-enhanced product ion (MRM-IDA-EPI) scans on the API 4000QTrap system. Pooled rat plasma (0–24 h), bile (0–24 h), urine (0–72 h), and feces (0–72 h) samples were precipitated with acetonitrile. The mobile phase consisted of a methanol/ammonium acetate buffer [(10 mmol/L, pH=4.0): 15/85 (*v*/*v*)]. Other analytical conditions were the same as those applied to the quantification of SPRC, described above.

Mass spectrometer conditions were optimized by infusing 5 μg/mL SPRC solution in distilled water via a syringe pump at a 10 μL/min flow rate. The EPI analyte spectra were collected to identify the major fragments of SPRC ($[M+H]^+$=160.1). The three most abundant fragments were *m/z* 143.0, 114.0, and 97.0. Therefore, three MRM survey channels at 160.1→143.0, 160.1→114.0, and 160.1→97.0 were used to identify the metabolites of SPRC. Metabolite identification was accomplished using LightSight software, by matching the product ions and neutral losses of the EPI spectra of detected metabolites to the parent compound.

The IDA threshold was set to 500 cps, above which the EPI scan was triggered to collect the fragment ion spectra. The EPI scan rate was 4000 amu/s, and the scan range was 80 to 400 amu. The CEs were set at 30 eV, with a CE spread of 15 eV. Other parameters were set as follows: ion source voltage, +4500 V; temperature, 400 °C; curtain gas, 15 psi; ion source gas 1, 20 psi; ion source gas 2, 20 psi.

Other types of mass spectrometric analyses, including enhanced mass spectrometry (EMS), precursor ion (PI), and neutral loss (NL) scans, were performed to ensure that unexpected metabolites were not missed.

Data analysis

The amount of SPRC excreted into bile and urine during each time interval was calculated by multiplying the SPRC concentration by the volume of sample. The cumulative amount of SPRC (X) over a certain time period was calculated by adding all excreted amounts within the period. The same data were also expressed (in the form of % of dose) by dividing X with the total dose administered.

A one-way ANOVA, followed by S-N-K multiple comparisons, was used to evaluate the statistical significance of interspecies differences in plasma protein binding. The differences were considered significant when $P<0.05$.

Results

Tissue distribution of [^{35}S] SPRC-derived radioactivity

The distribution of [^{35}S] SPRC-derived radioactivity in various organs at three time points was determined after an oral administration of a 75 mg/kg [^{35}S] SPRC solution. SPRC-derived radioactivity was broadly distributed in all of the tissues examined (Table 1). At 0.5 h (the T_{max} in the plasma kinetics), the concentrations observed were in the following order: kidney>plasma>stomach>liver>lung>intestine>spleen>heart>muscle>brain. When compared with the corresponding plasma concentrations, the kidney tissues showed the highest exposure. The mean concentrations in the kidney tissue were 1.1, 1.5, and 1.8 times that present in the plasma at 0.5 h, 1.5 h, and 6 h, respectively. SPRC-related radioactivity in all the other tissues was the same as or lower than the corresponding plasma concentration.

Table 1. Tissue distribution of [^{35}S]-SPRC derived radioactivity after oral administration (25 μCi/mg, 75 mg/kg) of SPRC in rats. Data represent Mean±SD (n=5).

Tissue	Distribution amount of [^{35}S]-SPRC derived radioactivity (%ID/g)		
	0.5 h	1.5 h	6 h
Plasma	0.40±0.04	0.31±0.08	0.18±0.07
Brain	0.07±0.01	0.08±0.02	0.05±0.01
Muscle	0.11±0.02	0.12±0.03	0.05±0.02
Heart	0.15±0.06	0.10±0.02	0.05±0.02
Spleen	0.15±0.05	0.13±0.04	0.07±0.02
Kidney	0.44±0.19	0.47±0.14	0.32±0.12
Stomach	0.29±0.22	0.12±0.03	0.08±0.02
Liver	0.23±0.04	0.21±0.02	0.15±0.07
Lung	0.19±0.09	0.17±0.07	0.12±0.06
Intestine	0.17±0.06	0.09±0.01	0.10±0.06

Plasma protein binding

The extent of SPRC bound to human, rat, and dog plasma was studied at three concentration levels using a rapid equilibrium dialysis method. The protein binding to the positive control compound (warfarin) was within the normal range (98.4%±1.1%), indicating the reliability of the equilibrium dialysis study. The fraction bound ranged from -0.8% to -14.5% for human, 3.7% to 10.9% for rat, and -5.2% to 0.6% for dog. The total SPRC recovery after dialysis was >98%. No statistical differences were found at the three concentration levels tested. The statistical analysis revealed no significant difference in the plasma protein binding fractions of SPRC among

the three species.

Excretion of SPRC in rats

The excretion of unchanged SPRC after oral administration has been studied in rats using the LC-MS/MS method. No unchanged SPRC was found in rat feces up to 72 h post-dose using a relatively sensitive analytical method (the low limit of quantification was 50 ng/mL). After oral administration in rats, only 2.18%±0.61% and 0.77%±0.61% of the dose was excreted in the bile and urine as the parent drug up to 24 and 72 h, respectively (Figure 2). Less than 3% of the oral SPRC dose was recovered unchanged.

Identification of the major metabolites of SPRC in urine, bile, feces and plasma

The representative total ion current (TIC) chromatograms of the drug-treated rat biological samples were compared with the corresponding blank samples. Only one metabolite (M1, RT=10.2 min) of SPRC was found in rat urine, bile, and plasma (Figure 3). However, neither the parent drug nor the *N*-acetyl metabolite was observed in rat feces (data not shown).

The extracted ion chromatograms (EICs) and representative EPI spectra of M1 were also compared with the parent SPRC (Figure 4). M1 was proposed to be an acetylated metabolite because the precursor ion (*m/z* 202.1) was 42 *m/z* larger than the corresponding precursor ion (*m/z* 160.1) of SPRC. In addition, the fragmentation pattern of M1 is similar to that of SPRC, indicating that the same ions (*m/z* 143, *m/z* 114, and *m/z* 97) were found in the EPI spectra.

To ensure that no unexpected metabolites were missed using the MRM survey scan, different types of survey scan triggering EPI method, were used to detect any other metabolites of SPRC. These methods included EMS-EPI, PI-EPI, and NL-EPI. However, no other metabolites were found using these methods (data not shown).

Discussion

SPRC, a novel sulfur-containing amino acid derivative, has been proven to be a potent H_2S donor. It was selected for development, in part because of its potent *in vitro* and *in vivo* biological activities. However, the lack of comprehensive knowledge about the pharmacokinetic properties of SPRC hampers its further development as a new drug candidate. In the present study, we analyzed the pharmacokinetic properties of SPRC, including the tissue distribution, identification of major metabolites, and route of excretion.

SPRC shares pharmacokinetic properties with other cysteine derivatives, such as SAC[16, 17]. These cysteine derivatives were all bioavailable and were absorbed rapidly and easily in the gastrointestinal tract[15]. After oral administration, [^{35}S] SPRC-derived radioactivity was extensively distributed in various tissues. An accumulation of [^{35}S] SPRC-derived radioactivity exceeding plasma concentrations was mainly observed in the kidney at three different time points. The radioactivity in other tissues was approximate to or lower than the observed plasma concentration. Previous studies showed that SAC was retained at a fairly high concentration in the kidney, and it was speculated that SAC was reabsorbed in the kidney[16]. Therefore, the kidney may play a major role in the elimination of cysteine derivatives in rats and deserves further study.

In the rat excretion study, less than 3% of the oral dose of unchanged SPRC was recovered in the urine and bile. This result indicates that the drug is almost completely metabolized before elimination from the body. The major metabolic pathway of SPRC was N-acetylation, which forms the conjugate compound found in urine, bile, and plasma. The N-acetylated SAC was also the major metabolite of SAC[16]. Neither the parent drug nor the N-acetyl metabolite was found in rat feces. Previous studies demonstrated that *S*-allyl-*L*-cysteine sulfoxide and *N*-allyl-*L*-cysteine sulfoxide were the expected metabolites of SAC in rat urine[18]. However, these sulfoxide metabolites of SPRC were not observed in our experiment.

In summary, this study examined in detail the pharmacokinetic properties of SPRC in Sprague-Dawley rats. Our study examined the tissue distribution, plasma protein binding, excretion, and metabolites of SPRC. The tissue distribution of [^{35}S] SPRC-derived radioactivity in rats was rapid and extensive. SPRC was distributed mainly in the kidney. The levels of human, rat, and dog plasma SPRC protein binding were low. Only approximately 0.77% and 2.18% of the parent SPRC could be recovered after oral administration in rat urine and bile, respectively. The major metabolite of SPRC in rat urine, bile, and plasma was the N-acetylated metabolite. No parent drug or metabolite was found in rat feces. In addition to

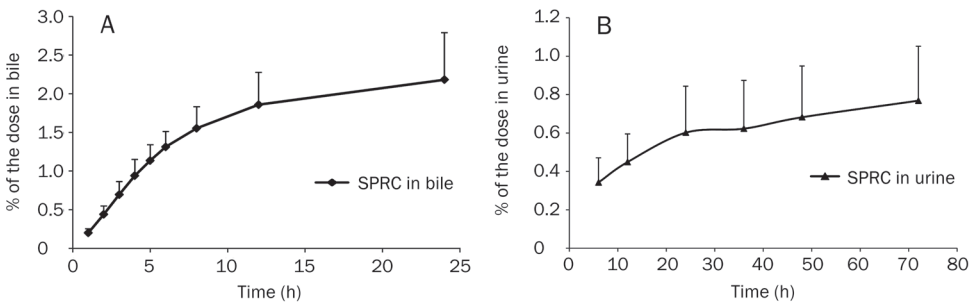

Figure 2. The cumulative excretion of unchanged SPRC in rat bile (A) and urine (B) after oral administration. SPRC concentrations were determined by the LC-MS/MS method. All values are expressed as the mean±SD. (*n*=6).

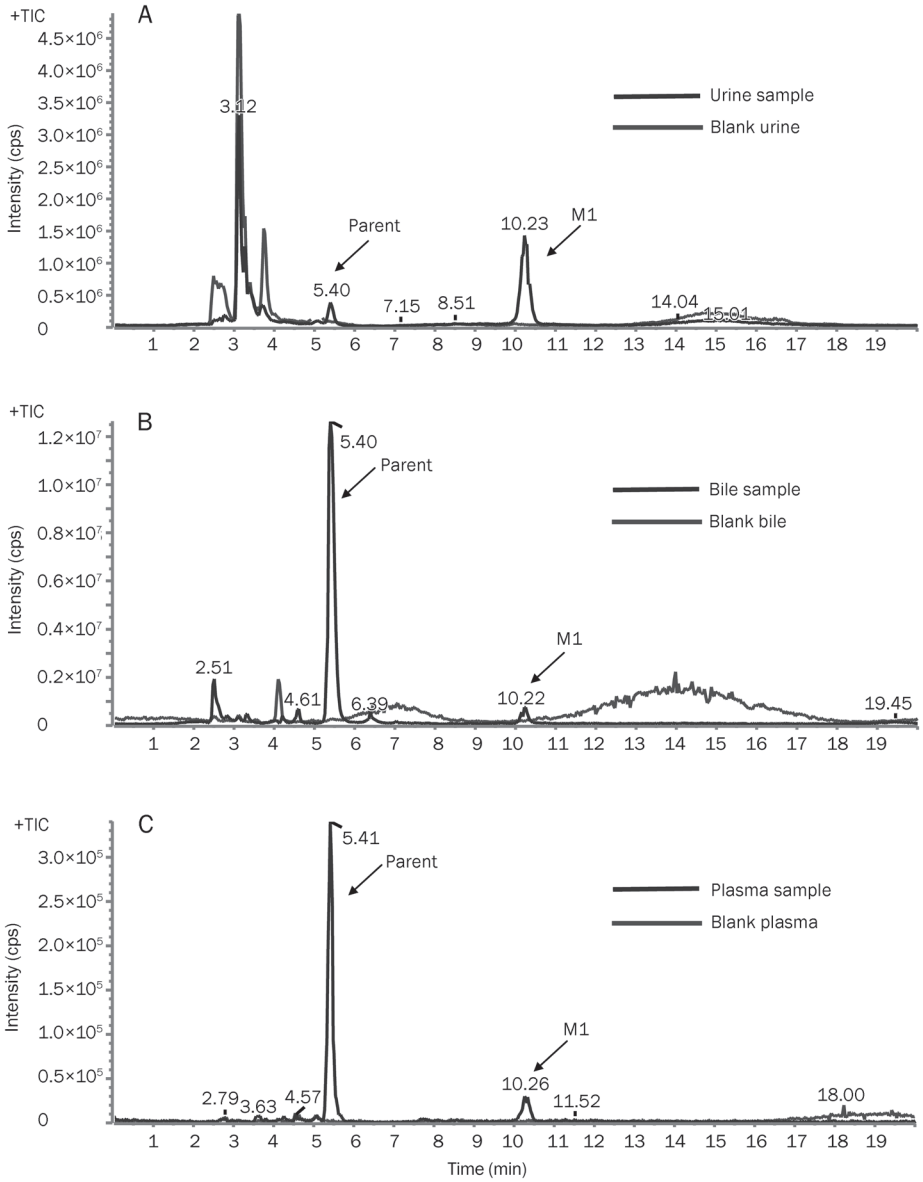

Figure 3. The representative total ion current (TIC) chromatogram obtained from rat biological samples following oral administration of SPRC using the MRM-IDA-EPI method. (A) TIC chromatograph of a rat urine sample collected 96 h post-drug administration; (B) TIC chromatograph of a rat bile sample collected 24 h post-drug administration; (C) TIC chromatograph of a rat plasma sample collected 24 h post-drug administration.

increasing the knowledge of SPRC biological activities, this pharmacokinetic study contributes to the further development of this new drug candidate.

Acknowledgements

This project was supported by the National Drug Innovative Program (2009ZX09301-011) and Traditional Chinese Medicine Modernization (10DZ1972100).

Author contribution

Yuan-ting ZHENG, Yi-zhun ZHU, and Wei-min CAI designed the experiments, Yuan-ting ZHENG, Jian-hua ZHU, Guo MA, Qing ZHU, Ping YANG, Bo TAN, Jin-lian ZHANG, Hai-xing SHEN, and Jia-lin XU performed the experiments, Yuan-ting ZHENG, and Wei-min CAI wrote the manuscript.

References

1 Abe K, Kimura H. The possible role of hydrogen sulfide as an endogenous neuromodulator. J Neurosci 1996; 16: 1066–71.
2 Wang R. The gasotransmitter role of hydrogen sulfide. Antioxid Redox Signal 2003; 5: 493–501.
3 Dello Russo C, Tringali G, Ragazzoni E, Maggiano N, Menini E, Vairano M, *et al*. Evidence that hydrogen sulphide can modulate hypothalamo-pituitary-adrenal axis function: *in vitro* and *in vivo* studies in the rats. J Neuroendoctinol 2000; 12: 225–33.
4 Laggner H, Hermann M, Esterbauer H, Muellner MK, Exner M, Gmeiner BM, *et al*. The novel gaseous vasorelaxant hydrogen sulfide inhibits angiotensin-converting enzyme activity of endothelial cells. J Hypertens 2007; 25: 2100–4.
5 Chu Q, Ling MT, Feng H, Cheung HW, Tsao SW, Wang X, *et al*. A novel anticancer effect of garlic derivatives: inhibition of cancer cell invasion through restoration of E-cadherin expression. Carcinogenesis 2006; 27: 2180–9.

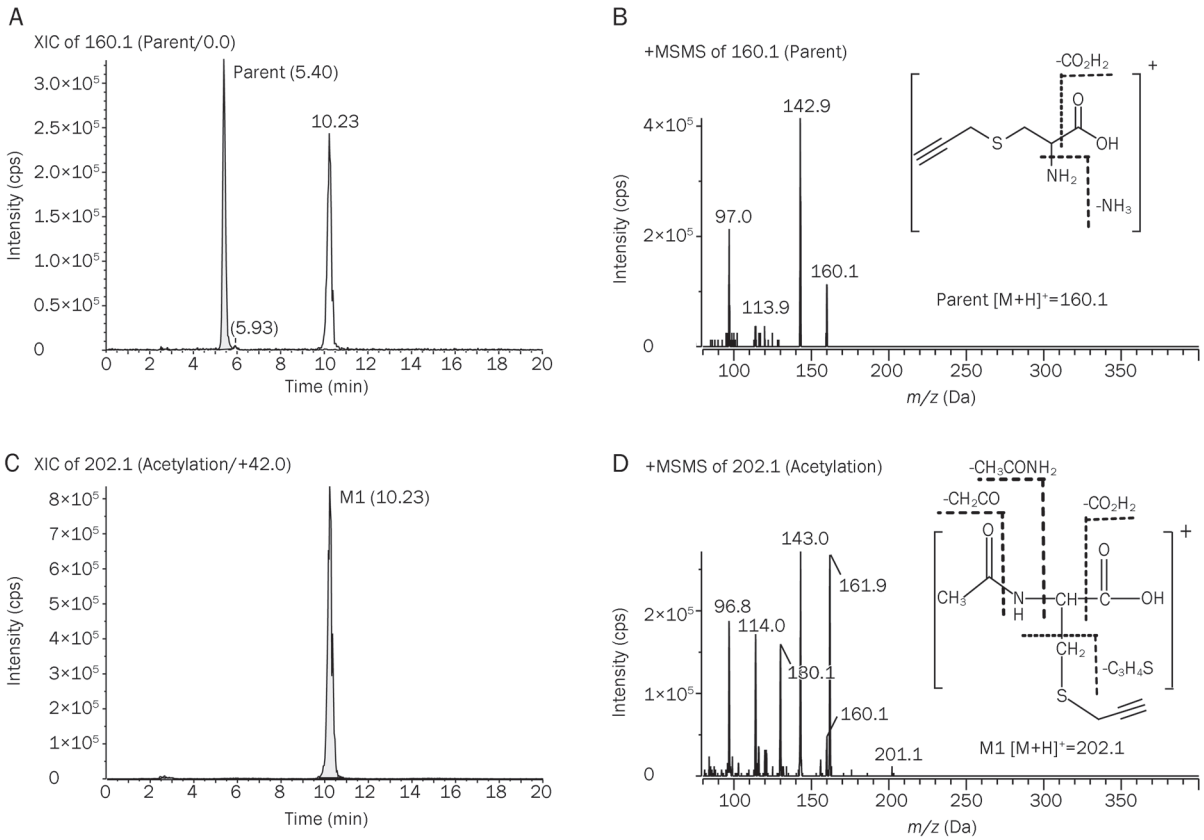

Figure 4. The representative extracted ion chromatography (EIC) and its enhanced product ion (EPI) spectra obtained from the urine sample after oral dosing of the SPRC solution using the MRM-IDA method. (A) EIC of parent drug (160.1 *m/z*); (B) EPI spectra and structure of parent drug; (C) EIC of M1 (202.1 *m/z*); (D) EPI spectra and structure of M1.

6 Cao Y, Adhikari S, Ang AD, Moore PK, Bhatia M. Mechanism of induction of pancreatic acinar cell apoptosis by hydrogen sulfide. Am J Physiol Cell Physiol 2006; 291: C503–10.
7 Garcia E, Limon D, Perez-De La Cruz V, Giordano M, Diaz-Muñoz M, Maldonado PD, *et al*. Lipid peroxidation, mitochondrial dysfunction and neurochemical and behavioural deficits in different neurotoxic models: protective role of *S*-allylcysteine. Free Radic Res 2008; 42: 892–902.
8 Rose P, Whiteman M, Moore PK, Zhu YZ. Bioactive *S*-alk(en)yl cysteine sulfoxide metabolites in the genus Allium: the chemistry of potential therapeutic agents. Nat Prod Rep 2005; 22: 351–68.
9 Wang Q, Liu HR, Mu Q, Rose P, Zhu YZ. *S*-propargyl-cysteine protects both adult rat hearts and neonatal cardiomyocytes from ischemia/hypoxia injury: the contribution of the hydrogen sulfide-mediated pathway. J Cardiovasc Pharmacol 2009; 54: 139–46.
10 Wang Q, Wang XL, Liu HR, Rose P, Zhu YZ. Protective effects of cysteine analogues on acute myocardial ischemia: novel modulators of endogenous H_2S production. Antioxid Redox Signal 2010; 12: 1155–65.
11 Pan LL, Liu XH, Gong QH, Zhu YZ. *S*-Propargyl-cysteine (SPRC) attenuated lipopolysaccharide-induced inflammatory response in H9c2 cells involved in a hydrogen sulfide-dependent mechanism. Amino Acids 2011; 41: 205–15.
12 Gong QH, Wang Q, Pan LL, Liu XH, Xin H, Zhu YZ. *S*-propargyl-cysteine, a novel hydrogen sulfide-modulated agent, attenuates lipopolysaccharide-induced spatial learning and memory impairment: involvement of TNF signaling and NF-kappaB pathway in rats. Brain Behav Immun 2011; 25: 110–9.
13 Gong QH, Pan LL, Liu XH, Wang Q, Huang H, Zhu YZ. *S*-propargyl-cysteine (ZYZ-802), a sulphur-containing amino acid, attenuates beta-amyloid-induced cognitive deficits and pro-inflammatory response: involvement of ERK1/2 and NF-kappaB pathway in rats. Amino Acids 2011; 40: 601–10.
14 Ma K, Liu Y, Zhu Q, Liu CH, Duan JL, Tan BK, *et al*. H_2S donor, *S*-propargyl-cysteine, increases CSE in SGC-7901 and cancer-induced mice: evidence for a novel anti-cancer effect of endogenous H_2S? PLoS One 2011; 6: e20525.
15 Zheng YT, Liu HR, Ma G, Yang P, Zhang L, Gu Y, *et al*. Determination of *S*-propargyl-cysteine in rat plasma by mixed-mode reversed-phase and cation-exchange HPLC-MS/MS method and its application to pharmacokinetic studies. J Pharm Biomed Anal 2011; 54: 1187–91.
16 Nagae S, Ushijima M, Hatono S, Imai J, Kasuga S, Matsuura H, *et al*. Pharmacokinetics of the garlic compound *S*-allylcysteine. Planta Med 1994; 60: 214–7.
17 Yan CK, Zeng FD. Pharmacokinetics and tissue distribution of *S*-allylcysteine in rats. Asian J Drug Metab Pharmacokinet 2004; 5: 61–9.
18 Krause RJ, Glocke SC, Elfarra AA. Sulfoxides as urinary metabolites of *S*-allyl-*L*-cysteine in rats: evidence for the involvement of flavin-containing monooxygenases. Drug Metab Dispos 2002; 30: 1137–42.

Acta Pharmacologica Sinica (2012) 33: 845–851

www.nature.com/aps

Original Article

Population pharmacokinetics modeling of levetiracetam in Chinese children with epilepsy

Ying-hui WANG[1], Li WANG[1, *], Wei LU[2], De-wei SHANG[2], Min-ji WEI[1], Ye WU[1]

[1]Pediatric Department of Peking University First Hospital, Beijing 100034, China; [2]Department of Pharmaceutics, School of Pharmaceutical Sciences, Peking University, Beijing 100191, China

Aim: To establish a population pharmacokinetics (PPK) model of levetiracetam in Chinese children with epilepsy.
Methods: A total of 418 samples from 361 epileptic children in Peking University First Hospital were analyzed. These patients were divided into two groups: the PPK model group (n=311) and the PPK validation group (n=50). Levetiracetam concentrations were determined by HPLC. The PPK model of levetiracetam was established using NONMEM, according to a one-compartment model with first-order absorption and elimination. To validate the model, the mean prediction error (MPE), mean squared prediction error (MSPE), root mean-squared prediction error (RMSPE), weight residues (WRES), and the 95% confidence intervals (95% CI) were calculated.
Results: A regression equation of the basic model of levetiracetam was obtained, with clearance (CL/F)=0.988 L/h, volume of distribution (V/F)=12.3 L, and K_a=1.95 h^{-1}. The final model was as follows: K_a=1.56 h^{-1}, V/F=12.1 (L), CL/F=1.04×(WEIG/25)$^{0.563}$ (L/h). For the basic model, the MPE, MSPE, RMSPE, WRES, and the 95%CI were 9.834 (-0.587–197.720), 50.919 (0.012–1286.429), 1.680 (0.021–34.184), and 0.0621 (-1.100–1.980). For the final model, the MPE, MSPE, RMSPE, WRES, and the 95% CI were 0.199 (-0.369–0.563), 0.002082 (0.00001–0.01054), 0.0293 (0.001–0.110), and 0.153 (-0.030–1.950).
Conclusion: A one-compartment model with first-order absorption adequately described the levetiracetam concentrations. Body weight was identified as a significant covariate for levetiracetam clearance in this study. This model will be valuable to facilitate individualized dosage regimens.

Keywords: levetiracetam; epilepsy; population pharmacokinetics; pediatric; Chinese children

Acta Pharmacologica Sinica (2012) 33: 845–851; doi: 10.1038/aps.2012.57

Introduction

Levetiracetam (LEV; (*S*)-ethyl-2-oxo-pyrrolidine acetamide (Keppra®), UCB Pharma, Braine-l'Alleud, Belgium) is a new antiepileptic drug. It is mainly used for the adjunctive treatment of partial-onset seizures in adults and children, as well as myoclonic and primary generalized tonic-clonic seizures in patients with idiopathic generalized epilepsy[1–3]. The primary mechanism of action of LEV relates to its binding to synaptic vesicle proteins[4]. The results of clinical trials in a Chinese population have demonstrated that LEV is effective and well tolerated in adults with inadequately controlled partial-onset seizures[5].

LEV shows linear pharmacokinetics, and its major route of elimination is through the kidneys, with approximately 66% of a dose eliminated unchanged and 27% as inactive metabolites[6–9]. Renal function determines the rate of elimination of LEV. The half-life is 6–8 h in healthy adults, and 5–7 h in children aged 6–12 years. However, the apparent clearance is 30%–40% higher in children than in adults[10]. The initial daily dose is 20 $mg^{-1}\cdot kg^{-1}\cdot d^{-1}$ (10 mg/kg twice daily) and can go up to 60 $mg^{-1}\cdot kg^{-1}\cdot d^{-1}$. Even higher doses (>60 $mg^{-1}\cdot kg^{-1}\cdot d^{-1}$) have also been reported[11].

Measuring the serum concentration (SC) of LEV can be useful in assessing compliance and managing patients in situations associated with pharmacokinetic (PK) alterations in pathological states such as renal impairment, as well as in specific age groups such as children and the elderly[12, 13]. Numerous chromatographic methods for the quantification of LEV in serum have been described. These include high performance liquid chromatography (HPLC) with ultraviolet (UV) detection and gas chromatography (GC) with various detection systems[14–16].

Levetiracetam has been used in the treatment of children with epilepsy in China since 2007; however, the PK parameters in Chinese children are not known. Therefore, the aims of the present study were to develop a population pharmacokinetics (PPK) model of levetiracetam in Chinese children with epilepsy.

* To whom correspondence should be addressed.
E-mail wangli5000@126.com.cn
Received 2011-10-18 Accepted 2012-04-28

Materials and methods

Patients

Children with epilepsy aged 0.5–14 years were recruited by pediatricians at outpatient clinics in Peking University First Hospital. They were treated with LEV monotherapy or adjunctive therapy for 1 week at least on a stable LEV dose treatment. They presented with various types of epilepsy syndromes, including partial, generalized and undetermined. For each patient, the time between dosing and sampling, gender, age, weight, serum concentration, and co-administered medications were recorded. LEV tablets were administered in daily doses of 20–60 mg/kg. The LEV dose regimen could be adjusted in cases of inadequate seizure control or side effects.

Sample collection

The sampling times to last LEV intake were generally between 1 h and 13 h (Figure 1). Blood samples were kept at room temperature for 30 min before they were centrifuged, and the separated serum was preserved at -20 °C in our laboratory for less than a week before analysis.

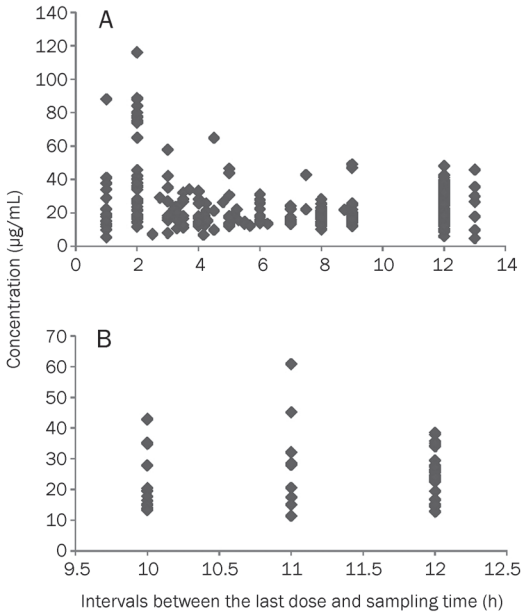

Figure 1. Scattergram of concentrations and intervals between the last dosage time and the sampling time of patients. (A) the PPK model group. (B) the PPK validation group.

Analytical method

This method has already been successfully established in China[17]. Briefly, the HPLC system consists of a Waters 1525 (Waters company), including a manual sampler, a degasser, a quaternary pump, a thermostatted column compartment and a variable wavelength detector. The chromatographic separation of the analyte is done on an Alltima C18 (Grace Davison Discovery Sciences Company, Deerfield, IL, USA, 150 mm×4.6 mm, 5 mm particle size) analytical column protected with a pre-filter. Data were collected and analyzed using a Breeze software package, version 3.03. LEV and an internal standard UCB17025 were provided by UCB Pharma (Brain-l'Alleud, Belgium). By spiking drug-free human serum with a working solution, calibration samples between 160 and 1.25 mg/L were obtained. A linear regression was performed from chromatographic data that allowed us to extrapolate the LEV concentration in each patient sample. Quality control samples were prepared at three concentration levels, with target values of 2, 16, and 80 mg/mL. An internal standard (100 μL of a 40 μg/mL solution) and 1 mL dichloromethane were added to 100 μL serum sample. After vortexing for 1 min, ultrasonication for 10 min and centrifuging at 4000×*g* for 10 min, the upper layer was removed and evaporated to dryness under a nitrogen stream at room temperature. The residue was reconstituted in 100 μL methanol, of which 20 μL was injected into the chromatographic system. The flow rate was 1 mL/min and the column temperature was 37 °C. The wavelength detection was set at 210 nm. The retention time of LEV and UCB17025 was 5.45±0.10 and 7.50±0.20 min under the described conditions, respectively.

PPK modeling

After parameterization according to previous studies[11, 18], the LEV concentrations were suited to using a one-compartment model and a first-order absorption process. The PPK modeling included the base model and final model.

PPK model of LEV

The PK data were analyzed with the use of nonlinear mixed effects modeling (NONMEM, version 7, level 1.2). To describe the PK of LEV, the PK disposition model was tested using a standard one-compartment model with subroutine ADVAN2 TRANS2. The first order conditional estimation (FOCE) was used to develop the model. Firstly, the basic model with inter-individual variability was set up. The model was parameterized for apparent clearance (*CL/F*), the apparent volumes of distribution of the central compartment (*V/F*), and the absorption rate constant (K_a). $CL/F=\theta_{CL/F}\cdot\exp(\eta_{CL/F})$; $V/F=\theta_{V/F}\cdot\exp(\eta_{V/F})$; $K_a=\theta_{Ka}\cdot\exp(\eta_{Ka})$. Secondly, the covariate variability was added step by step and the full PPK model was set as follows:

$$P_i=\theta_i\times(COV/mCOV)^{\theta j}\times e^{\eta i}$$

where P_i is the individual predicted parameter value, θ_i is the typical population estimate of P_i, ηi is the proportional difference, COV and mCOV are the individual and median covariate values, and θ_j is the power factor for the effect of the covariate on P_i. The effects of categorical covariates on the structural parameters were modeled as follows:

$$P_j=[\theta_{1j}\times N_{1j}+\theta_{2j}\times N_{2j}+\ldots]\times e^{\eta j}$$

where P_j is the individual predicted parameter value, θ_{1j} is the typical population value of P_j for category 1 of the covariate, and N_{1j} is an indicator variable that has a value of 1 when the covariate is present and 0 when the covariate is absent. The covariates of this study included: age (year), weight (WEIG), dose [the dosage of whole day (mg) before sampling] and co-administered medications (CO)].

Data analysis

When the important covariates were selected, a stepwise forward and backward approach was used and each covariate was added or deleted individually. Sex and CO were the categorical covariates. These categorical covariates were modeled by the use of indicator variables. The influences of continuous covariates, such as age, weight, dosage, were also explored. The likelihood ratio test was used to determine the appropriateness of a selected covariate. A decrease in the objective function values (OFV) (-2 log-likelihood) of 7.88 units was considered significant (χ^2 P<0.005, df=1). Throughout the process of model development, graphic methods were also used to judge the general goodness of fit.

Statistical model

When an influence of the fixed effect was not considered, individual PK parameters were typical population values plus the random deviation. According to the experiential formulations, inter-individual and intra-individual deviations (residual deviation) were presented as follows:

$$P_j=P_{TV}\times e^{\eta p}$$
$$E_{ij}^{0}=E_{ij}+\varepsilon_{ij},$$

where P_j is the jth patient PK parameter; P_{TV} is the typical value of P for the population, η^P is inter-individual deviation (a mean of 0 and variance ω_P), E_{ij}^{0} is the observation value, E_{ij} is the prediction value of E_{ij}^{0}, and ε_{ij} is the intra-individual deviation(its mean is 0 and variance is σ_E^2).

Model validation

To validate the basic and the final model, concentrations from 50 patients in the valid group were predicted by the two models. These patients were enrolled at random. To assess the accuracy and precision of the concentration prediction, the mean prediction error (MPE), mean squared prediction error (MSPE), root mean-squared prediction error (RMSPE), weight residues (WRES), and the 95% confidence intervals (95% CI) were calculated. Then, the values of the two models were compared[19]. The shrinkage for each of the parameters in the model was evaluated using the method described by Karlsson[20].

Results

Patient demographics

A total of 418 samples obtained from 361 patients aged from 0.5–14 years were available for PK modeling. The characteristics of the studied population are summarized in Table 1. The intervals between the last dosage time and sampling time were distributed over 1–13 h (Figure 1). The distributions of the intervals between the last dosage time and sampling time in the model group are shown in the Figure 2. All of the patients had normal renal and hepatic function. In this population, 40% and 60% used one or two concomitant anti-epileptic drugs (AEDs), respectively. The most frequently used concomitant AEDs were valproic acid (VPA), lamotrigine (LTG), carbamazepine (CBZ), oxcarbazepine (OXC), and topiramate (TPM).

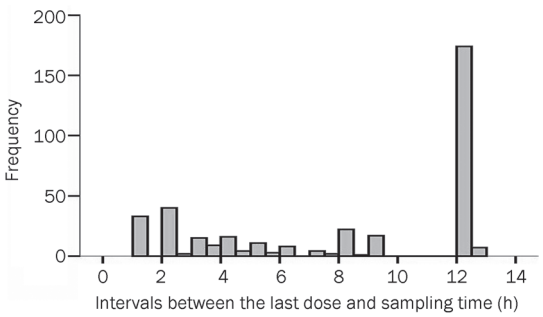

Figure 2. Frequency of intervals between the last dose and sampling time in the model group.

PPK modeling

A classical one-compartment model with first-order absorption, and linear elimination (ADVAN2 and TRANS2) best described the data. The distributions of concentration data and sampling times in the PPK model and PPK valid groups are shown in Figure 1. In the basic model, K_a=1.95 (h^{-1}),

Table 1. Baseline characteristics of patients included in this study.

Characteristics	PPK model group	PPK validation group
Patient data		
No patients	311	50
Gender (male: female)	160:151	27:23
Mean age (years) (range)	6.34 (0.5–14)	5.78 (1.5–13)
Mean weight (kg) (range)	25.17 (5–70)	21.77 (11–35)
Mean dosage (mg/d) (range)	655.17 (250–2000)	529.17 (250–1000)
Sample data		
Mean sampling time (h) (range)	7.35 (0.1–13)	11.01 (10–12)
Total no. concentration-time points	368	50
Mean dose ($mg{\cdot}kg^{-1}{\cdot}d^{-1}$) (range)	35.7 (5.1–62.5)	31.4 (10–50.7)
Mean LEV concentration (μg/mL) (range)	27.99 (4.85–116.11)	25.11 (11.27–60.88)

V/F=12.3 (L), and CL/F=0.988 (L/h). In the full regressive model, the results of all the covariates were validated by a hypothesis test (Table 2). The parameters of the final model are shown in Table 3, and the final model was as follows: K_a=1.56 (h^{-1}), V/F=12.1 (L), CL/F=1.04×(WEIG/25)$^{0.563}$ (L/h). No significant interaction with the concomitant AEDs was found. The estimated levetiracetam CL/F was 1.04 L/h and the corresponding half-life estimate in these subpopulations was 8.13 h.

Table 2. Results of the hypothesis validation for the full regression model.

Parameter	Covariate	ΔOFV	*P*-value
CL/F	Age	-6.714	*P*>0.005
	Weight	-128.412	*P*<0.005
	CO	-0.431	*P*>0.005
	Dose	-3.242	*P*>0.005
	Gender	-1.105	*P*>0.005
V/F	Age	-0.154	*P*>0.005
	Weight	-0.528	*P*>0.005
	CO	-3.644	*P*>0.005
	Dose	-2.145	*P*>0.005
	Gender	-2.233	*P*>0.005
K_a	Age	-2.550	*P*>0.005
	Weight	-1.476	*P*>0.005
	CO	-1.560	*P*>0.005
	Dose	-2.279	*P*>0.005
	Gender	-2.410	*P*>0.005

Model validation

Comparison between scattergrams of basic and final model

Diagnostic plots are shown in Figure 3, including Dependent Variable (DV) versus Prediction (PRED), DV versus Individual Prediction (IPRED), weighted residual error (CWRES) versus PRED, and CWRES versus TIME.

Comparison of prediction errors between the final model and basic model

MPE, MSPE, RMSPE, WRES and 95% CI in the basic model and final model are defined in Table 3. The indicators in the final model, such as MPE, MSPE, and RMSPE, decreased and showed more accurate predictions. The shrinkage for each of the parameters in the model is shown in Table 4.

Discussion

In this study, a one-compartment model with first-order absorption and elimination best characterized the data. The model describes the data adequately. The mean CL/F, V/F, and K_a were 1.04 L/h (0.69 mL·min^{-1}·kg^{-1}), 12.1 L and 1.56 h^{-1}, respectively. No drug-drug interaction was observed in this study. In this model, the median WEIG in our population was 25 kg. Weight was identified as the most important covariate that explained the inter-individual variability of the apparent serum clearance of LEV.

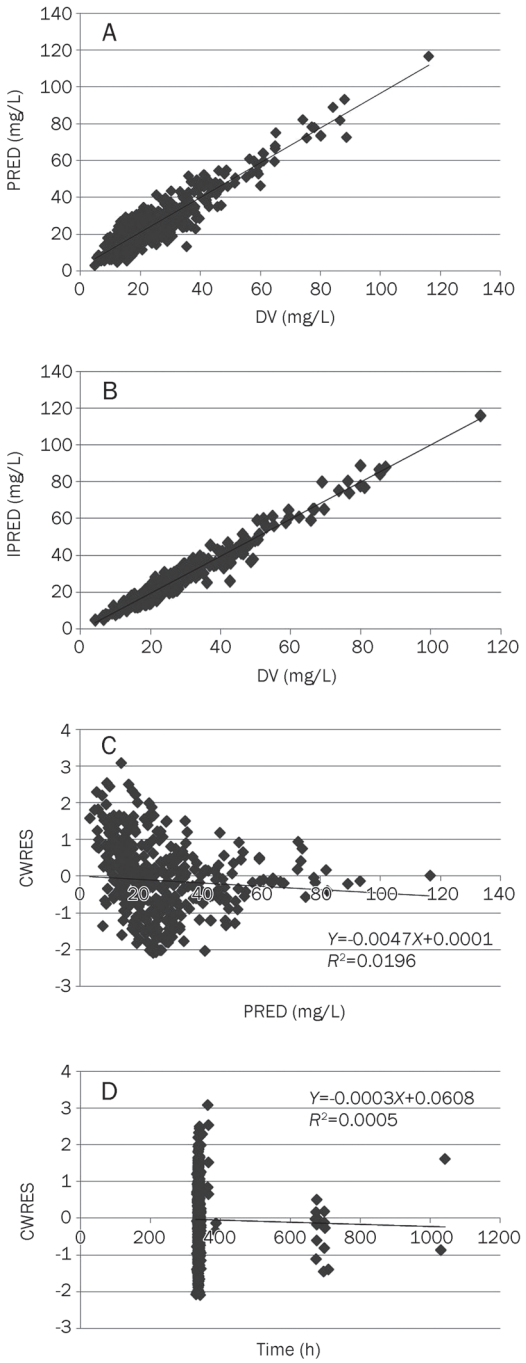

Figure 3. Diagnostic plots of the final PK model. (A) Plot of the observed concentrations versus population predicted levetiracetam concentrations (PRED). B) Plot of the observed concentrations versus individual population predicted levetiracetam concentrations (IPRED). (C) Plot of population predicted levetiracetam concentrations (PRED) versus CWRES. (D) Plot of CWRES versus TIME. DV: Dependent Variable.

Patient data

There are very sparse PK samples for modeling. There were not enough points in the absorption phase (Figures 1 & 2); therefore, the ωK_a was fixed at 0. There was insufficient information about the absorption and distribution phases, which

Table 3. Comparison of the prediction accuracy between the basic and the final models.

Error	Basic model	Final model
MPE (95% CI)	9.834 (-0.587–197. 720)	0.199 (-0.369–0.563)
MSPE (95% CI)	50.919 (0.012–1286.429)	0.002082 (0.00001–0.01054)
RMSPE (95% CI)	1.680 (0.021–34.184)	0.0293 (0.001–0.110)
WRES (95% CI)	0.0621 (-1.100–1.980)	0.153 (-0.030–1.950)

Table 4. Population parameter values for the final model.

Parameter	Estimate	RSE (%)	95% CI	Shrinkage
CL/F (L/h)	1.04	1.4	1.011–1.069	
V/F (L)	12.1	5.6	10.767–13.433	
K_a (h^{-1})	1.56	14.3	1.230–1.997	
Weight (kg)	0.567	6.7	0.489–0.637	
ω*CL/F*	0.195	7.0	0.106–0.141	20%
ω*V/F*	0.163	45.5	0.127–0.175	44.9%
ε	0.028	18.6	0.018–0.035	31%

RSE (%), percentage of relative standard error (100%×SE/EST); ω*CL/F*, ω*V/F*, variance of the *CL/F*, *V/F*, parameters, respectively; ε, variance of intra-individual deviation of fitted concentration. The ωK_a was fixed at 0, as there were not enough points in the absorption phase.

may have resulted in potential bias and imprecision regarding the parameter estimates. More attention should be paid to the distribution of the blood sampling time.

Comparison with similar domestic research

Zhao *et al*[21] studied healthy Chinese male subjects following a single-dose of either 500 mg and 1500 mg of levetiracetam, the median t_{max} was 0.5 h; $t_{1/2}$ was 7.3±0.8 and 7.3±0.7 h. The pharmacokinetic data obtained in these Chinese subjects were similar to the historical data from a matched group of white subjects. There are no related studies of PPK of LEV in Chinese adults with epilepsy.

Comparison with similar overseas studies

Pigeole *et al*[22] found the following parameters in Japanese and Western adults: $K_a(h^{-1})$=2.44 (fed intake) or 4.80 (fasted intake), L/F(L/h)=4.02*$(WT/70)^{0.268}$*$(CL_{CR}/110)^{0.122}$*S*M, F(L)=52.7*$(WT/70)^{0.952}$*P*VA, where WT is the bodyweight in kg; CL_{CR} is creatinine clearance in mL/min; *S*=1 for males and 0.896 for females; *M*=1.09 for enzyme-inducing AEDs, 0.812 for valproic acid and 1 for other AEDs; *P*=1 for epileptic subjects and 0.861 for healthy subjects, and VA=0.776 for valproic acid and 1 for other AEDs. Glauser *et al*[23] found that *CL/F* was 1.46±0.42 $mL{\cdot}min^{-1}{\cdot}kg^{-1}$ in patients aged from 2.3 to 46.2 months. Toublanc *et al*[17] found in children aged between 3 months and 18 years, *CL/F* (L/h)=2.18*K*$(WEIG/30)^{0.753}$, *K*=1 for children not receiving enzyme-inducing AEDs and *K*=1.22 in the presence of enzyme-inducing AEDs. *K* corresponds to the typical fold increase in LEV clearance by enzyme inducers. *V/F* (L/h)=21.4*$(WEIG/30)^{0.898}$, K_a (h^{-1})=1.48*$(Age/10)^{0.277}$. Chhun *et al*[18] found that, from 4 to 16 years, *CL/F* (L/h)= 2.47*$(BW/33)^{0.89}$, *V/F* (L)=21.9*$(BW/33)^{0.93}$, and K_a (h^{-1})=3.83. The *CL/F* of this study was lower than in the children in the studies by Toublanc and Chhun[17, 18]. In Merhar's study of neonates[24], clearance was 1.21 $mL{\cdot}min^{-1}{\cdot}kg^{-1}$. In Pellock's study[12] of 6–12 years old, *CL/F* was 1.43 $mL{\cdot}min^{-1}{\cdot}kg^{-1}$, which was higher than that in adults (0.96 $mL{\cdot}min^{-1}{\cdot}kg^{-1}$) and than the 0.69 $mL{\cdot}min^{-1}{\cdot}kg^{-1}$ observed in the current study. It appears that the *CL/F* of Chinese children is lower than that of white Caucasian children. The trough serum concentration was also higher than in the white children (Table 5).

It appears that the *CL/F* in Chinese children was approximately 50% lower than in Western children based on the published data (*eg*, 0.69 $mL{\cdot}min^{-1}{\cdot}kg^{-1}$ *vs* 1.21–1.46 $mL{\cdot}min^{-1}{\cdot}kg^{-1}$). LEV was mainly eliminated by the kidneys, and significant ethnic differences were not expected in previous studies; however, racial differences are likely to be at least partly responsible for the difference in *CL/F* that we observed, and these differences will be the subject of future studies. Our study has a good representation of Chinese children with epilepsy with ages that ranged from 0.5 to 14 years.

Validation of the PPK model

The final model contained covariates, such as age, weight, concomitant medication, and different formulations, and it was more accurate in predicting the patients' blood concentrations than the basic model that had no covariates. For the basic model, the MPE, MSPE, RMSPE, WRES, and their 95% CIs were 9.834 (-0.587–197.720), 50.919 (0.012–1286.429), 1.680 (0.021–34.184), and 0.0621 (-1.100–1.980), respectively. For the final model, the MPE, MSPE, RMSPE, WRES, and their 95% CIs were 0.199 (-0.369–0.563), 0.002082 (0.00001–0.01054), 0.0293 (0.001–0.110), and 0.153 (-0.030–1.950). Furthermore, the RMSPE (95% CI) of 0.0293 (0.001–0.110) in the final model outweighed the basic model's value of 1.680 (0.021–34.184). Therefore, the final model had a better accuracy and precision than the basic model. The shrinkage values of ω*CL/F*, ω*V/F* and ε were 20%, 44.9%, and 31%, respectively. The shrinkage of ω*V/F* (44.9%) was caused by insufficient information regarding the distribution phase (Figure 2). Based on this final PPK model, individual PK parameters will be estimated by the Bayesian approach in the near future, which will facilitate individualized dosage regimens.

Table 5. Levetiracetam pharmacokinetic parameters from the published literature and from our study.

Dose	Parameters	Fountain[25]	Pellock[12]	Chhun[18]	Our study
10 mg/kg, bid	$C_{12\,h}$ (mg/L)	8.4±3.8	–	6.4±2.7	11.25±3.10
	$t_{1/2}$ (h)	4.9±0.6	–	6.8±1.5	8.13±0.3
	CL/F (mg·kg^{-1}·min^{-1})	1.14±0.18	–	1.24±0.29	0.69±0.1
20 mg/kg, bid	$C_{12\,h}$ (mg/L)	15.6±5.3	–	12.7±4.7	17.5±2.63
	$t_{1/2}$ (h)	4.9±0.4	6.0±1.1	6.8±1.5	8.13±0.22
	CL/F (mg·kg^{-1}·min^{-1})	1.10±0.16	1.43±0.36	1.24±0.29	0.69±0.13
30 mg/kg, bid	$C_{12\,h}$ (mg/L)	20.6±5.8	–	19.1±7.2	31.25±3.8
	$t_{1/2}$ (h)	4.9±0.7	–	6.8±1.5	8.13±0.35
	CL/F (mg·kg^{-1}·min^{-1})	1.12±0.119	–	1.24±0.29	0.69±0.09

CL/F, apparent oral clearance; $t_{1/2}$, elimination half-life.

Conclusion

The population analysis has been successful in describing the pharmacokinetics of LEV in children aged 0.5–14 years. A one-compartment model with first-order absorption adequately described the LEV concentrations. The findings indicate that weight was the most influential factor for the CL/F of LEV in children with normal renal function. This will be invaluable for the development of individualized dosage regimens.

Acknowledgements

This work was supported by grants from the UCB Pharma (Braine-l'Alleud, Belgium) and the Capital Development Fund of Medical Research of China (No 2009-2021). The authors thank the pediatricians at Peking University First Hospital (Beijing, China), for their contributions to the study.

Author contribution

Li WANG designed research; Ye WU and Min-ji WEI performed research; Wei LU and De-wei SHANG contributed new analytical tools and reagents; De-wei SHANG and Ying-hui WANG analyzed data; Ying-hui WANG wrote the paper.

References

1 Stefan H, Feuerstein TJ. Novel anticonvulsant drugs. Pharmacol Ther 2007; 113: 165–83.
2 Shorvon SD, Lowenthal A, Janz D. Multicenter double-blind, randomized, placebo-controlled trial of levetiracetam as add-on therapy in patients with refractory partial seizures. European Levetiracetam Study Group. Epilepsia 2000; 41: 1179–86.
3 Hwang H, Kim KJ. New antiepileptic drugs in pediatric epilepsy. Brain Dev 2008; 30: 549–55.
4 Stockist A, Lu S, Tonner F. Clinical pharmacology of levetiracetam for the treatment of epilepsy. Expert Rev Pharmacol 2009; 2: 339–50.
5 Zhou B, Zhang Q, Tian L, Xiao J, Stefan H, Zhou D. Effects of levetiracetam as an add-on therapy on cognitive function and quality of life in patients with refractory partial seizures. Epilepsy Behav 2008; 12: 305–10.
6 Patsalos PN. Clinical pharmacokinetics of levetiracetam. Clin Pharmacokinet 2004; 43: 707–24.
7 Fay MA, Sheth RD, Gidal BE. Oral absorption kinetics of levetiracetam: the effect of mixing with food or enteral nutrition formulas. Clin Ther 2005; 27: 594–8.
8 Patsalos PN, Ghattaura S, Ratnaraj N, Sander JW. *In situ* metabolism of levetiracetam in blood of patients with epilepsy. Epilepsia 2006; 47: 1818–21.
9 Allegaert K, Lewi L, Naulaers G, Lagae L. Levetiracetam pharmacokinetics in neonates at birth. Epilepsia 2006; 47: 1068–9.
10 Glauser TA, Mitchell WG, Weinstock A, Bebin M, Chen D, Coupez R, *et al*. Pharmacokinetics of levetiracetam in infants and young children with epilepsy. Epilepsia 2007; 48: 1117–22.
11 Toublanc N, Sargentini-Maier ML, Lacroix B, Jacqmin P, Stockis A. Retrospective population pharmacokinetic analysis of levetiracetam in chidren and adolescents with epilepsy. Clin Pharmacokinet 2008; 47: 333–41.
12 Pellock JM, Glauser TA, Bebin EM, Fountain NB, Ritter FJ, Coupez RM, *et al*. Pharmacokinetic study of levetiracetam in children. Epilepsia 2001; 42: 1574–9.
13 Ensom MH, Chang TK, Patel P. Pharmacogenetics: the therapeutic drug monitoring of the future? Clin Pharmacokinet 2001; 40: 783–802.
14 Juenke J, Brown PI, Urry FM, McMillin GA. Drug monitoring and toxicology: a procedure for the monitoring of levetiracetam and zonisamide by HPLC-UV. J Anal Toxicol 2006; 30: 27–30.
15 Lancelin F, Franchon E, Kraoul L. Therapeutic drug monitoring of levetiracetam by high-performance liquid chromatography with photodiode array ultraviolet detection: preliminary observations on correlation between plasma concentration and clinical response in patients with refractory epilepsy. Ther Drug Monit 2007; 29: 576–83.
16 Contin M, Mohamed S, Albani F, Riva R, Baruzzi A. Simple and validated HPLC-UV analysis of levetiracetam in deproteinized plasma of patients with epilepsy. J Chromatogr B Analyt Technol Biomed Life Sci 2008; 873: 129–32.
17 Wang Y, Wei MJ, Wang YX, Wang L. Therapeutic drug monitoring of levetiracetam by HPLC-UV. J Pediatr Pharm 2010; 16: 34–7.
18 Chhun S, Jullien V, Rey E, Dulac O, Chiron C, Pons G. Population pharmacokinetics of levetiracetam and dosing recommendation in children with epilepsy. Epilepsia 2009; 50: 1150–7.
19 Jiang DC, Wang L, Wang YQ, Li L, Lu W, Bai XR. Population pharmacokinetics of valproate in Chinese children with epilepsy. Acta Pharmacol Sin 2007; 28: 1677–84.
20 Karlsson MO, Savic RM. Diagnosing model diagnostics. Clin Pharmacol Ther 2007: 82; 17–20.
21 Zhao Q, Jiang J, Li X, Lu ZS, Hu P. Epilepsy Therapy: Study data from Peking Union Medical College, Medical college update knowledge of epilepsy therapy. Pain Central Nerv Sys Week 2007; 5: 83.
22 Pigeolet E, Jacqmin P, Sargentini-Maier ML, Stockis A. Population

pharmacokinetics of levetiracetam in Japanese and Western adult. Clin Pharmacokinet 2007; 46: 503–13.

23 Glauser TA, Mitchell WG, Weinstock A, Bebin M, Chen D, Coupez R, *et al*. Pharmacokinetics of levetiracetam in infants and young children with epilepsy. Epilepsia 2007; 48: 1117–22.

24 Merhar SL, Schibler KR, Sherwin CM, Meinzen-Derr J, Shi J, Balmakund T, *et al*. Pharmacokinetics of levetiracetam in neonates with seizures. J Pediatr 2011; 159: 152–4.

25 Fountain NB, Conry JA, Rodríguez-Leyva I, Gutierrez-Moctezuma J, Salas E, Coupez R, *et al*. Prospective assessment of levetiracetam pharmacokinetics during dose escalation in 4- to 12-year-old children with partial-onset seizures on concomitant carbamazepine or valproate. Epilepsy Res 2007; 74: 60–9.

Acta Pharmacologica Sinica (2012) 33: 852–858
 1671-4083/12 $32.00
www.nature.com/aps

Original Article

Pharmacokinetic characteristics of vincristine sulfate liposomes in patients with advanced solid tumors

Zhao YAN[1, *], Zhong-ling ZHU[1], Zheng-zi QIAN[1], Ge HU[1], Hua-qing WANG[1], Wan-hui LIU[2], Guang CHENG[2]

[1]*Tianjin Medical University Cancer Institute and Hospital, Key Laboratory of Cancer Prevention and Therapy, Tianjin 300060, China;*
[2]*State Key Laboratory of Long-acting and Targeting Drug Delivery System, Yantai 264003, China*

Aim: To evaluate the single- and multiple-dose pharmacokinetics of vincristine sulfate liposomes (VSLI) in patients with advanced solid tumors.
Methods: In single-dose pharmacokinetic study, 16 patients were administered VSLI (1.5, 2.0, or 2.3 mg·m^{-2}) through intravenous infusion. Another 6 patients receiving vincristine sulfate (VCR, 2.0 mg) were taken as the control. In multiple-dose pharmacokinetic study, 12 patients were administered VSLI (1.5 or 1.8 mg·m^{-2}) through intravenous infusion weekly for 4 consecutive weeks. The plasma concentration of VSLI was determined using the liquid chromatography-tandem mass spectrometry (LC-MS/MS) method.
Results: After intravenous infusion of the single dose of VSLI, the plasma concentrations were characterized by bi-exponential decline curves. No statistically significant differences were observed between the main pharmacokinetic parameters in the 3 dose groups. Compared with the patients receiving VCR, the patients treated with VSLI displayed an increase in the area under the plasma concentration *vs* time curve (AUC), and a decrease in plasma clearance rates. On the 4th cycle in the multiple-dose study, the plasma concentration of VCR in all subjects prior to the weekly administration was below the lower limit of quantification (LLOQ). The calculated pharmacokinetic parameters from the subjects in the multiple- and single-dose (1.5 mg·m^{-2}) groups had no significant differences. Although the administration of liposomal VCR may significantly elevate the plasma concentration of VCR, VSLI-associated adverse events were similar to those associated with conventional VCR.
Conclusion: VSLI exhibits a lower clearance and a higher AUC compared with conventional VCR. No accumulation was observed in patients exposed to VSLI for 4 consecutive weeks. VSLI was generally tolerated in the subjects. The phase II dose of VSLI may be recommended as 4 doses of 1.5 mg·m^{-2} for treatment of patients with advanced solid tumors.

Keywords: advanced solid tumors; vincristine sulfate; liposome, pharmacokinetics, liquid chromatography-mass spectrometry

Acta Pharmacologica Sinica (2012) 33: 852–858; doi: 10.1038/aps.2012.44

Introduction

Vinca alkaloids vincristine (VCR) is a widely used chemotherapeutic agent since the 1960s[1] and its cytotoxic activity is based on its capability to alter the tubulin polymerization equilibrium and arrest cell growth during metaphase[2, 3]. VCR has a broad antitumor activity and is an important component of combination chemotherapy regimens for the treatment of childhood and adult acute lymphocytic leukemia, Hodgkin's and non-Hodgkin's lymphoma, rhabdomyosarcoma, neuroblastoma and Wilms' tumor[4, 5]. However, the rapid elimination of VCR from the blood after IV administration due to a short plasma half-life as well as dose-limiting peripheral neurotoxicity limits its anticancer activity[6].

VCR is a cell cycle-specific anticancer agent, so its therapeutic efficacy may be enhanced by prolonging the retention time of free VCR in the blood, resulting in the exposure of more tumor cells to the drug during the sensitive stage of their cell cycles[7]. Previous studies have demonstrated that the liposomal encapsulation of VCR increased its antitumor efficacy without increasing toxicity[8–11]. Marqibo® (Vincristine sulfate liposomes injection, Hana Biosciences, Inc) has been extensively studied for its capability to prolong the pharmacokinetics and subsequent exposure of VCR to cancer cells[5, 6, 12], thus increasing its antitumor activity[5, 13, 14]. However, Marqibo® was developed as a 3-vial kit containing 100 mg/mL of injectable sphingomyelin/cholesterol liposomes, 14.2 mg/mL of injectable sodium phosphate and Oncovin (injectable vincristine sulfate). Moreover, the preparation of vincristine sulfate

* To whom correspondence should be addressed.
E-mail yanzhaotj@126.com
Received 2011-12-22 Accepted 2012-04-05

liposomes (VSLI) requires an encapsulation procedure.
The liposomal formulation of VCR (VSLI) was rediscovered in the People's Republic of China the past ten years and a wide range of preclinical studies have been completed. VSLI (Luyesike Pharmaceutical Co, Ltd) was supplied as a two-vial kit containing 1 mg of VSLI freeze-dried powder and 5.68 mg/mL of injectable sodium phosphate. Thus, this formulation could be more convenient for pharmacists because an encapsulation procedure would not be necessary at the time of administration.

Pharmacokinetic (PK) studies of VSLI in Chinese subjects have not been reported to date. Therefore, this study was performed to characterize the PK profiles of VSLI in Chinese subjects with advanced solid tumors and to observe the toxicities after IV administration of this new agent. The PK profile of VSLI was also compared with conventional, unencapsulated VCR.

Materials and methods

Patient selection

This study received approval from the Ethics Committee of the Tianjin Medical University Cancer Institute and Hospital. All patients were informed about the study and were requested to sign informed consent forms prior to participating. Eligible patients had histologically confirmed malignant tumors that were either refractory to conventional forms of cancer therapy or for which no effective conventional therapy existed. It was required that patients had not undergone surgery, chemotherapy, biotherapy, endocrine therapy, or radiotherapy for at least 4 weeks prior to the start of the study. Other inclusion criteria were as follows: age of between 18 and 75 years; life expectancy of at least 12 weeks; Eastern Cooperative Oncology Group performance status of 0 to 2; adequate bone marrow function, as defined by a leukocyte count exceeding 4.0×10^9/L, an absolute granulocyte count of more than 1.5×10^9/L, a platelet count exceeding 100.0 g/L and a hemoglobin count beyond 9.0 g/L; adequate hepatic function, as defined by alanine aminotransferase (ALT), aspartate aminotransferase (AST) and total bilirubin concentration of less than 1.5 times normal; adequate renal function, as defined by a serum creatinine concentration of less than 1.5 times normal; and no evidence of preexisting neurologic dysfunction. The exclusion criteria were sensitivity to VSLI or vinca alkaloids, neurological disease, severe complications that may have a negative effect on compliance, and pregnancy or lactation.

Dosage and administration

The VSLI for injection was obtained from Luyesike Pharmaceutical Co, Ltd (Jiangsu, China). VSLI is manufactured as freeze-dried powder. Each vial contains 1 mg of VSLI powder. To prepare VSLI, 10 mL of disodium hydrogen phosphate solution was added to the VSLI powder and mixed. The solution was heated in a 50 °C water bath and mixed for 5 min in order for the internal and external aqueous phases of the liposomes to reach acid-base balance and to ensure that 90% of the VCR was encapsulated. The control drug, injectable VCR, was obtained from Shenzhen Main Luck Pharmaceuticals Inc. (Guangdong, China). A total of 16 patients in the single-dose PK study received 1.5, 2.0, or 2.3 $mg\cdot m^{-2}$ VSLI as a 60 min IV infusion. Six patients in the control group received 2.0 mg of VCR. Patients in the multiple-dose PK study received 1.5 or 1.8 $mg\cdot m^{-2}$ of VSLI weekly (one cycle) for 4 consecutive weeks.

PK sample collection

Single-dose PK 3 mL blood samples were taken at the following time points: before treatment, after infusion for 30 min, at the end of the 60 min infusion, at 5, 15, 30, and 45 min, and subsequently 1, 2, 4, 8, 12, 24, 36, and 48 h after the end of infusion. On the second and third weeks of the multiple-dose PK study, 3 mL blood samples were collected before and after the infusion. On the 4th cycle, blood samples were collected before treatment, after infusion for 30 min, at the end of the 60 min infusion, at 5, 20, and 40 min, and subsequently 1, 2, 4, 8, 12, and 24 h after the end of infusion. Blood samples were collected in heparinized tubes. Plasma was prepared by centrifugation (10 min at $600\times g$) and was subsequently stored at -80 °C until analysis.

Reagents and instruments

VCR was obtained from Luyesike Pharmaceutical Co, Ltd (Jiangsu, China). Vinblastine sulfate (VBL, internal standard) was purchased from Yifang Science and Technology Co, Ltd (Tianjin, China). High-performance liquid chromatography (HPLC) grade acetonitrile, methanol and isopropanol were purchased from Honeywell Burdick & Jackson (Muskegon, MI). Analytical grade *n*-hexane and dichloromethane were purchased from Fuchen Chemical Reagent Factory (Tianjin, China).

The chromatographic system consisted of an Agilent 1100 HPLC system (Agilent Technologies, Palo Alto, CA, USA) coupled to an API 4000 triple quadrupole mass spectrometer (Applied Biosystems, Concord, Ontario, Canada) and an Agilent Eclipse XDB C_{18} column (50 mm×4.6 mm, 5 μm, Agilent Technologies, Palo Alto, CA, USA). Data were processed using Analyst 1.4.1 software (Applied Biosystems/MDS SCIEX, Concord, Ontario, Canada).

Bioanalytical methods

The solvents used for gradient elution were A) methanol and B) water; each was adjusted to pH 3 by the addition of 10 mmol/L ammonium acetate and 2.9 mL/L formic acid. The conditions for the gradient elution were as follows: 0 to 0.5 min, 55% to 95% solvent A; 0.5 to 2.0 min, isocratic 95% solvent A; 2.0 to 2.1 min, 55% to 95% solvent A; and 2.1 to 5.5 min, isocratic 55% solvent A. The flow rate was 0.45 mL/min, and the column temperature was set to 40 °C. During the analysis, 10 μL of sample was injected using the autosampler, and the sample was then carried into the column. A mass spectrometer with a TurboIonSpray (ESI) source was operated in positive ion mode. The source temperature was maintained at 500 °C, and the spray voltage was set to 5500 V. The nebulizer (Gas 1), heater (Gas 2), curtain, and collision activated

dissociation (CAD) gases were set to 50, 55, 15, and 8 psi, respectively. The declustering potential values were 119.2 and 105 V, and the collision energy values were 50.5 and 59.7 V for VCR and VBL, respectively. Quantification was performed using multiple reaction monitoring of the transitions *m/z* 825.8→807.5 for VCR and *m/z* 811.7→224.0 for VBL (Figure 1).

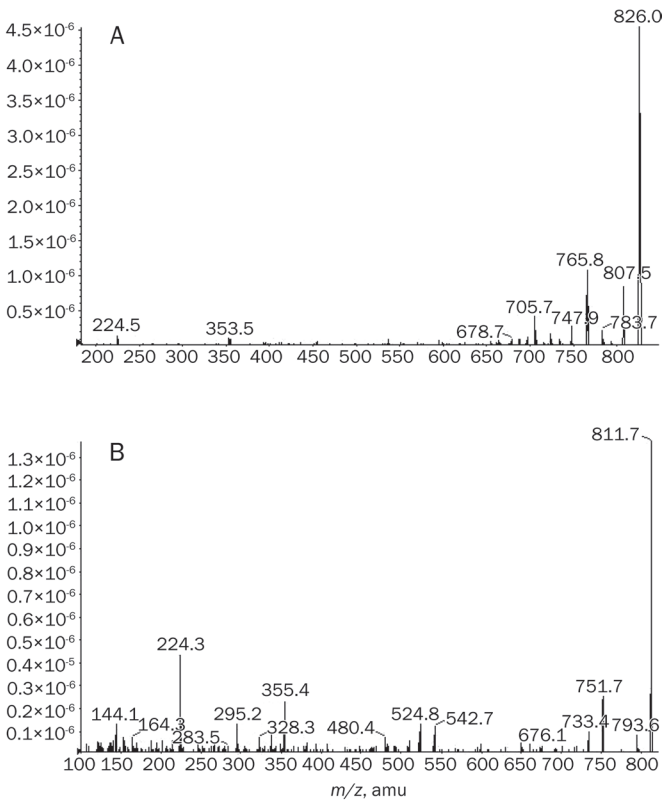

Figure 1. Production of mass spectra of (A) VCR and (B) VBL.

Serial calibration standards at concentrations of 0.5, 2, 10, 40, 100, 400, and 800 ng/mL were prepared by adding 100 μL of the appropriate working solutions to 100 μL of the blank plasma. The calibration curves were established by determining the peak area ratio [VCR/internal standard (Y) versus VCR concentration (X)]. QC samples were prepared in the same way to obtain concentrations of 1 (low), 80 (medium) and 600 (high) ng/mL. All frozen plasma samples were thawed at room temperature. For sample extraction, 100 μL plasma sample was added to a 10 mL centrifuge tube, along with 100 μL solvent A-solvent B (7:3, *v/v*, pH=3), 100 μL 150 ng/mL VBL solution, 100 μL acetonitrile and 200 μL water. The mixture was vortexed for 2 min, and 3 mL *n*-hexane-dichloromethane-isopropanol (2:1:0.1, *v/v/v*) was then added. After vortexing for 7 min, the mixture was centrifuged at 3600 r/min for 10 min. The upper organic phase was placed into another centrifuge tube and evaporated to dryness under a nitrogen stream. The residue was reconstituted in 100 μL of the solvent A-solvent B (7:3, *v/v*) solution, and 10 μL of that solution was injected into the LC-MS/MS system.

PK data analysis and statistical analysis

The plasma concentration-time data were analyzed using non compartmental methods. The PK analysis system DAS 2.1 (Anhui, China) was used to assess the PK parameters. The peak plasma concentration (C_{max}) and the time to peak plasma concentration (T_{max}) were obtained via experimental observations. The elimination half-life ($t_{1/2}$) was calculated as 0.693/Zeta (Zeta is the slope of terminal phase). The area under plasma concentration *vs* time curve (AUC) from zero to infinity ($AUC_{0-\infty}$) was equivalent to the sum of the areas from time zero to the time of the last measured concentration and was calculated using the linear trapezoidal method (until C_{max}), the log-trapezoidal method (until the last measurable concentration), and the extrapolated area. The extrapolated area was determined by dividing the final measured concentration by the slope of the terminal log-linear phase. Trough values on cycle 2 and cycle 3 were averaged for each dose level. All statistical tests were two-tailed, and a *P* value of 0.05 was considered significant. Differences in the mean values of the physical examinations and in PK parameters among the 3 groups were compared with analysis of variance or the Kruskal-Wallis test using SPSS (Statistical Package for the Social Sciences) software, version 16.0. The *t*-test or Wilcoxon's test was used to investigate the differences between the two groups.

Results

Representative chromatogram and validation of the analytical method

The retention times of VCR and the internal standard were 2.7 and 2.8 min, respectively. VCR and the internal standard in plasma were completely separated without significant interferences. The calibration curve was linear over the concentration range of 0.5 ng/mL to 800 ng/mL. The equation for the calibration curve was Y=0.00157X+0.00273 (r=0.9982, n=5). The LLOQ was 0.5 ng/mL. The intra-day precision for the low, medium and high concentration QC samples was 9.1%, 4.1%, and 4.8%; the inter-day precision was 3.2%, 5.2%, and 6.6%; and the accuracy was 99.5%, 102.8%, and 100.4%. The relative standard deviation (RSD) was less than 10.0%. The extraction recoveries for the three gradient concentration of VCR were 77.5%, 76.7%, and 78.7% and the extraction recovery for the internal standard was 86.8%. The matrix suppression for the QC samples and the internal standard was -3.0%, 31.1%, 44.6%, and 26.5%. The concentration of VCR was stable in the working solution at room temperature for 10 h or at -4 °C for one month and was stable in human plasma for 3 freeze-thaw cycles, at room temperature for 12 h, or at -80 °C for 4 months prior to extraction. The differences between stored and freshly prepared solutions were within 15%.

Patient characteristics

A total of 34 eligible and consenting patients with advanced carcinoma were recruited for this study. There were 22

patients enrolled in the single-dose and 12 patients enrolled in the multiple-dose PK studies. No statistically significant differences were found in age, height, weight, body surface area, or body mass index (BMI) among the patient groups. The characteristics of the patients are shown in Table 1. All of the subjects had received prior chemotherapy and 13 of the subjects had received prior radiation therapy.

Single-dose PK study

The total VCR plasma concentration versus time profiles of the patients who received 1.5 to 2.3 mg·m^{-2} of VSLI or 2 mg of VCR were shown in Figure 2. The plasma concentration profiles for all patients were characterized by a biexponential decline after infusion. The VCR concentrations fell below or were marginally above LLOQ within 48 h after infusion.

PK parameters were determined for the 22 subjects. The primary PK parameters are summarized in Table 2. The mean peak concentration (C_{max}) for the patients in the 3 VSLI groups was 141.3, 127.0, and 218.7 ng/mL. The mean AUC from time zero to infinity (AUC_{0-inf}) was 229.3, 242.9, and 316.1 ng·h·mL^{-1} for the 3 groups. The mean values of C_{max}, AUC_{0-inf}, $t_{1/2}$ and clearance (CL_z) were not different among the 3 doses (P>0.05); however, significant differences in the mean volume of distribution (V_z) values were observed (P<0.05). No correlation was found between the observed PK profile (AUC) and patient characteristics (age, height, weight, body mass index, or body surface area). When compared with patients who received the conventional 2-mg dose of VCR, patients who received 1.5 to 2.3 mg·m^{-2} VSLI had an increased AUC_{0-t} and AUC_{0-inf}, as well as decreased CL (P<0.05).

Multiple-dose PK study

A total of 12 patients in the multiple-dose study received 1.5 or 1.8 mg·m^{-2} VSLI weekly for 4 consecutive weeks. The mean

Table 1. Summary of patient characteristics. Data are expressed as mean (Range).

	Single-dose pharmacokinetics				Multiple-dose pharmacokinetics	
	1.5 mg·m^{-2} VSLI (n=5)	2.0 mg·m^{-2} VSLI (n=6)	2.3 mg·m^{-2} VSLI (n=5)	2 mg VCR (n=6)	1.5 mg·m^{-2} VSLI (n=6)	1.8 mg·m^{-2} VSLI (n=6)
Sex						
Male	1	2	2	2	2	3
Female	4	4	3	4	4	3
Age (years)						
Median, Range	64 (56–73)	53 (37–63)	45 (18–59)	54 (22–65)	41 (19–62)	41 (28–54)
Height (cm)						
Median, Range	168 (153–182)	162 (154–178)	168 (155–175)	164 (160–168)	166 (157–178)	167 (156–175)
Weight (kg)						
Median, Range	72 (60–82)	61 (55–69)	70 (61–85)	64 (50–75)	70 (55–85)	64 (42.5–90)
Body surface area (m^2)						
Median, Range	1.83 (1.62–1.98)	1.65 (1.54–1.86)	1.77 (1.61–2.01)	1.69 (1.54–1.82)	1.77 (1.54–2)	1.69 (1.38–2.01)
BMI (kg·m^{-2})						
Median, Range	25.7 (22.6–27.8)	23.1 (21.8–24.6)	24.7 (21.1–28.1)	23.6 (18.1–27.5)	25.6 (22–32.4)	22.7 (17.5–29.4)
ECOG status at entry						
0–1	5	6	5	6	5	6
2	0	0	0	0	1	0
Tumor types						
Lymphoma	4	4	2	6	4	5
Breast cancer	1	0	1	0	0	0
Lung cancer	0	1	1	0	0	1
Others (Ewing's sarcoma, Ovarian cancer, Renal carcinoma, laryngocarcinoma)	0	1	1	0	2	0
Prior therapy						
Chemotherapy	5	6	5	6	6	6
Radiotherapy	3	3	2	0	1	4

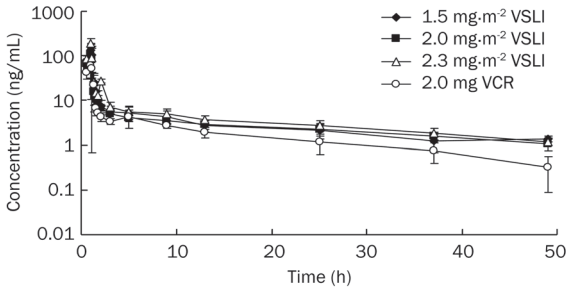

Figure 2. Mean logarithmic concentration versus time plot after administration of 1.5 mg·m^{-2} (♦, *n*=5), 2.0 mg·m^{-2} (■, *n*=6), 2.3 mg·m^{-2} (△, *n*=5) of VSLI and 2 mg of VCR (○, *n*=6).

PK parameters for the 4th cycle are summarized in Table 2. As shown in Figure 3, the mean concentration-time curves of the subjects after multiple doses of VSLI were comparable to the corresponding mean values from subjects after a single dose of VSLI. These findings demonstrate that the administration of 4 doses of VSLI does not markedly alter the clearance of total vincristine from the plasma. Total VCR plasma concentrations from all subjects before the weekly treatments were below the LLOQ. A comparison of the calculated PK parameters among the subjects in the multiple- and single-dose 1.5 mg·m^{-2} groups did not show significant differences, indicating that that no detectable accumulation was observed in total VCR with repeated doses of VSLI for 4 consecutive weeks.

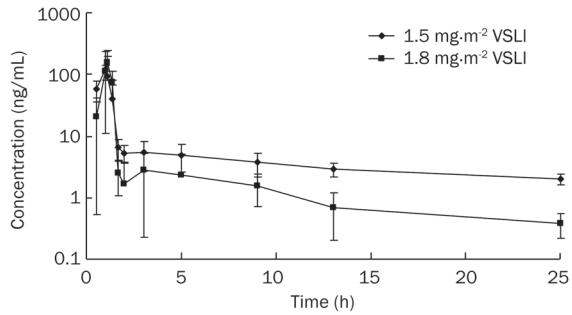

Figure 3. Mean logarithmic concentration versus time plot after multiple doses of VSLI on the 4th cycle (♦, *n*=5; ■, *n*=6).

Safety

The National Cancer Institute's Common Terminology Criteria for Adverse Events (AEs) (version 3.0) were used to grade AEs. Table 3 presents a summary of the toxicities that were associated with VSLI administration. All of the VSLI doses had similar toxicity profiles. The most common toxicities irrespective of grade, causality, or VSLI dose included peripheral neuropathy (75%), neuropathic pain (61%), constipation (46%) and abdominal distention (36%). Nausea, vomiting, anorexia and hypocalcemia were also common. Non-hematologic toxicity was more common than hematologic toxicity. Grade 3/4 toxicities were neuropathic pain, insomnia, alterations in numbers of neutrophils or other leukocytes, hypermagnesemia and hyponatremia. Other reported AEs were mild.

Discussion

A 3-vial kit of Marqibo® consists of empty liposomes, VCR and buffer solution, and requires an encapsulation procedure. However, the VSLI in this study was developed as freeze-dried powder containing encapsulated VCR. Such a freeze-dried formulation of VCR liposomes could be more convenient for pharmacists. In addition, this formulation could increase the stability of VCR and prevent the settlement and aggregation of empty liposomes during storage. The encapsulation efficiency of VSLI exceeds 85%, and its diameter is stable in the range of 100 to 200 nm. Previous stability data showed that the diameter and VCR content of VSLI remained stable within 7 h when administered intravenously. The animal VSLI PK study showed that the V_z and CL of total VCR in VSLI-treated rats was significantly reduced as compared with the V_z and CL in rats that had been treated with the free drug, resulting

Table 2. Main PK parameters of total VCR after IV administration of VSLI or VCR. Values are expressed as mean (SD). [a]*P*>0.05 *vs* 2.0 mg VCR group. [b]*P*<0.05 *vs* 2.0 mg VCR group. [d]*P*>0.05 *vs* 1.5 mg·m^{-2} single-dose VSLI group. [e]*P*<0.05 *vs* 1.5 mg·m^{-2} single-dose VSLI group. [g]*P*>0.05 *vs* 2.0 mg·m^{-2} single-dose VSLI group.

Parameters	Single-dose pharmacokinetic study				Multiple-dose pharmacokinetic study	
	1.5 mg·m^{-2} VSLI (*n*=5)	2.0 mg·m^{-2} VSLI (*n*=6)	2.3 mg·m^{-2} VSLI (*n*=5)	2.0 mg VCR (*n*=6)	1.5 mg·m^{-2} VSLI (*n*=6)	1.8 mg·m^{-2} VSLI (*n*=6)
C_{max}/ng·mL^{-1}	141.3 (40.8)[b]	127.0 (80.4)[ad]	218.7 (127.4)[adg]	83.4 (39.5)	134.8 (138.6)[d]	85.2 (28.3)[d]
AUC_{0-t}/ng·h·mL^{-1}	205.1 (57.4)[b]	201.2 (51.4)[bd]	281.8 (95.0)[bdg]	121.3 (15.6)	169.8 (88.3)[d]	130.3 (15.7)[d]
AUC_{0-inf}/ng·h·mL^{-1}	229.3 (66.3)[b]	242.9 (60.8)[bd]	316.1 (106.5)[bdg]	140.3 (25.0)	216.7 (77.6)[d]	155.5 (25.2)[d]
MRT_{0-t}/h	8.9 (1.7)[a]	11.8 (1.6)[be]	10.6 (2.7)[adg]	8.4 (2.8)	5.9 (1.2)[e]	5.8 (0.6)[d]
MRT_{0-inf}/h	15.1 (3.9)[a]	24.9 (9.4)[ad]	17.8 (4.5)[adg]	15.9 (8.2)	17.6 (8.2)[d]	12.3 (4.7)[d]
$t_{1/2z}$/h	17.5 (6.7)[a]	24.9 (8.3)[ad]	19.2 (2.5)[adg]	16.0 (7.9)	17.4 (6.2)[d]	13.0 (6.0)[d]
T_{max}/h	1.05 (0.04)[a]	0.85(0.27)[ad]	0.8 (0.27)[adg]	0.89 (0.31)	0.93 (0.21)[d]	0.83 (0.26)[d]
CL_z /L·h^{-1}	7.0 (1.9)[b]	8.7 (2.3)[bd]	8.0 (2.7)[bdg]	14.6 (2.7)	7.6 (2.4)[d]	11.8 (1.9)[e]
V_z/L	166.3 (42.2)[b]	309.0 (119.8)[ae]	217.5 (70.8)[adg]	321.9 (123.4)	202.1 (112.2)[d]	212.7(82.0)[d]

Table 3. Summary of VSLI-associated AEs.

Toxicity (CTC)	No with grade 1–4 toxicity VSLI dose level ($mg \cdot m^{-2}$)				
	Single-dose group			Multiple-dose group	
	1.5 (*n*=5)	2.0 (*n*=6)	2.3 (*n*=5)	1.5 (*n*=6)	1.8 (*n*=6)
Neurology					
Peripheral neuropathy	2	5	3	5	6
Neuropathic pain	–	2	5	4	6
Gastrointestinal					
Constipation	2	3	3	1	4
Nausea	2	2	2	1	2
Emesis	2	1	2	1	1
Diarrhea	1	–	–	1	1
Abdominal pain	1	–	1	1	3
Abdominal distention	1	1	1	3	4
Anorexia	–	–	–	4	5
Oral cavity mucositis	–	–	–	1	–
Blood					
Leukocytes	2	2	1	1	3
Anemia	–	1	2	2	3
Lymphopenia	1	–	–	–	1
Neutrophils	–	1	–	2	3
Constitutional					
Fever	–	–	2	3	3
Fatigue	–	1	–	1	3
Insomnia	–	–	1	–	1
Weight Loss	–	–	–	–	1
Skin					
Alopecia	–	–	2	–	–
Cardiovascular					
Supraventricular arrhythmia	–	1	–	1	–
Metabolic					
Hypokalemia	–	–	–	1	–
Hypomagnesemia	1	1	–	–	–
Hypermagnesemia	–	1	–	–	–
Hyponatremia	–	–	–	2	–
Hypocalcemia	–	–	2	4	2
Hypercholesteremia	–	–	–	–	1
Hypertriglyceridemia	–	–	–	1	2
ALT	–	–	–	3	2
AST	–	1	–	1	2
Bilirubin	–	–	–	1	–
Alkaline phosphatase	–	–	–	1	–

in a significantly increased AUC (unpublished data). Previous studies have demonstrated that following the administration of VSLI, levels of free VCR in plasma were below the lower limits of quantitation [12]. Therefore, the VCR levels measured in plasma following the administration of VSLI reflected liposomally encapsulated drug[5].

In this study, the PK of VSLI in patients with advanced solid tumors was evaluated and compared with the corresponding PK data for conventional VCR. The total VCR plasma concentration values for patients treated with VSLI were measured using the LC-MS method. The LLOQ for VCR was 0.5 ng/mL. The method was specific, sensitive and convenient for the assessment of total VCR in biological samples. The plasma concentration of total VCR in all of the patients followed a biexponential decline after a single IV administration of VSLI. Bedikian *et al*[6] reported that the total VCR of some metastatic melanoma patients with adequate liver function followed a biexponential decline, but that of others followed a monoexponential decline. Interpatient variability in the rate of decline resulted in the monoexponential or biexponential profiles. However, differences in elimination at each dose level were not observed in the current study. In addition, the pharmacokinetic parameters in this study were not consistent with previous international studies. One previous study[12] of Marqibo® indicated that the mean±SD AUC_{0-inf} and C_{max} at a dose of 2.0 $mg \cdot m^{-2}$ were 15.6±11.9 $\mu g \cdot h \cdot mL^{-1}$ and 11.0±0.3 μg/mL, respectively, which were higher than the results obtained in this study. The differences in pharmaceutical formulations of VSLI or in characteristics of the patients (*ie*, race) in the previous study versus the current study may have contributed to these inconsistencies. It is also possible that methodological differences applied in different laboratories may be responsible for these inconsistencies. No significant differences were observed in the main PK parameters among the 3 dose groups ($P>0.05$), indicating that the effect of the dose on single-dose pharmacokinetics of VSLI was insignificant. Moreover, the results of this study indicate that the liposomal encapsulation of VCR significantly increases plasma AUC and decreases plasma clearance rates compared with conventional VCR. Therefore, total plasma VCR exposure following the administration of VSLI appears to be greater than that of conventional VCR because of the difference in elimination. The liposomal encapsulation of VCR protects the drug from the early phase of rapid elimination that is observed with nonliposomal VCR[15]. Previous studies have demonstrated that increasing VCR retention in liposomal systems improves the therapeutic index by increasing the duration of drug exposure to the tumor tissue[8, 10, 16–18]. These PK properties of VSLI may potentially increase VCR accumulation in tumors and obtain greater efficacy over conventional VCR.

The mean AUC, $t_{1/2}$, C_{max}, T_{max}, and V_z from the subjects in the multiple-dose 1.5 $mg \cdot m^{-2}$ group were similar to those from the subjects in the single-dose 1.5 $mg \cdot m^{-2}$ group. No significant differences were observed in the main PK parameters between the two groups, indicating that that no accumulation was observed with repeated administration of VSLI for 4 consecutive weeks. These data indicate that the pharmacokinetics of VSLI had no apparent change after repeated administration, which is consistent with previous data[6].

In this study, PK parameters from patients who tolerated VSLI administration well were calculated. A previous tolerability study reported that 4 subjects who received 1.8 $mg \cdot m^{-2}$ of VSLI weekly for 4 consecutive weeks withdrew from the

study because of treatment-associated peripheral neurotoxicity[19]. In the current study, most VSLI-associated AEs varied from mild to moderate. Grade 3/Grade 4 toxicities were neuropathic pain, insomnia, alterations in numbers of neutrophils or other leukocytes, hypermagnesemia and hyponatremia. The most frequently observed AEs included peripheral neuropathy, neuropathic pain and gastrointestinal disorders. Based on the differences in body surface areas, the total dosage of VSLI for 4 cycles ranged from 9.24 to 14.47 mg, which was significantly higher than the routine dosage of VCR. The results of this study show that VSLI-associated AEs were similar to those associated with conventional VCR, although the administration of liposomal VCR may greatly increase the dosage. Correlation analyses were conducted to determine if a relationship could be established between the observed PK profile and toxicities; no correlation was found, possibly because of the small sample size. Out of the 12 patients with 4 consecutive weeks of VSLI treatment, 8 were assessed to have stable disease as measured by an increase in tumor size of less than 25%.

In conclusion, VSLI exhibited a longer circulation half-life and higher AUC compared with conventional VCR, which provides VSLI with an advantage over conventional VCR. After repeated administration of VSLI, the accumulation of total vincristine was not observed in the plasma. Furthermore, the pharmacokinetics of VSLI were not altered significantly after 4 doses of 1.5 or 1.8 $mg \cdot m^{-2}$. The prolonged plasma retention of VSLI compared with conventional VCR may potentially improve antitumor efficacy. VSLI was generally tolerated in the subjects. Considering previously published data on VSLI tolerability[19, 20], the phase II dose of VSLI may be recommended as 4 doses of 1.5 $mg \cdot m^{-2}$ for the treatment of patients with advanced solid tumors.

Acknowledgements

This work was supported by a grant from Major Science and Technology Project of "National Significant New Drug Creation" (No 2010ZX09401-401).

Author contribution

Zhao YAN designed the research; Zhao YAN, Zhong-ling ZHU, Hua-qing WANG, Ge HU, Zheng-zi QIAN, Wan-hui LIU, and Guang CHENG performed the research; Zhao YAN and Zhong-ling ZHU analyzed the data; Zhao YAN and Zhong-ling ZHU wrote the paper.

References

1 Embree L, Gelmon K, Tolcher A, Hudon N, Heggie J, Dedhar C, *et al*. Pharmacokinetic behavior of vincristine sulfate following administration of vincristine sulfate liposome injection. Cancer Chemother Pharmacol 1998; 41: 347–52.

2 Schou M, Amdisen A, Thomsen K. Clinical and experimental observations concerning the absorption and elimination of lithium and on lithium poisoning. Acta Psychiatr Scand Suppl 1968; 203: 153–5.

3 Owellen RJ, Hartke CA, Dickerson RM, Hains FO. Inhibition of tubulin-microtubule polymerization by drugs of the Vinca alkaloid class. Cancer Res 1976; 36: 1499–502.

4 Gidding CE, Kellie SJ, Kamps WA, De Graaf SS. Vincristine revisited. Crit Rev Oncol Hematol 1999; 29: 267-87.

5 Bedikian AY, Silverman JA, Papadopoulos NE, Kim KB, Hagey AE, Vardeleon A, *et al*. Pharmacokinetics and safety of marqibo (vincristine sulfate liposomes injection) in cancer patients with impaired liver function. J Clin Pharmacol 2011; 51: 1205–12.

6 Bedikian AY, Papadopoulos NE, Kim KB, Vardeleon A, Smith T, Lu B, *et al*. A pilot study with vincristine sulfate liposome infusion in patients with metastatic melanoma. Melanoma Res 2008; 18: 400–4.

7 Zhigaltsev IV, Maurer N, Akhong QF, Leone R, Leng E, Wang J, *et al*. Liposome-encapsulated vincristine, vinblastine and vinorelbine: a comparative study of drug loading and retention. J Control Release 2005; 104: 103–11.

8 Boman NL, Masin D, Mayer LD, Cullis PR, Bally MB. Liposomal vincristine which exhibits increased drug retention and increased circulation longevity cures mice bearing P388 tumors. Cancer Res 1994; 54: 2830.

9 Webb MS, Logan P, Kanter PM, St-Onge G, Gelmon K, Harasym T, *et al*. Preclinical pharmacology, toxicology and efficacy of sphingomyelin/cholesterol liposomal vincristine for therapeutic treatment of cancer. Cancer Chemother Pharmacol 1998; 42: 461–70.

10 Webb MS, Harasym TO, Masin D, Bally MB, Mayer LD. Sphingomyelin-cholesterol liposomes significantly enhance the pharmacokinetic and therapeutic properties of vincristine in murine and human tumour models. Br J Cancer 1995; 72: 896.

11 Kanter PM, Klaich GM, Bullard GA, King JM, Bally MB, Mayer LD. Liposome encapsulated vincristine: preclinical toxicologic and pharmacologic comparison with free vincristine and empty liposomes in mice, rats and dogs. Anticancer Drugs 1994; 5: 579–90.

12 Bedikian AY, Vardeleon A, Smith T, Campbell S, Namdari R. Pharmacokinetics and urinary excretion of vincristine sulfate liposomes injection in metastatic melanoma patients. J Clin Pharmacol 2006; 46: 727–37.

13 Rodriguez MA, Pytlik R, Kozak T, Chhanabhai M, Gascoyne R, Lu B, *et al*. Vincristine sulfate liposomes injection (Marqibo) in heavily pretreated patients with refractory aggressive non-Hodgkin lymphoma. Cancer 2009; 115: 3475–82.

14 Thomas DA, Kantarjian HM, Stock W, Heffner LT, Faderl S, Garcia-Manero G, *et al*. Phase 1 multicenter study of vincristine sulfate liposomes injection and dexamethasone in adults with relapsed or refractory acute lymphoblastic leukemia. Cancer 2009; 115: 5490–8.

15 Gelmon KA, Tolcher A, Diab AR, Bally MB, Embree L, Hudon N, *et al*. Phase I study of liposomal vincristine. J Clin Oncol 1999; 17: 697–705.

16 Mayer LD, Masin D, Nayar R, Boman NL, Bally MB. Pharmacology of liposomal vincristine in mice bearing L1210 ascitic and B16/BL6 solid tumours. Br J Cancer 1995; 71: 482–8.

17 Mayer LD, Nayar R, Thies RL, Boman NL, Cullis PR, Bally MB. Identification of vesicle properties that enhance the antitumour activity of liposomal vincristine against murine L1210 leukemia. Cancer Chemother Pharmacol 1993; 33: 17–24.

18 Shan S, Flowers C, Peltz CD, Sweet H, Maurer N, Kwon EJ, *et al*. Preferential extravasation and accumulation of liposomal vincristine in tumor comparing to normal tissue enhances antitumor activity. Cancer Chemother Pharmacol 2006; 58: 245–55.

19 Hu G, Wang HQ, Yan Z, Hao XS. A phase I clinical trial of vincristine sulfate liposome: tolerance and safety evaluation of successive administration. Chin J New Drugs Clin Rem 2010; 29: 766–70.

20 Hu G, Wang HQ, Yan Z, Hao XS. A phase I clinical trial of vincristine sulfate liposome for evaluating its single-dose tolerance and safety. Chin J New Drugs 2009; 18: 628–31.